Generalization of 3D mesostructures for a microstructural approach of soil behavior

João Chueire

N° d'ordre NNT : 2023ISAL0045

THESE de DOCTORAT DE L'INSA LYON
membre de l'Université de Lyon

Ecole Doctorale N° 162
Mécanique, Energétique, Génie Civil, Acoustique

Spécialité / Ingénierie Civil

Soutenue publiquement le 30/06/2023, par :
João GONCALVES DE O CHUEIRE

Generalization of 3D mesostructures for a microstructural approach of soil behavior

Devant le jury composé de :

O'SULLIVAN Catherine	Professeure des Universités, Imperial College London	Rapporteur
WAN Richard	Professeur des Universités, University of Calgary	Rapporteur
DARVE Félix	Professeur des Universités, Université Grenoble Alpes	Examinateur
KUHN Matthew	Professeur des Universités, University of Portland	Examinateur
NOUGUIER-LEHON Cecile	Maîtresse de Conférences, École Centrale de Lyon	Examinatrice
RADJAI Farhang	Directeur de Recherche, Université de Montpelier	Examinateur
DAOUADJI Ali	Professeur des Universités, INSA Lyon	Directeur de thèse
NICOT François	Professeur des Universités, Université Savoie Mont-Blanc	Co-directeur de thèse
WAUTIER Antoine	Ingénieur Docteur, INRAE	Co-encadrant de thèse

Aknowledgments

First of all, I would like to thank my thesis directors, Ali Daouadji, François Nicot, and Antoine Wautier, for supporting me both in the construction of my thesis project and in its realization. I thank them for their patience and confidence in my work, which helped me stay on course during the time of my thesis. Thank you for considering me as a colleague from the beginning of the thesis.

I would also like to express my gratitude to the members of the jury for their interest in my thesis work and for agreeing to evaluate it. Thanks to Catherine O-Sullivan and Richard Wan, who agreed to take on the crucial task of referees. I would also like to warmly thank Félix Darve, Matthew Kuhn, Cecile Nougueir, and Farang Radjai, who have accepted to be part of my thesis committee and who have taken a keen interest in monitoring the progress of my work. I thank them for the precious time they gave me and for the quality of their feedback and advice.

Furthermore, I would like to thank all my colleagues from GEOMAS for the countless discussions and for the good atmosphere that they contributed to, in particular the PhD and PhD candidates that accompanied me throught the way (Nicole, Rosy, Gianlucca, Thomas La., José, Samer, Janet, Nour, Adnan, Julien, Clara, Sadek, Nisrine, Asterios, Maryam, Jean-Baptiste, Thomas Lh., Hamza, Garance, Yining).

I would like to extend a special thought to Adriane Clerc, Ma Qiriu, Marie Miot, Na Deng, and Tao Wang, who formed the group of weekly Ph.D. meetings, where most of the ideas that form the basis of this thesis were perfected.

On a more personal level, I would like to highlight the constant support of my parents and my family throughout my studies – without them, I certainly would not have arrived to where I am today! In particular for Pedro, Audrey et Thiago for supporting me here in France!

I will end these acknowledgments with a special thought for my dear wife, Izabel, (and our cats Amora, Rebelle and Lola) who shared my successes and my doubts throughout my thesis. Thank you for your encouragement and your kindness, as I would never have gotten here without you!

Résumé

Dans le domaine des matériaux granulaires, le lien entre les variables microscopiques (forces de contact et déplacements) et les variables macroscopiques (contraintes et déformations) nécessite l'utilisation d'une échelle intermédiaire appelée échelle mésoscopique. À cette échelle, plusieurs mésostructures ont été identifiées et étudiées en tant qu'agrégats de grains ou de vides attachés tels que par exemple les boucles, les espaces poreux et les chaînes de force.

Parmi ces mésostructures, les boucles sont particulièrement intéressantes car elles sont riches d'informations et sont les seules à ne pas être définies dans des conditions 3D. Ces boucles forment des polygones simples capables de diviser un milieu 2D en espaces fermés plus petits se sorte à ce que la somme de la surface des boucles est égale à la surface totale de l'échantillon. Par conséquent, l'application directe de la définition des boucles à des conditions 3D conduit à la formation de formes 2D dans un milieu 3D ce qui est irréaliste.

Dans cette thèse, nous proposons d'étendre la définition des boucles au cas tridimensionnel. Dans un premier temps, une méthode d'identification des boucles (2D) basée sur la fusion de cellules créées par une triangulation de Delaunay est analysée. Ensuite, une extension de cette procédure à des conditions 3D est proposée. Comme les structures identifiés ne sont plus représentatives du concept mathématique de boucle (ou cycle), elles sont appelées Clusters. Ces structures se révèlent plus complexes que leurs homologues en 2D, ce qui nécessite un plus grand nombre de métriques pour les quantifier. C'est pourquoi les concepts de taille et d'ordre se distinguent respectivement par le nombre de grains et le nombre de frontières externes. En outre, le concept de déformabilité est introduit comme moyen de quantifier l'interconnectivité d'une structure en clusters.

Une série d'essais triaxiaux 3D complexes a été réalisée grâce au logiciel LIGGGHTS qui est basé sur la méthode des éléments discrets (DEM) . Par la suite, une application a été développée pour analyser les propriétés des clusters pendant le trajet de chargement et en fonction de la proximité d'autres structures granulaires internes coexistantes (chaînes de force et bandes de cisaillement).

Il est démontré que l'indice des vides moyen et la déformabilité (capacité à se déformer) des clusters augmentent avec leur taille. En outre, une augmentation du nombre de clusters plus denses est observée pendant la phase de contraction de la déformation macroscopique et des clusters plus lâches pendant la dilatation. Enfin, une relation entre les chaînes de force, les bandes de cisaillement et les clusters est établie. Toutes les caractéristiques des clusters mentionnées sont connues pour les boucles 2D. Les clusters peuvent

donc être considérés comme des extensions des boucles dans des conditions 3D.

Mots clés : Méthode des éléments discrets (DEM), Milieux granulaires, Mésostructures, Clusters, Boucles, Tessellation de Delaunay, Chaines de force, Bande de cisaillement.

Abstract

In the field of granular materials, a link between microscopic variables (contact force and displacement) and macroscopic variables (stress and strain) requires the use of an intermediate scale called "the mesoscopic scale." At this scale, several mesostructures have been identified and studied as aggregates of attached grains or voids, such as loops, pore spaces, and force chains.

From these mesostructures, loops are particularly noteworthy, as they are the only structures not yet defined in 3D conditions. Loops form simple polygons that are capable of partitioning a 2D media into smaller closed spaces, where the sum of the loop surfaces is equal to the total surface of the specimen (known as the pavement property). Therefore, direct application of the definition of loops to 3D conditions leads to the formation of 2D shapes in a 3D media, thereby compromising the pavement property.

In this thesis, we propose to extend the loop definition to the 3D case. First, a method to identify loops (2D) based on the merger of cells created through a Delaunay triangulation is analyzed. Then, an extension of this procedure to 3D conditions is proposed. As the newfound structures are no longer representative of the mathematical concept of a loop or cycle, they are named "clusters." These structures are shown to be more complex than their 2D counterpart, necessitating a larger number of metrics to quantify them. For this reason, the concepts of size and order are distinguished as the number of grains and the number of external frontiers, respectively. Furthermore, the concept of deformability is introduced as a way to quantify the interconnectivity of a loop-like structure.

A series of 3D discrete element method (DEM) triaxial tests were performed in the software LIGGGHTS. An application was then developed to analyze the properties of clusters during the loading path and in regard to proximity to other coexisting internal granular structures (force chains and shear bands).

It is shown that the average void ratio and deformability (capacity to deform) of clusters increase with their size. Furthermore, an increase in the number of denser clusters is observed during the macroscopic strain contraction phase and of looser ones during the dilation. Finally, a relation between force chains, shear bands, and clusters is established. All the aforementioned cluster characteristics are known for 2D loops. Thus, clusters can be seen as extensions of loops in 3D conditions.

Keywords: Discrete element method (DEM), Granular materials, Mesostructures, Clusters, Loops, Delaunay tessellation, Force chains, Shear bands.

Contents

List of Figures

List of Tables

Chapter 1

Introduction

Motivation

Granular materials, such as sand, rocks, coffee beans, and rice, are widespread in everyday life. Loosely speaking, the behavior of these materials is akin to a simple solid under the effects of gravity. However, granular assemblies comprise a multitude of individual particles of finite sizes, each presenting their own degrees of freedom [1]. Thus, the individual movement of particles gives granular materials incredible complexity.

The emerging properties of granular materials can be analyzed at three different scales. At the microscopic scale, the material behavior is dictated by the contact laws governing pairs of grains. Therefore, at this local scale, granular materials are inherently discrete. Conversely, at the macroscale, the specimen behaves as a continuum material for which the constitutive law results from a combination of the intergranular contact forces and geometrical properties. In between, the mesoscale bridges these two extremes, linking the properties of individual grains to the behavior of a collective. Several structures have been identified and studied at this intermediate scale as aggregates of attached grains or voids, such as loops, pore spaces, and force chains.

Three main groups of numerical models exist to simulate the behavior of granular materials. The first group of models comprises those based on continuum theory. Through a constitutive law, the continuum deformation is obtained and later related to the motion of particles. However, these models fail to consider local fluctuations in particle displacements and particle rotations, which significantly influence the bulk behavior of granular media [2].

By contrast, the second group of models consists of those based on the discrete element method (DEM). DEM models simulate each particle individually, and the specimen's response is directly related to the inter-particle interaction. Nevertheless, simulating natural materials is complex, as computational costs increase drastically with the number of particles and complexity of shapes.

Finally, there is multiscale modeling. This group combines the benefits of both previous classes by simulating a continuum-scale system but with a constitutive law enriched from numerical models of finer scale instead of resorting to empirical constitutive models through homogenization techniques.

Thus, the performance of these models is directly linked to a good understanding of fine-scale physics.

An excellent example of multiscale modeling is the so-called H-model, which describes the fine scale of a granular assembly through the distribution of mesostructures with varying orientations [3]. The inspiration for this model comes from the structure of loops, a closed circuit of grains in contact enclosing a common void space. Loops form simple polygons capable of partitioning a 2D media into smaller closed spaces, where the sum of the surface of the loops is equal to the total surface of the specimen (known as the "pavement property").

However, applying loops identification techniques in 3D conditions would lead to the formation of 2D shapes in a 3D media. The newfound structures would have no volume and be often imbricated, thus losing the important pavement property. Consequently, extending this definition to a convenient 3D structure is necessary in order to properly expand the 2D framework and the related results to 3D cases.

Over the past few years, this dimension change has been regarded as a significant challenge, and several methods to extend the notion of loops to 3D have been proposed. These methods included partitioning the specimen into tetrahedrons through a weighted Delaunay tessellation and then applying a merging criterion to join neighboring tetrahedrons into larger structures. The proposed merging criterion was mainly based on applications of another field of study, the pore space. However, they have yet to be proven entirely successful [4].

Objective

This thesis proposes a procedure to extend the 2D loop structure to 3D, keeping the properties that make it an essential feature of a granular assembly.

Chapter 2 summarizes some of the relevant background literature. A brief description of the mechanics of granular material at the macro-, meso-, and microscales is given. Several concepts essential for the development of this study are introduced, such as the properties of the loop structure. Later, the principles of the discrete element method (DEM) are presented, followed by the intricacies of LIGGGHTS, the chosen software to apply it.

Chapter 3 encompasses the theoretical and numerical procedures developed to accomplish the proposed task. First, a review of a method to identify loops (2D) is shown, followed by the proposal of a procedure to extend this notion to 3D conditions. The resulting structures are named "clusters," as this nomenclature better matches their observed topological features. Next, procedures to identify cluster characteristics and interactions

with other mesostructures are proposed. Finally, the numerical tools used or developed to test the theoretical methods are presented. Resulting in several numerical prismatic triaxial simulations of dense soil under three loading paths: drained, undrained, and constant deviatoric stress.

Chapter 4 outlines the mechanical response of the numerical triaxial simulations, validating the behaviors expected for dense soils. The macroscopic and mesoscopic responses of the granular assembly are analyzed and correlated.

Chapter 5 presents the results related to clusters, with the aim of validating known loop characteristics in 3D conditions. First, all identified clusters are studied as a group, highlighting the scope of characteristics of clusters. Next, clusters are categorized based on whether they are destroyed or created with regard to the drained loading path. Then the transition between cluster categories will be analyzed for each loading path, highlighting the evolution of the specimen's internal structure. Finally, the influence of clusters in other coexisting internal structures of granular materials is investigated.

Chapter 2

Granular materials behavior and material approaches at different scales

2.1 Foreword

In this chapter the overall mechanical behavior of granular materials will be delineated at several scales, laying a foundation for the tools developed in this work. First, the analytical behavior of the soil will be presented at the three previously mentioned scales (micro, meso, and macro). Notably, the loop structure will be presented in 2D, leading the way to the development of an equivalent 3D structure. Finally, a short introduction will be made to the discrete element method (DEM) numerical mode and its application in the software LIGGGHTs.

2.2 Macro-mechanics, instabilities, and shear band

A granular assembly, when inspected as a whole, behaves homogeneously. However, the underlying discrete nature of the particles makes their overall behavior highly nonlinear and dependent on load history and previous deformation states. Thus, the conditions in which the specimen was assembled and the loads applied will have a major influence on its mechanical behavior.

For example, Figure 2.1 illustrates the classic response of three soil specimens with the different initial void ratios for the same drained triaxial loading path.

A loose specimen can be identified by the predominance of contraction (negative value for the volumetric strain) and hardening (increase in deviatoric stress) during the entirety of the test. Conversely, dense and medium-dense specimens will present a dilation (expansion) phase after an early contraction. In addition, these last two cases go through an early hardening phase until a deviatoric peak value is reached, where failure occurs, leading to a softening phase (decrease in overall strength).

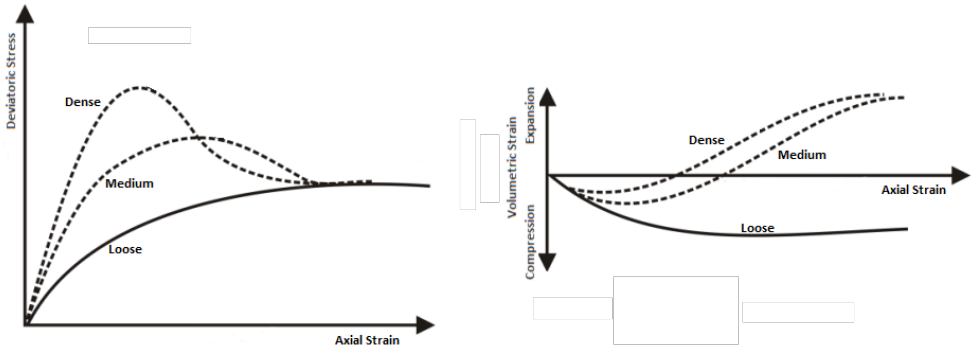

Figure 2.1: Shear stress and volumetric strain evolution for general categories of soil under a triaxial test: loose, medium, and dense. [5]

At the microscopic level, from the beginning of the loading, a network of regions of concentrated deformation starts to form, known as "slip lines." Depending on the initial density and confining stress, these smaller concentrated deformations persist even at large strains, thus causing a failure in all specimen regions [6, 7, 8]. This generalized failure is known as a "diffuse failure" [9]. However, for other configurations, the deformation concentrates into a narrow band traversing the specimen forming one or multiple shear bands, as illustrated in Figure 2.2. These bands divide the sample into regions that seemingly move as separate rigid-body objects.

Figure 2.2: Shear band formation in a cylindrical specimen [10].

Despite these differences, for a given material and initial mean effective stress, at large strains, they all reach an equivalent steady state, where the volume and the deviatoric stress stay constant for an increase in axial strain. When the material's void ratio and volumetric strain also reach a steady

state, the specimen is in the so-called critical state, where shearing may continue indefinitely without any changes in volume or effective stresses.

2.2.1 Shear bands properties

Although shear bands have been extensively studied, the specific details of their origin proved elusive to decipher [11, 12, 13, 14, 15, 16, 17, 18, 19, 7, 8, 20, 21]. Even in controlled conditions, it is hard to predict, with precision, exactly when and where these patterns form and how they evolve. Experimental studies have identified that shear band formation is altered by several factors linked to the specimen condition, including porosity, the inherent anisotropy, the particle shape and size, and effective mean stress [22, 23, 24].

A long-standing question on the origins and transformation of slip lines and shear bands has existed due to the complexity of plastic deformation in the pre-failure domain. In fact, most of the observations of their co-evolution have been restricted to numerical simulations [21]. However, recent experimental results on the formation of slip lines imply that shear bands are not formed from microbands. Instead, it is suggested that both patterns coexist near failure, generating the final failure pattern [25]. Indeed slip lines are predominant in the pre-failure regime while shear bands persist in the failure domain [26, 8].

It has been shown that each shear band in granular materials involves a significant number of grains. Several studies have approximated the width of the shear band as a function of the average grain diameter using experimental and theoretical formulations [14, 16]. However, a conclusive quantity was not observed, and results vary from 8 to 18 average grain diameters obtained for different experiments [27, 15, 19, 28]. In addition, shear bands are not a perfect plane of constant thickness but maintain a wavy form with varying thickness throughout the structure [16].

The formation of the shear band results from plastic strain, which is reflected microscopically as the reorganization of grains, creating large voids in the region. In fact, the volumetric and deviatoric strain concentration in a narrow band implies an increase in volume. Furthermore, it has been shown that the local void ratio around the shear band can be larger than the maximal void ratio for the whole specimen obtained by standard experimental methods [16, 29, 30].

Under a microscope, soil particles such as sand show very irregular and rough surfaces. Contact between two particles generates a rolling resistance that impacts the behavior of the soil. Indeed, this effect allows larger void ratios to persist that would have collapsed otherwise. It can be noted that

particle orientation (ellipsoidal particles) changes sharply on the boundary of shear bands, and a high gradient of particle rotations develops during the formation of the shear band [16, 19, 31].

Finally, the values of several of the characteristics of granular materials inside the shear band differ from the rest of the specimen. Thus, a common practice to identify the shear band is computing the characteristics of the granular material locally, highlighting regions of concentrated values. The most used characteristics are, among others, particle rotation, translational particle velocity, void ratio, and deviatoric strain [16, 32, 33, 34, 29, 7, 30].

2.2.2 A note on instability and second-order work

The classic approach of failure in soils considers its limit as a surface in the stress space, generally through the Mohr–Coulomb criterion, characterized by friction angle and cohesion. Consequently, all the failure states are assumed to correspond to the stress points of this failure surface [35].

However, it has been shown that soil failure can be observed before the classic theory surface limits are reached in some cases, e.g., sand liquefaction. For example, in loose sand isotropically consolidated under undrained triaxial conditions, instability occurs in the domain contained between the critical state line (CSL) and the instability line (IL) [36, 37].

Generally, reaching the CSL is the reason for soil failure, since it can be seen as the upper limit of the soil strength (Mohr–Coulomb). However, if specific loading paths are adopted (different from the isochoric loading path), conditional failure may occur before this limit. Therefore, a different criterion is needed to identify these paradoxical instabilities (before classic limit states).

Following Hill's sufficient condition of stability [38], a specimen may be considered unstable if at least one existing loading direction leads to a negative value of the second-order work. The bifurcation domain can then be defined as the set of points that fulfill this condition. In these cases, the system regime can evolve from a quasi-static regime to a dynamic one [39]. Hill's criterion applied at the material point scale in the general framework of the continuum mechanics says that for any strain-specific loading paths adopted (different from the isochoric loading path), conditional failure may occur before this limit for an additional $(\Delta\sigma, \Delta\varepsilon)$ couple where $\Delta\sigma$ and $\Delta\varepsilon$ are conjugated through the constitutive relation. [40, 41, 42].

Over the past few decades, and irrespective of the scales considered (from the elementary microstructural scale to the macrostructural scale for engineering purposes), the second-order work criterion has proved its capability to identify unstable states [43]. The vanishing of the second-order work has

been shown to be a necessary condition and a precursor of inertial transition, characterizing failure. Furthermore, this criterion has been used at all three scales pertaining to granular materials: the macroscale [40, 41], the mesoscale [42], and the microscale [44, 45, 46].

2.3 Obtaining information from the grain scale

At the elementary scale, the microscale, the study of granular materials is condensed to discrete particles as solids of their own. At this scale, interaction between pairs of particles occurs through physical contact, as illustrated in Figure 2.3. A study of this scale is generally made through numerical methods, as acquiring information at the grain scale is rarely feasible for experimental projects.

For each contact between particles, a repulsion force is generated between them, which is generally considered punctual and does not necessarily have the same direction as the contact plane. Each particle has its position, movement, and forces acting upon it.

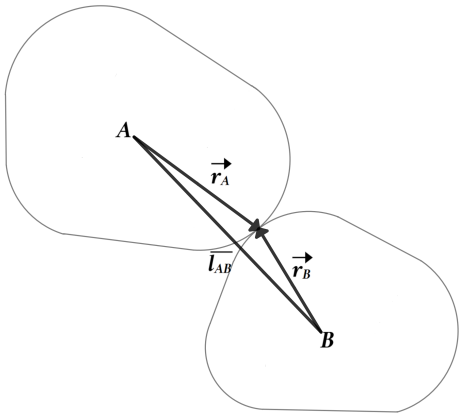

Figure 2.3: Illustration of a simple contact between two particles in 2D. Branch vector $\overline{l_{AB}}$ and each particle contact vector $\vec{r}_A$ and $\vec{r}_A$ are represented

Using these elementary properties, physical quantities can be constructed in three perspectives: configuration, force, and movement [47]. Configuration quantities, such as anisotropy and coordination numbers, reveal information on the statistical distribution of contact and force inside the specimen. Force quantities allow for an approximation of particle and region stress. Movement quantities, such as particle translation, highlight the path through which external deformation permeates the specimen. Any of these properties can be computed for a wide range of closed domains, enabling either a local

analysis or an approximation of the macroscopic properties from the average of the local values to be obtained.

2.3.1 Anisotropy: quantifying contact networks

The contacts described above form a network that will assure the equilibrium of the system at a particular state in a static or quasi-static condition. Thus, the contact network will evolve with the displacement of each grain during loading. To quantify this evolution, a second-order tensor called fabric tensor is calculated through the normal of each vector [48], as shown by equation (2.1).

$$F_{ij} = \frac{1}{N_c} \sum_{k=1}^{N_c} n_i^k n_j^k \tag{2.1}$$

N_c is the total number of contacts in the specimen, n_k^i is the i-th component of the normal vector k of the characteristics studied (force normal or contact normal).

The given tensor brings forth the particularities of the contact direction distributions through the anisotropy value (obtained by computing the square root of its second invariant) and the analysis of its eigenvectors. A high anisotropy value indicates that contacts were formed in a privileged direction, while a null value indicates an even distribution. Furthermore, two origins for the anisotropy can be distinguished: inherent and induced. The former results from the technique used to create the specimen, while the latter is generated by the loading history.

It has been shown that the macroscopic response of a specimen is directly linked to the anisotropy state, thus defining a stress–force–fabric relation for 2D systems [49]. In general, tests show that the maximum value of contact force anisotropy occurs alongside the measured peak resistance of the material [49]. Furthermore, the ratio between normal and tangential stress (frequently associated with the mobilized angle of friction for cohesionless materials) can be inferred from force and contact anisotropy. This suggests that cohesion-less granular assemblies carry deviatoric loads through their ability to develop an anisotropic contact network [50, 49, 51, 29].

2.3.2 Average stress on a discrete system

In continuum mechanics, the stress state of a region can be approximated by averaging the stress of all the points included within it. However, this defi-

nition is only valid for continuous media and is not adapted for the discrete nature of granular materials.

It has been shown that, under static or quasi-static conditions, a consistent definition of the stress tensor for a closed domain of a granular assembly can be derived through the volume average of the tensorial product between the contact forces and the branch vectors of contacts [52, 53, 49, 54, 55, 56, 57], as defined in Figure 2.3. Thus, defining the classic Love–Weber formula depicted by equation (2.2) as:

$$\bar{\sigma}_{ij} = \frac{1}{V} \sum_{c=1}^{C} f_i^c l_j^c \tag{2.2}$$

with the summation over all contacts C, where f_k^i is the i-th component of the force of the contract c, l_k^j is the j-th component of the branch vector of the contact c, and V is the volume of the analyzed region.

This tensor has been a staple in the granular materials community for its ease of use and precision. Furthermore, it enables the computation of the stress over almost any closed domain, making an in-depth analysis of local granular behavior possible.

2.3.3 Average strain on a discrete system

Strain can be defined as the measure of change in the length, area, or volume of a system. Thus, the discrete nature of granular materials renders convoluted the definition of this quantity with the complex motion of grains. Many researchers have developed techniques of diverse theoretical origins to compute the strain locally with varying degrees of complexity and success [58, 59, 60, 1, 61, 62, 63, 30].

In the article by Bagi [59], the author describes a granular assembly as a dual system composed of material and space cells. The first consists of all the space closer to a particular grain than any other grain in the specimen. Thus, each grain will have its own material cell surrounding it, forming a closed domain. A common face between the material cell of two neighboring grains is formed by the region located at the same distance between each grain. Thus, if two grains are in contact, there must be a material face between their cells.

Space cells, however, are a sub-product of material cells. They are formed by creating a line between the center of the grains whose material cells share a surface. These lines will then partition the granular media into triangular

shapes (or tetrahedra in 3D) with grain centers as nodes and encompass a common void space between them.

It can be shown that the deformation of the granular assembly is directly correlated with the deformation of the space cell system, thus with the strain tensor. Furthermore, the material system is directly connected to the stress tensor, making the dual system an incredible tool for analyzing the granular macrostructure [59].

In the particular case of spherical particles, the material cell is equivalent to the Dirichlet tessellation, while space cells are equivalent to the Delaunay tessellation. The latter can map a cloud of points into triangles in 2D or tetrahedra in 3D. Thus, by applying it to the center of the particles, we obtain a triangulated mesh that subdivides the domain into several smaller elementary shapes that will henceforth be referred to as cells. Furthermore, the connections formed between the grain's centers will be known as edges, and the element that divides two cells will be called a frontier (edge in 2D and surface in 3D). This is illustrated in Figure 2.4 where a 2D example is shown.

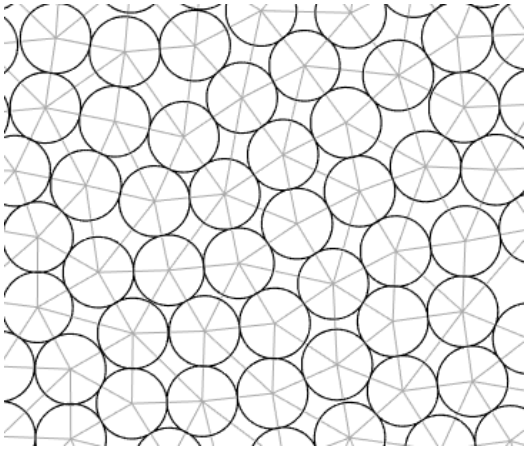

Figure 2.4: Delaunay tessellation of a 2D granular material showing the triangular cells formed by the tessellation edges.

Each cell is a simplex formed by $D + 1$ grains and frontiers. When analyzing any single cell, a frontier will have the same identification number as the only grain from the cell that does not form part of it. Thus, a surface vector b^k of a frontier k can be defined as the outward vector whose length is equal to the surface (or length in 2D) of the frontier k.

To quantify something akin to the region of influence of an edge, the complementary area vector d^e is defined. For a specific edge e between two grains m and n, d^e is the sum of all cells that share the edge e of the difference

between the surface vectors with the same ID as the grains forming the edge, as described by equation (2.3).

$$d^e = d^{mn} = \frac{1}{D(D+1)} \sum_{c=1}^{C} (b^{n(c)} - b^{m(c)}) \tag{2.3}$$

To create a second-order tensor capable of quantifying the strain locally, the complementary area vector d^{mn} is multiplied by the difference between the incremental displacements of the grains connected through the edge e. For a given closed domain, the average incremental gradient tensor is provided by the following equation:

$$\bar{E}_{ij} = \frac{1}{V} \sum_{e=1}^{N} \Delta u_i^e d_j^e \tag{2.4}$$

N is the number of all edges of the specimen, Δu^e the difference of incremental displacements between both nodes of the edge e, and d^e the complementary area vector of the edge e .

The incremental strain tensor is the symmetric part of the tensor of equation (2.4), while the skew-symmetric tensor reflects the average rotation of the cells. It can be concluded that knowledge of the position and displacement of particles allows for an approximation of the strain tensor of a granular assembly. Furthermore, this definition can be applied to any closed domain inside the specimen, thus enabling a thorough analysis of the strain distribution.

Finally, it is interesting to note that the strain formulation based on a linear interpolation of the incremental displacements of the particles [58, 63, 30, 42] can be transformed to match equation (2.4). The main difference between both formulations is the base element of the analysis: The former requires a closed domain (i.e., 2D loop or cell), while the latter can be applied to a single edge.

2.4 The intermediate scale

Several structures in an intermediate scale have been identified to bridge the microscale of individual grains and the macroscale of the whole specimen. These mesostructures are agglomerations of at least three grains that share common properties, allowing them to combine the physics of individual particles with that of larger structures. In the scope of this thesis, only the mesostructures force chain and loops will be analyzed.

2.4.1 Force chains

As mentioned earlier, the externally applied force is transmitted inside the granular matter through contact forces. They propagate from grain to grain, forming a highly ramified force network. Through photo-elastic disks, many researchers performed tests to identify the characteristics of this force propagation [64, 65, 66, 67, 68]. This material can change its light transmission properties depending on the stress state of the molecules. Thus, by applying loads to an assembly of these disks, the path of the force could be observed with the naked eye, as illustrated in Figure 2.5.

It has been shown that two force network systems appear inside granular materials. The weak network, representing most of the specimen (approximately 60%), is composed of particles in which the stress value is inferior to the mean value of the force within the sample [55, 69]. On the contrary, the strong network is organized into chains of highly stressed particles. Both networks have an influence on the strength of the granular assembly. The strong one is responsible for most of the force transmission, while the weak one will ensure the stability of the strong network.

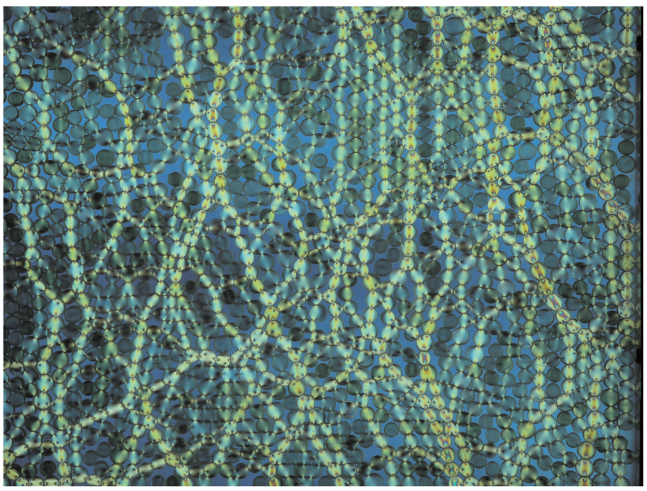

Figure 2.5: Force chain obtained during a biaxial compression test of photo-elastic disks [68].

An objective description of force chain structures can be summarized as follows [70] :

- A force chain is formed by at least three particles;
- The most compressive principal stress of each particle within a chain must be above the average value of the specimen;

- The difference between the direction of a particle's most compressive principal stress and the direction of the branch vector of the contact with the next chained particle must be inferior to a defined θ value (commonly chosen at 45°).

The stress tensor of each particle can be obtained through the Love–Weber formula defined in Section 2.3.2. For each particle, the summation is made over all the contact forces acting in the particle and divided by the volume of the particle.

The importance of force chains on the macroscopic behavior of granular materials has been shown in many numerical experiments [71, 72, 70, 67, 73, 2, 74, 75, 76]. The stability of these structures is directly connected to the resistance and the volumetric performance of granular materials. Furthermore, the bending and buckling of force chains have been shown to be directly related to the loss of strength of the specimen and the development of shear bands [77, 78, 79, 30, 80]. As force chains are deformed inside shear bands, the void ratio increases, thus highlighting the dilatancy of this region. [2, 74, 81]. Force chains have also been regarded as responsible for non-affine strain and the mechanisms of energy dissipation inside granular materials [2].

It has been shown that the granular material properties influence the formation of force chains [73]. Increasing inter-particle friction, specimen density, or grain size dispersion tends to create force chains that are straighter, less ramified, and more stable. In addition, denser systems also tend to produce shorter chains. Consequently, the increased strength of denser materials can be seen as a product of the characteristics of their force chains.

2.4.2 Loops as a contact cycle

In 2D, loops are geometric shapes formed by contacts between grains forming a closed circuit that encloses a common void space. They were first identified by Satake [82] in groundbreaking research of a graph-theoretical approach to granular materials. As illustrated in Figure 2.6, loops emerge in several shapes and sizes (number of grains).

Loops are a direct product of the force and geometry of the contact between grains. While the physical contact determines the form of the loop, contact forces assure the stability of the entire mesostructure.

It can be demonstrated that the physical capabilities of loops are directly linked to their size (number of grains forming it). Smaller loops tend to be more stable while larger ones are capable of changing forms to adapt to external stimuli, thus being deformed without breaking any contacts. For this reason, the analysis of loops quantities is generally made through the

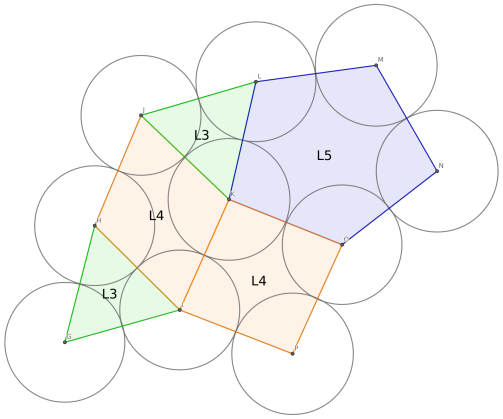

Figure 2.6: Example of loops of different sizes (L3, L4, and L5) being formed in a theoretical granular specimen.

definition of categories based on their size, as follows: loops 3, loops 4, loops 5, and loops 6+. The last one contains all loops of a size larger than 6 as they have equivalent physical capabilities and become increasingly rare with the growth in size (in 2D).

Loops have the potential to partition the entire granular media into small unique elements. These are closed domains where stress and strain values can be defined using the formulations presented in section 2.3. Furthermore, macroscale properties can be upscaled as the surface weighted average of loops properties [55, 56, 57]. This local analysis at the mesostructure level can highlight the unique properties of the granular assembly.

It has been shown that the average void ratio of loops increases with their size, indicating that as the number of grains forming a loop increases, so does the amount of void they encapsulate. Furthermore, recent works reported that the volumetric behavior of granular materials is linked to the evolution of loops L3 and L6+ [20, 28], showing a direct relationship between local loop surface area and specimen-wide properties.

Loops composed of three grains are demonstrated to be a key source of stability and reinforcement of force chains [75, 20, 30]. As force chains start buckling, their surrounding loops start to merge, increasing in size and void ratio.

Furthermore, the buckling of force chains has been directly linked to the formation of shear bands, as mentioned in Section 3.2.2. Thus, a link between the local increase in loop size and shear bands could be implied. In fact, direct analysis of the local distribution of loops has shown that inside the shear bands, loops of greater size are more prevalent in relation to the

rest of the specimen [28].

The measure of the elongation of loops obtained through a *loop fabric tensor* has been used to investigate the relation between loops and local strain tensor [83]. It has been shown that loops elongated through the minor principal strain direction were prone to dilatancy, while loops elongated through the major principal direction showed more often a contracting behavior [75, 20].

When the critical state of a specimen is reached, the distribution percentage of each loop category has been shown to attain a constant value [84, 20]. Further analysis of the topological evolution of loops indicated that this steady state originates from an equilibrium between the creation and destruction of loops, as their difference is shown to fluctuate near zero [28].

In addition, a constitutive model has been created based on the topological properties of loops [3]. The H-directional model describes the material through a combination of mesostructures oriented in different directions. In the 2D case, the base structure is the hexagonal loop L6, and the collective rearrangement in granular materials is accounted for in the H-model through the deformation of the H-cells.

2.5 Discrete element method numerical simulation

The discrete element method model, better known as DEM, was first developed by Cundal [85] and later improved by Cundal and Strack [86]. It uses the position and velocity of discrete particles to study their movements, thus being able to compute the next instant in time of all grains in a granular specimen. Among the different methods applied in the field of the micromechanics of granular materials, DEM is the most widely used and developed tool, thanks to the simplicity it is able to simulate the discrete nature of the particles. Since the creation of DEM, computational power has increased greatly and the use of this technique became widely used by the scientific community [49, 87, 88, 89, 90, 91, 76, 30].

Since each particle is simulated as its own rigid body with many degrees of freedom, a simulation containing thousands of particles becomes a very complex system. As shown in the previous sections, homogenization techniques are capable of averaging the local data to transform them into quantities corresponding to the macroscopic variables observed. Thus, a DEM model enables the acquisition of data capable of linking the behavior of the micro- and macroscales in a way that is almost impossible to obtain in experimental

settings.

2.5.1 LIGGGHTS

LIGGGHTS(R)-PUBLIC is an open-source software for particle simulations using the DEM. It is distributed by DCS Computing GmbH, Linz, Austria.

LIGGGHTS is built on the foundations of LAMMMPS, a well-known molecular dynamics software largely utilized in physics and chemistry. It has been modified for the general case of granular materials, using physical contact instead of electrical potentials to quantify the interaction between particles [92]. As LIGGGHTS is not programmed to handle particle breakage, each particle is considered unbreakable.

LIGGGHTS has seen use in the industrial and academic fields. Among others, Huang et al. [93] have studied the behavior of stress paths in 3D in the critical state, Hurley and Andrade [94] have modeled a simple shear test, and Sufian et al. [95] have analyzed the evolution of the pore network under cyclic loading.

2.5.2 Calculation cycle

The calculation cycle of a DEM model consists of the determination of the position of the particles at the next timestep through the use of the contact forces in a time interval Δt between t_n and t_{n+1}. At t_n, the position and velocity of particles are known. Two particles are considered in contact if there is an interpenetration of their exterior walls. Once the forces are calculated, the new position and velocity of particles are determined for the next step, t_{n+1}. This cycle can be written in the following steps:

- Through the velocity and position of particles, update the list of particles in contact at the instant t_n;
- Calculate, for each contact, the force of contact between two grains in contact using the contact law;
- For each particle, integrate the contact forces and calculate the acceleration for the time interval Δt;
- Update the position and velocity of the particles for the next timestep t_{n+1}.

At the end of the last step, all the data needed to execute the first step are available, forming a closed and repeatable cycle.

2.5.3 Particle shape and contact law

For a DEM simulation, contact detection is the most time-consuming task, which is directly related to the shape of the simulated particle. The least demanding shapes to simulate are spheres, which only require the position and radius of particles for a contact to be detected. However, particles of real granular materials can be presented in many different geometries, from more uniform materials such as coffee grains and seeds to amorphous ones such as sand. In this regard, many techniques have been developed, for example, the use of clumped spheres [96, 29], polygonal particles [97, 98, 99], or more complex algorithms such as the level-set DEM [100]. Nevertheless, a simplification of grain geometry dramatically improves the time needed for execution, and thus the use of spherical particles will be envisioned for this work as no specific type of material is being modeled.

A contact law can be defined as the function that will determine the force of contact $\overrightarrow{F}$ considering the position of implicated particles. Thus, the choice of the contact law will have a deep impact on the mechanical response at all scales, as it is an integral part of the calculation cycle.

The most common contact law in DEM is the elasto-frictional law, introduced by Cundall and Strack [86]. When a contact is detected, two virtual springs are created, one normal and one perpendicular to the contact plane, illustrated in Figure 2.7a.

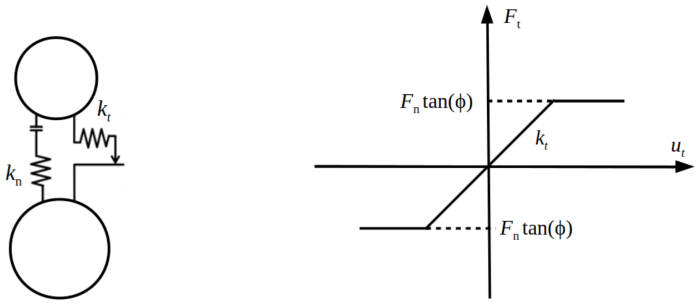

(a) Illustration of contact springs. (b) Limitation of tangential spring force.

Figure 2.7: Illustration of the elasto-frictional contact law. On the left is the representation of virtual springs and on the right is the limitation of the tangential force through the normal force and a friction coefficient [47].

The first contact spring, of rigidity k_n, simulates the physical contact between two particles. The laws of physics prevents the superposition of two rigid undeformable objects, and thus this spring will create a repulsion force between contacting particles that increases with the interpenetration

of the two modeled particles. Furthermore, as the materials simulated are non-cohesive, this spring cannot exert a negative force.

The second contact spring, of rigidity k_t, models the friction physics between particles in contact and is limited through a friction coefficient μ inherent to the simulated material, as illustrated in Figure 2.7b.

LIGGGHTS uses a variation of the elasto-frictional law, adding a damping effect to the force values. The contact force between two particles i and j is given by the following equations :

$$\begin{aligned} F &= F_n + F_t \\ F_n &= (k_n.\delta n_{ij} - \gamma_n V_{n,ij}) \\ F_t &= min(\, k_t \delta t_{ij} - \gamma_t V_{t,ij} \;,\; \mu F_n \,) \end{aligned} \tag{2.5}$$

with k_n the rigidity of the normal spring, δn_{ij} the particle interpenetration in the normal direction, $V_{n,ij}$ the relative velocity of the particles in the normal direction, k_t the rigidity of the transversal spring, δt_{ij} the particle interpenetration in the transversal direction, $V_{t,ij}$ the relative velocity of the particles in the transversal direction, and μ the friction coefficient of the material. γ_n and γ_t are coefficients with no physical meaning calculated as a function of material parameters, as further described in equations (2.6).

The value of these linear spring rigidities can be estimated in many ways. For the case of the software LIGGGHTS, they are calculated in function of the material parameters of the particles in contact. With i and j being two grains in contact, the rigidity of the springs simulating the contact between them is calculated through the following equations:

$$\begin{aligned} k_n &= \tfrac{4}{3} E' \sqrt{R' \delta_n}, \quad \gamma_n = -2\sqrt{\tfrac{5}{6}} \beta \sqrt{S_n m'} \geq 0, \\ k_t &= 8 G' \sqrt{R' \delta_n}, \quad \gamma_t = -2\sqrt{\tfrac{5}{6}} \beta \sqrt{S_t m'} \geq 0, \\ S_n &= 2E' \sqrt{R' \delta_n}, \qquad S_t = 8G' \sqrt{R' \delta_n}, \\ \beta &= \frac{ln(e)}{\sqrt{ln^2(e) + \pi^2}}, \quad \frac{1}{E'} = \frac{(1-\nu_i^2)}{E_i} + \frac{(1-\nu_j^2)}{E_j}, \\ \frac{1}{G'} &= \frac{2(2-\nu_i)(1+\nu_i)}{G_i} + \frac{2(2-\nu_j)(1+\nu_j)}{G_j}, \\ \frac{1}{R'} &= \frac{1}{R_i} + \frac{1}{R_j}, \quad \frac{1}{m'} = \frac{1}{m_i} + \frac{1}{m_j} \end{aligned} \tag{2.6}$$

with, for particle i, R_i the radius i, m_i the mass, ν_i the rigidity ratio, E_i the elasticity modulus, G_i the shear modulus and e the restitution coefficient.

Furthermore, perfectly spherical grains have the capacity to rotate around any axis without affecting their neighbors, a characteristic that is not very common in real materials. To decrease the influence of this effect, a common

practice is to add a rolling resistance to the model, through the addition of a third virtual spring to the contact law. Furthermore, it has been shown that phenomena like shear banding can only be well developed on DEM simulations of spherical particles when rolling resistance is applied [88, 101, 96, 102, 103].

The method "elastic-plastic spring-dashpot 2" (EPSD2) proposed by Iwashita and Oda [88] was added to the contact law, as described in equation (2.7):

$$\begin{aligned} k_r &= k_t R^2 \\ \Delta M_r^k &= -k_r \Delta \Theta_r \\ M_{r,t+\Delta t}^k &= M_{r,t}^k + \Delta M_r^k \\ M_{r,t+\Delta t}^k| &\leq M_r^m \\ M_r^m &= \mu_r R' F_n \end{aligned} \tag{2.7}$$

with k_r the rolling spring rigidity, k_t the transversal spring rigidity (cf. equation 2.6), R the radius of the particle, and μ_r the rolling friction coefficient.

The spring torque M_r^k can be easily calculated through the relative rotation between the two particles $\Delta\Theta_r$. Later the total rolling resistance torque is limited by the value M_r^m calculated in function of the user-defined rolling friction coefficient μ_r. This coefficient is a dimensionless parameter representing the tangent of the maximal angle of a slope upon which the rolling resistance torque balances the torque produced by the acceleration of gravity [104].

2.5.4 Critical timestep and model stabilization

As shown in the section 2.5.2, the calculation cycle of a DEM simulation occurs for a time interval Δt, which must be chosen wisely to ensure the validity of the contact physics of the discrete model. If, for example, the interval taken is too high, the movement of particles may generate a high interpenetration of particles or even superposition, which no longer has a physical meaning thus invalidating the model. Conversely, a simulation with a low timestep requires several more calculation cycles to reach equivalent results to those obtained with an efficient timestep.

To do so, the way the efforts are transmitted inside the granular matter must be considered. The modeled particles must not transmit forces faster than would happen in reality. Miller and Pursey have shown that Rayleigh waves are responsible for 67% of the energy irradiated, in comparison with the 7% for dilation waves and 26% for distortion waves. Since the latter have the same velocity as the first waves, the hypothesis that the energy is totally

transmitted by Rayleigh waves can be asserted [90]. This approximation has been widely used in academic and industrial applications [105, 106, 107, 108]. For a certain material M, the critical timestep Δt_c is calculated by the following equation :

$$\Delta t_c = \frac{\pi r}{0.1631\nu + 0.8766}\sqrt{\frac{\rho}{G}} \tag{2.8}$$

with r the radius of the smallest grain, ν the stiffness ratio, and ρ the density G the shear modulus.

Δt_c is the maximal value that can be chosen for an interval between two timesteps. If more than one material is being used in the simulation, Δt_c must be calculated individually and the smallest value should be taken.

The critical timestep, described in equation (2.8), determines the maximal value upon which the simulation timestep should be chosen to maintain the physical properties of the model. In the case of the software LIGGGHTS, a further reduction of 80% of this value is indicated, resulting in a timestep $\Delta t = 0.2\Delta t_c$.

It is interesting to note that the shear modulus G is in the denominator of equation (2.8). Thus, a common technique to increase the critical timestep is to lower the elastic modulus of the chosen material. This approximation should be handled with caution, as decreasing the elastic modulus impacts the stiffness of the particles. Keeping a value above 10^7Pa is indicated as it has been shown to maintain the average normal overlap between particles below 0.5% [109, 110].

2.6 Concluding remarks

This chapter provided fundamental concepts and reviewed recent advances in the understanding of granular materials and presented the three internal structures that will be the focus of the thesis (loops, force chains, and shear bands). It was shown that there is a deep connection between these three structures; however, loops have only been defined in a 2D environment. The present thesis proposes the definition of a loop-like structure in 3D conditions capable of maintaining the properties that make it so attractive to the scientific community.

Chapter 3

Procedures and tools for identification of internal structures

3.1 Foreword

In this chapter, the theoretical procedures to identify the sought structures will be presented, beginning with a loop-like structure in 3D conditions and followed by force chains and shear bands. Next, the parameters of the script developed for the DEM simulation in the software LIGGGHTS will be presented, followed by a succinct presentation of the post-processing tool developed for this work.

3.2 Identification procedures and characteristics of mesostructures

3.2.1 Loops and clusters

To be able to transpose the definition of loops to 3D conditions, a procedure to identify the former needs to be developed. To do so, the domain will be subdivided into contact-based partitions using the space cell domain [59]. In the particular case of spherical particles, it is translated to the use of a Delaunay tessellation.

This definition will be shown to be effective in the identification of 2D loops, and later transposed to 3D conditions generating the cluster structures. Finally, the definition of quantities capable of extracting cluster characteristics will be presented in the form of anisotropy, size, order, and void ratio.

Space cell systems as contact-based divisions

To create a procedure to identify loop-like structures in 2D and 3D, first a parceling of the granular assembly into elementary contact-based structures

is envisioned. Then a merging criterion will be introduced to join these building blocks to create the sought structures.

Granular media formed by convex-shaped particles can be partitioned into a dual system formed by material cells and space cells [59].

A material cell consists of the region delimiting all the points that are closer to a certain grain than any other. Thus, each grain will have its own material cell surrounding it, thereby forming a closed domain. The common frontier (face in 3D or edge in 2D) between two neighboring material cells is formed by the set of points that are at the same distance between both grains. Thus, if two grains are in contact there must be a face between their material cells.

On the other hand, to create space cells, the center of the grains whose material cells have a common surface is joined by a line. These lines will then partition the granular media into triangular surfaces forming space cells in the form of tetrahedra (or triangles in 2D) that have grain centers as vertices comprising an internal void space.

In the special case of spherical particles, the material cell is equivalent to the Dirichlet tessellation of the assembly, while the space cell system counterpart is the Delaunay tessellation. This duality is exemplified in Figure 3.1, showing a monodisperse 2D sample. If a polydisperse system is created, a weighted tessellation is needed to take into account the influence of the radius of each grain.

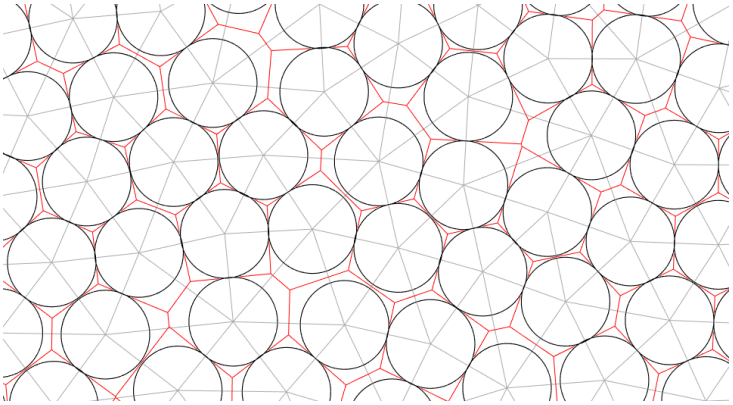

Figure 3.1: Representation of the duality of Dirichlet (red) and Delaunay tessellation (gray) for a monodisperse 2D sample.

Using a Delaunay tessellation, a granular material will mesh into elementary shapes through the connection between grain centers. By doing so, two grains that are in physical contact will always have a connection between them.

The nomenclature definition proposed in Section 2.3.3 for the strain calculation will be maintained. The Delaunay tessellation will divide the granular assembly into elementary shapes that will be known as *cells*, the connections between grains will be known as *edges*, and the triangular faces formed by three edges as *surfaces*.

Loop identification

In 2D, the domain analyzed is a surface, thus the representative elements generated by the Delaunay tessellation are triangles. Each cell is then a triangle formed by three edges and each edge forms a frontier with only one adjacent cell. As the triangles are created, pairs of grains are connected through edges irrespective of physical contact. Hence, two categories of edges arise: closed and open. Closed edges are defined as those in which the connected grains are in physical contact, while open edges correspond to grains that are not in contact.

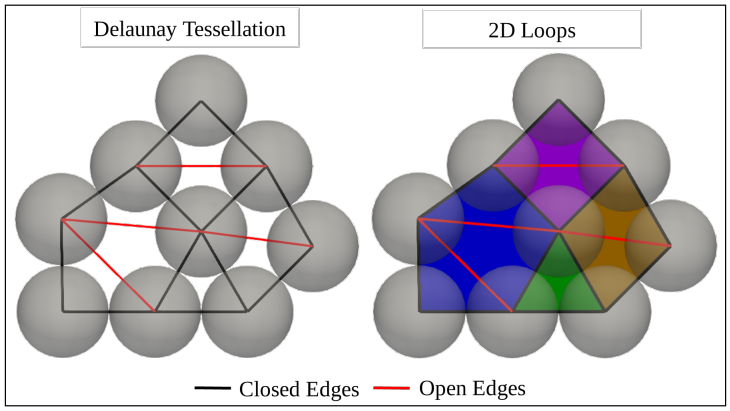

Figure 3.2: Example of 2D loop identification using a Delaunay tessellation.

The loop structure is formed by a group of grains in contact enclosing a common void space. In other words, it is equivalent to polygons composed of only closed edges on their boundaries. As each edge marks a frontier of exactly two cells, a convenient merging criterion consists in joining adjacent cells that share a common open edge. Thus, the merging criterion can be defined as the presence of an open frontier between two distinct cells, as illustrated in Figure 3.2.

Generalizing the procedure for a 3D specimen

To extend the 2D algorithm to 3D conditions, an open frontier must be defined taking into account 3D properties. As the domain analyzed is now a

volume, the elementary partition of the tessellation is a tetrahedron. Thus, in 3D conditions, the cells are tetrahedra composed of four surfaces and six edges, as seen in Figure 3.3.

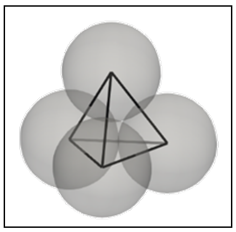

Figure 3.3: Example of a 3D cell.

As the dimension of the system has been incremented, edges no longer mark the frontier between two cells. The domain that is now shared exactly by two distinct cells is a surface. Therefore, the merging criterion for 3D cells must be described as the presence of a common open surface between two cells. Nonetheless, the characterization of a 3D frontier as open or closed is not as straightforward. In fact, as each surface presents a combination of three edges that can be open or closed, and four categories of surface can be defined, as illustrated in Figure 3.5a.

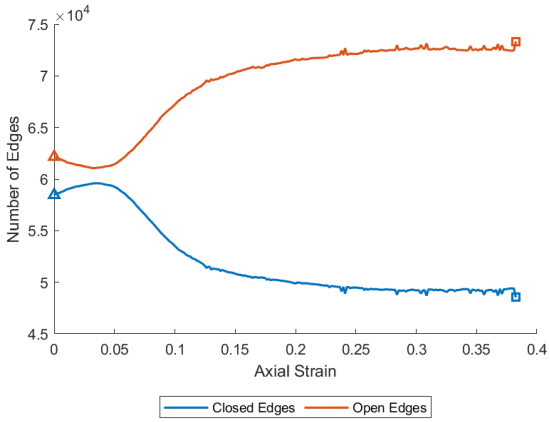

Figure 3.4: Evolution of the number of open and closed edges for a dense drained triaxial test at 100kPa (test D100 later presented in Section 4)

Previous works [4] stated that a surface is considered open when at least one of its edges is open. However, in 3D conditions, each edge is shared by a multitude of cells, and thus an open edge would lead to the merger of all cells that surround it. Furthermore, even for dense specimens, most of the edges generated by the triangulation are open, as illustrated in Figure 3.4.

This definition leads to the detection of a loop that contains most of the cells within the considered specimen (70%), as proclaimed by Nguyen et al. [4]. This merging criterion is therefore not restrictive enough to avoid merging a disproportionate number of tetrahedra.

The definition proposed here is that an open surface exists only when all edges forming it are open. As a result, a closed surface corresponds to all other cases where at least one edge is closed, as illustrated in Figure 3.5a.

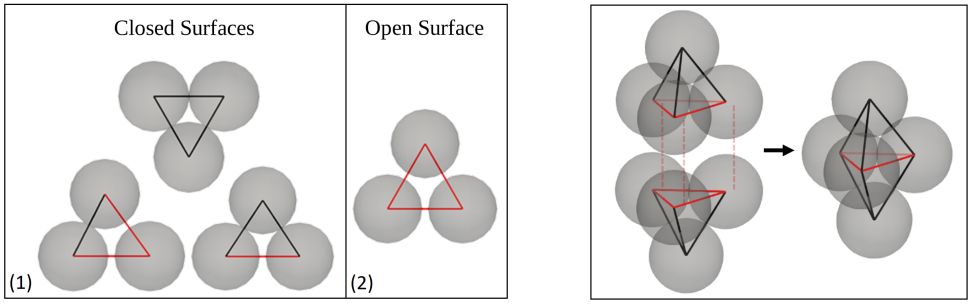

(a) Classification of surfaces into closed (1) or open (2).

(b) Example of the merger of cells sharing an open surface to create a cluster.

Figure 3.5: Illustration of the merging criterion for 3D conditions: 3.5a illustrates surface classification, while 3.5b exemplifies the formation of a cluster.

With the merging criterion now clearly defined, the detection algorithm used in the 2D condition can be directly extended to 3D. Figure 3.5b illustrates the creation of a 3D mesostructure by joining two cells.

In a mathematical framework, a loop can be described as a chain of edges in which no vertex besides the first appears more than once [1]. Therefore, the loop definition as described in Section 2.4.2 introduces a bijection between a polygon and the loop composed of its vertices. However, in the 3D structures presented in Figure 3.5b, it is impossible to cycle through all the grains and edges without repeating an element. Thus the word "loop" is not adopted for the 3D framework and henceforth these structures will be called "clusters." In the following, the term “loop” refers to 2D conditions while the term “cluster” is used in 3D conditions.

[1] The given mathematical definition is that of a cycle and not a loop. The term "cycle" represents more accurately the 2D mesostructure. However, the "loop" nomenclature is kept as it has been widely used by the granular materials community.

Size vs order

Classically, a loop is categorized by the number of grains it contains, which is a known quantity, as the size is. This metric can be directly estimated using the characteristics of the identification procedure of loops. Since each cell has three grains and each open edge is shared between two cells, the size S_{loop} of a loop can be expressed in 2D conditions as:

$$S_{Loop} = 3 \times N_{Cells} - 2 \times N_{OpenEdges} \tag{3.1}$$

For illustration purposes, let us take the blue loop in Figure 2.6(b). This loop is created through the merging of three cells through two open edges. Therefore, its size is $S_{loop,blue} = 3 \times (3) - 2 \times (2) = 5$, corresponding to the number of grains constituting the loop.

The given definition can then be extended to 3D conditions. However, in this case, each cell is a tetrahedron constructed from four distinct grains and the presence of an open frontier between cells infers three repeated grains instead of two. The size of a cluster can then be calculated through the following modification of Eq. (3.1) :

$$S_{Cluster} = 4 \times N_{Cells} - 3 \times N_{OpenSurfaces} \tag{3.2}$$

In the same vein, with the objective of exemplifying, Eq.(3.2) can be applied to the cluster illustrated in Figure 3.5b. In this case, the cluster was created by merging two individual cells through one open surface, resulting in a size of $S_{Cluster,F.5} = 4 \times (2) - 3 \times (1) = 5$, which corresponds to the number of grains observed.

However, it can be shown that Eq.(3.2) is not valid for all cases, since the resulting answer does not match the number of grains forming the cluster. For example, the structure illustrated in Figure 3.6 is a cluster formed by six grains and four cells joined through four open surfaces. In this case, Eq.(3.2) returns a value of $S_{Cluster,F.6} = 4 \times (4) - 3 \times (4) = 4$ grains, which differs from the reality.

Therefore, for a cluster, the number of grains (size) that compose it is not directly related to the number of cells and open frontiers and thus cannot be calculated from only these metrics. However, as the identification procedure is heavily based on these concepts, a new metric also based on these ideas, thereafter denoted as the "order," can be conveniently introduced. The order of a loop or cluster is defined as the number of closed frontiers forming the boundary of the structure. It can be computed as the difference between the

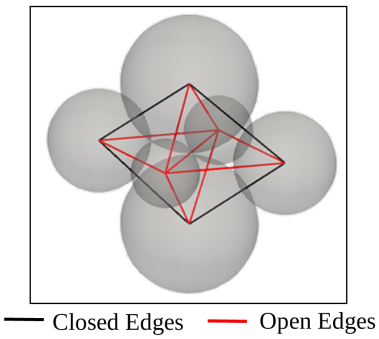

Figure 3.6: Pathological case: the order (exterior faces) of a cluster does not correspond to its size (the number of grains).

total number of frontiers and the number of open ones, as represented by Equations (3.3) and (3.4) showing the order O of loops and cluster:

$$O_{Loop} = S_{Loop} = 3 \times N_{Cells} - 2 \times N_{OpenEdges} \tag{3.3}$$

$$O_{Cluster} = 4 \times N_{Cells} - 2 \times N_{OpenSurfaces} \tag{3.4}$$

Applying equation (3.4) to the pathological case shown in Figure 3.6 returns a value of $O_{Cluster,F.6} = 4 \times (4) - 2 \times (4) = 8$, which corresponds to the correct number of external faces forming the boundary of the cluster, thus validating the definition. In addition, equation (3.3) proves that both quantities are equivalent in 2D conditions.

In the following, order will be favored for the overall analysis. However, size is an interesting metric as it can be used to distinguish clusters of different shapes, since they may have the same order but different sizes.

Deformability

A configuration of a loop-like structure can be defined as a geometrical pattern bounded by the relative position of the grains making up part of it. As the definition of clusters is heavily dependent on the contact network of a granular system, the characteristics of the contacts will influence how loop-like structures behave when stimulated by a given external loading, thus changing in configuration.

As an example, the case of a loop of order 3 can be considered. As the three grains are in physical contact, the given structure has only one possible configuration and cannot be deformed by grain rearrangement. By contrast, a loop of order 4 or greater is able to adopt several configurations

to accommodate the displacement of neighboring grains imposed by external solicitations, as illustrated in Figure 3.7. In addition, the number of possible configurations a loop can take increases with the order of the structures.

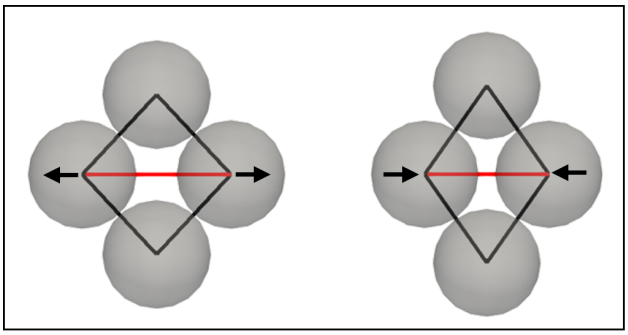

Figure 3.7: Illustration of a change in configuration for a loop of order 4, in 2D.

This capacity of a loop-like structure to adapt to external loads influences directly the strength of the specimen. It has been shown that the presence of less deformable loops around force chains increases their stability, resulting in a stronger specimen [80]. When different loops start merging with each other, generating larger structures, they become more deformable, consequently leading to the loss of stability of force chains and an increase in their probability of bending, finally generating a general loss of mechanical strength for the sample.

The deformability of a loop-like structure is introduced here as a new metric to quantify the capacity to deform, according to its topological characteristics. It is defined as the capacity of a loop or cluster to deform without creating or breaking contacts.

The feature that allows a loop to admit more configurations, and thus to be more deformable, is the presence of open edges. An open edge represents a void space between grains, thus leaving a margin of space for grains to move around. The level of deformability of a loop-like structure is then measured as a dimensionless ratio between the number of open edges and total edges, as shown in Eq. (3.5):

$$D = \frac{N_{OpenEdges}}{N_{TotalEdges}} \tag{3.5}$$

In a 2D framework, because the size and order have the same formulation, the number of edges can be directly calculated from these properties. The

minimal loop, of order 3, is composed of three closed edges with a deformability $D_{Loop3} = 0$. For each unit increment in the order of greater than 3, two edges are added to the total, one open and one closed. Thus, Eq. (3.5) can be rewritten in 2D as:

$$D_{Loop} = \frac{O_{Loop} - 3}{2O_{Loop} - 3} \tag{3.6}$$

with O_{loop} being the loop order. It can be noted that, as the order increases to greater than 3, so does the deformability with a maximal possible value approaching 0.5.

The deformability principle in Eq. (3.5) is directly applicable to 3D conditions. Even though edges are no longer the frontier between 3D cells, they still portray the connections between two grains. In this way, the existence of open edges is still the necessary condition for a cluster to be deformable.

However, as discussed in Section 3.2.1, both open and closed surfaces are comprised of a combination of open edges and closed edges. Hence, in 3D, a direct deformability equation equivalent to Eq. (3.6) cannot be established and no simple relation between the deformability and the order of a cluster exists.

Direction of elongation of loop-like structures

The deformability property explained in the previous section highlights the capacity of loops and clusters to take different forms in a granular assembly. As mentioned in Section 2.4.2, the shape and elongation direction of loops have a direct influence on the strength of granular materials [84, 83, 75, 20]. Thus, it is wise to introduce an equivalent notion for the case of clusters.

A common procedure to analyze loop forms is through a second-order tensor, in a similar way to the procedure proposed to evaluate the contact network in Section 2.3.1. However, instead of the whole specimen, the analysis would be made over every single loop-like structure separately. For the cluster case, two tensors will be constructed from vectorial data of two different properties of the clusters: a mass tensor and a surface tensor.

The first one, the mass tensor, will provide information on the distribution of the mass inside the cluster. It will be constructed with the distance vectors from the center of mass of the cluster to each of the grains forming it, as indicated by equation (3.7), thus showing the overall positioning of the grains in the three dimensions.

$$M = \frac{1}{N_g} \sum_{g \epsilon L} G\vec{P}_g \otimes G\vec{P}_g \tag{3.7}$$

with L being the cluster analyzed, g a grain belonging to L, P_g the coordinates of the grain g, G the coordinates of the center of gravity, and N_g the number of grains forming the cluster.

On the other hand, the surface tensor will be defined from the surface vectors of the closed surfaces forming the cluster boundaries. These vectors are the outward normal whose magnitude is equivalent to the area of the surface they represent. This type of tensor has already been used to study other Delaunay-tessellation-based structures such as the pore structure of a granular system [111]. This way, the distribution and orientation of the external surfaces will be highlighted, providing a second point of view in the cluster forms.

$$M = \frac{1}{O_s} \sum_{s \epsilon L} \vec{V_s} \otimes \vec{V_s} \tag{3.8}$$

with L being the cluster analyzed, s a closed surface belonging to L, V_s the coordinates of the surface vector of s, and O_s the order of the cluster (number of closed surfaces).

The direction of elongation can then be obtained through the analysis of the principal values of the tensor. For the mass tensor, the major principal value is envisioned, as it points toward the direction where mass is mostly concentrated. However, for the surface tensor, the minor principal value is retained, as the most elongated direction is the one to which the lowest number of surface normal vectors point.

The chosen vectors will be expressed in terms of their azimuthal and elevation angle [111]. The former represents the rotation in the x–y plane in relation to the y-positive direction, while the latter will indicate the uplift of the vector in relation to the x–y plane, with x being the smallest dimension of the specimen (axes are defined in Figure 3.11a).

3.2.2 Force chains

Since force chains have been studied for a long time, procedures capable of identifying them have already been developed. In this section, the procedure introduced by J. Peters [70] will be presented and further modified to identify structures adapted to our analysis.

The force inside granular materials has been shown to be transmitted mostly by the strong network, containing grains with higher than average local stresses [55]. Thus, to identify the force chains, the stress level of each grain must be quantified. The Love–Weber formula, shown in equation (2.2), can be modified to account for the domain of spherical particles as shown in equation (3.9).

$$\bar{\sigma}_{ij} = \frac{1}{V} \sum_{c=1}^{C} f_i^c r_j^c \tag{3.9}$$

the summation is extended over all contacts C, where f_k^i is the i-th component of the force of the contact c, r_k^j is the j-th component of the vector from the center of grain to the point of the contact c, and V the volume of the grain.

From each of the particle's tensors, the principal values and vectors are obtained. The strong network is detected by selecting only the grains whose major principal stress (most compressive) is higher than the average. Furthermore, to identify force chains, contacts between grains A and B of the strong network are checked by equation (3.10). The angle between the major principal stress of both particles and the branch vector of the contact must be smaller than a predefined θ value (commonly chosen equal to 45°).

$$cos(\theta) < min\left(\frac{|l_{AB}.\sigma_A^M|}{|l||\sigma_A^M|}, \frac{|l_{BA}.\sigma_B^M|}{|l||\sigma_B^M|}\right) \tag{3.10}$$

with l_{AB} the branch vector of the contact between the grains A and B, σ_A^M the most compressive principal stress of particle A, and σ_B^M the most compressive principal stress of particle B.

With this definition, an algorithm capable of identifying force chains can be defined, as proposed by J. Peters [70]. However, this algorithm has a flaw: It cannot take into account the ramification of force chains. As the algorithm can only choose one grain at a time, whenever a ramification appears a different force chain is created, as illustrated in Figure 3.8.

To correct this drawback, an algorithm based on contacts is proposed. Once the strong network is detected, a list of contacts between highly stressed grains is built. The condition described by equation (3.10) is then checked for all contacts in the mentioned list. Contacts that were validated are then joined into chains. The chains containing at least three grains aligned in the force transmission direction are then considered force chains.

To take into account the force chain ramification phenomenon, two definitions can be established: chains and branches. Chains will represent the

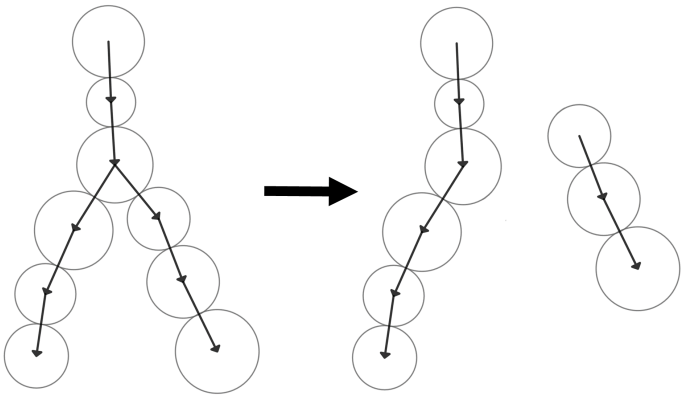

(a) Ramified force chain. (b) Force chains identified.

Figure 3.8: Illustration of J. Peters algorithm [70] drawback for ramified force chains. 3.8a represents a ramified force chain, while 3.8b shows the two identified force chains.

totality of the force chain with all its ramifications, while branches represent each possible force path. This proposal is illustrated in Figure 3.9.

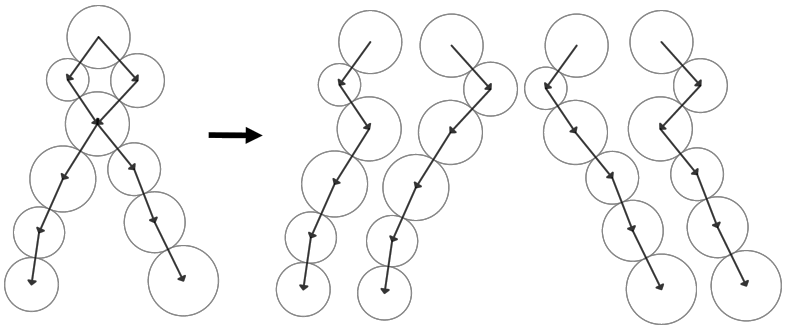

(a) Force chain. (b) Force chain branches.

Figure 3.9: Illustration of the definition of a force chain (3.9a) and its branches (3.9b).

It is important to note that a branch must have two extremities, one enduring an external load and one transmitting it forward (to grains outside the chain or to the boundary conditions). Thus, the connection between grains inside the chain must follow the direction of the most compressive stress characterized by equation (3.10). Consequently, a branch connecting the two

bottom-most grains of the force chain illustrated in Figure 3.9a is impossible, as it would require a force to be transmitted in the opposite direction. This way branches may (and most likely will) have common particles with other branches originating from the same force chain.

The phenomenon of force chain bending has been shown to have a direct impact on the softening phase of granular materials and even the formation of shear bands [112, 71, 2, 75, 81, 113, 80]. In the literature, several authors use the names bending and buckling interchangeably. However, a rigorous definition of buckling requires an analysis of the stress saturation besides the geometrical evolution [30]. Thus the nomenclature "bending" will be kept throughout this work.

According to the definition given in Section 2.4.1, elementary parts of force chains are built from groups of three heavily stressed particles in contact in the direction of the force transmission, known as 3-p force chains [30]. A bending event will be considered if, between two calculation steps, the angle between each 3-p force chain has evolved of a value larger than θ_c. As illustrated in Figure 3.10, $|\theta_t - \theta_{t+dt}| > \theta_c$.

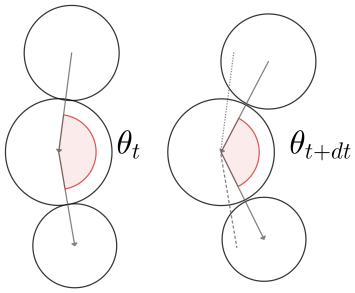

Figure 3.10: Illustration of a force chain bending event.

For a bending event to take place, the 3-p force chain must survive during the time interval. Consequently, the disappearance of the 3-p element does not count as a bending event.

It must be noted that the number of bending events obtained through this definition is highly dependent on the limit value θ_c and the calculation interval chosen. If a high interval is chosen, the likelihood of the survival of 3-p force chains will decrease. On the other hand, a sufficiently low interval would result in almost negligible angle variations between force chain contacts, thus a large θ_c would not be able to identify the bending events.

3.2.3 Shear bands

As mentioned in Section 2.2, inside shear bands several granular material properties differs from the rest of the specimen. Thus, a local analysis of these properties allows for the identification of the band.

In this work, the local calculation of deviatoric strain and second-order work will be shown to be capable of highlighting the appearance of the shear band inside a specimen. A negative second-order work value of a sub-domain of the specimen does not indicate the presence of the shear band in itself, but a negative value is a necessary (but not sufficient) condition for the band formation.

A method to acquire the strain tensor of a discrete material has already been defined in Section 2.3.3. However, the local element upon which the calculation will be executed and exploited remains to be chosen. Throughout this work, two structures have been considered for micromechanical analysis: cells and grains.

Cells, as mentioned in Section 2.3.3, are elementary volumes in tetrahedral shapes (triangular in 2D) formed with the grain centers as vertices. It can be shown that the cells vastly outnumber the grains. This way, the specimen is compartmentalized into numerous small closed domains that will highlight, with great detail, the internal characteristics of the specimen. Furthermore, cells are closed domains where the strain tensor previously defined can be directly applied. However, the cells are perishable by nature. Thus, with this element, a persistent analysis of the evolution of any quantity over time becomes unattainable.

On the other hand, as any sort of particle rupture and physical deformations are absent in the chosen DEM model, each grain is considered persistent over time. Furthermore, since the stress tensor is defined for a particle volume, the definition of a strain tensor for the region situated around each grain would allow for a continuous measure of this quantity and the analysis of the second-order work criterion.

Upon closer inspection of the strain definition in Section 2.4, the minimal element on which the strain is defined is an edge. By considering the strain constant for the whole edge, the volume displacement tensor defined by the multiplication $d^e \otimes \Delta u^e$ (complementary area vector of the edge times the relative displacement of the grains forming the edge from Eq. (2.4)) can be estimated through the volume of both grains concerned, thus distributing this quantity for each grain.

Equation (2.4) can then be modified to calculate a strain tensor on the grain level. It can be computed as the sum of the weighted volume displacement tensor of all edges that are connected to it, later divided by the grain

volume as represented in the following equations.

$$e_{ij}^{g} = \frac{1}{V^{g}} \sum_{m=1}^{M} \left[d_{i}^{mg} \Delta u_{j}^{mg} * \left(\frac{V^{g}}{V^{g} + V^{m}} \right) \right] \tag{3.11}$$

with e_{ij}^{g} the ij-th component of the incremental strain tensor of the grain g, M representing all the grains forming edges with the grain g, V^{m} being the volume of the grain m, d_{i}^{mg} the i-th component of the complementary area vector of the edge mg, and Δu_{j}^{mg} the j-th component of the relative incremental displacements of grains m and g.

It must be noted that the grain itself is not physically deformed, the value obtained measures the incremental deformation of the space surrounding each grain for a given time increment.

To summarize, a calculation with grain as a base element will allow for the acquisition of the second-order work and a persistent measure of strain. The latter highlights regions that have been deformed along the totality of the loading path. On the other hand, as cell elements far outnumber grains, they will provide information on instantaneous deformation with incredible detail. In addition, the latter does not require the approximation of equation (3.11), resulting in a more accurate value in relation to the grain version. Finally, both analyses may be seen as complementary and thus resulting in a more complete view of the specimen.

3.3 Software and 3D DEM numerical simulations

As mentioned in Section 2.5, LIGGGHTS is a software based on the DEM. Therefore, it calculates particle location, speed, and forces at each timestep as a means to observe the evolution of the specimen. These quantities are the output from LIGGGHTS, which need to be treated before any conclusions on the state of the specimen can be inferred.

With the objective of allowing further works to be developed on the same platform, all execution scripts have been written in such a way as to allow researchers less fluent with LIGGGHTS language to replicate easily the same tests that were used in this work. In addition, an application capable of transforming LIGGGHTS output data into meaningful physical quantities was created and will be briefly presented.

The tools developed for this thesis can be obtained from the following public repositories:

- Rectangular Triaxial Analysis for LIGGGHTS (RTAL)
  git@github.com:magosemana/RTAL.git
- LIGGGGHTS Rectangular Triaxial Script (LRTS)
  git@github.com:magosemana/LRTS.git

3.3.1 Shape and material properties

Several specimen geometrical shapes have been used to simulate triaxial tests, with cylindrical shapes being the most common in experimental work, as they facilitate a plane-symmetrical analysis. However, in numerical work, a simple prismatic shape is frequently used to ease sample preparation and possibly use periodic boundary conditions. In this work, the apparatus will consist of a simple prismatic shape with a fixed base (normal z+) and five moving pistons in the other principal directions, as illustrated in Figure 3.11a.

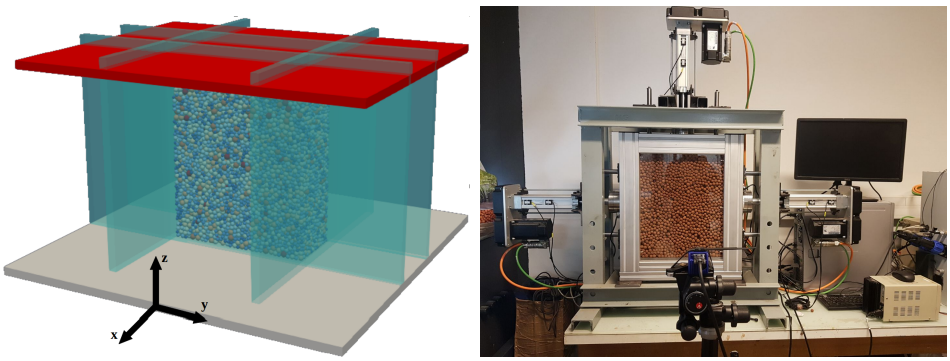

(a) Triaxial model simulation. (b) Biaxial test at INSA de Lyon.

Figure 3.11: Model illustration. On the right (b) is the rectangular biaxial test that served as inspiration for the numerical model, which is situated on the left (a). The vertical piston is represented in red (z-axis), the fixed base is represented in gray, and the four horizontal pistons are represented in a transparent blue (x-y plane).

The red piston in Figure 3.11a is called a "vertical piston" hereafter while the other four are named "horizontal pistons." The sample dimensions are presented in Table 3.1. Note that the sample is considered thin since the width (x-axis) of the box is less than half of the other dimensions. One of the reasons for this narrow prismatic shape is the existence of a similar experiment at INSA de Lyon (see Figure 3.11b), a prismatic biaxial test of around the same size using expanded clay spheres as soil media. Although a comparison between experimental and numerical tests will not be made,

the tools developed for this work will make it possible in future studies. In addition, a thin prismatic specimen is expected to display failure patterns closer to 2D specimens, as, for example, shear bands traversing the full width (x direction) of the specimen. This makes the comparison between 2D and 3D results simpler.

To avoid crystallization pathology linked to mono-disperse simulations, a ratio of 2 between minimal and maximal diameter was chosen. From an implementation point of view, LIGGGHTS does not have a predefined function to create particles of varying diameters. To create a polydisperse simulation, a mass distribution percentage histogram must be provided. The chosen distribution is illustrated in Figure 3.12.

Table 3.1: DEM simulation material information.

Parameter	Value
Dimensions	450 x 350 x 150 mm
Stiffness ratio (ν)	0.25
Elasticity modulus	0.1GPa
Friction coefficient particle–particle	0.57
Friction coefficient particles–wall	0.00
Rotational friction coefficient	0.30
Restitution coefficient	0.50
Number of particles	18.165
Particle diameter	[8,10,12,14,16] mm

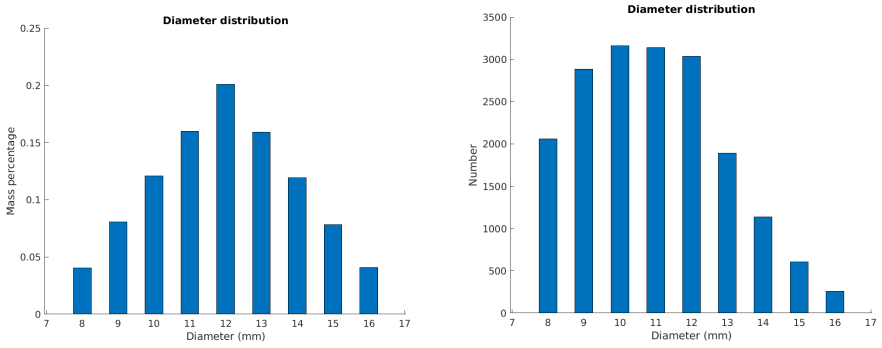

(a) Mass percentage distribution (b) Number of particles distribution

Figure 3.12: Histogram of the granular distribution for the DEM triaxial simulations. On the left (a) mass percentage, and on the right (b) number of particles.

3.3.2 Specimen preparation

In LIGGGHTS particles are inserted through gravity deposition, as illustrated in Figure 3.13a. Random points are chosen for particle creation within a prescribed domain. Particles then fall under gravity until the kinetic energy is dissipated through collisions with walls and other particles. This method creates an inherent anisotropy in the gravity direction with contacts preferentially oriented vertically. This will influence the mechanical behavior of the sample.

A common practice to create specimens of different densities is to change the friction and rolling friction coefficients during the gravity deposition phase. More significant coefficients allow for larger tangential forces and rolling momentum, which decrease particle reorganizations, thus generating looser soils. On the other hand, smaller coefficients will limit the tangential forces and rolling momentum, thus forcing particles to move around in a denser configuration to find an equilibrium position. In this work, only dense soils are considered.

After insertion and before the triaxial test, the specimen is submitted to an isotropic compression, as shown in Figure 3.13b. All pistons are moved at a constant speed until the same stress value is reached in all directions.

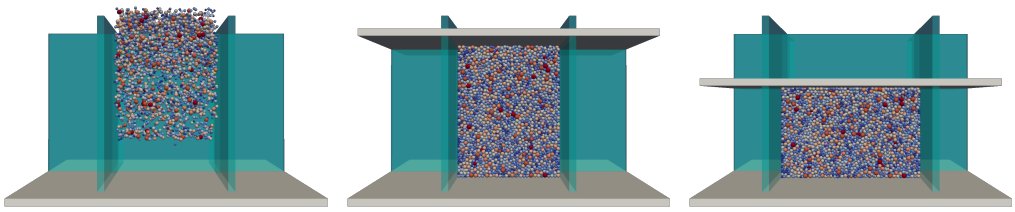

(a) Insertion (b) Isotropic compression (c) Test execution

Figure 3.13: Illustration of three phases of the simulation for a drained triaxial test. From left to the right : (a) insertion, (b) isotropic compression, and (c) test execution.

3.3.3 Triaxial tests

Three different triaxial tests are simulated to test the validity of propositions made in Chapter 3: drained, undrained, and constant deviatoric stress. The specimen chosen will be a dense material with no addition of water. Thus, there will be no difference between effective and normal stress values.

The drained triaxial test is the classic triaxial test. The four horizontal pistons maintain a constant stress (equal to the fixed isotropic compression

stress), while the vertical piston moves downward at a constant speed. Expressly, it is a compression test with constant lateral pressure.

The undrained triaxial test consists in vertically compressing the specimen while preserving its volume constant. This is attained by attributing a fixed descending speed to the vertical piston and controlling the movement of the horizontal ones. For a given state of the test, the incremental width dw and length dl for a fixed height increment dh are computed as follows:

$$dw = w\left(\sqrt{\frac{h}{h+dh}} - 1\right) \qquad dl = l\left(\sqrt{\frac{h}{h+dh}} - 1\right) \tag{3.12}$$

with w the width, l the length, and h the height of the specimen.

Finally, the constant deviatoric stress (q-constant) triaxial test is separated into two parts. A drained triaxial test is conducted in the first part until the desired deviatoric stress value is reached. In the second part, the control parameters are changed to gradually decrease applied stress in all pistons at a constant rate while maintaining the deviatoric stress fixed. Thus, the mean stress will gradually decrease to a point where the sample can no longer support the applied deviatoric load, resulting in the rupture.

The different tests will be named with the following codification "AXXX." Where the letter "A" represents the type of triaxial test, with "D" for drained, "U" for undrained, and "Q" for the q-constant. The suffix "XXX" represents a two- or three-digit number equal to the stress applied during the isotropic compression phase in kPa. However, the q-constant test depends on a second fixed value: the targeted deviatoric stress. Thus, a second number will be attached to this test name to identify the target deviatoric stress in kPa.

For example, the test Q100-150 is a q-constant triaxial test with an isotropic compression phase of 100 kPa and a target deviatoric stress of 150 kPa, whereas D100 is a drained triaxial test with an isotropic compression phase of 100 kPa.

3.3.4 Inertial number

All procedures previously defined require the specimen to be loaded in a quasi-static condition, as the contribution of inertial terms in equations is ignored. However, loading speeds must be chosen high enough to decrease the computational power necessary, since real-time scales of quasi-static laboratory tests still require several days of c.p.u. time [114].

Thus, the inertial number (I) will be introduced to quantify the influence of the inertial terms in equations. It is a dimensionless ratio relating the

shear speed and inertial ratio of the specimen quantities as the following [115, 116, 114]:

$$I = \dot{\gamma}\sqrt{\frac{m}{Pd}} \tag{3.13}$$

with I being the inertial number, $\dot{\gamma}$ the incremental shear strain rate, m the mass, P the mean pressure, and d a characteristic length.

The inertial term is calculated along two scales: macroscopic and microscopic. At the macroscale, I is a scalar representing the inertial number for the whole specimen. Thus, all quantities of equation (3.13) are calculated for the entire specimen, and the characteristic length d represents its height. By contrast, the inertial term is calculated per grain at the microscopic scale. Consequently, d represents the diameter of each grain, and all quantities of equation (3.13) are calculated with the procedures described in Section 3.2.

For the quasi-static regimen to be validated, an IN of approximately 10^{-3} or lower is recommended in the literature [115, 116, 114].

3.3.5 Development of a post-processing tool

Tool presentation

A user-friendly application was created with the software Matlab to execute the post-processing of the raw LIGGGHTS data. Two factors influenced the choice of Matlab. First, Matlab has a long list of ready-to-use tools such as AppDesigner and Delaunay tessellation functions; second, my experience with the software made it a sound choice. However, were I to redo it today, I would probably create it in python as it is a more common language in the scientific community, implementable inside other software, and does not require a subscription.

Upon running the developed LIGGGHTS script, all data concerning the displacement and forces of both grains and pistons are saved in individual files. In addition, a log file containing information about the specimen's initial state, time, and folder location is created. The Matlab application will use the log file to prepare the calculation environment, opening the main menu as illustrated in Figure 3.14.

On the right, a draft of the y-z plane is plotted for the current timestep, showing the current dimensions of the specimen. From this point, the calculation can be executed through the left panel. Specific simulation periods can be analyzed by choosing the beginning and end timesteps. The precision

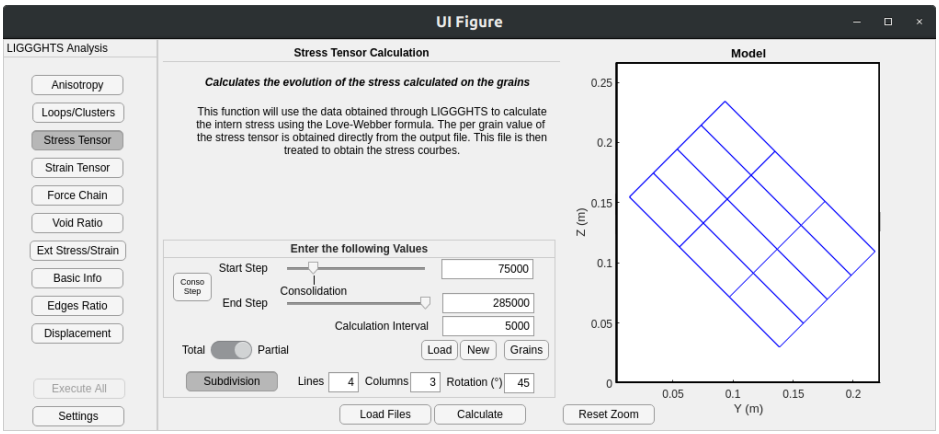

Figure 3.14: Matlab application main menu.

of the results can be further adjusted by selecting the timestep increment (interval) between two calculation points.

In addition, for most of the developed functions, a region inside the specimen can be chosen for local analysis, represented in blue in Figure 3.14. The partition tool is rectangular in the y-z plane that goes through the entire width (x direction) of the specimen. This shape can later be subdivided into several equal parts for a more precise analysis.

The developed application could analyze rectangular triaxial tests from any DEM software results if the data are appropriately formatted. Alternatively, the function responsible for file reading could easily be modified to adapt to new input formats.

Table 3.2 summarizes all the developed post-processing tools and specifies whether local treatments can be performed.

Calculation	Total	Local
Anisotropy	Yes	Yes
Force Chains	Yes	No
Loops/Clusters	Yes	No
Void Ratio	Yes	Yes
Stress through grain quantities	Yes	Yes
Strain through grain quantities	Yes	Yes
Stress through piston quantities	Yes	No
Strain through piston quantities	Yes	No

Table 3.2: Calculations developed for the Matlab application, and whether they can perform local analysis.

Several functions of the developed application 3.2 are outside the scope of this work and will not be used. Their development was still an important part of this thesis as it allowed for a better comprehension of the overall mechanics of granular material. Furthermore, it will facilitate the future continuation of this work.

The Delaunay tessellation

To apply the Delaunay tessellation to the specimen, the Matlan function *delaunayTriangulation* was chosen. A weighted Delaunay tessellation (also known as "regular tessellation") should be preferred, as the specimen distribution described in Section 3.3.1 is polydisperse. However, as the range between minimal and maximal diameter is 2, the contact network is preserved by a normal Delaunay tessellation.

Next, if the Delaunay tessellation is directly applied to the center of grains, highly elongated cells connecting the grains located near the boundary conditions are created. From the literature, two techniques two overcome this pathology have been reported: deletion of the outer 10% of the specimen [117, 118] or creation of large spheres representing the exterior walls of the specimen [119].

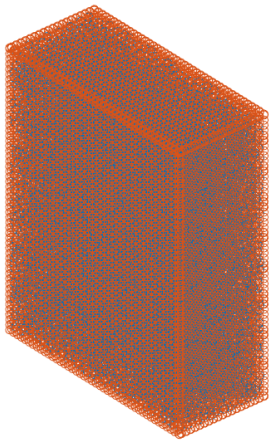

Figure 3.15: Example of the mesh of virtual particles replacing the walls for the Delaunay tessellation. Virtual particles are represented in red, and real granular particles are represented in blue.

Both approaches are interesting but have their flaws. The first removes part of the data from the analysis, while the second constrains the calculation to the volume comprised of the center of the outermost particles. For this

reason, a mesh of virtual particles in the location of the external walls was created, as illustrated in Figure 3.15.

Consequently, the tessellation is bounded by the mesh of virtual grains. For cluster analysis, only cells formed by real grains will be analyzed. However, for strain calculations, using the data from the entire simulation returns a better match to the strain measured macroscopically.

3.4 Concluding remarks

This chapter proposed a procedure to identify a loop-like structure in 3D conditions. The name "cluster" was chosen as it is a better fit for the morphology of the structures. It was shown that clusters cannot be characterized only through the number of grains forming them, thus introducing the order metric as the number of exterior frontiers. Deformability and elongation direction were also introduced to characterize the cluster properties further.

Procedures to identify force chains based on algorithms previously defined in the literature were proposed. The notion of force chain bending and a method to identify it was also presented. Finally, two categories of force chains were introduced, concerning the presence of ramifications.

Several procedures to identify shear bands were proposed based on the local analysis of several quantities of the granular assembly. Grains and cells were presented as suitable bases for the calculation, highlighting these two different ways of partitioning the granular assembly.

Finally, the numerical tools developed to simulate granular materials and apply the proposed procedures were presented. The proposed discrete element model (DEM) simulation consists of spherical particles inserted into a rectangular specimen and later submitted to three triaxial loading paths (drained, undrained, and constant deviatoric stress). An application was developed using the software Matlab to execute the raw post-processing data obtained from the simulation. The simulation script and post-processing tool were designed to facilitate the reproduction of this work.

Chapter 4

Mechanical behavior of granular materials under triaxial conditions

4.1 Foreword

In this chapter, the behavior of the simulated triaxial tests will be analyzed regarding mechanical and internal topological characteristics. First, it will be shown that the specimens behave like dense soil during the proposed loading paths. Next, the behavior of force chains and shear bands will be analyzed and compared with the macroscopic evolution observed, resulting in a complete analysis of the mechanical response of each specimen.

4.2 Triaxial tests

4.2.1 Test presentation

For each triaxial condition presented in Section 3.3.3, several specimens with varying consolidation stress levels were simulated, for a total of 12. A single sample was created and saved just after the insertion phase in order to initialize all simulations from the same initial state. Figure 4.1 compares the three triaxial loading paths that will be analyzed in this chapter.

Three drained triaxial tests with confining pressures of 50 kPa, 100 kPa, and 200 kPa, respectively, were considered. However, a fourth simulation was added with a confining pressure of 28 kPa as it will be shown to reach failure at around the same deviatoric and mean stress values as the constant deviatoric stress in Section 4.5. The velocity of the vertical piston is fixed at a value of $2mm/s$.

Three undrained triaxial tests were executed with simulated confining pressures of 50 kPa, 100 kPa, and 200 kPa, respectively. The vertical piston descends at a constant speed of $2mm/s$ while the others move according to the formulas given in Section 3.3.3.

Unlike the previous triaxial conditions, the constant deviatoric test relies on two specific values: the initial confining pressure and the targeted

deviatoric stress. Three tests with varying confining pressure (50 kPa, 100 kPa, and 200 kPa) were simulated for targeted deviatoric stress of 100 kPa (Q50-100, Q100-100, and Q200-100). In addition, two tests with increasing targeted deviatoric stress (150kPa and 200kPa) and departing from an equivalent confining pressure of 100 kPa (Q100-150 and Q100-200) were simulated. During the drained phase, the vertical piston descends at a fixed velocity of $2mm/s$. Later, pistons are stress controlled and have their targeted stress decreased by a rate of $2.5kPa/s$.

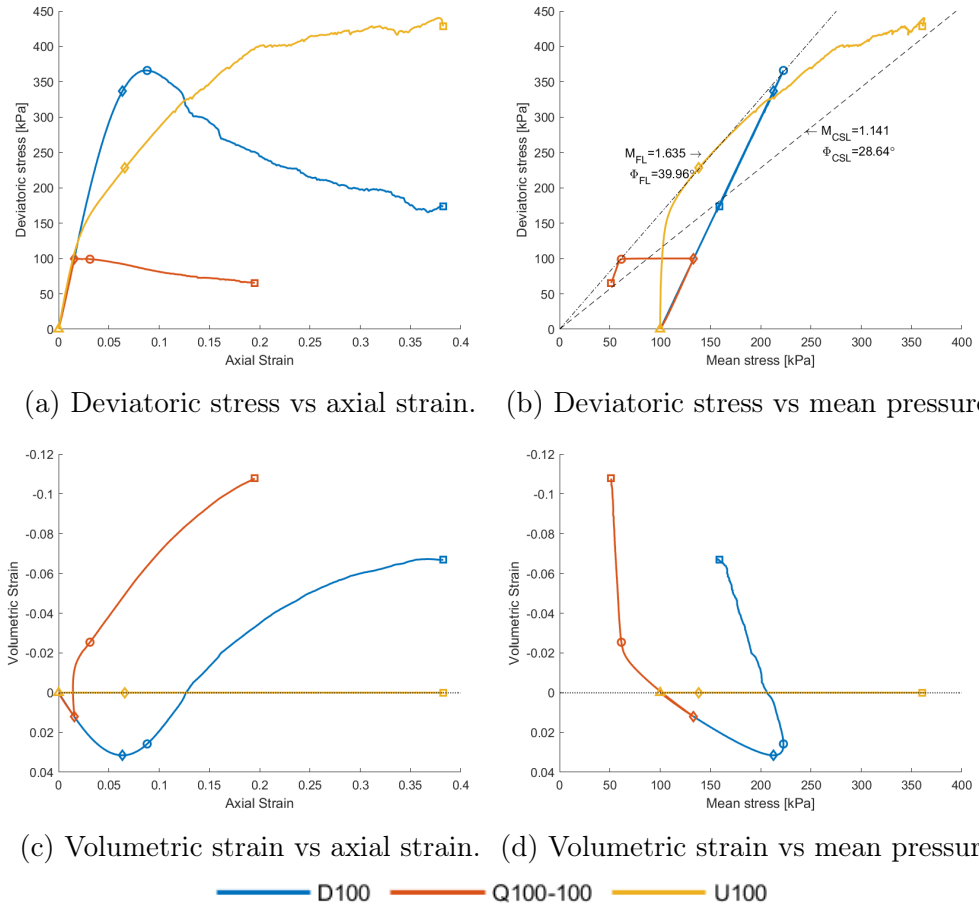

(a) Deviatoric stress vs axial strain. (b) Deviatoric stress vs mean pressure.

(c) Volumetric strain vs axial strain. (d) Volumetric strain vs mean pressure.

Figure 4.1: Macroscopic response for different triaxial paths with equivalent initial isotropic pressure (D100, Q100-100, and U100). The triangle marks the initial state, the square the final state, while the circle and diamond mark important points for the respective test. (a) Deviatoric Stress vs axial strain;(b) deviatoric stress vs mean pressure;(c) volumetric strain vs axial strain;(d) volumetric strain vs mean pressure.

It can be observed in Figure 4.1 that the drained and undrained tests reached axial strains of approximately 0.38 while q-constant tests were limited to 0.2. This is due to the increased computational time necessary for q-constant simulations, which required 4 times the execution time of the other two conditions.

The macroscopic results were obtained using the force and displacement information of the five moving pistons. The slope M that characterizes the failure line (M_{FL}) or the critical state line (M_{CSL}) in the mean-deviatoric stress plane (p–q plane) will be derived from the drained tests. Furthermore, the internal structure of each specimen will be examined by identifying force chains and shear band formation. Their evolution allows for a correlation between the macro- and mesostate of the specimen.

4.2.2 Inertial number

The inertial number was calculated for all simulations at both micro- and macroscales, as presented in Section 3.3.4 and illustrated in Figure 4.2. In the first column (Figures 4.2a, 4.2b and 4.2c), the macroscopic result is shown for all specimens. However, in the second column (Figures 4.2d, 4.2e and 4.2f) the microscopic result is presented, with the red curve being the mean value and the blue lines the standard deviation. The microscopic results of tests D100, U100, and Q100-100 only are shown as the conclusions derived for each triaxial test type are roughly the same.

The macroscopic inertial number (I) remains below the 10^{-3} limit during the loading path for all triaxial tests, respecting the quasi-static condition mentioned in Section 3.3.4. It can be noted that the increase in mean pressure applied to the specimens results in a decrease in the inertial number. This is well illustrated by specimens Q200-100 and Q100-200. The former is submitted to a higher confining pressure, resulting in a lower I initial value compared to the latter. However, the test Q100-200 ruptures at a higher mean pressure, resulting in a lower final I.

Furthermore, the I curves for q-constant conditions, illustrated in Figure 4.2c, show two discontinuities (jump in I value), which can be traced directly to a change in the piston control parameters. The first one is the transition between the end of the drained triaxial phase and the start of the unloading. The second one was artificially introduced to decrease the inertial term of the simulation. During previous iterations of this triaxial condition, the specimen was observed to suddenly collapse. Thus, when approaching failure, the maximal displacement speed of the piston was divided by a factor of 100.

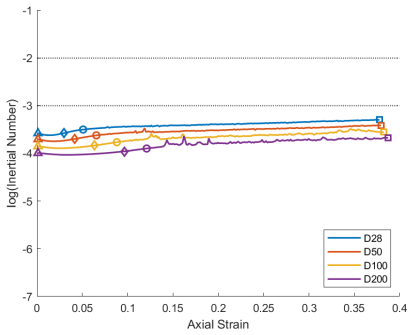

(a) Macro I for drained cases.

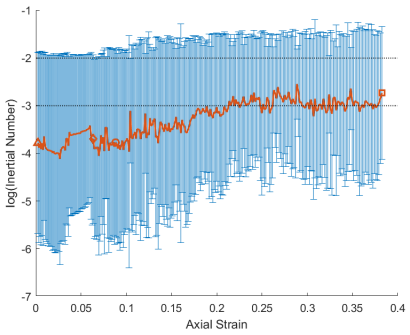

(d) Micro I for D100 test.

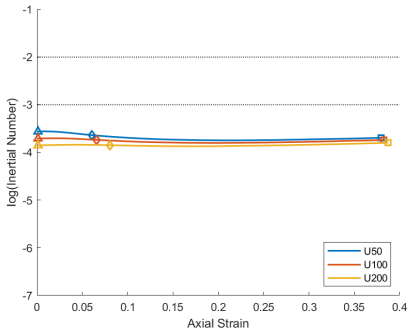

(b) Macro I for undrained cases.

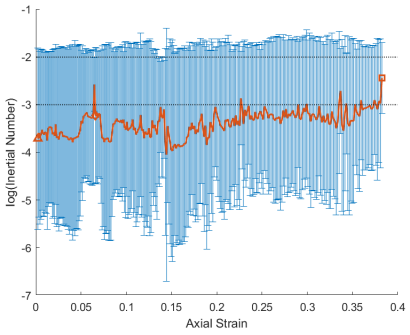

(e) Micro I for U100 test.

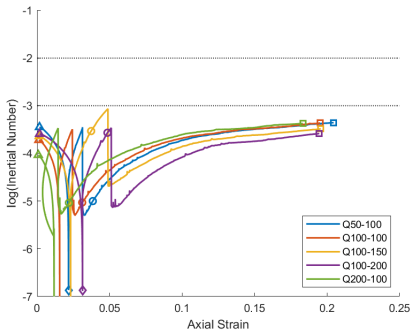

(c) Macro I for q-constant cases.

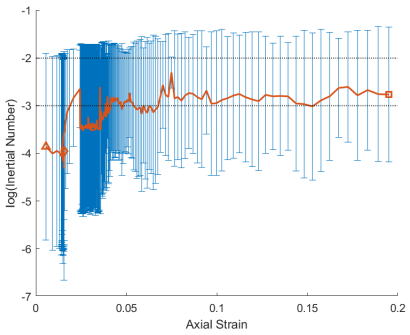

(f) Micro I for Q100-100 test.

Figure 4.2: Evolution of the logarithm of the specimen inertial number (I) in function of the axial strain. In Figures (a), (b), and (c), I is calculated macroscopically for all simulated samples for drained, undrained, and q-constant conditions, respectively. On the right, I was calculated microscopically for tests D100 (d), U100 (e), and Q100-100 (f) showing the mean value (in red) and the standard deviation (in blue).

The microscopic results reveal a similar trend. However, the average microscopic I is observed to surpass the 10^{-3} limit in all triaxial tests, mostly for large strains. The standard deviation illustrates the dispersion of values inside the specimen, revealing the heterogeneity within the specimen. It can be noted that the average microscopic I was calculated before the logarithmic conversion. Consequently, it can be concluded that the number of particles with an inertial value higher than 10^{-2} is small, as their contribution to the average is several orders of magnitude higher than particles with a 10^{-5} I.

The presented simulations will be considered as the upper limit of quasi-static conditions, even though the microscopic calculations surpass the recommended value for large strains. Execution with a lower shear rate (piston displacement speed) would be preferable; however, it would involve a much higher computational cost.

4.3 Drained triaxial conditions

4.3.1 Macroscopic response

Figure 4.3e illustrates the evolution of the volumetric strain. At early stages, all specimens show a contracting behavior (i.e., decrease in volume). Then a peak value (diamond mark) is reached, followed by a dilation phase as the specimen expands in volume until a steady state is reached near the end of each simulation.

The stress behavior is given in Figure 4.3a. First, a hardening phase is observed, characterized by a non-linear increase in the strength of the specimen. After a peak value (circle mark), a softening phase occurs, leading to a decrease in strength until a steady state is reached for high axial strain values.

Figure 4.3d illustrates the void ratio evolution. It can be seen that the final states of the samples are not aligned. Furthermore, a steady state in the volumetric strain curves of specimens D28 and D50 was not observed in Figure 4.3e. Thus, the arrival to the critical state cannot be fully inferred.

Overall, the stress–strain behavior of the specimen is divided into three phases: contracting and hardening from the beginning until the characteristic point (diamond mark); dilatancy and hardening between the characteristic point and the peak deviatoric stress (circle mark); dilatancy and softening from the peak deviatoric stress and forward. This corresponds to what was previously observed in the literature [120, 121, 29, 30]

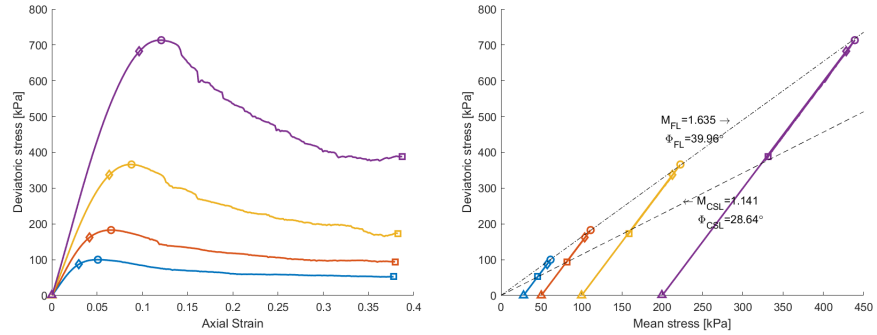

(a) Deviatoric stress vs axial strain. (b) Deviatoric stress vs mean stress.

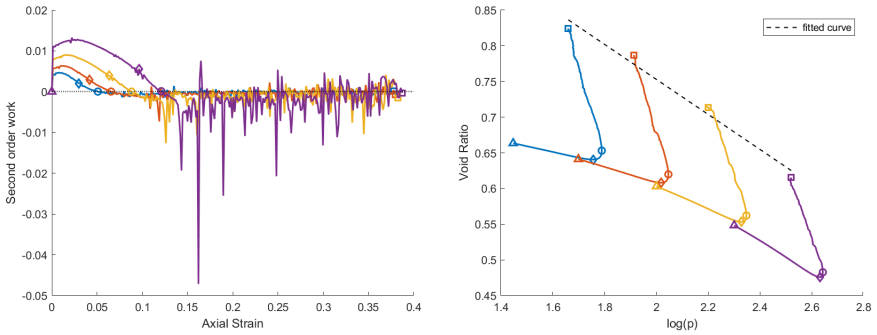

(c) Second-order work vs axial strain. (d) Void ratio vs log of mean stress.

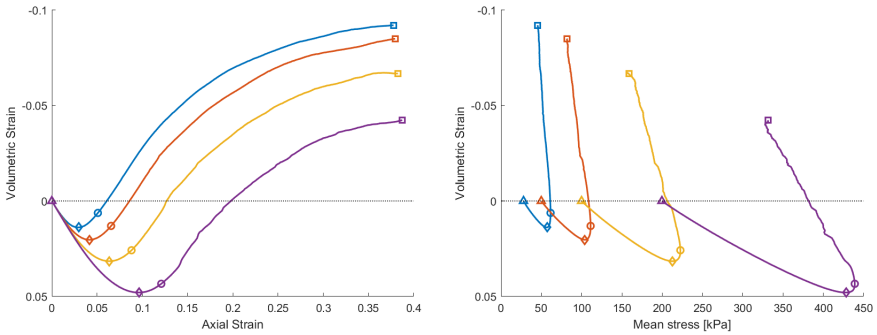

(e) Volumetric strain vs axial strain. (f) Volumetric strain vs mean stress.

Figure 4.3: Macroscopic results of drained triaxial simulations with different confining stresses (28 kPa, 50 kPa, 100 kPa, and 200 kPa). The triangle marks the initial stage, the square the final stage, the diamond the characteristic point, and the circle the peak deviatoric stress. (a) Deviatoric stress vs axial strain; (b) deviatoric stress vs mean stress; (c) second-order work vs axial strain; (d) void ratio vs log of mean stress; (e) volumetric strain vs axial strain; (f) volumetric strain vs mean stress.

A measure of the macroscopic value of the second-order work is shown in Figure 4.3c, highlighting the state at which the specimen achieves instability for each confining pressure. It can be noted that negative values are only reached after the peak deviatoric stress, thus indicating that the softening phase of the drained triaxial loading direction belongs to the cone of instability.

Figure 4.3b illustrates the mean stress–deviatoric stress plane (p–q plane), where the peak stress line and the critical state line (CSL) are identified through their coefficients, M_{FL} and M_{CSL}, respectively. The first is related to the upper strength limit of the simulated material. It is obtained through linear interpolation with the origin of the peak deviatoric stress values (circle points) in each test. The former represents an equivalent stress ratio reached by granular materials at high strain levels.

In geomechanics, a relation between the slope M and the friction angle of the soil φ can be obtained through the following equation:

$$M = \frac{6sin\varphi}{3 - sin\varphi} \qquad \varphi = arcsin\left(\frac{3M}{6 + M}\right) \tag{4.1}$$

Thus, an approximation of the friction angle can be obtained from the identified lines. The φ values obtained differ greatly from the contact friction angle defined in the DEM software of 55°. However, this result is expected since the internal friction angle includes geometrical effects.

4.3.2 Force chains

Force chains were identified through the procedures defined in Section 3.2.2. The identified structures are classified into two categories, namely, single-branch force chains (no ramification) and multibranch force chains (presence of ramification). The results are presented in Figure 4.4.

Figure 4.4a is the classic representation of force chain evolution, illustrating the ratio of grains structuring force chains (chained grains) in relation to the total amount of grains. A decrease in this ratio is observed in the very early stages, which is more pronounced in specimens submitted to lower isotropic stresses. Before compression, force chains were developed in all directions, as none was privileged during the isotropic consolidation. However, as the vertical load increases, grains that carry the load in the non-preferred direction are no longer submitted to higher-than-average stresses. Consequently, the number of chained grains decreases. Furthermore, Figure 4.4d shows that this decrease is mainly due to the loss of multibranch force chains, with the number of single-branch structures remaining unimpacted.

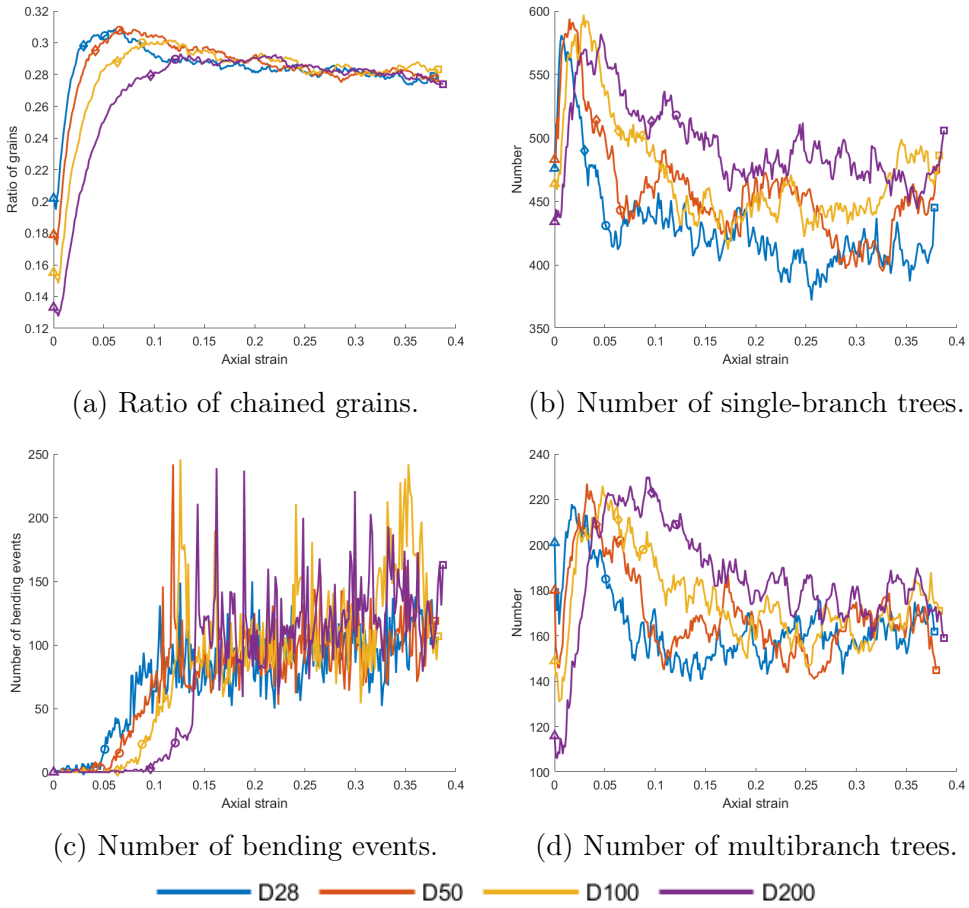

(a) Ratio of chained grains.

(b) Number of single-branch trees.

(c) Number of bending events.

(d) Number of multibranch trees.

Figure 4.4: Force chain results of drained triaxial simulations with different consolidation stresses (28 kPa, 50 kPa, 100 kPa, and 200 kPa). The triangle marks the initial stage, the square the final stage, the diamond the characteristic point, and the circle the peak deviatoric stress. (a) Ratio of chained grains; (b) number of single-branch trees; (c) number of bending events; (d) number of multibranch trees.

After this early phase, the number of grains structuring the force chain increases until a peak is reached, roughly corresponding to the peak deviatoric stress (circle mark). A direct relation between these two quantities can be established. The increase in strength of the specimen (hardening phase) comes from the rise in the number of grains actively participating in the force transmission. When a limit is reached, grain reorganization occurs, decreasing the number of chained grains. Consequently, the specimen loses strength (softening phase) [113].

Furthermore, the peak number of chained grains increases with the decrease in the lateral confining stress applied. To identify the reason behind this relation, the probability density function (PDF) of the stress distribution at the peak deviatoric state of each test was calculated and is illustrated in Figure 4.5;

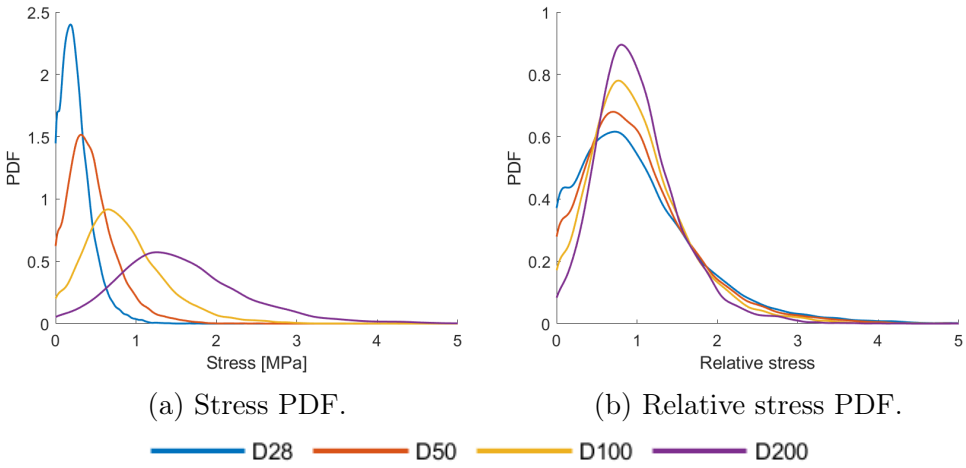

(a) Stress PDF. (b) Relative stress PDF.

Figure 4.5: Probability density function (PDF) of the stress distribution in the peak deviatoric stress for drained triaxial simulations with different consolidation stresses (28 kPa, 50 kPa, 100 kPa, and 200 kPa). On the left (4.5a) the PDF of the stress distribution, while on the right (4.5a) the stress is normalized in relation to the mean value.

Figure 4.5b shows the PDF of the stress normalized to the mean value. It can be seen that specimens with higher confining stress present a narrower PDF, indicating that stress is more evenly distributed.

Furthermore, it can be noted in Figure 4.5a, that specimens with lower confining pressure present a large amount of low-stressed grains, thus lowering the average grain principal stress. Consequently, a higher proportion of grains have higher than average stress and may be considered chained grains. In this case, the loss of chained particles results in a lesser decrease in the macroscopic stress compared to samples with higher confining pressure. Finally, all samples converge to an equivalent number of chained grains at large strains.

Single-branch and multibranch force chains can be seen to reflect a similar evolution to chained particles, as illustrated in Figures 4.4b and 4.4d. It can be noted that the observed peak for both curves appears before the characteristic point (diamond mark), with the single-branch curve reaching

it before the multibranch curve. Furthermore, single-branch structures vastly outnumber multibranch ones.

As the specimen is being loaded, it starts contracting, thus increasing the number of force chains and hardening the sample. During this early stage, the specimen behavior is elastic, with particles submitted to low displacements. Consequently, most force chains appear as smaller single-branch structures permeating the specimen through the previously formed granular skeleton.

When the existing contact network can no longer sustain an increase in force, particle rearrangement occurs. Existing force chains ramify and merge, creating increasingly longer structures. Consequently, a decrease in the number of single-branch force chains is observed, later followed by multibranch ones.

The phenomenon of force chain bending is summarized in Figure 4.4c. Bending events start occurring when approaching the characteristic point (diamond mark). After that, the number of bending events increases until a steady value is reached. Three phases can then be distinguished between force chain bending and the stress behavior in Figure 4.3a. First, the material is hardened (increase in strength of the specimen) while no bending event occurs. Later, a few bending events start while the sample is still in the hardening phase. Finally, the softening phase begins.

Furthermore, force chain bending has been shown to be associated with the growth of surrounding voids [112, 71]. As force chains start bending, the void spaces surrounding them increase in volume, leading to dilation of the specimen [112, 71, 2]. This decrease in the void ratio around force chains makes force chains less stable, increasing the probability of bending and ultimately leading to the peak deviatoric stress and later softening phase of the specimen.

Figure 4.6 illustrates the elevation angle of force chain contacts for the D100 test. The elevation is defined as the angle between the contact vector and the x–y plane, thus returning a 90° for vertical and 0° for horizontal contacts. Only the D100 test results will be shown since the conclusion is equivalent to the remaining tests.

It can be noted that no preferential direction is present at the beginning of the test, which is in accord with the isotropic condition applied. As the vertical force increases, the force chain contact with angles greater than 45° increases rapidly. Furthermore, contacts with an angle less than 30° rapidly approach zero and will only increase once bending events occur.

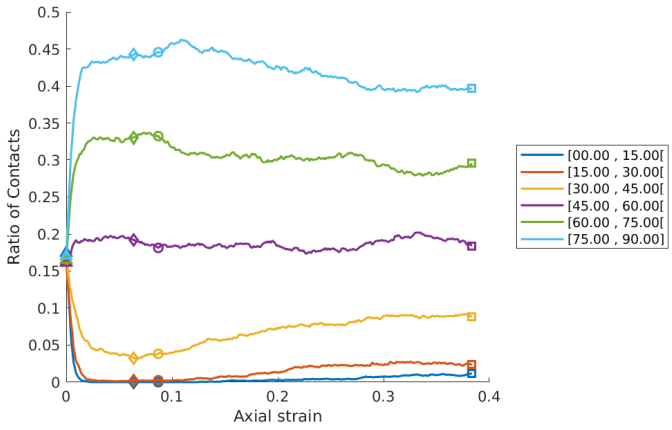

Figure 4.6: Evolution of the elevation angle of force chain contacts for the D100 test. It is defined as the angle between each contact and the x–y plane, with values between 90° and 0° for vertical and horizontal contacts, respectively.

4.3.3 Shear bands

With the procedures previously defined in Section 3.2, the numerical results will be visualized using ParaView software. Shear banding phenomena will then be identified through the localization of the following characteristics: cumulative deviatoric strain (grain scale), second-order work (grain scale), and incremental deviatoric strain (cell scale).

Shear banding was observed for all drained triaxial tests performed. As the conclusions taken from the analysis in this subsection are equivalent for all four tests, only the results related to sample D100 will be shown. The remaining test results in drained conditions can be found in Appendix A. Figure 4.7 illustrates the evolution of the shear band during different stages of the D100 test, using the three types of calculations proposed in Section 3.2.3.

No localization pattern can be clearly distinguished in the cumulative calculation at the deviatoric stress peak, as illustrated in Figure 4.7a. However, both incremental calculations show a hint of the shear band formation. Next, in Figure 4.7b a clear shear band can be distinguished from the bottom-left corner to the top-right corner. A reflection of the shear band can be observed three times: first on the top wall, then on the right wall, and finally on the bottom wall. Figure 4.7d illustrates the final stage of the specimen.

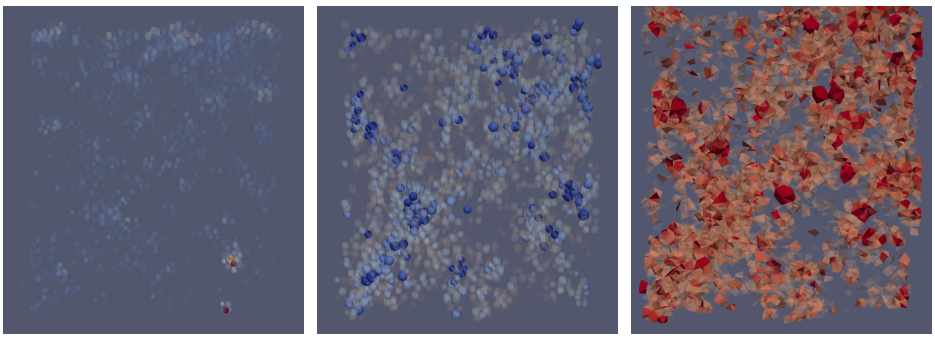

(a) Shear band identification at $\varepsilon_z = 0.088$ (peak deviatoric stress).

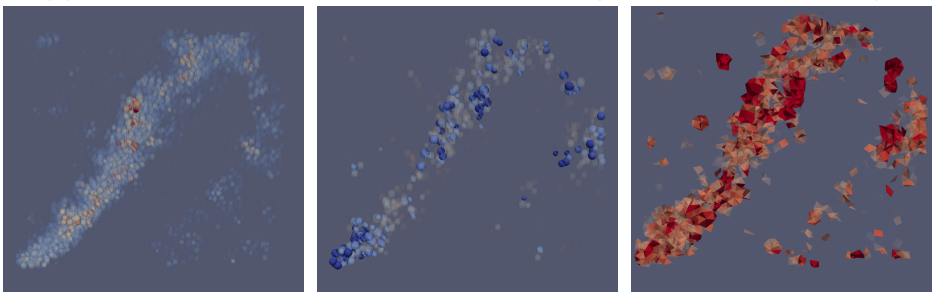

(b) Shear band identification at $\varepsilon_z = 0.221$.

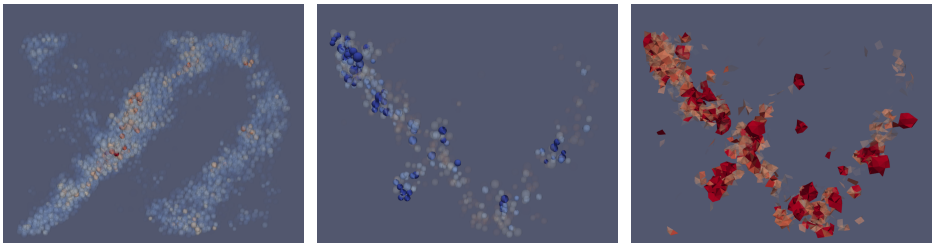

(c) Shear band identification at $\varepsilon_z = 0.295$.

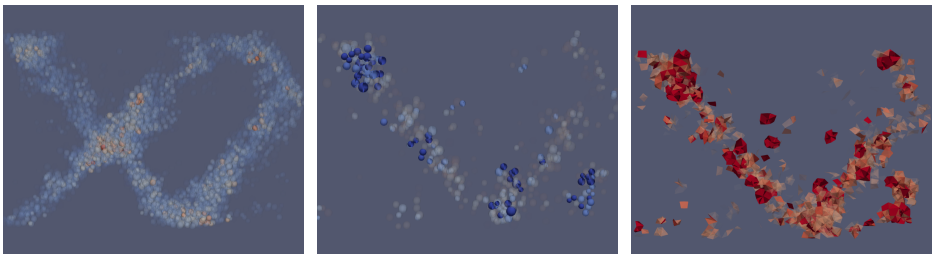

(d) Shear band identification at $\varepsilon_z = 0.381$.

Figure 4.7: Shear band evolution for the D100 test. Figures (a), (b), (c), (d) illustrate axial strains 0.088, 0.221, 0.295, and 0.381, respectively. Each column shows a different identification method, from left to right: cumulative deviatoric strain (grain scale), negative second-order work (grain scale), and incremental deviatoric strain (cell scale).

A difference between incremental and cumulative methods of identification of the shear band can be inferred. The former illustrates the instantaneous localization, while the latter shows all the shear band of the region has appeared throughout the loading path. This discrepancy can be better analyzed in Figure 4.7c, where the cumulative calculation does not register the third reflection observed for instantaneous ones. In addition, in Figure 4.7d, the first branch of the shear band becomes barely visible for the incremental calculations but remains present for the cumulative method.

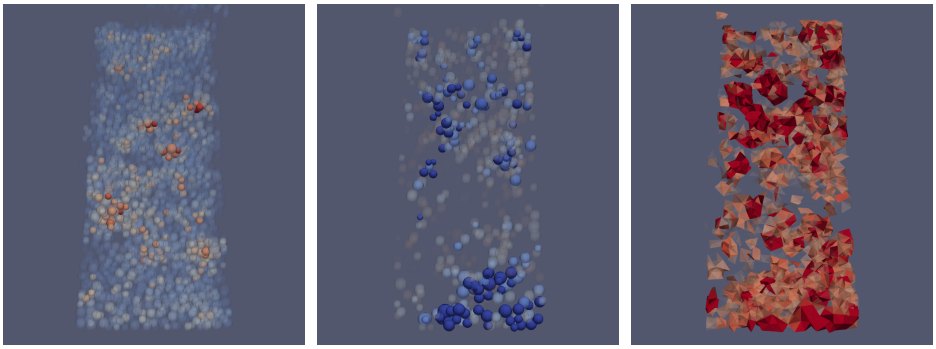

Figure 4.8: Lateral view of the shear band represented in Figure 4.7c. Each column shows a different identification method, from left to right: cumulative deviatoric strain (grain scale), negative second-order work (grain scale), and incremental deviatoric strain (cell scale).

All shear bands were observed to traverse the entire width of the specimen, as illustrated in Figure 4.8 where a rotation of 90° around the z-axis of Figure 4.7c is represented. Since the width of the specimen (x direction) remains several times smaller than the other two dimensions, its impact on the localization pattern of the sample is lessened. Consequently, shear band analysis can be performed from a lateral view (y–z plane).

4.4 Undrained triaxial conditions

4.4.1 Macroscopic response

Figure 4.9e illustrates the volumetric strain evolution of the three tests, reaching a maximal value of approximately 8×10^{-7}. As the incremental vertical displacement applied between each measure (point of the curves) represents a vertical strain of -1.25×10^{-4}, the volumetric variations can be considered negligible, thus validating the constant volume constraint required for undrained conditions.

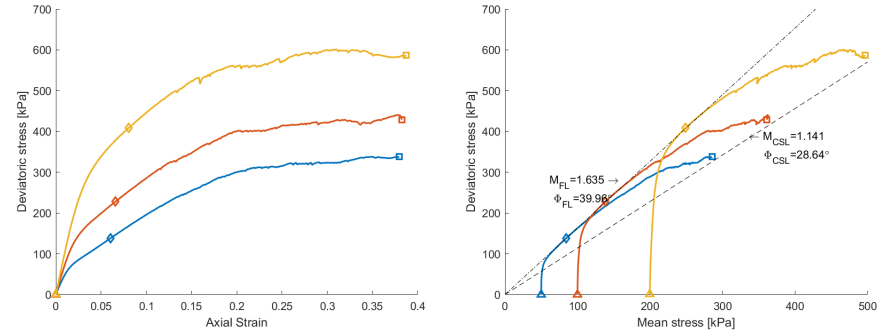

(a) Deviatoric stress vs axial strain. (b) Deviatoric stress vs mean stress.

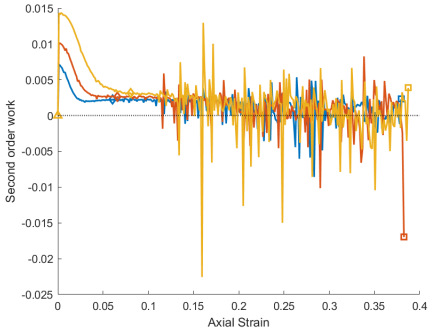

(c) Second-order work vs axial strain.

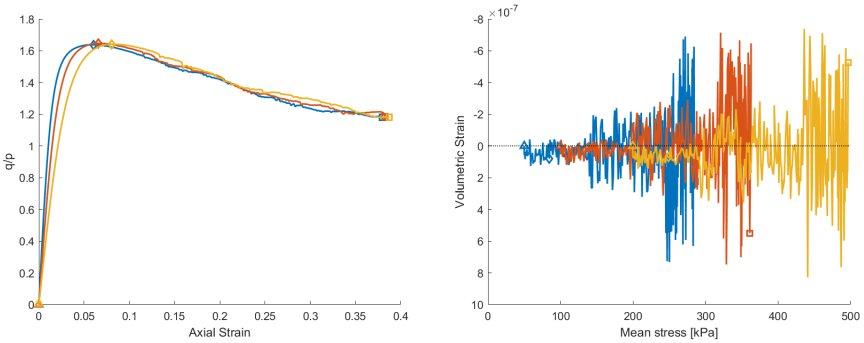

(d) Relative strength vs axial strain. (e) Volumetric strain vs mean stress.

Figure 4.9: Macroscopic results of undrained triaxial simulations with three different consolidation stresses: 50 kPa, 100 kPa, and 200 kPa. The triangle marks the initial state, the square the final state, and the diamond the peak relative strength. Peak stress and critical state lines derived from drained tests are displayed. (a) Deviatoric stress vs axial strain; (b) deviatoric stress vs mean stress; (c) second-order work vs axial strain; (d) relative strength vs axial strain; (e) volumetric strain vs mean stress.

Figure 4.9a shows the influence of consolidation stress on the strength of the specimen. As for the drained case, higher consolidation stress generates a stronger macroscopic response. Furthermore, it can be observed that approaching the end of the test, a steady state is reached for all specimens. Note that no failures through liquefaction is observed (vanishing of the mean pressure and the deviatoric stress), which is expected for a dense granular material (also visible in undrained tests through contractive/dilative and hardening/softening behaviors).

In fact, no sudden failure was ever observed, as indicated by the second-order work represented in Figure 4.9c. The value decreases continuously, fluctuating around zero for large strains; this indicates the approach of the critical state, as it corresponds to the plastic limit yield surface where the expected value of the second-order work is null for some incremental direction. Several negative peaks are present throughout the test. These can be referred to as small instabilities and local fluctuations of the stress state.

The failure and critical state lines obtained for the drained case are plotted in the deviatoric–mean stress plane (p–q plane) represented in Figure 4.9b. It can be noted that all three undrained specimens evolve coincidentally with the failure line for a portion of their loading path. This region can also be identified in Figure 4.9d by a small plateau around the highest attained relative strength value (diamond mark). Later this ratio decreases in value, representing a loss of relative strength and the tendency of the former curve to be attracted toward the CSL [122].

An undrained M_{CLS} value was calculated using the final points (square mark) of the undrained tests returning a value of $M = 1.2$, sufficiently close to the previously defined $M_{CSL} = 1.141$ obtained in the drained case. It can be assumed that if the loading were continued, the undrained specimens would evolve to reach an equivalent state to the drained ones.

4.4.2 Force Chains

In the early stages of the test, the specimen goes through a rapid hardening phase until the failure line is reached, as illustrated in 4.9b. This phase results in a rapid augmentation of the number of chained grains, as shown in Figure 4.10a. Consequently, the number of force chains is observed to increase, as illustrated in Figures 4.10d, 4.10b and 4.10a. Since grain rearrangement has not yet started, force chains mainly comprise smaller structures permeating the specimen.

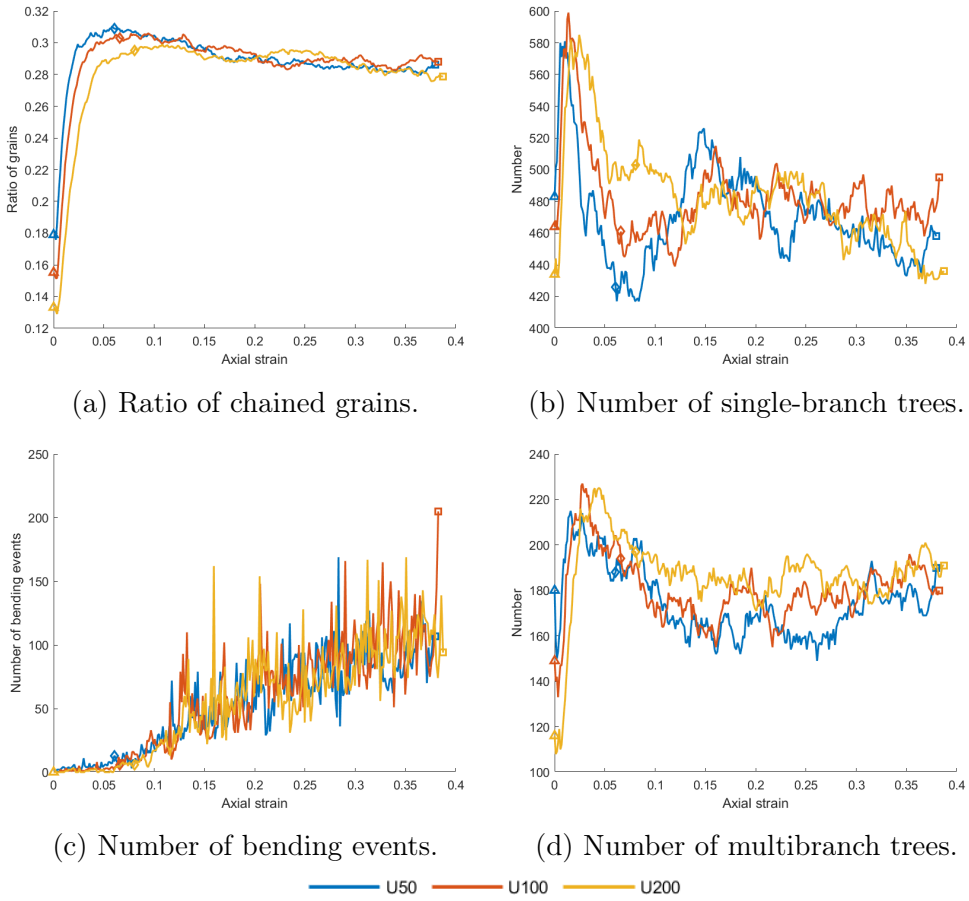

(a) Ratio of chained grains.

(b) Number of single-branch trees.

(c) Number of bending events.

(d) Number of multibranch trees.

Figure 4.10: Force chain results of undrained triaxial simulations with different consolidation stresses (50 kPa, 100 kPa, and 200 kPa). The triangle marks the initial state, the square the final state, and the diamond the peak relative strength. (a) Ratio of chained grains; (b) nNumber of single-branch trees; (c) number of bending events; (d) number of multibranch trees.

Next, force chains start ramifying and merging, which results in increasingly larger chains. A decrease in single-branch structures and later multibranch ones is observed. This phase is accompanied by the start of force chain bending, further confirming the grain rearrangement.

When new grains stop being incorporated into force chains, the specimen can no longer support the incremental load being applied, leading to a decrease in relative strength. During this phase, Figure 4.10c shows increasing bending events, leading to the localization patterns observed in the following section.

4.4.3 Shear bands

Shear bands were identified using the same procedures applied in drained conditions. The results of specimen U100 are presented in Figure 4.11, while the remaining undrained tests can be found in Appendix A.

The presence of a shear band was not identified at the peak relative strength of the U100 test (diamond mark in Figure 4.9b), as illustrated in Figure 4.11a. Both incremental calculations show a mostly homogeneous specimen.

A clear localization pattern can be observed from Figure 4.11b onward. The initial shape of the band is similar to the one observed in the D100 test, starting from the bottom-left corner and rising to the top-right corner.

Figures 4.11c and 4.11d show indications of shear band reflection in the top wall and right wall, with the latter being more apparent for incremental calculations.

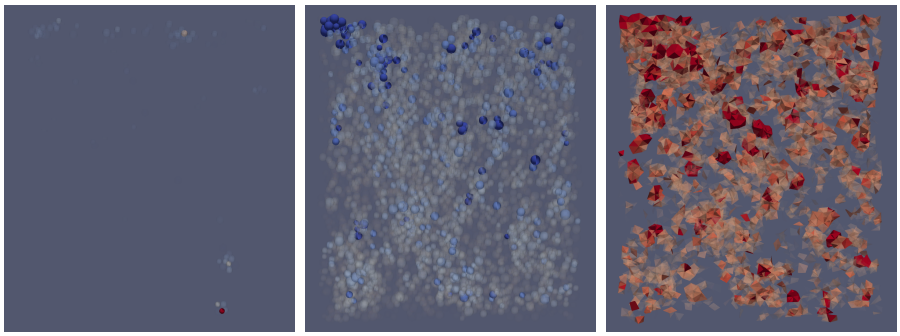

(a) Shear band identification at $\varepsilon_z = 0.067$ (diamond mark).

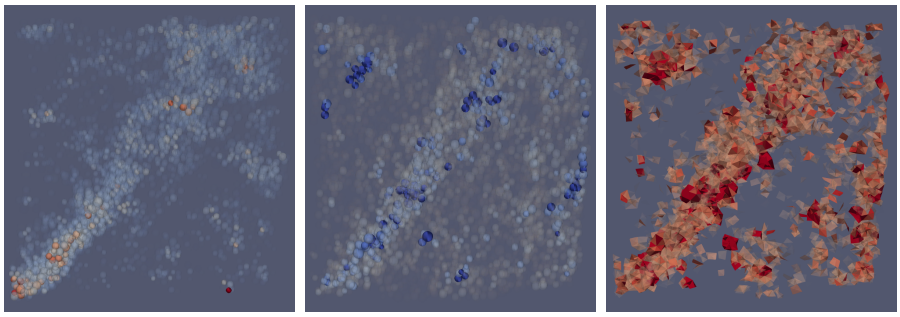

(b) Shear band identification at $\varepsilon_z = 0.146$.

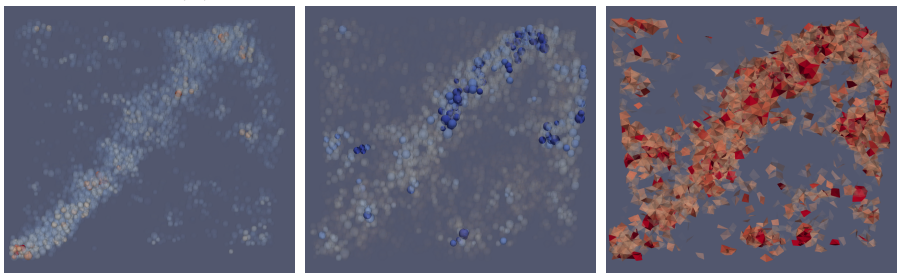

(c) Shear band identification at $\varepsilon_z = 0.255$.

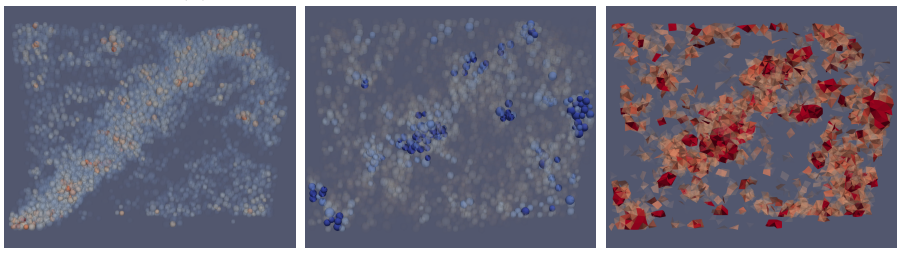

(d) Shear band identification at $\varepsilon_z = 0.378$.

Figure 4.11: Shear band evolution for the U100 test. Figures (a), (b), (c), (d) illustrate axial strains of 0.06, 0.12, 0.23, and 0.38, respectively. Each column shows a different identification method, from left to right: cumulative deviatoric strain (grain scale), negative second-order work (grain scale), and incremental deviatoric strain (cell scale).

4.5 Q-constant triaxial conditions

4.5.1 Macroscopic response

In the context of this work, failure of q-constant tests is defined as a drop in the deviatoric stress to 99.9% of the targeted value and is represented by a diamond mark in each of the curves in Figure 4.12. For all tests, the failure occurs when the stress state reaches the failure line (FL), as shown in Figure 4.12b. Furthermore, as illustrated in Figure 4.12c, the second-order work shows that negative values only appear after the chosen criterion, thus validating this approach.

When effective failure occurs, a drop in deviatoric stress is visible corresponding to a loss of controllability. During this phase, the specimens can no longer sustain the required deviatoric stress for the applied pressure. Consequently, the axial strain increases rapidly, and the specimens undergo a stress-softening phase (decrease in stress value), as illustrated in Figure 4.12a. At the final stages, the stress stabilizes for high strain values resulting in the specimen approaching the critical state.

It can be noted that the response of all specimens crosses through the critical state line (CSL) without presenting any influence on the macroscopic behavior, thus inferring the absence of a bifurcation domain for the presented tests until the failure line is reached.

After failure, the specimen stress-state shifts rapidly to the CSL with a similar slope to the drained part of the test (tests Q100-150 and Q100-200 were stopped before the line could be reached). By lowering the mean pressure, the specimen strength decreases until it can no longer sustain the applied deviatoric stress, leading to the observed drained equivalent failure.

In Figures 4.12e and 4.12f, an early contraction phase is imposed during the first phase of the test (drained compression). Later a dilatative behavior occurs, which is the intuitive response of a material subjected to a decrease in the isotropic part of the stress. During this phase, the volumetric strain evolves proportionally to the mean stress. Finally, a sudden increase in volumetric and axial strain is observed around the failure point of the specimen.

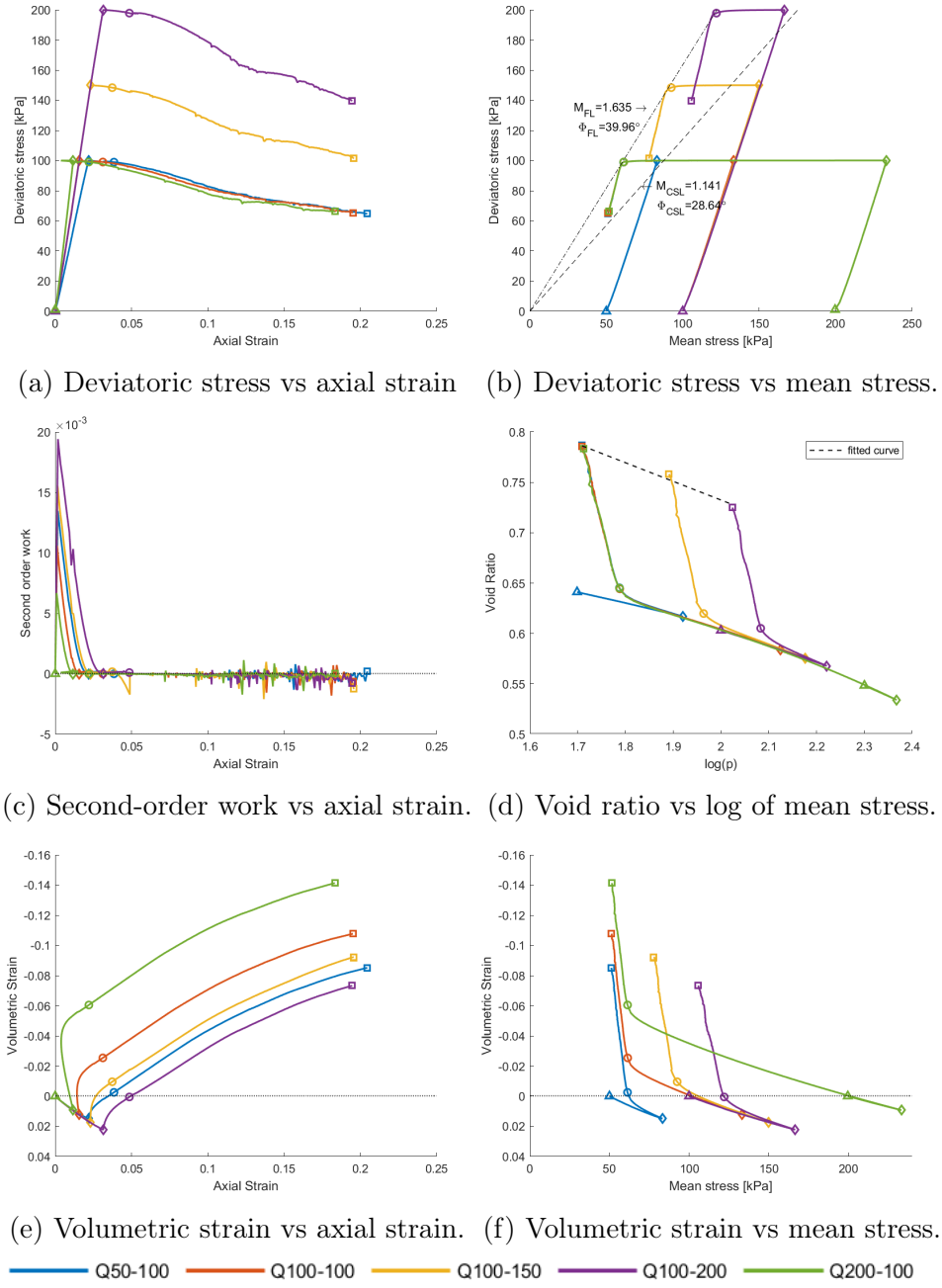

(a) Deviatoric stress vs axial strain (b) Deviatoric stress vs mean stress.

(c) Second-order work vs axial strain. (d) Void ratio vs log of mean stress.

(e) Volumetric strain vs axial strain. (f) Volumetric strain vs mean stress.

Figure 4.12: Macroscopic results of constant deviatoric stress (q-costant) triaxial simulations, with varying isotropic compression stresses (50 kPa, 100 kPa, and 200 kPa) and deviatoric stress targets. The triangle marks the initial state, the square the final state, the diamond the end of the drained phase, and the circle the failure point. (a) Deviatoric stress vs axial strain; (b) deviatoric stress vs mean stress; (c) second-order work vs axial strain; (d) void Ratio vs log of mean stress; (e) volumetric strain vs axial strain; (f) volumetric strain vs mean stress.

It can be noted that the nature of the volumetric deformation sustained during the drained compression phase differs for the two groups of tests. During the Q100-100, Q100-150, and Q200-100 tests, the deformation is elastic as the specimens return to their initial state with the subsequent decrease of pressure, while the remaining tests do not (Q50-100 and Q100-200). This phenomenon is related to the fact that, for the latter, the ending point of the drained phase is around the CSL, as shown in Figure 4.12b. Plastic deformation creates grain rearrangement, making the return to the initial state impossible.

4.5.2 Force chains

The global conclusions made from the analysis of the force chain behavior in q-constant conditions will be shown to follow the same trends highlighted for the drained cases.

It can be noted that the change in stress during the isotropic compression phase does not have a significant effect on the number of chained grains, as illustrated in Figure 4.13a. All three specimens with equivalent targeted deviatoric stress show a coincidental behavior for the final phases of the test. Furthermore, the change in target deviatoric stress only seems to shift the observed response in the x-axis.

During the first phase, the specimens are charged until the target deviatoric stress is reached. In Figure 4.13a an increase in the number of grains structuring force chains can be observed, reflecting the macroscopic hardening behavior of the specimen.

Next, the specimen is discharged while maintaining the deviatoric load applied. In other words, the relative strength of the specimen increases. Consequently, the number of force chains and chained grains increases while the specimen is still being submitted to a stress hardening phase, as illustrated in Figure 4.13.

This effect can also be analyzed as a loss of strength of the weak network of the specimen (grains with below-average stress states). With the decrease in the mean pressure, the contribution of the deviatoric stress to the stress state of the grains becomes more important. Thus, as the average grain stress decreases, more grains are identified as part of force chains.

Later the number of grains structuring force chains reaches a peak value around the failure point of the specimen (circle mark), as illustrated in 4.13. It can be concluded that the decrease in the number of chained grains results in an overall reduction in the specimen strength, as was observed for the drained and undrained cases.

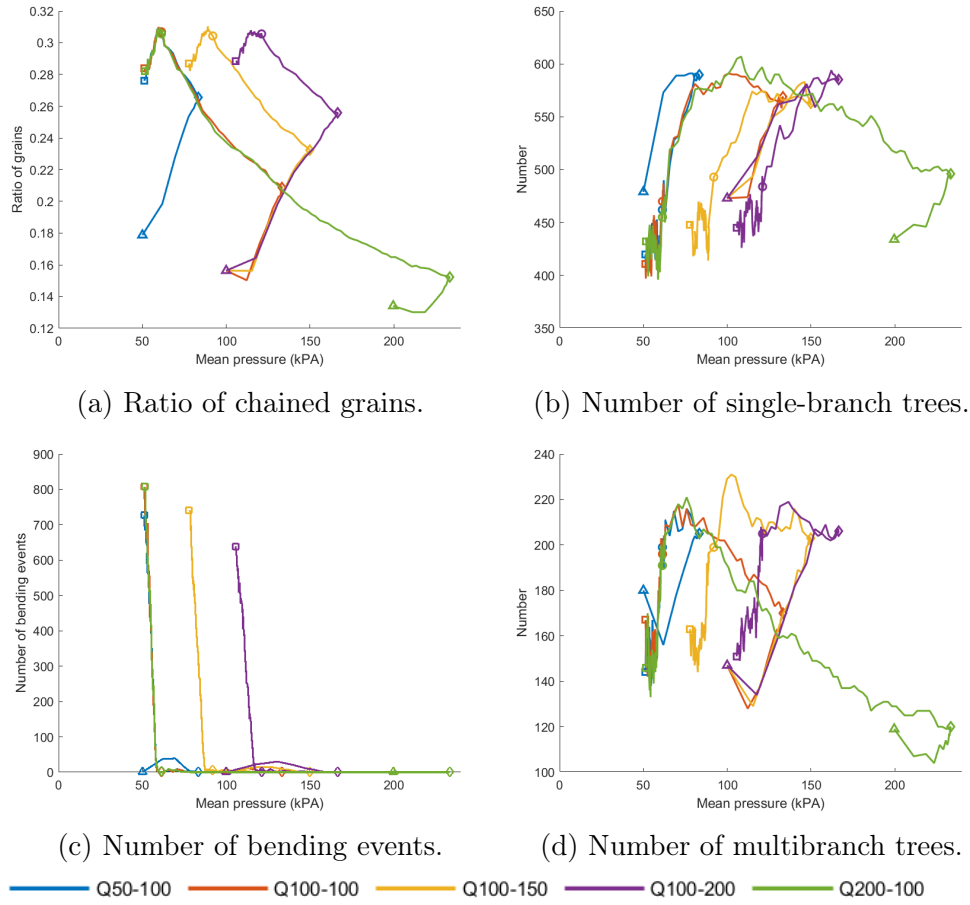

(a) Ratio of chained grains.

(b) Number of single-branch trees.

(c) Number of bending events.

(d) Number of multibranch trees.

Figure 4.13: Force chain results for the constant deviatoric stress (q-constant) triaxial simulations with different consolidation stresses (28 kPa, 50 kPa, 100 kPa, and 200 kPa). The triangle marks the initial state, the square the final state, the diamond the end of the drained phase, and the circle the failure point. (a) Ratio of chained grains; (b) number of single-branch trees; (c) number of bending events; (d) number of multibranch trees.

4.5.3 Shear bands

As for the previous cases, Figure 4.14 illustrates the shear band formation for one test, the Q100-100, while the remaining can be found in Appendix A.

Around the failure point, a clear localization pattern was not identified for the cumulative deviatoric strain (grain-based), as shown in Figure 4.14a. However, the second-order work (grain-based) and incremental deviatoric strain (cell-based) show a few concentrated values starting on the lower-left corner and traversing the specimen to the upper-right corner.

Later, the shear band can be identified as a single band traversing the specimen, as shown in Figures 4.14b and 4.14c.

Furthermore, the initial shape of the shear band is similar for all specimens. As all tests depart from the same initial state, a predisposition to this shape can be asserted. However, the final form of the shear band varies with the loading conditions, with the phenomenon of shear band reflection being observed primarily in the drained cases.

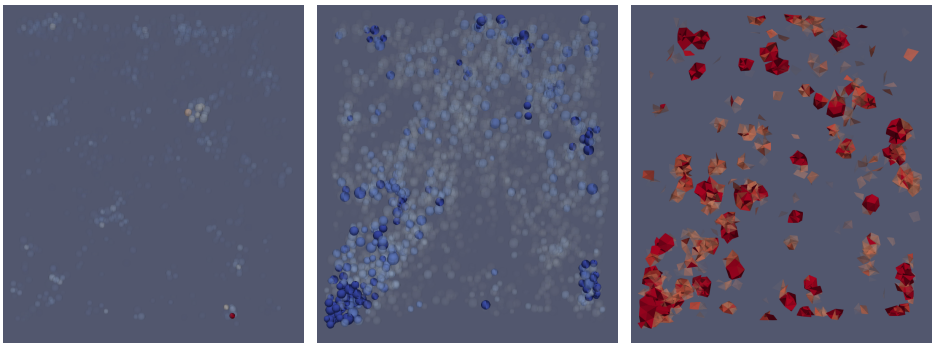

(a) Shear band identification at $p = 89.89kPa$ (failure point).

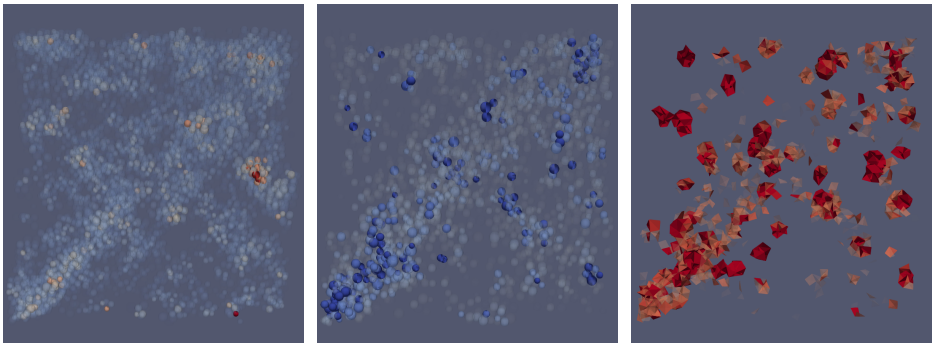

(b) Shear band identification at $p = 79.20kPa$.

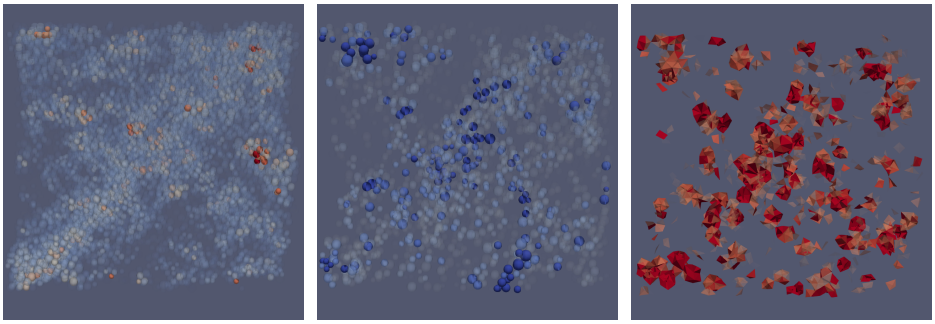

(c) Shear band identification at $p = 66.31kPa$.

Figure 4.14: Shear band evolution for the Q100-100 test. Figures (a), (b), (c) illustrate mean pressure of 61.47 kPa, 58.13 kPa, and 49.70 kPa, respectively. Each column shows a different identification method, from left to right: cumulative deviatoric strain (grain scale), negative second-order work (grain scale), and incremental deviatoric strain (cell scale).

4.6 Comparison between drained and q-constant conditions

To analyze the impact of the loading path on the failure at an equivalent stress state, tests D28 and D100 will be compared.

4.6.1 Macroscopic response

Figure 4.15b illustrates that, for both tests, failure occurs at a similar stress state, represented by a circle for both tests. Furthermore, Figure 4.15c illustrates that the void ratio is equivalent between both failure points, illustrating that both specimens are in the same state.

It is interesting to note that the nature of both loading paths is opposed. The constant deviatoric stress tests consist of lowering the stress level applied, while the drained triaxial tests increase it. Thus, in Figures 4.15b,4.15c, and 4.15d they approach the failure point from opposite directions.

Figure 4.15a shows the evolution of the deviatoric stress between both paths. It is interesting to note that even though the failure occurred at different strains, the slope of the softening phase is concurrent, thus inferring that the failure mechanism is identical between the two tests.

The volumetric strain, illustrated in Figure 4.15d, represents the volume variation in relation to the initial state of the test (after the isotropic compression). Since both tests were subjected to different initial confining pressure, their initial volumetric conditions are not comparable. To this effect, the void ratio was plotted in Figure 4.15c to illustrate an internal characteristic of the specimens. It can be seen that both samples reach failure at almost the same void ratio. Consequently, failure can occur for the same state of pressure, deviatoric stress, and void ratio.

4.6.2 Force chains

It is noteworthy in Figure 4.16 that the curves from both specimens start at different states and converge to the failure point of both specimens, from where they behave similarly.

Figure 4.16c shows that the number of bending events is several times larger for the Q100-100 test than for the D100 test. As bending events are calculated by comparing two successive states of the specimen, the interval choice directly impacts the resulting value. Consequently, both values are not comparable since the interval chosen for both tests is not adapted for this

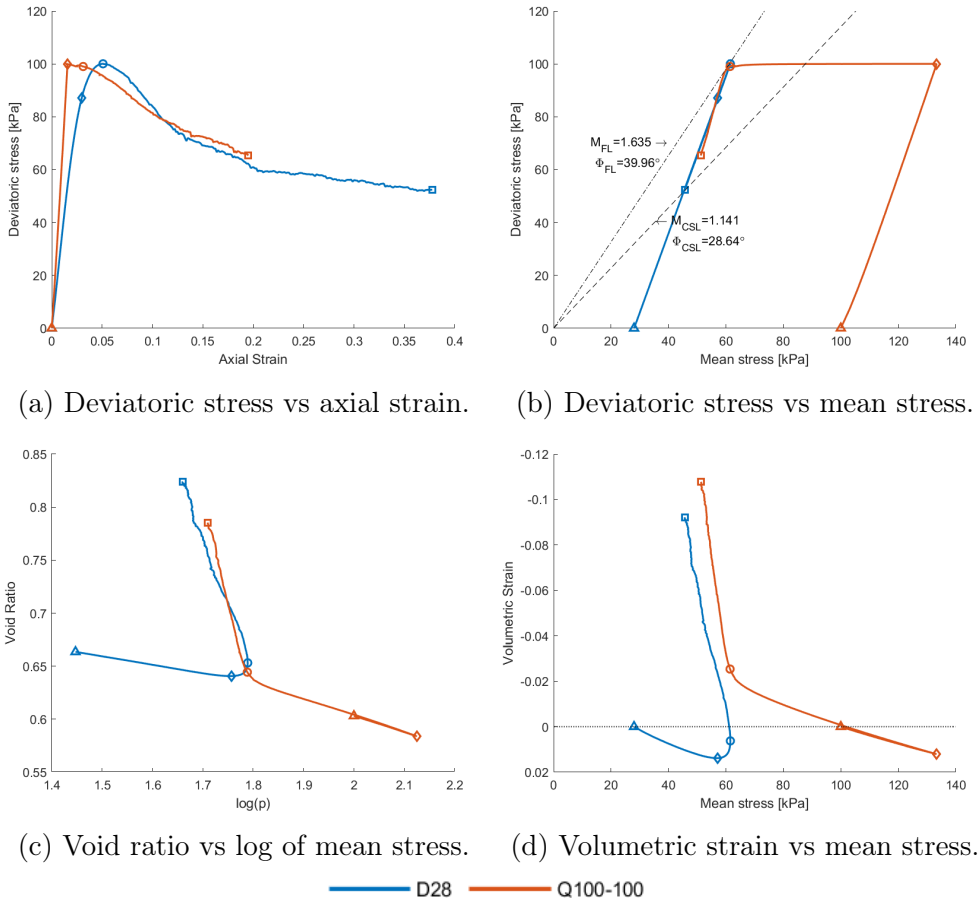

(a) Deviatoric stress vs axial strain. (b) Deviatoric stress vs mean stress.

(c) Void ratio vs log of mean stress. (d) Volumetric strain vs mean stress.

Figure 4.15: Macroscopic results comparison between constant deviatoric stress (Q100-100) and drained (D28) triaxial simulations reaching failure at around the same stress state. The triangle marks the initial state, the square the final state, while the circle and diamond mark important points for the respective test. (a) Deviatoric stress vs axial strain; (b) deviatoric stress vs mean stress; (c) void ratio vs log of mean stress; (d) volumetric strain vs mean stress.

analysis. However, Figure 4.16c is still interesting, as it shows that bending events mostly occur after the rupture for both tests.

Globally, these results complement the conclusions of Section 4.6.1, showing that the state (internal and external) of both specimens is equivalent in the instant of failure and tends to evolve similarly afterward.

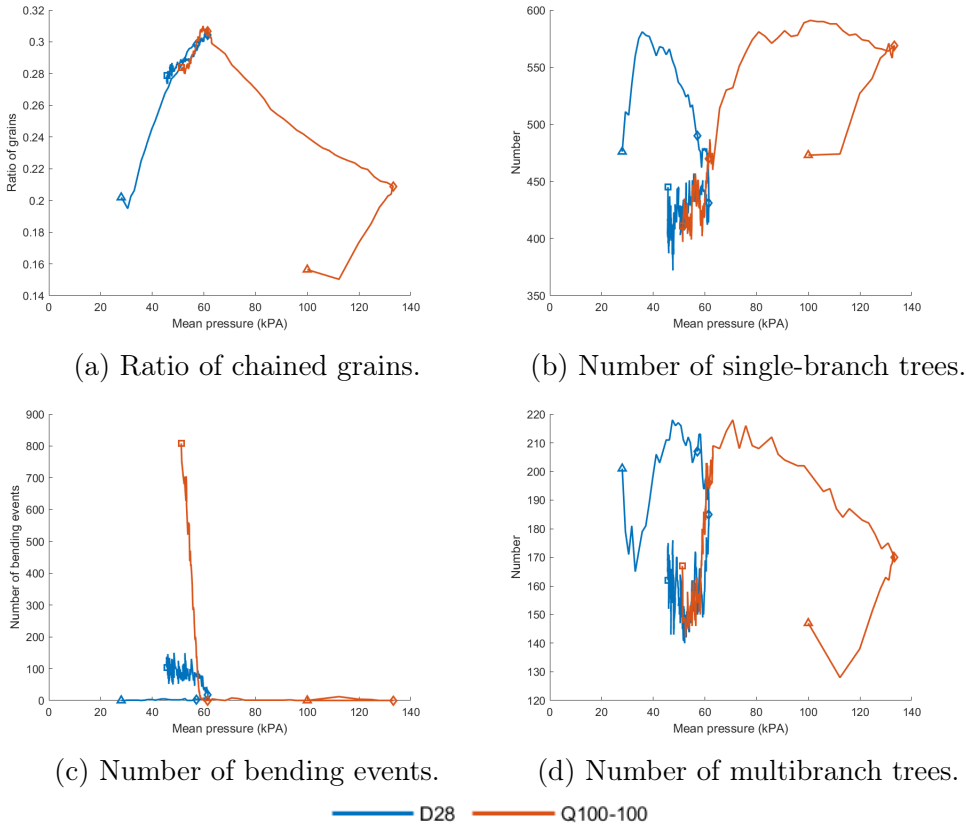

(a) Ratio of chained grains.

(b) Number of single-branch trees.

(c) Number of bending events.

(d) Number of multibranch trees.

Figure 4.16: Force chain results comparing constant deviatoric stress (Q100-100) and drained (D28) triaxial simulations reaching failure at a similar stress state. The triangle marks the initial state, the square the final state, while the circle and diamond mark important points for the respective test. (a) Ratio of chained grains; (b) Number of single-branch trees; (c) Number of bending events; (d) Number of multi-branch trees.

4.7 Concluding remarks

In this chapter, it was shown that all the specimens behave like dense soil under the different loading paths applied.

The failure line (FL) and critical state line (CSL) were identified in the drained loading path and later applied to the other triaxial cases. In the q-constant simulations, failure appeared around the instant when the specimen tried to cross the CSL. At the same time, the undrained simulations show no signs of failure. However, undrained behavior was shown to be bounded between both lines, matching the FL at the peak relative strength and later approaching CSL for large strain values.

The evolution of force chain structures is directly linked to the macroscopic behavior of the specimen. Their general behavior can be summarized as follows: Force chains are created in the hardening phase. Next single-branch force chains start merging with multibranch force chains. Then, as no more force chains are being created, force chains start bending and leading to the softening phase of the material.

The Q28 and Q100-100 tests were planned to fail at an equivalent macroscopic stress state with a similar failure point. Further analysis of the force chain structures of both tests revealed a convergence between the behavior of these structures around the failure point.

Strain localization in the form of shear bands appeared in all specimens. The three different methods of identifying the shear band were effective. Incremental calculations show the instantaneous transformation of the sample, while the cumulative version allows for the observation of the history of the shear band inside the specimen.

Furthermore, the initial shape of the shear band is similar for all specimens, starting in the lower-left corner and finishing in the top-right corner. As all tests depart from the same initial state, a predisposition to this shape can be asserted. However, the final form of the shear band varies with the loading conditions, with the phenomenon of shear band reflection being observed primarily in the drained cases.

Finally, the analysis of the inertial number of the triaxial tests executed showed that they are in the upper limit of quasi-static conditions. Furthermore, all q-constant tests surpass the $10^{-}2$ mark after failure, directly impacting the observed results. For example, the number of bending events of q-constant tests is much higher than in other triaxial conditions.

Chapter 5

Clusters characteristics and relation to coexisting internal structures

5.1 Foreword

In this chapter, clusters will be identified using the procedures described in Section 3.2.1 and later analyzed to validate them as extensions for loops in 3D conditions. First, several internal characteristics of clusters will be explored, giving an overview of the properties of these structures. Next, clusters will be categorized with regard to whether they are created or destroyed during the loading path. Finally, the relation of clusters to co-existing internal granular structures, namely, force chains and shear bands, will be explored.

5.2 Cluster characteristics

Using the tools presented in Section 3, the newly proposed cluster structures will be studied in a 3D granular material simulation. The first question that arises is about the appearance of these structures. Loops can be clearly visualized in 2D conditions as simple geometric shapes. However, this is far from the case for clusters. In this regard, Figure 5.1 illustrates a few clusters of different orders and sizes, their varying geometrical configurations, and their location for a rectangular drained triaxial test.

Figure 5.1 reveals that these structures adopt different forms, from more elongated ones like cluster A (Order 70, Size 33) to more clumped ones like cluster C (Order 72, Size 30). A comparison between both of these clusters shows that the form of a cluster has an impact on its order and size. Although cluster A is made up of a significantly higher number of grains than cluster C, the manner in which its cells are arranged creates fewer external surfaces, thus a lower order (exterior surfaces).

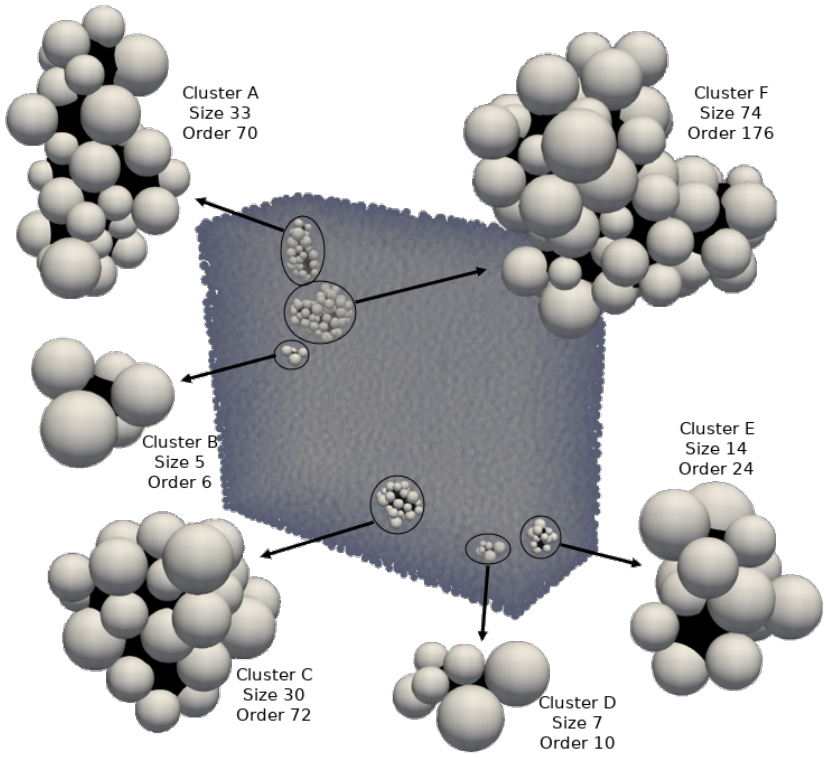

Figure 5.1: Examples of clusters of varying sizes and orders for a rectangular drained triaxial test.

5.2.1 Size and order

To quantify the range of orders reached by these structures, Figure 5.2 illustrates the evolution of the maximal cluster order for tests D28, Q50-100, and U50. Only these tests are shown as they present the largest cluster orders in their respective triaxial category.

The maximal cluster order observed is approximately 350 for test D28, 240 for test Q50-100, and 190 for test U50. If specimens under q-constant conditions were continued past 20% axial strain, clusters of a higher order would be identified, as the post-failure behavior is equivalent to drained conditions. By contrast, the mean pressure only increases during the undrained loading path, and thus clusters of orders larger than 200 are less probable.

It was previously affirmed in Subsection 3.2.1 that there is no bijection between the size and order of clusters. However, the evolution of these quantities is very similar for each test, as illustrated in Figure 5.2. Thus, a relation between them can be inferred.

Let there be a cluster C of size S and order O. To add a random grain G

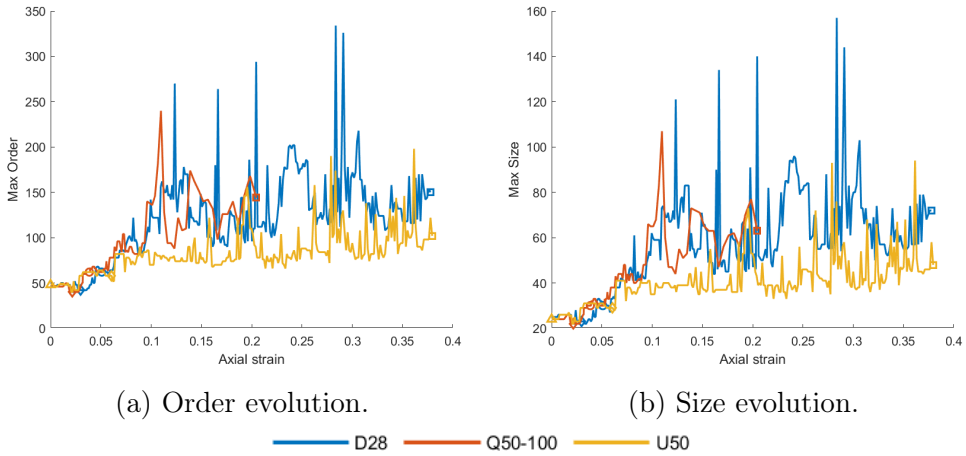

(a) Order evolution. (b) Size evolution.

Figure 5.2: Evolution of the maximal cluster order (a) and size (b) for tests D28, Q50-100, and U50.

to C (increasing S by 1), new cells between G and other grains belonging to C are created. Each of the newfound cells can only share one open surface with C, as the three other surfaces of the newly created cells contain the grain G, and thus could not previously be part of C. Consequently, the cells created between G and C must follow one of these cases:

- 1) The newfound cell shares one open surface with C. Thus, this cell will increment C order by 3. However, C had to lose one of its closed surfaces for the new cell to be joined. Finally $O_{new} = O + 2$.
- 2) The newfound cell shares one open surface with C and one with other newfound cells. Thus, this cell will increment C order by 2. However, C had to lose one of its closed surfaces for the new cell to be joined. Finally $O_{new} = O + 1$.
- 3) The newfound cell shares one open surface with C and two with other newfound cells. Thus, this cell will increment C order by 2. However, C had to lose one of its closed surfaces for the new cell to be joined. Finally $O_{new} = O$.
- 4) The newfound cell shares one open surface with C and three with other newfound cells. Thus, this cell will not increment the order of C. However, C had to lose one of its closed surfaces for the new cell to be joined. Finally $O_{new} = O - 1$.

For an incremental increase in size, if only one cell or several cells joined by open surfaces is created, the overall order sum always turns out to be

$O_{new} = O + 2$. Thus, departing from the minimal cluster (order and size of 4) and adding n grains, the following relation can be established:

$$\frac{S}{O} = \frac{4+n}{4+2n} \tag{5.1}$$

However, two pathologies invalidate equation (5.1). The first one appears if several separate sets of structures are created by adding a single grain into a previously formed cluster. Take, for example, the 2D representation of an almost closed ring-like structure illustrated in Figure 5.3. Adding the red grain to this structure creates two separate cells. Applying the same principle in 3D increases the order by 4 and the size by 1, resulting in a lower value than expected from equation (5.1).

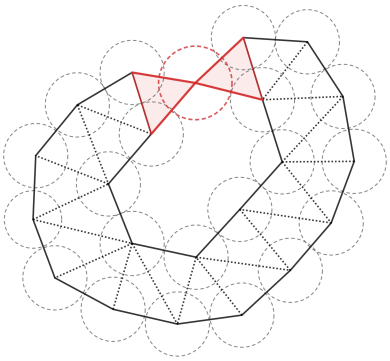

Figure 5.3: Representation of a circular structure composed of cells in 2D. Adding the red grain creates two separate cells, thus invalidating equation (5.1).

On the other hand, if a grain is completely enclosed inside a cluster, it would increase the total structure size without adding an external frontier. Consequently, a higher value than expected from equation (5.1) is obtained.

Figure 5.4 illustrates the evolution of the ratio size over the order in function of the order value. The red line represents Equation (5.1), and the black line represents the average value.

It can be noted that the black and red lines are superposed up to around order 26. From there, most of the clusters obtained are shown to be below the limit defined by the red line. This indicates that adding one grain to high-order clusters generates, on average, several separate structures increasing the order by more than 2. The first incidence of clusters below the red line appears relatively early for order 12; on the other hand, clusters above the

red line appear after order 20. However, these early cases can be considered rare cases, as the mean value for this order still coincides with the red line.

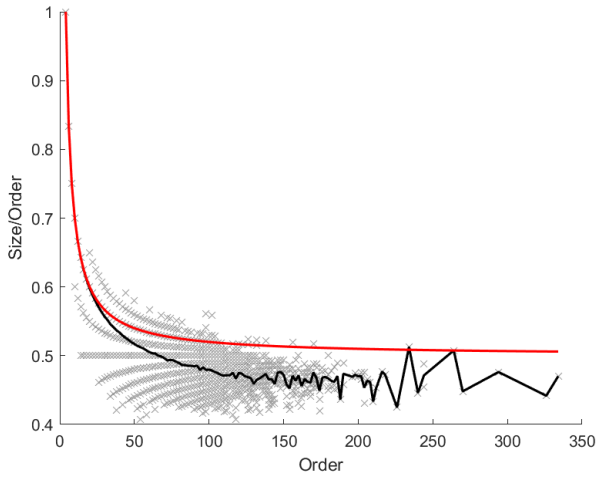

Figure 5.4: Evolution of the ratio size over the order in function of the order. The black line is the mean curve, while the red line represents equation (5.1).

At the extreme, the first pathology leads to the formation of clusters of order 4 inside high-order clusters, as illustrated in Figure 5.5. The cell shown in red is a cluster of order 4, containing four closed surfaces, inside a large cluster of order 30. Consequently, the latter is formed by 26 closed surfaces pointing outward and four pointing inward toward the red cell.

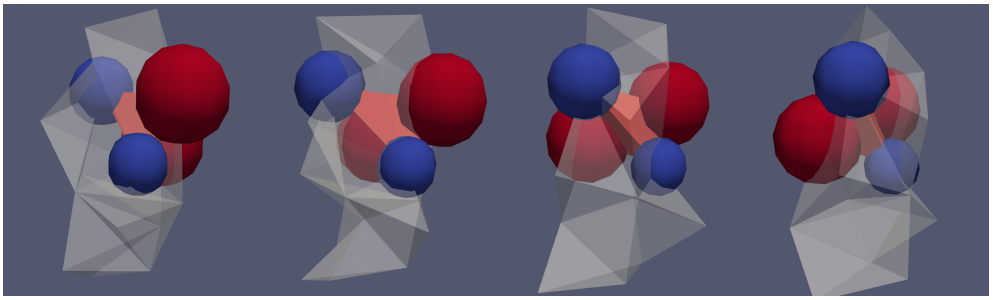

Figure 5.5: Cluster of order 30 and size 17 containing a cluster of order 4, illustrated in red, completely inside its domain. The four grains composing this cluster 4 are also illustrated.

This pathology often occurs through the formation of clusters of order 4 from two unconnected pairs of grains. This is illustrated in Figure 5.5, where each red particle is connected to a blue particle. As all surfaces of the

smaller cluster are shared with the larger one, the smaller cluster could be integrated into the larger one. Yet, this would require creating an exception rule or modifying the merging criterion defined in Section 3.2.1. However, in the context of this thesis, the previously defined merging criterion will not be modified.

Next, to identify a relation between order and size values, the observed values of cluster order and size properties are summarized in Figures 5.6 and 5.4.

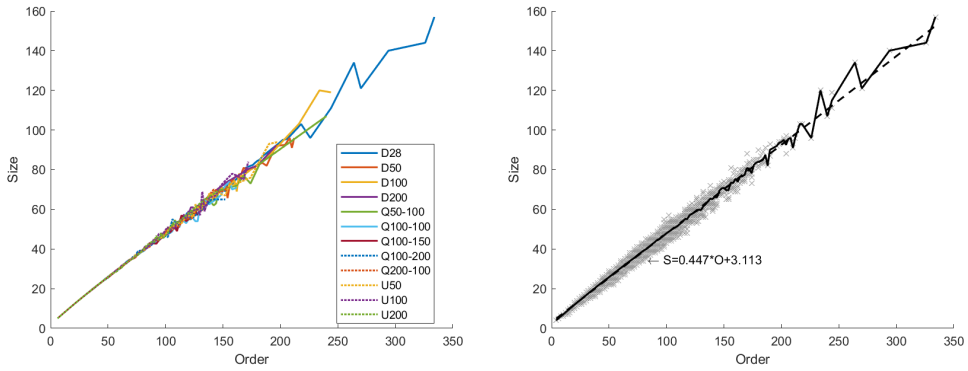

(a) Analysis per specimen. (b) Total identified cluster analysis.

Figure 5.6: Evolution of size in function of order. In (a) linear regression of the data obtained for each simulation is represented on the left. In (b), a scatter of the joint data of all simulations is shown with a linear regression illustrating the relation between these two quantities.

Each line in Figure 5.6a was obtained from a linear regression of the size distribution and order values observed during each simulation. These lines can be seen to follow a similar tendency between the different tests. For this reason, data obtained throughout all simulations were scattered in Figure 5.6b, where each gray speck represents an observed cluster. From the latter, a linear correlation between size and order results in an evolution law between size and order. Furthermore, it can be noted that the gray specs represented in Figure 5.6b do not stray far from this linear relation, indicating low variability for the possible size and order values.

5.2.2 Deformability

It was previously established that the evolution of the form and order of the loops influences their internal properties, with deformability being a good

example. The deformability values for all clusters identified in all simulations were collected and scattered in Figure 5.7 to observe whether the same trends apply to clusters. Each gray spec represents a cluster observed in the previously presented triaxial tests. Furthermore, three curves were added; the blue curves are the fit of the minimal and maximal values per order, and the black curve represents the average value per order.

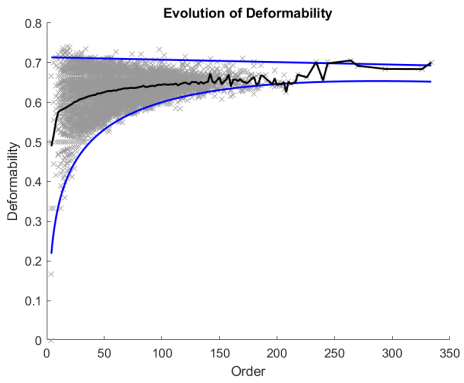

Figure 5.7: Deformability distribution in function of cluster order for the entirety of clusters identified throughout all simulations. Blue curves are the fit of the minimal or maximal values per order, while the black curve represents the average value per order.

It can be noted that the average deformability value increases with the order of the cluster, stabilizing for high orders. The average deformability value observed for the minimal cluster is approximately 0.49, indicating that most of these clusters are indeed deformable, in contrast to the non-deformable 2D counterpart. Hence, this confirms the increase in complexity of the minimal cluster with the change in dimension.

In addition, the blue curve in Figure 5.7 marking the upper boundary of the observed deformability values represents almost a straight line. This indicates that clusters may have a maximum deformability value of approximately 0.7. Thus, using the definition of deformability from Section 3.2.1, it could be inferred that a minimum of approximately 30% of closed edges are required to form a cluster.

The dispersion of values is much more prevalent for clusters of a smaller order. In fact, it can be shown that the minimal deformability value increases with the order, as an increasingly higher number of open edges is necessary to form the cluster. Thus, the deformability values of very high order clusters (i.e., order 200) are restricted by an increasingly smaller interval with the cluster growth.

In Figure 5.7, certain areas lack values for lower orders. Indeed each cluster has a fixed number of configurations of its open and closed edges, meaning that only certain specific deformability values can be attained for each order. For example, the minimal cluster of order 4 has six edges, and zero to four may be open. Thus it has only five possible values for deformability.

In addition, the number of possible cluster configurations increases with the order. For very high order clusters, this results in a large number of points bounded by a small interval between the minimal and maximal value related to each order.

Overall deformability indicates the interconnectivity between the grains of a cluster. Thus, on average, smaller clusters are better connected than larger ones, providing more stability for surrounding structures (as force chains).

Finally, the deformability of clusters may represent one aspect of the macroscopic behavior of the specimen. Small clusters (of lower deformability) are more prevalent in the early stages, resulting in a sturdier structure. However, as larger and more deformable clusters appear, the specimen becomes more deformable, thus losing strength.

5.2.3 Void ratio

To obtain the void ratio of a region, the void and solid volume must be identified. In the case of clusters, only one of these quantities is needed, as the total volume of each cell is known.

From the perspective of a cell, its solid volume is the enclosed volume of the four grains forming it. In other words, it is the intersection of four individual spheres and a tetrahedron. Thankfully, this problem has already been solved in the literature as an analytical equation [123].

Figure 5.8 illustrates the density distribution of the void ratio of clusters for test D100. The black line represents the mean value per order. The results of the remaining tests are presented in Appendix B.

The cluster density was estimated in relation to the maximum number of points of each order. First, the number of structures located inside rectangular regions spanning a 0.05 void ratio and a single order was calculated. Then, the values observed were divided by the maximum of each order. Consequently, red regions represent high-density regions and yellow represents low-density regions for the same order of clusters. An analysis based on colors cannot be made between clusters of different orders.

It can be seen that, in all stages of the D100 test, the average void ratio tends to increase with the cluster order, which is a logical result of the conclusion on the deformability property. This is further reinforced by the

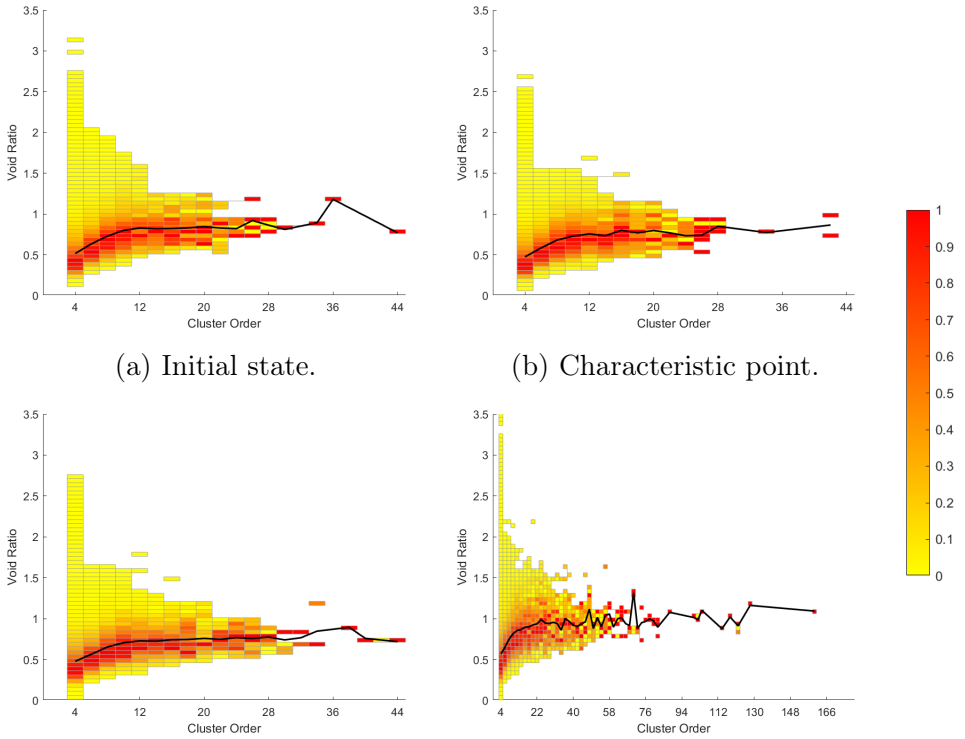

(a) Initial state. (b) Characteristic point.

(c) Peak stress. (d) Final state.

Figure 5.8: Void ratio density map in function of cluster order for test D100 at (a) initial state, (b) characteristic point, (c) peak stress, and (d) final state. Point density is calculated in relation to the rectangle containing the maximum number of points for each order. The black curve represents the mean value.

density map, where regions containing numerous clusters (red regions) are located around the black curve.

On the other hand, the maximal void ratio observed tends to decrease with the increase in order. Several smaller clusters present a very high void ratio (larger than 1.5), peaking at 3.5 for clusters of order 4. In addition, these anomalies become more apparent for large strains, as illustrated in Figure 5.8d.

These void ratio anomalies come from a pathological case where a cluster is formed from two unconnected strings of grains. This can be exemplified by the cluster previously illustrated in red in Figure 5.5, where this pathological case appeared inside a larger cluster. Consequently, the void space between both groups of grains can be several times larger than the solid volume of the cluster.

As large clusters are formed by several cells, the probability of a structure to be formed from two separate sets of grains decreases with the increase in order. This explains the decrease in the maximal void ratio with the increase in order.

Finally, it can be concluded that, on average, the void ratio increases with the order of the cluster. Larger clusters tend to be less interconnected and thus have void space between grains, resulting in a higher void ratio.

5.3 Statistics and categorization of clusters

5.3.1 Drained conditions

Categorization

It is known that the statistical distribution of loops varies during the loading path [80, 28, 122]. Thus, an analogous evolution was anticipated for their 3D counterpart. Generally, loops are categorized following their order into four groups: Loops 3, Loops 4, Loops 5, and Loops 6+. As briefly mentioned in Section 5.2.1 and illustrated in Figure 5.9, the maximal cluster order observed in drained conditions is approximately 350 for test D28. This value is much higher than what is known for loops, which have been shown to grow rarely beyond order 8, highlighting a clear difference between the range of orders for these two structures.

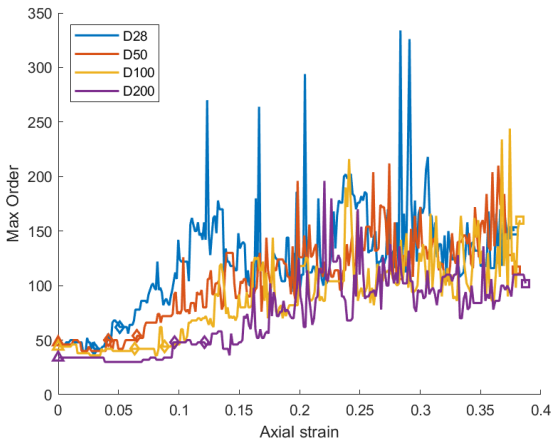

Figure 5.9: Evolution of the maximal cluster order for the drained triaxial tests with confining pressures between 28 kPa and 200 kPa.

Categories were created to better study cluster distributions in light of their behavior regarding being created or destroyed at a certain axial strain

value, as shown in Figure 5.10. The four defined categories can be summarized as follows:

- **Small - Order 4**. This category is by far the most abundant. They increase in number during the contraction phase, but when approaching the dilation regime, their number decreases until a constant value is reached at large strain values.

- **Submedium - Order 6**. In the early stages, these clusters evolve in an opposite way to small clusters, decreasing in number during the contraction phase and increasing during the dilation. However, near the deviatoric stress peak, their behavior changes, and their number decreases until a steady state is reached at large strain values.

- **Medium - Order 8 to 20**. Medium clusters evolve similarly to submedium ones until the peak deviatoric stress, from where a steady state is reached for large strains. In fact, the behavior of the medium category is the direct opposite of the small category.

- **Large - Order 22+**. These clusters are not present in representative numbers in the early phases, mostly appearing only after the characteristic point. This category contains all clusters of an order higher than the upper limit of the medium category. Once they appear, they only grow in number until an asymptotic value is reached for large vertical strains.

In the first-column images in Figure 5.10, it is challenging to observe the behavior of clusters beside the small category, as they represent most of these structures. The studied material being dense soil contributes to this effect. However, so does the narrow rectangular geometry of the specimen. It was observed that the majority of the cells located in the interface with the wall belong to the small category. Choosing a specimen shape with a higher volume-to-surface ratio would probably smoothen the cluster distribution.

Although the number of clusters and strain value of peaks differs between the three tests for each cluster category, the shape of the curves along the drained loading path is similar. In the early stages, the samples are in a contraction regime, which signifies a decrease in the total volume and, thus, a reduction in the specimen void ratio. Therefore, the soil particles are slowly being reorganized within the sample, destroying structures of high void ratio to form denser ones. In other words, as large category clusters are not yet present, medium and submedium clusters are broken down to create smaller ones.

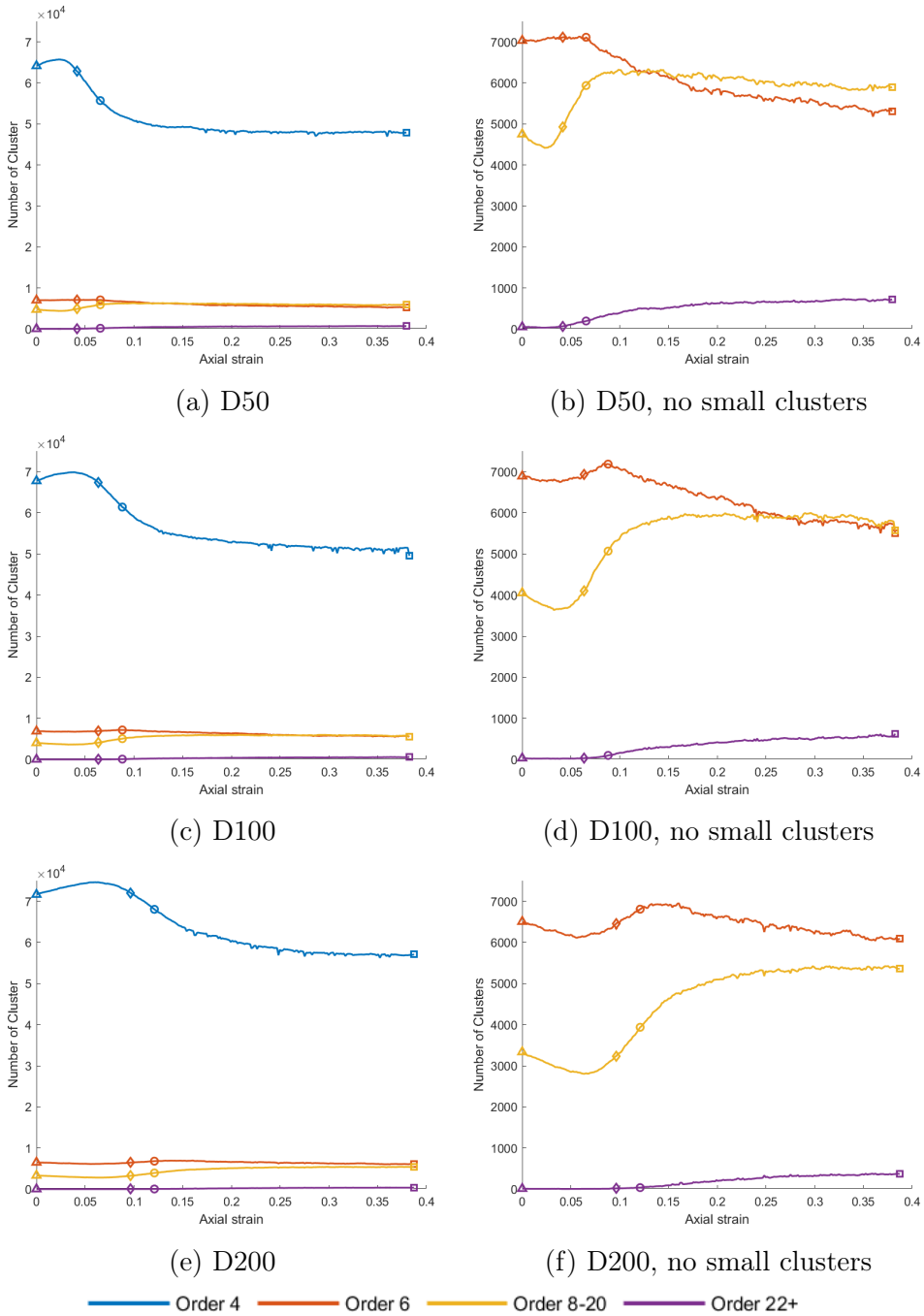

Figure 5.10: Evolution of the number of the clusters in each category in drained conditions. Figures (a), (c), and (e), illustrate the distribution of clusters for the tests D50, D100, and D200, respectively. Figures (b, (d), and (f) are a zoom-in of the former for higher cluster categories. The triangle marks the initial state, the square the final state, the diamond the characteristic point, and the circle the peak deviatoric stress.

Next, the number of clusters in the small category peaks, leading to the start of the cluster merging phase. Consequently, small clusters can be observed to decrease in number, while all other categories increase in number. In other words, denser structures merge to create clusters of increasingly higher void ratios. This phase is reflected macroscopically in the decrease of the volumetric strain rate, later ushering in the characteristic point and the macroscopic strain dilation.

Near the deviatoric stress peak (circle mark), medium and submedium categories diverge in behavior as the latter decreases in number. This results from a decrease in small clusters merging to create submedium clusters, while the latter are still being consumed to form increasingly larger clusters.

Not long after this, the number of small and medium clusters reaches an equilibrium, while clusters of submedium and large categories only stabilize in number for large strains. The balance between cluster categories indicates a plateau of the volumetric strain, characterizing the approach of the critical state.

An equivalent analysis can be made by evaluating the number of cells in each cluster category, as shown in the first column of Figure 5.11. As each cluster of submedium and large categories is composed of several cells, the impact of clusters of more significant categories becomes more visible, especially at higher axial strains, where the number of large clusters may have seemed underwhelming in the previous analysis method.

In addition, the cell evaluation makes it possible to approximate the volume distribution per cluster category, as seen from a direct comparison with the evolution of total volume per cluster category, illustrated in the second column of Figure 5.11.

It can be noted that more than half of the volume of the specimen is occupied by small clusters at any point of the loading path. Furthermore, the initial and final cell ratio values of each category depend on the confining stress applied during the isotropic compression phase. The lower the pressure applied, the more prevalent the clusters of larger order.

Going forward, the number of cells will be favored for cluster analysis as it gives a better representation of cluster distribution than the number of clusters.

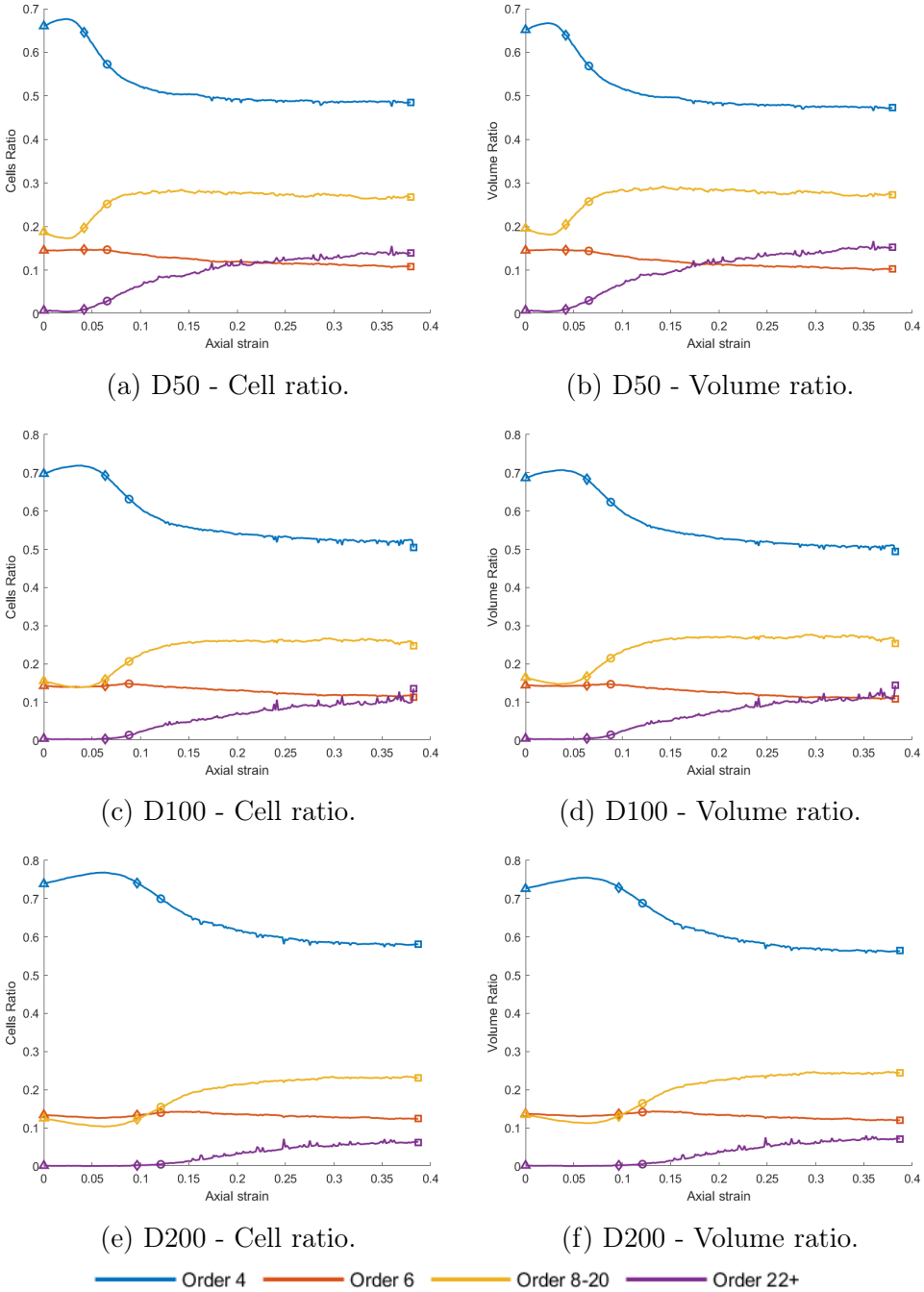

(a) D50 - Cell ratio.

(b) D50 - Volume ratio.

(c) D100 - Cell ratio.

(d) D100 - Volume ratio.

(e) D200 - Cell ratio.

(f) D200 - Volume ratio.

Figure 5.11: Evolution of the volume and ratio of cells in each cluster category in drained conditions. Figures (a), (c), and (e), illustrate the distribution of the ratio of cells for the tests D50, D100, and D200, respectively. Figures (f), (f), and (f) illustrate the distribution of the volume for the tests D50, D100, and D200, respectively. The triangle marks the initial state, the square the final state, and the diamond the peak relative strength.

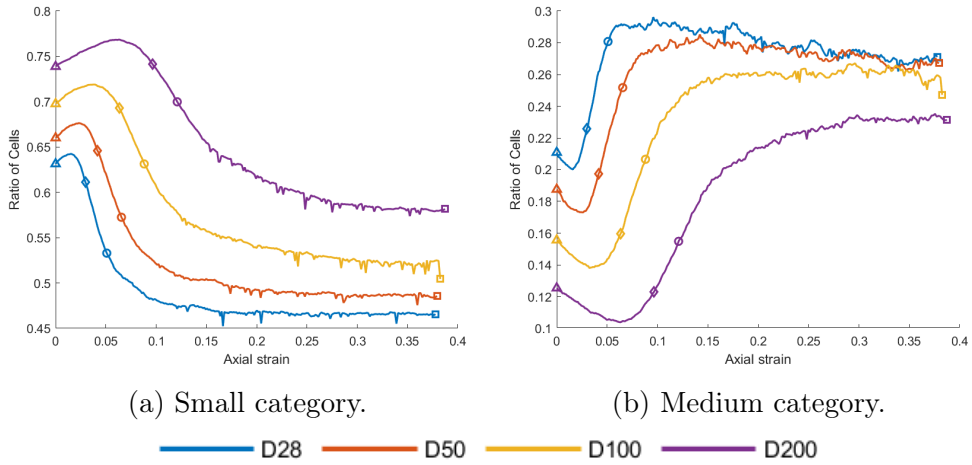

(a) Small category. (b) Medium category.

Figure 5.12: Evolution of the small (a) and medium (b) cluster category for the drained triaxial tests. The triangle marks the initial state, the square the final state, and the diamond the peak relative strength.

The change in the isotropic pressure applied during the drained triaxial test makes the turning point of the behavior of each cluster categories occur for larger axial strains. This effect can be observed in Figure 5.12, which compares the evolution of small and medium clusters between the three different consolidation stresses. A similar effect is observed in Figure 4.3 depicting the macroscopic results for the drained tests. An increase in the consolidation pressure leads to a delay in the stress peak and the critical state regime. It can be concluded that both effects are intertwined, and a change in the macroscopic level directly affects the mesoscopic scale.

Void ratio

For each test, the average void ratio of each cluster category was calculated, illustrating the impact of the macroscopic state of the specimen on the cluster void ratio. Figure 5.13 illustrates the results related to the drained triaxial tests.

Figure 5.13d shows substantial noise. This is due to the low number of large clusters identified compared to the other categories. This is further confirmed by the late behavior of specimens D28 and D50, where the number of large clusters sharply increases and the void ratio curve becomes more stable.

It can be noted in Figure 5.13 that, for any test and at any mean pressure, the mean void ratio observed increases with the clusters category. This confirms the increase in void ratio with order observed in Section 5.2.3.

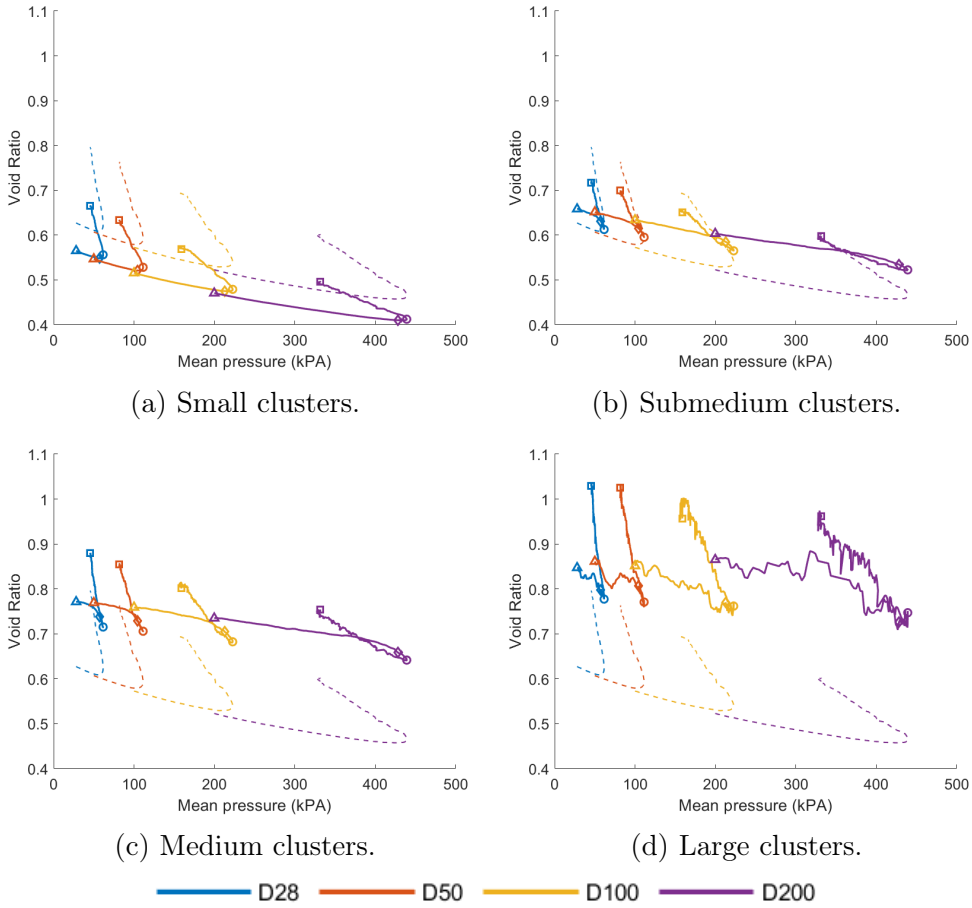

(a) Small clusters.

(b) Submedium clusters.

(c) Medium clusters.

(d) Large clusters.

Figure 5.13: Evolution of the average void ratio of each cluster category for all drained triaxial tests performed. Figures (a), (b), (c), and (d) illustrate small clusters, submedium clusters, medium clusters, and large clusters, respectively. The dashed lines represented the average void ratio of each specimen. The triangle marks the initial state, the square the final state, the diamond characteristic state, and the circle the peak deviatoric stress.

From the early phases until the characteristic point (diamond mark), the average void ratio of each cluster category decreases. This is an expected behavior as the specimen goes through a macroscopic compression phase, thus favoring the decrease in the void ratio of internal structures. Furthermore, during this phase, the average void ratio of all categories decreases almost linearly with the increase in mean pressure, implying a relationship between these two quantities for this early phase.

Just after the characteristic point, a slow macroscopic void ratio dila-

tion phase starts, as shown in Figure 4.3d. The average void ratio of small clusters, illustrated in Figure 5.20a, is seen to increase slowly, following the macroscopic trend. At the same time the average void ratio of all other categories sharply decreases, which is counter-intuitive. However, it can be shown to be a product of the transition between cluster categories.

The void ratio of the specimen can be estimated from the average void ratio of each cluster category as follows:

$$e = \frac{1}{N} \sum_{c=1}^{4} N_c e_c \tag{5.2}$$

where e is the macroscopic void ratio, N is the number of clusters, N_c is the number of clusters of the category c, and e_c is the average void ratio of the category c.

Equation 5.2 shows that two mechanisms govern the evolution of the macroscopic void ratio: the average void ratio and the number of clusters of each category. Consequently, increasing the macroscopic void ratio is possible even if the average void ratio of all categories decreases.

As seen in Figure 5.10, during this phase, clusters of large, submedium, and medium categories are being created in distinction to small clusters. It can be assumed that the newly formed structures have a lower void ratio than the previous average of the respective category, resulting in the observed decrease in value. However, as the number of clusters of the larger categories increases, the macroscopic dilatative trend is respected.

Finally, the specimen ruptures, leading to a highly dilatative phase until the critical state is reached. The average void ratio of all cluster categories behaves similarly, as illustrated in Figure 5.14.

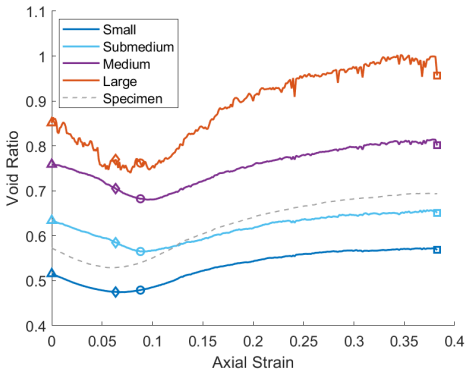

Figure 5.14: Void ratio evolution of cluster categories for test D100.

5.3.2 Undrained conditions

Categorization

The cluster categories previously defined are maintained and applied for the analysis of the simulations in undrained conditions. Figure 5.15 illustrates the evolution of the number of cells in each cluster category as a function of axial strain.

At the starting point, clusters of the small category are predominant, while the fraction of higher categories is minimal. This early configuration

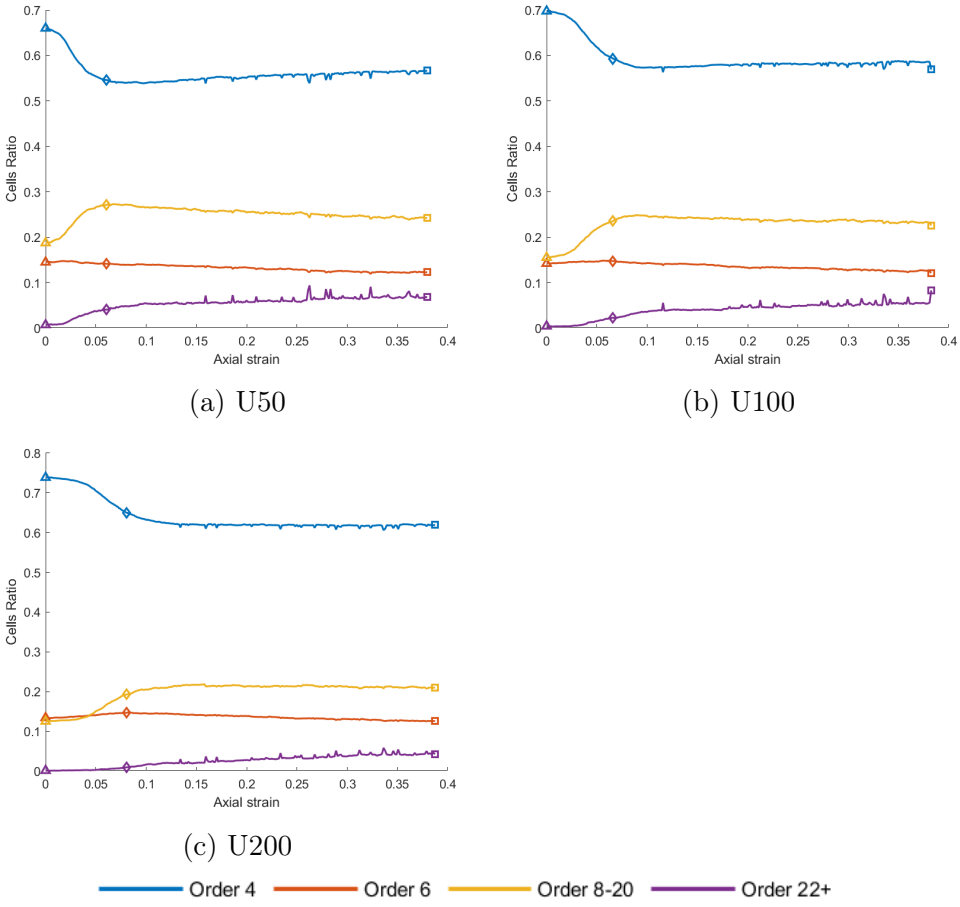

(a) U50

(b) U100

(c) U200

Figure 5.15: Evolution of the ratio of cells in each cluster category for all undrained triaxial tests performed. Figures (a), (b), and c), illustrate the distribution of cells in each category for the tests U50, U100, and U200, respectively. The triangle marks the initial state, the square the final state, and the diamond the peak relative strength.

remains constant for small deformations, as grain reorganization has not yet started.

After the early stages, a phase of rapid transition between categories is established, with a decrease in the number of small categories in favor of an increase in larger ones. This phase coincides with the force chain reorganization observed in Section 4.4, starting at increasingly large strains for higher initial confining stresses. Clusters and force chains are being reorganized to support increasingly higher external loads being applied.

Around the diamond mark of each undrained test, a phase of slow transitions appears. Clusters of submedium and medium categories merge to form increasingly larger clusters.

Throughout the loading path, less dense clusters are formed. This result should not be possible since, under undrained conditions, the total volume (and consequently void ratio) of the specimen is supposed to remain constant. However, two volumes must be considered: the volume enclosed by the specimen piston walls and the volume delimited by clusters. The former comprises the center of all particles. Consequently, the region between the walls and the center of the outermost grains is not part of the cluster volumes. Figure 5.16 illustrates the void ratio evolution of both volume calculations in undrained conditions.

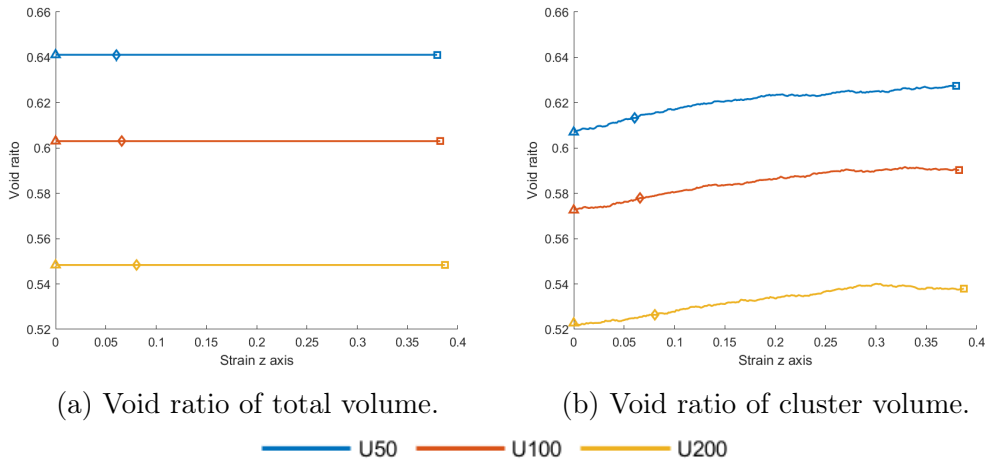

(a) Void ratio of total volume. (b) Void ratio of cluster volume.

Figure 5.16: Comparison between the void ratio evolution of two different volume envelopes. In Figure (a), the volume is delimited by the triaxial test walls, while in Figure (b) the volume is delimited by the center of the outermost grains. The triangle marks the initial state, the square the final state, and the diamond the peak relative strength.

In drained and q-constant conditions, both calculations showed an equiv-

alent trend. However, this is no longer true in the undrained case. As pistons control the loading conditions, the constant volume is valid for the entirety of the specimen. Consequently, the void ratio illustrated in Figure 5.16a remains constant. However, Figure 5.16b shows that the void ratio of the region delimited by the clusters constantly increases. Consequently, the dilation observed through the analysis of the cluster void ratio is confirmed.

It can be noted that all categories still follow the general premise of the properties defined in the drained case: Small and medium clusters present a mirrored behavior, large clusters are not present in the initial phase of the tests and only increase in number from their appearance; the behavior of submedium clusters differs from all the others. At first glance, submedium and medium categories appear to behave similarly. However, the peak of submedium clusters is reached before that of the medium categories, thus justifying the separation.

However, cluster categories in drained conditions go through an early peak or valley that is not observed in the undrained case. This can be referred to as the variation in the volumetric strain behavior (compressive then dilatative) of the former that is not present in the undrained case.

Void ratio

The results of the mean void ratio evolution for each cluster category from the undrained triaxial tests are illustrated in Figure 5.17.

From the beginning of the test until peak relative strength (diamond mark), all categories show a decrease in average void ratio even though the macroscopic behavior is dilatative. During this phase, clusters are rapidly merging, creating larger structures. Thus, the transitions between cluster categories govern the macroscopic void ratio.

After the peak relative strength, the rate of transitions between cluster categories decreases. Consequently, an increase in the average void ratio for medium and large categories can be observed following the macroscopic trend.

At this point, an interesting discrepancy can be observed in the behavior of small clusters between the different triaxial conditions. For the drained cases, the behavior of the void ratio of small clusters seemed to follow the volumetric trends of the specimen. However, small clusters behave oppositely to the macroscopic volume trend under undrained conditions. In reality, another macroscopic quantity is at play: the mean pressure. In both triaxial conditions, an increase in mean pressure leads to a decrease in the void ratio of small clusters , with the opposite also being true.

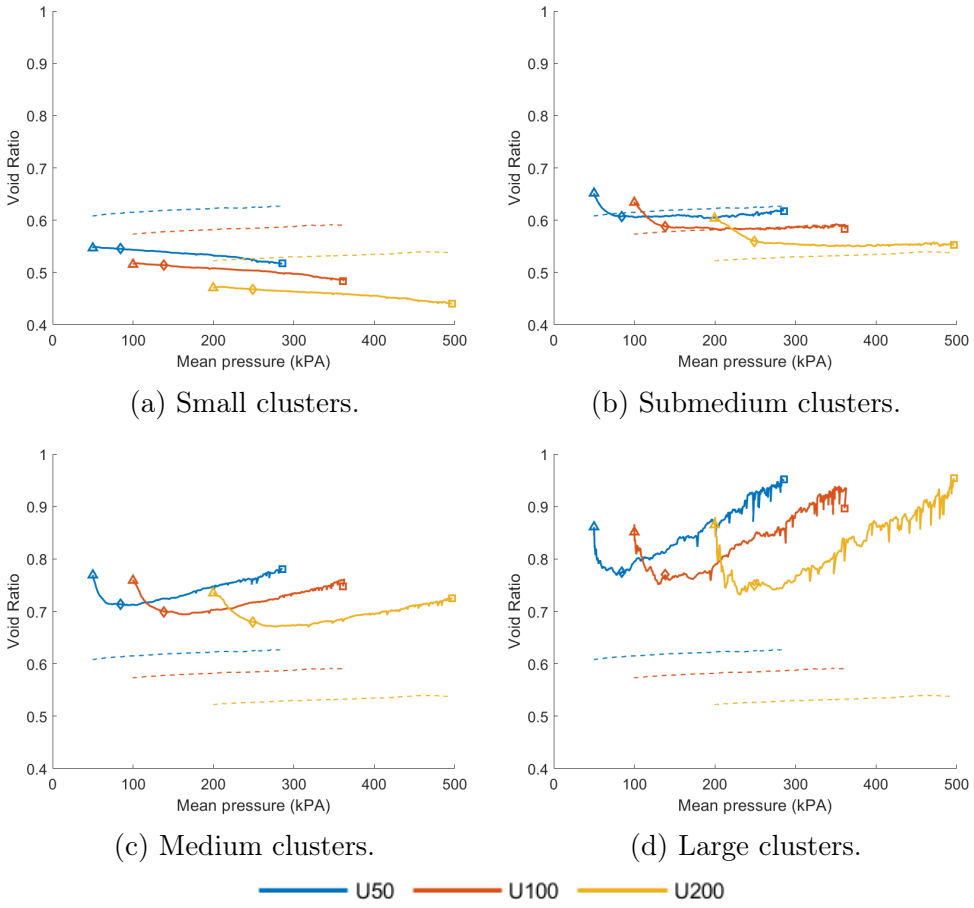

(a) Small clusters.

(b) Submedium clusters.

(c) Medium clusters.

(d) Large clusters.

Figure 5.17: Evolution of the average void ratio of each cluster category for undrained triaxial tests performed. Figures (a), (b), (c), and (d) illustrate small clusters, submedium clusters, medium clusters, and large clusters, respectively. The dashed lines represented the average void ratio of each specimen. The triangle marks the initial state, the square the final state, and the diamond the peak relative strength.

5.3.3 Q-constant conditions

Categorization

Differently from the previous cases, the constant deviatoric stress test results will be presented in two phases. First, the values of the Q50-100 and Q200-100 tests will be discussed to exemplify the relations between each cluster category. Later the five different q-constant tests will be compared, showing the influence of the initial confining pressure and target deviatoric stress on

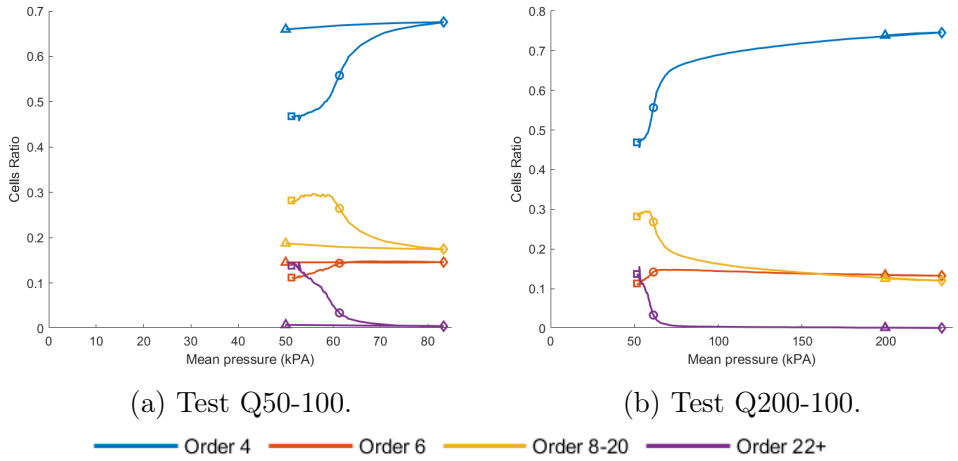

(a) Test Q50-100. (b) Test Q200-100.

Figure 5.18: Evolution of the ratio of cells in each cluster category for the constant deviatoric stress triaxial tests Q50-100 and Q200-100, illustrated in Figure (a) and (b), respectively. The triangle marks the initial state, the square the final state, the diamond the end of the drained phase, and the circle the failure point.

the cell ratio of each cluster category.

Figure 5.18 illustrates the evolution of each cluster category of the Q50-100 and Q200-100 tests following the constant deviatoric stress loading path.

First, the specimen is subjected to a drained triaxial phase until the targeted deviatoric stress is reached. It can be observed that clusters of small categories are being created, while larger ones are being destroyed. Thus resulting in the macroscopic compression observed in Section 4.12.

Next, the specimen is discharged. Clusters of small order are slowly merging to create clusters of medium and submedium order. This phase is better illustrated for specimen Q200-100 in Figure 5.18b, where an almost linear transition can be identified, starting from the diamond mark until a mean pressure of approximately 95 kPa is reached. The end of this phase can be related to the region around where the stress state of the specimen crosses the critical state line (CSL) represented in 4.12b. Thus, as the drained phase of test Q50-100 ends after the CSL, this linear phase cannot be identified.

Next, the rate of transitions between cluster categories rapidly increases, leading to the rupture of the specimen. Clusters of increasingly higher order are appearing at a fast pace, thus justifying the observed rapid dilatative macroscopic response previously observed.

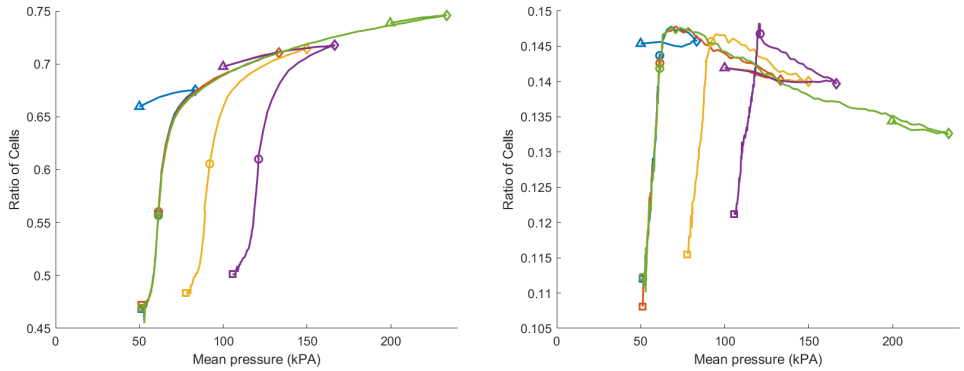

(a) Small clusters.

(b) Submedium clusters.

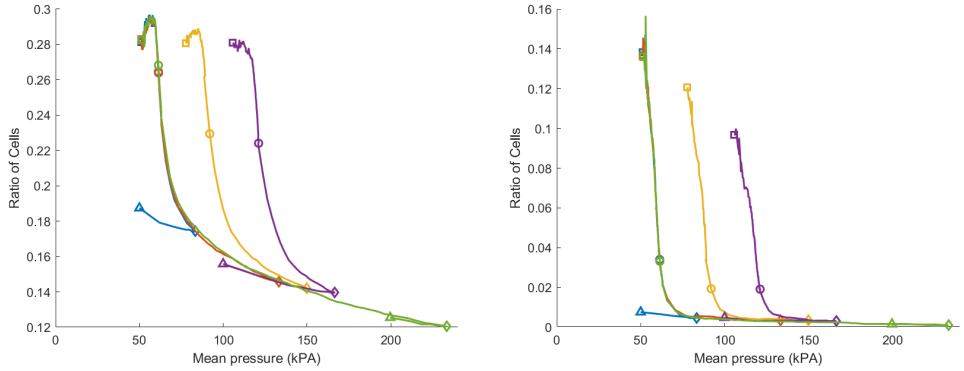

(c) Medium clusters.

(d) Large clusters.

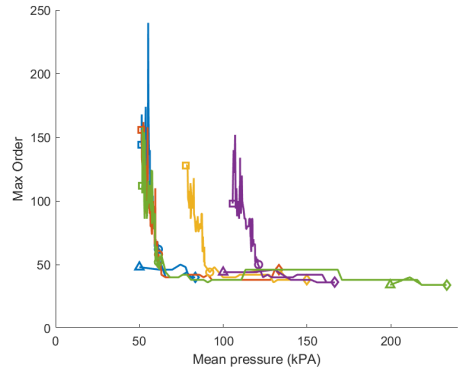

(e) Maximal cluster order.

Figure 5.19: Evolution of the ratio of cells in each cluster category for all constant deviatoric stress (q-constant) triaxial tests performed. Figures (a), (b), (c), and (d) illustrate the distribution of cells in each category, while Figure (e) shows the evolution of maximal order observed. The triangle marks the initial state, the square the final state, the diamond the end of the drained phase, and the circle the failure point.

The described behavior is observed for all constant deviatoric stress tests, as illustrated in Figure 5.19, which compares the results between tests for each cluster category.

The value of the initial phase of confining pressure applied has little to no impact on the final ratio of clusters in each category. In fact, all three tests with the target deviatoric stress of 100 kPa (Q50-100, Q100-100, and Q200-100) follow a very similar path after the drained compression phase, with test Q100-100 (represented in red) being barely visible.

However, the impact of the targeted deviatoric stress appears more important, as an increase in value results in a decrease in the ratio of clusters of larger order in favor of smaller ones. In addition, this quantity also impacts the maximal order of clusters, which is seen to decrease in Figure 5.19e.

Void ratio

The results of the mean void ratio evolution for each cluster category related to the q-constant triaxial tests are illustrated in Figure 5.20.

As found for the previous loading conditions, for any test from Figure 5.20 and at any mean pressure, the mean void ratio observed increases with the cluster category.

Furthermore, the results illustrated in Figure 5.20a confirm the relation between mean pressure and the average void ratio of small clusters, as proposed in Section 5.3.2.

During the drained phase of the test, the average void ratio of each cluster category decreases until the targeted deviatoric stress is reached, which is expected from a volumetric compression phase.

Next, the mean pressure of the specimen gradually decreases, causing macroscopic dilation. This is reflected locally by an increase in the average void ratio of all cluster categories.

When approaching the rupture point, two groups of behavior appear. Small clusters see an increase in void ratio following the macroscopic trend. At the same time, all other categories observe a rapid decrease in the void ratio. As seen for the previous loading conditions, this is attributed to a phase of relatively slow evolution of the macroscopic void ratio and the rapid merger of clusters. Thus, the transitions between cluster categories govern the macroscopic void ratio.

Finally, a phase of rapid dilation is reached after the specimen rupture, resulting in an increase in the mean void ratios of all categories.

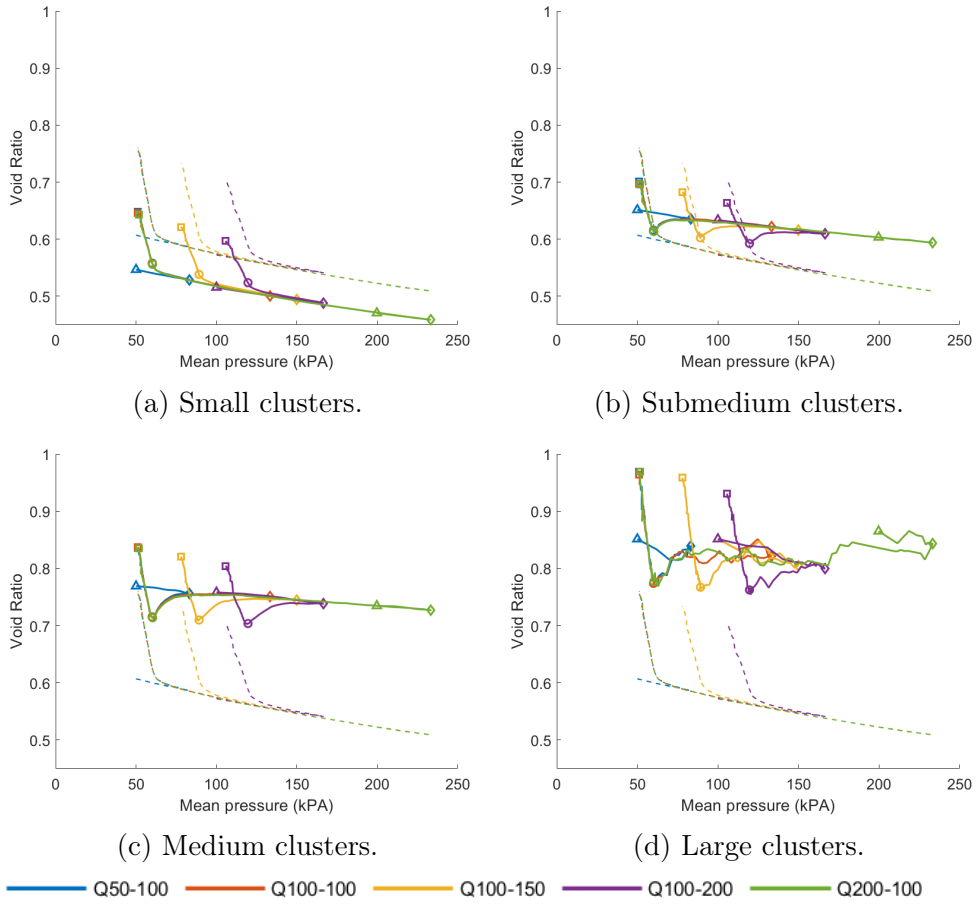

(a) Small clusters.

(b) Submedium clusters.

(c) Medium clusters.

(d) Large clusters.

Figure 5.20: Evolution of the average void ratio of each cluster category for all constant deviatoric stress (q-constant) triaxial tests performed. Figures (a), (b), (c), and (d) illustrate small clusters, submedium clusters, medium clusters, and large clusters, respectively. The dashed lines represented the average void ratio of each specimen. The triangle marks the initial state, the square the final state, the diamond the end of the drained phase, and the circle the failure point.

5.3.4 Comparison between drained and q-constant conditions

Categorization

It was shown in Section 4.6 that tests D28 and Q100-100 have an equivalent failure point in relation to several macroscopic and force chain characteristics. Figure 5.21 compares cluster categories between these two tests to identify

whether the same tendency is observed for clusters.

A clear convergence of the cell ratio of each cluster category around the failure point (circle mark) can be observed, thus confirming the equivalence of both mesoscopic states. The post-rupture behavior of both specimens appears to be similar. However, test Q100-100 was stopped at 20% axial strain, thus rendering impossible the comparison at very large strains.

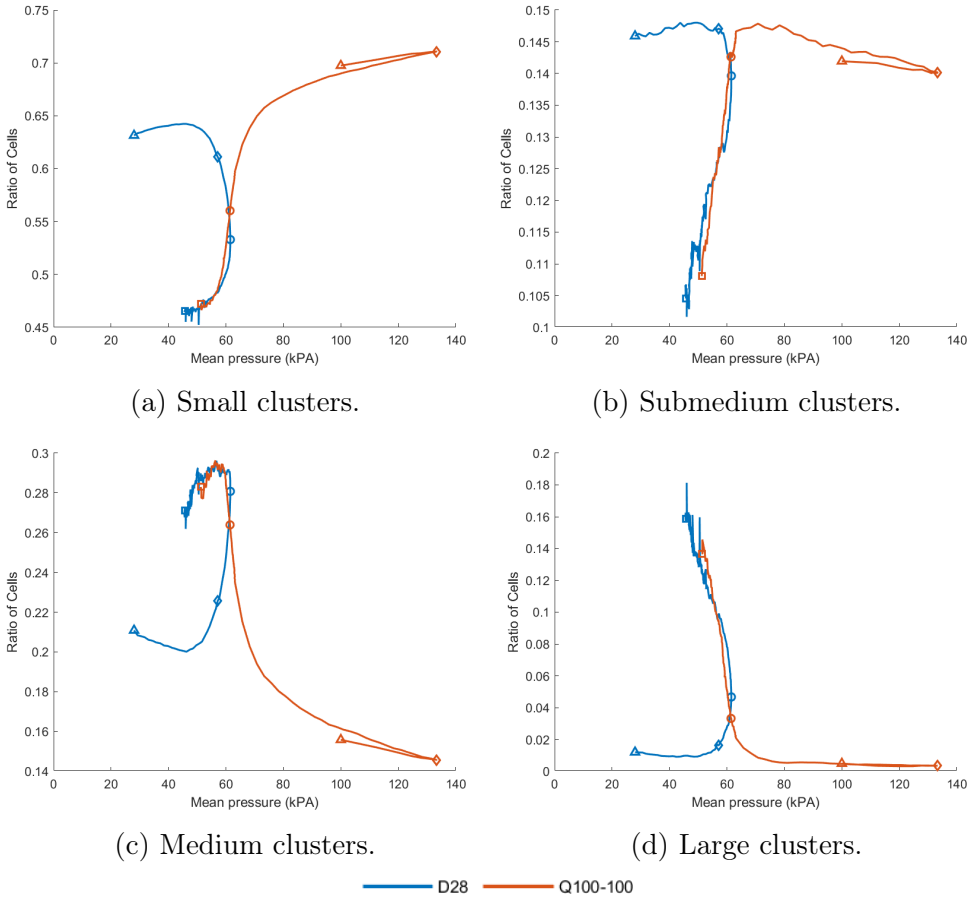

(a) Small clusters.

(b) Submedium clusters.

(c) Medium clusters.

(d) Large clusters.

Figure 5.21: Evolution of the ratio of cells in each cluster category for tests D28 and Q100-100. Figures (a), (b), (c), and (d) illustrate the distribution of cells in small, submedium, medium, and large categories, respectively. The triangle marks the initial state, the square the final state, the diamond the end of the drained phase, and the circle the failure point.

Void ratio

It was shown in Section 5.3.4 that the cluster distribution of tests D28 and Q100-100 was similar around an equivalent rupture point. To further verify the equivalence of the mesostructures, the cluster void ratio results related to tests D28 and Q100-100 are illustrated in Figure 5.20.

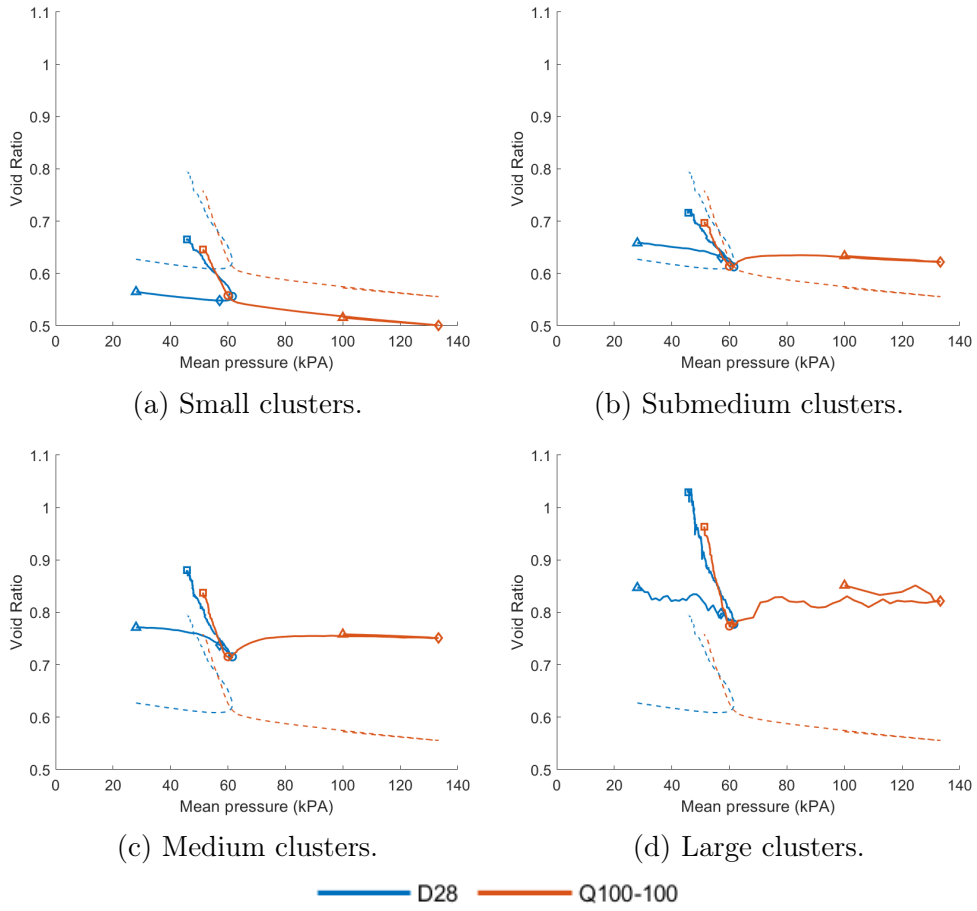

(a) Small clusters.

(b) Submedium clusters.

(c) Medium clusters.

(d) Large clusters.

Figure 5.22: Evolution of the average void ratio of clusters in each cluster category for tests D28 and Q100-100. Figures (a), (b), (c), and (d) illustrate the distribution of cells in small, submedium, medium, and large categories, respectively. The dashed lines represented the average void ratio of each specimen. The triangle marks the initial state, the square the final state, and the circle the failure point.

The initial average void ratio of all cluster categories of test D28 is higher than that of test Q100-100, as the former was subjected to lower mean pressure. However, as the tests advance, the average void ratios of each cluster

category converge around the rupture point.

Together with Section 4.6, this result illustrates how a specimen subjected to different loading paths reaches the failure point at an equivalent macroscopic and mesoscopic state (cluster and force chain).

In the literature, the unicity of the mesoscopic distribution at the critical state has already been proven using loops (2D conditions) [124, 122]. Departing from different initial void ratios, specimens were subjected to the same loading path. The distribution of loops observed in the critical state inside the failure area of all specimens was identical.

It can be concluded that the microscopic structure of a given specimen is independent of the loading path.

5.4 Interaction between coexisting internal granular structures

5.4.1 Clusters and force chains

Statistics of the interaction

A concrete relationship between loops and force chains in 2D conditions has already been established by several authors [75, 20, 30], as mentioned in Section 2.4.2. Consequently, an equivalent behavior should be identified between clusters and force chains based on the premise of clusters being the 3D version of loops to be validated.

To do so, the cluster distribution presented in Section 5.3 will be subdivided into two groups: force chain cluster (FCC) and non-force chain cluster (NFCC). An FCC is a cluster that actively participates in force transmission. As force chains are defined by the contact between grains, a cluster will be considered as an FCC if at least one of the closed edges forming it is part of a force chain. By contrast, an NFCC is a cluster that does not have a common edge with force chains and thus does not participate actively in force transmission.

As shown in Section 4.2 the number of force chains evolves during the loading path. Thus, to remove the influence of force chain numbers over the distribution of FCC and NFCC clusters, the ratio of cells belonging to each cluster category (small, submedium, medium, large) will be calculated for both FCC and NFCC separately. Figure 5.23 illustrates the cluster distribution for the drained case. The results for the remaining triaxial conditions can be found in Appendix D.

A clear disparity between FCC and NFCC can be observed during the

drained loading path. NFCC behaves similarly to what was observed for the whole specimen, illustrated in Figure 5.11. Alternatively, FCC shows a unique behavior. The distribution of submedium, medium, and large clusters is more prevalent for FCC, representing more than half of the cells around the end of the test. In fact, most - if not all - clusters of the large category are FCC, showing a direct link between the more voluminous clusters and force chains. However, the number of small FCCs is not negligible, principally in the early phases of the test.

At very early stages, there is a small variation in FCC distributions, which is not noticeable in NFCC. This is due to the restructuring of force chains that were not aligned with the charging direction created during the isotropic compression phase. As the number of current force chains is small, this restructuring is relevant for the FCC but not for the rest of the specimen (NFCC).

Later, the number of force chains increases rapidly, as illustrated in Figure 4.4. It can be concluded that force chains are being created uniformly, with no noticeable variations in FCC categories observed.

When approaching the characteristic point, bending events start to occur, as seen in Figure 4.4c. Force chain bending is known to increase the local void ratio around the bent structures [112, 71], resulting in the merger of surrounding clusters to form increasingly larger structures.

As the deformability of the cluster increases with the order, an FCC of higher orders leads to a decrease in the stability of force chains. Consequently, an increasing number of bending events start to occur. A feedback loop is formed between bending events promoting the merger of clusters and larger clusters, decreasing force chain stability until an equilibrium is reached at large strains.

A similar conclusion between the behavior of loops and force chains in 2D conditions has already been established for biaxial quasi-static conditions. Force chain loops (FCL) of order 3 have been shown to decrease rapidly before leveling off around the critical state [75, 80], illustrating the loss of stability that leads to force chain bending events. At the same time, FCL of orders larger than 6 show a mirrored behavior, increasing in number due to the increase in the void ratio around force chains [80].

It can be concluded that the interaction between force chains and loop-like structures is equivalent in 2D and 3D conditions, with small clusters behaving analogously to Loops 3 while clusters of medium and large categories behave as Loops 6+.

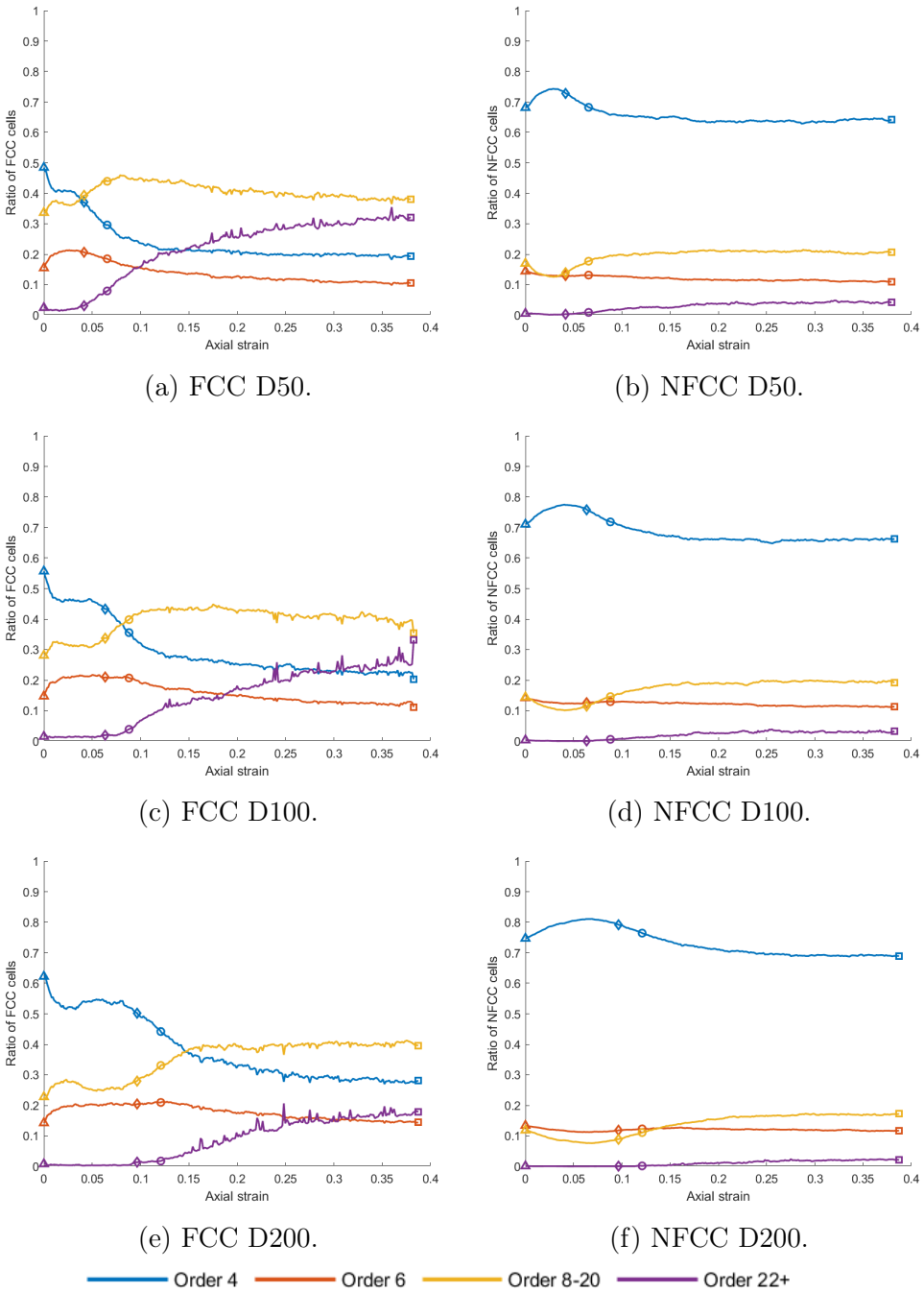

(a) FCC D50. (b) NFCC D50.

(c) FCC D100. (d) NFCC D100.

(e) FCC D200. (f) NFCC D200.

Figure 5.23: Distribution of the ratio of cells of force chain clusters (FCC) and non-force chain clusters (NFCC) in drained conditions. Figures (a), (c), and (e) illustrate FCC for triaxial tests D50, D100, and D200, respectively. Figures (b), (d), and (f) illustrate NFCC for triaxial tests D50, D100, and D200, respectively.

Morphology of the interaction

The presence of a force chain requires physical contact between two particles for the transmission of force to occur. Thus, in a cluster, it translates as the existence of a closed surface, following the definitions from Section 3.2.1. Figure 5.24 exemplifies the distribution of force chains around a large cluster of order 326 observed in test D28.

It can be seen in Figures 5.24b, 5.24c, and 5.24d that force chains are mostly situated around the exterior surface of clusters, where closed surfaces are expected. However, Figures 5.24e and 5.24f show that force chains may traverse the cluster structures, thus indicating the presence of closed surfaces inside a cluster.

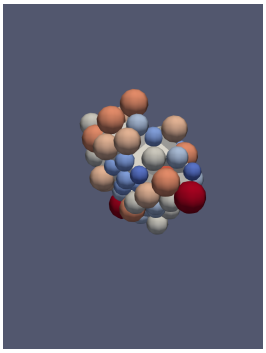

(a) Cluster cells and grains.

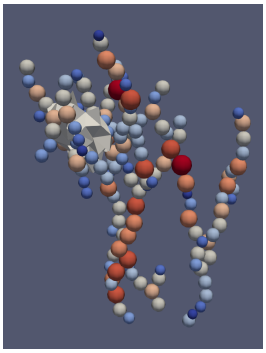

(b) Cluster cells and force chain grains.

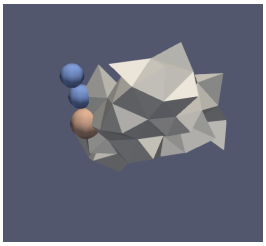

(c) Small force chain on cluster surface.

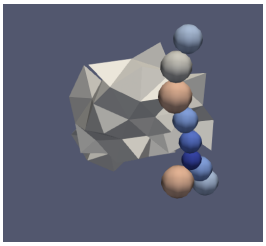

(d) Large force chain on cluster surface.

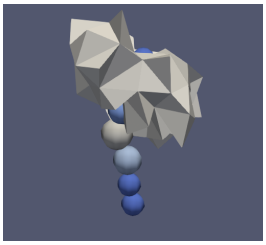

(e) Force chain traversing cluster.

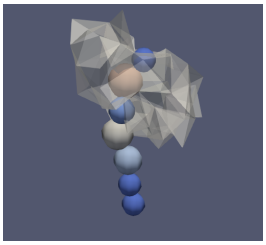

(f) Force chain traversing cluster.

Figure 5.24: Example of force chain positioning around a cluster of order 326, observed in test D28 at 0.2911 axial strain.

Indeed, closed surfaces can be present inside clusters as exemplified in Figure 5.25. The highlighted internal surface is closed, as it is composed of a closed edge. However, the separated cells are joined in a cluster through their connection to neighboring cells. In addition, as this closed surface does not form part of the boundary of the cluster, it is considered a "pseudo-open surface" and removed from the order calculation of equation 3.4.

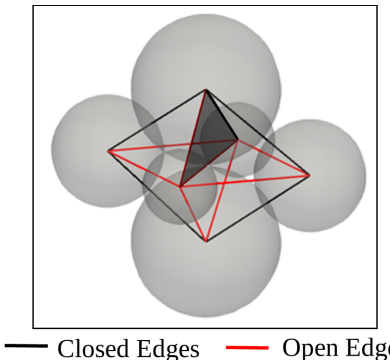

Figure 5.25: Example of a cluster (Order 8) containing a "pseudo-open surface" surface inside its domain. The black surface is closed. However, it is located inside a cluster after several connections through other cell surfaces.

The phenomena of force chain traversing clusters are more prevalent for larger and more voluminous clusters. However, even for these cases, they are rare compared to the normal occurrence (force chain running through cluster exterior surface).

Finally, force chains can only transverse loop-like structures in 3D conditions, as no equivalent of "pseudo-open surfaces" can be manifested in 2D conditions.

Direction of elongation

When particles of a granular system are mobilized by a shearing load, their contact network is rearranged. Generally, contacts in the major principal stress direction become more prevalent, generating an anisotropic state. This state is reflected in the internal structures of the specimen through the direction of force chains, pore spaces, and loops [91, 84, 125].

Through the procedures detailed in Section 3.2.1, the direction of elongation of clusters can be studied. However, only the orientation of structures composed of multiple cells was analyzed (no small clusters). In addition, as the conclusions are similar for all tests, only the results related to specimen D100 will be shown, while the results of the remaining tests can be found in Appendix C.

The azimuth and elevation angles will be categorized into portions of 15°. As the former represents the rotation in the x–y plane in relation to the y-positive direction, 12 categories are presented. However, only six were used for the elevation since positive and negative angles are considered equivalent. The results of test D100 for the cluster categories submedium, medium, and large are presented in Figures 5.26 and 5.27.

From Figure 5.26 it can be established that there are no preferred cluster orientations in the x–y plane during the loading path. All 12 curves fluctuate around a value of 0.085. The early variations in Figure 5.26c arise from the low number of large clusters in the early stages of the test. Representative numbers are only reached after the deviatoric stress (second dashed line), where the previous affirmation is validated.

The elevation angle of submedium and medium clusters is shown to be deeply influenced by the loading path, as illustrated in Figure 5.27. It should be noted that any evolution observed is essentially from the creation and destruction of clusters in each class instead of a change in direction of existing clusters. This is directly linked to force chain behavior.

In the early stages, a steady phase is presented without much change between the angle classes. In fact, grain reorganization is at its lowest, and force chains are distributed around the already-established contact networks. Thus, the elevation angle is representative of the inherent anisotropy of the specimen, generated mostly through the deposition under gravity.

Next, an increase in the number of clusters of submedium and medium categories located around force chains (FCC) was observed, as shown in Section 5.4.1. As the main stress direction is vertical, a decrease in low elevated clusters (0° to 45°) and increases in highly elevated ones (45° to 90°) are observed.

Finally, after the peak deviatoric stress (second dashed vertical line), force chain bending events start to rapidly increase in number, decreasing the verticality of these structures. Consequently, the trend between low-elevated clusters and highly elevated ones reverses, with a slow evolution taking place until a steady state is reached at the end of the test.

Furthermore, the fluctuations in elevation angle are more prevalent for medium clusters (Figure 5.27b) than for submedium ones (Figure 5.27a). This is due to the fact that the number of medium clusters created during this phase is far superior to the submedium ones, as previously illustrated in Figure 5.10.

The presented results confirm the impact of the loading conditions on the orientation of newly created clusters. The vertical compression suffered by the D100 specimen results in an increase of mesostructures with a higher elevation angle. In addition, as both horizontal directions have the same

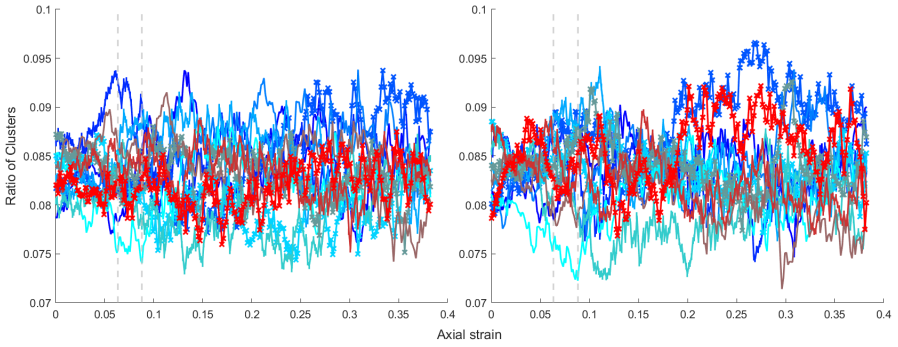

(a) Azimuth angle distribution for submedium clusters.

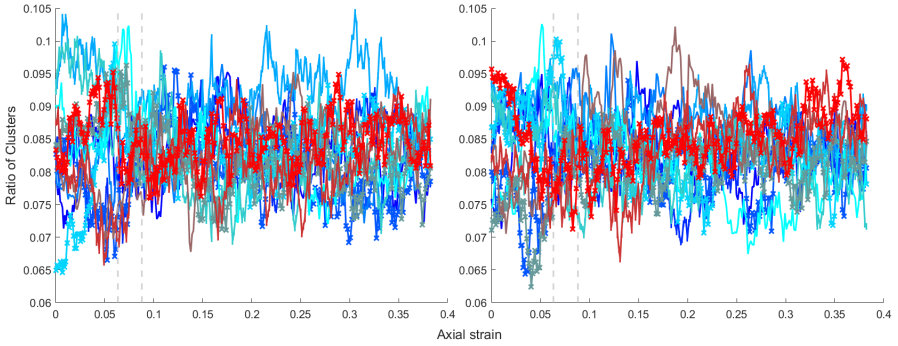

(b) Azimuth angle distribution for medium clusters.

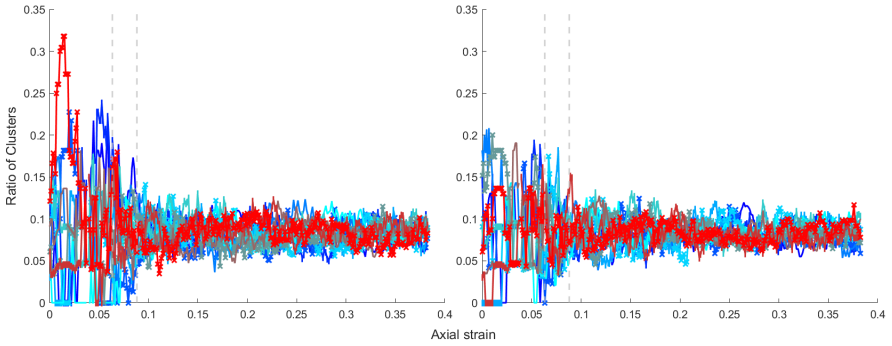

(c) Azimuth angle distribution for large clusters.

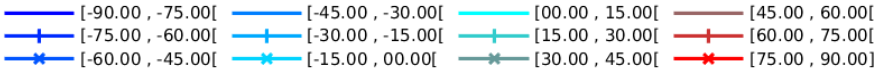

Figure 5.26: Evolution of the azimuth angle distribution of a cluster during the loading path for test D100. Surface tensor results are illustrated on the left and gravity on the right. Figures (a), (b), and (c) represent medium, submedium, and large categories, respectively. Azimuth is the rotation in the x–y plane in relation to the y-positive direction. Two dashed vertical lines were created to represent the characteristic point and the peak deviatoric stress, respectively.

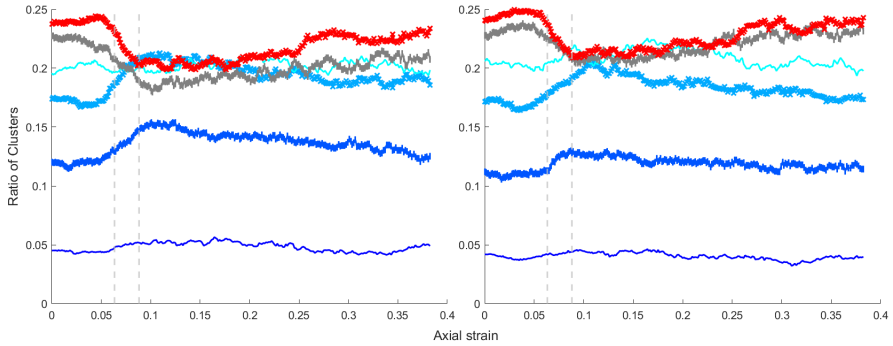

(a) Elevation angle distribution for submedium clusters.

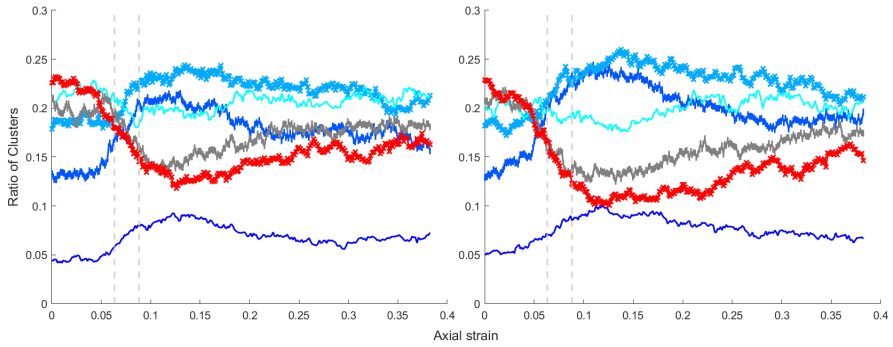

(b) Elevation angle distribution for medium clusters.

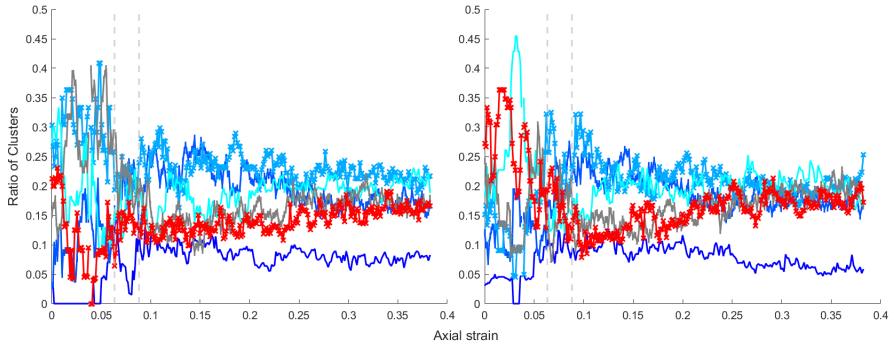

(c) Elevation angle distribution for large clusters.

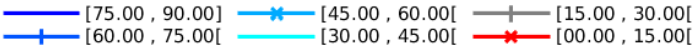

Figure 5.27: Evolution of the elevation angle distribution of a cluster during the loading path for test D100. Surface tensor results are illustrated on the left and gravity on the right. Figures (a), (b), and (c) represent medium, submedium, and large categories, respectively. Elevation is the rotation in relation to the x–y plane. The two dashed vertical lines represent the characteristic point and the peak deviatoric stress, respectively.

impact (equal stress applied) it is logical that the azimuth angle does not present any particular preferred direction.

5.4.2 Clusters and shear band

As for the previous section, a relationship between loops and shear bands has already been established in 2D conditions. It was shown that loops of larger orders are more prevalent inside the localization. At the same time, minimal loops of order 3 are better represented in the rest of the specimen [28].

Large voids were shown to appear during the shear band formation, increasing the local void ratio. As a result, structures of lower density are created inside the band. As a relation between cluster order and the void ratio has already been established in Section 5.2.3, it can be expected that clusters of larger order appear around shear bands.

To test this hypothesis between clusters and shear bands, two visual analyses are proposed:

- The average cluster order of a grain. Calculated as the average order of all cells forming part of a grain.
- Geometrical positioning of the sizable clusters. A sizable cluster is defined here as a cluster larger than 30% of the maximal order existent during the instant of the calculation.

Figure 5.28 illustrates, for test D100, the comparison between the identified shear band (incremental deviatoric strain method) and the analysis of both clusters.

It can be noted that sizeable clusters are mostly arranged in the regions where the shear band is formed. Furthermore, regions outside the shear band (void regions in the first two columns) also correspond to a less populated region in the cluster images, indicating the absence of sizable clusters.

This correlation is also observed for all remaining tests, which can be found in the Appendix E. This phenomenon is better observed for experiments where the shear band appeared at higher mean pressure (D100, D200, U200).

It can be concluded that there is a direct connection between the positioning of sizable clusters and shear bands.

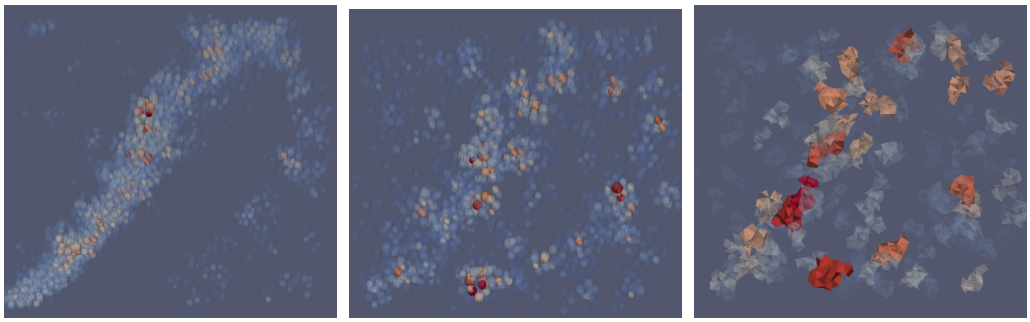

(a) Shear band identification at $\varepsilon_z = 0.106$.

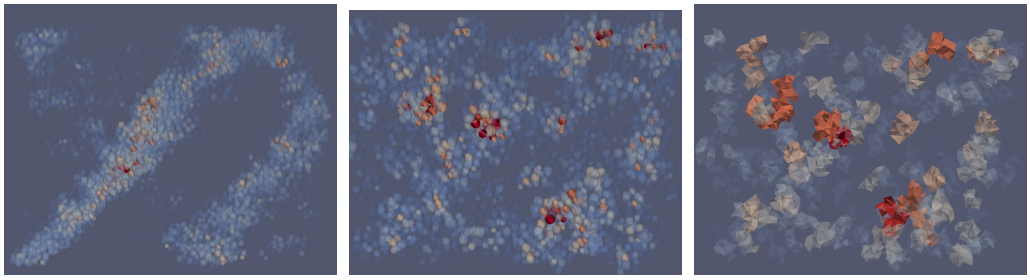

(b) Shear band identification at $\varepsilon_z = 0.236$.

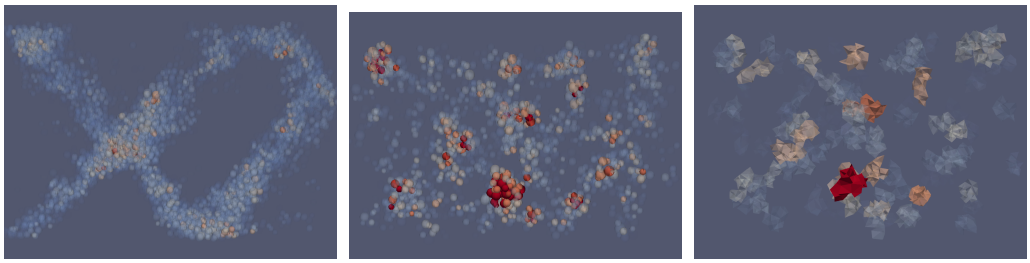

(c) Shear band identification at $\varepsilon_z = 0.380$.

Figure 5.28: Comparison between cluster and shear band locations for test D100. Figures (a), (b), and (c) illustrate axial strains 0.106, 0.236, and 0.380, respectively. The first column illustrates the the shear band (cumulative deviatoric strain method), the second column is the average cluster order of the grain, while the third represents the distribution of sizable clusters.

5.5 Concluding remarks

The procedures to identify a loop-like structure in 3D (clusters) described in Chapter 3 were applied to all simulated triaxial tests. Clusters were shown to appear in a wide range of orders, many times larger than that observed on loops.

It was shown that as the cluster increases in order it becomes, on average, more deformable. The deformability value seems to have an upper limit of

0.7, indicating that a minimum of 30% of closed edges are necessary for the formation of a cluster of larger orders. By contrast, the maximum possible deformability in 2D conditions is 0.5.

The void ratio of clusters was shown to increase, on average, with the increase in cluster order. However, a very large dispersion of possible values was observed, with smaller clusters showing results several times above the average. These results were attributed to the formation of structures formed by two unconnected sets of grains. In addition, these structures were shown to be uncommon and increasingly rare with the increase in the order of clusters.

It was proposed that a bijection between the properties of size and order does not exist. However, it was shown that the relation between these two quantities fluctuates around a linear relation. Furthermore, it was shown that small clusters (of order 4) are likely to be present inside clusters or large categories.

Clusters were divided into categories in regard to whether they are created or destroyed during each phase of the drained loading path, generating the four following categories:

- Small: minimal clusters of order 4.
- Submedium: clusters of order 6.
- Medium: clusters of order 8 to 20.
- Large: clusters of order 22+.

Although the categories were created for the drained loading path, they were shown to be representative of the material for all triaxial tests simulated. However, it is believed that the limit between the medium and large categories is dependent on the soil density, with looser soils returning a higher value.

The macroscopic volumetric comportment of the specimen is reflected by the transition between cluster categories. When larger clusters are breaking, thus creating denser structures, the specimen undergoes a contracting phase. However, when clusters start merging, the specimen dilates.

The average void ratio of each category was shown to be related to the macroscopic behavior of the specimen. The average void ratio of small clusters was shown to be most affected by the mean pressure applied to the specimen. At the same time, all other categories are also impacted by the volumetric strain rate of the specimen.

In addition, the behavior of clusters for tests D28 and Q100-100 was shown to converge around a similar rupture point. The convergence was

observed for the cell distributions and the average void ratio of each cluster category, indicating that the state of the mesostructures around the failure was equivalent for both tests.

The distribution of clusters attached to force chains (FCL) was shown to differ from clusters not attached to force chains (NFCL). Clusters of higher order tend to be formed around force chains, with most - if not all - clusters of the large category being FCL. By contrast, the number of clusters of small order is superior in NFCL.

It was established that the presence of larger clusters around force chains decreases their stability. In addition, less stable force chains are more prone to bending, which increases the void ratio of surrounding clusters. Thus, a feedback loop between force chain bending and the merger of clusters was constated.

Furthermore, force chains were shown to be able to traverse through clusters of a large order, as a result of the formation of "pseudo-open surfaces" (closed surfaces formed inside clusters). This pathology may manifest for two reasons: the presence of a small cluster inside a larger one; or through the merger of cells sharing the closed surface through other open surfaces.

The macroscopic loading path was demonstrated to have an impact on the direction of the elongation of clusters. It was shown that newly created clusters tend to orient themselves toward the direction of the major principal stress. This change in direction can be seen as the result of grain reorganization in the form of force chains. As the latter is oriented in the strongest principal stress direction (vertical), so are the newly created clusters.

A relation between high-order clusters and shear bands was implied. It was shown that for all specimens, sizable clusters (clusters with an order higher than 30% of the existent maximal) tend to be located in the region of shear bands.

Finally, comparing the above results with the behavior of loops presented in Section 2.4.2 enabled the validation of clusters as the extension of loops in 3D conditions.

Chapter 6

Conclusion

6.1 Synthesis of the main outcomes

In the context of granular materials, loops are mesoscale structures that can link the properties of each grain to the behavior of a collective. In Section 2.4.2, loops were shown to deeply influence the overall behavior of the granular assembly and other coexisting internal granular structures. However, their definition was bound to 2D conditions.

This work proposed a procedure to extend the definition of loops to 3D conditions. It is based on the use of a Delaunay tessellation to subdivide the 3D medium into tetrahedral cells, which are merged into larger structures following a merging criterion.

Cells are composed of edges between grains in contact or in proximity with each other, characterizing closed edges and open edges, respectively. These edges are combined in trios forming the exterior triangular surfaces of cells. A surface is characterized as open if all three edges forming it are open. Thus, the presence of at least one closed edge delineates a closed surface. Finally, the merging criterion is defined as the presence of an open frontier between two cells.

The identified structures are called "clusters," as this nomenclature is more aligned with their topological features. It was shown that the number of grains and external frontiers is not equal for clusters, distinguishing between size and order, respectively.

Several discrete element method (DEM) simulations of dense material under three triaxial types (drained, undrained, and constant deviatoric stress) were executed in the software LIGGGHTS to test the cluster identification procedure. First, the macroscopic behavior of the tests was validated. Then, the characteristics of the identified cluster were analyzed to investigate whether the newfound structures maintain the properties that make loops an important feature of granular assemblies.

6.1.1 Simulation mechanical response

In total, 12 triaxial loading paths departing from the same initial state were numerically conducted using the DEM.

To validate the different tests executed, two classic limits of soil mechanics

were calculated: the failure line (FL) and the critical state line (CSL). Both values were identified in the drained loading path and reported to the other triaxial conditions. In the constant deviatoric stress (q-constant) cas e, failure appeared around the instant when the specimen tried to cross the CSL. Undrained simulations showed no signs of failure. However, their behavior was shown to be bound between both lines, matching the FL at the peak relative strength and later approaching CSL for large strain values.

The evolution of force chain structures was shown to be directly linked to the macroscopic behavior of all specimens. It was shown that the variations in specimen strength are due to the change in the number of chained grains. Hardening is characterized by an increase in the number of chained grains and softening by a decrease or stabilization of this quantity.

In the early phases, force chains are created in the existent contact network of the material. This is reflected in a large number of small single-branch force chains. Once the granular skeleton starts reorganizing through plastic deformation, force chains merge and branch forming larger structures. Consequently, a decrease in single-branch structures and later multibranch structures is observed.

At the same time, force chain bending starts occurring. These events are known to increase the void ratio around the chains, decreasing their stability and increasing their probability of bending. This ultimately leads to the softening phase of the material.

Tests D28 and Q100-100 were shown to rupture at an equivalent macroscopic stress state. It was shown that the macroscopic state of both tests converges around the rupture point. In addition, an analysis of the force chain structures of both tests revealed a convergence between the behavior of these structures around the rupture point for all analyzed force chain metrics.

Strain localization in the form of shear bands was shown to appear in all specimens. Three methods to identify these structures were proposed: grain-based cumulative deviatoric strain, grain-based incremental second-order work, and cell-based incremental deviatoric strain. All methods were shown to be capable of identifying the presence and location of the shear band at different instants of the simulation. However, results are more apparent for specimens submitted to higher mean pressure during the shear banding (D100, D200, U200). Incremental calculations could capture the instantaneous transformations of the specimens, while cumulative ones allow the history of the shear band inside the specimen to be observed.

Furthermore, the initial shape of the shear band is similar for all specimens, departing from the lower-left corner and finishing in the top-right corner. As all tests depart from the same initial state, a predisposition to

this shape can be asserted. However, the final shape of the shear band varies with the loading conditions, with the phenomenon of shear band reflection being observed mostly in the drained cases (D50, D100, and D200).

6.1.2 Cluster characteristics

The identified clusters exhibited a large array of orders and sizes. Thus, to facilitate their characterization, clusters were categorized in terms of being created or destroyed during the different phases of the drained triaxial loading path. Later, the categories were validated in the remaining triaxial conditions (undrained and q-constant). The four classes created can be summarized as follows:

- **Small - Order 4**. This category is by far the most abundant, occupying most of the volume of the specimen. These clusters increase in number during the contraction phase, but when approaching the dilation regime, their number decreases until a constant value is reached.
- **Submedium - Order 6**. In the early stages, these clusters evolve oppositely to small clusters, decreasing in number during the contraction and increasing during the dilation. However, near the deviatoric stress peak, their behavior changes, and their number decreases until a steady state is reached.
- **Medium - Order 8 to 20**. Medium clusters evolve similarly to submedium ones until the peak deviatoric stress, from where a steady state is reached for large strains. In fact, medium and small populations dislay the opposite behavior.
- **Large - Order 22+**. These clusters only appear in significant numbers after the characteristic point and contain all clusters larger than the medium category. Once they appear, they only grow in number until an asymptotic value is reached for large vertical strains.

In 3D conditions, the number of external frontiers (order) and the number of grains (size) were shown to differ. However, both of these quantities were shown to be linked by a linear relation, illustrating the mechanisms that take place during the creation of large clusters. For small, submedium, and medium categories, a unitary increment in size results, on average, in two increments in order value. However, for the large category, the average order is increased by more than 2 for the same size increment. This phenomenon highlights a pathological case where small clusters (order 4) are formed completely inside large clusters.

The deformability was shown to be a valid measure of the capacity to deform loop-like structures. It was shown that, on average, the deformability increases with the order of a cluster. The upper limit of the envelope of observed values is a straight line of deformability value around 0.7. This result illustrates that a minimum of 30% of closed edges are needed to form clusters of larger order. Furthermore, it can be shown that the minimal deformability value increases with the order, as an increasingly higher number of open edges is necessary to form clusters.

The void ratio of clusters was analyzed in two separate ways. First, the fluctuation of the void ratio per cluster order for several timesteps was analyzed. It was concluded that the average void ratio for each cluster order increases with the growth in order. Furthermore, large void ratio values were observed mostly for medium and lower categories. It was concluded that these extreme values are due to a pathology where clusters are formed by two separate sets of grains. However, as these structures are infrequent, the probability of a cluster of this type being formed decreases with the increase in order. Consequently, the large category is less affected by this pathology.

Next, the average void ratio evolution of cluster categories was analyzed for each triaxial loading path. It was shown that the macroscopic state of the specimen impacts the average void ratio of clusters. The macroscopic void ratio was shown to be governed by two separate mechanisms: the transition between cluster categories and the evolution of the average void ratio of each category.

The void ratio of the small category is mostly influenced by the mean pressure applied. Conversely, the remaining categories are affected by both mechanisms. During the early phases, the void ratio of these categories is shown to evolve linearly with the mean pressure. Next, cluster transformations allow for a decrease in the cluster average void ratio in a dilatant environment. Finally, the late behavior of the cluster void ratio evolves in agreement with the macroscopic tendency observed.

The comparison between cluster characteristics of tests D28 and Q100-100 highlighted a convergence around an equivalent rupture point. The phenomenon was observed for the ratio of cells and average void ratio of each category.

Together with previous results comparing the same tests, this result illustrates how a single specimen subjected to different loading paths reaches the failure point at an equivalent macroscopic and mesoscopic state (cluster and force chain). This result indicates that the mesoscopic structure of a given specimen is independent of the loading path.

6.1.3 Interaction with other internal granular structures

Clusters and force chains are defined by the granular assembly contact network. To analyze the interaction between these two structures, the cluster categories were further subdivided into two groups. Force chain clusters (FCC) are composed of clusters that share at least one contact with a force chain and thus directly participate in the force transmission. At the same time, non-force chain clusters (NFCC) permeate the rest of the specimen and do not actively participate in the force transmission.

It was shown that the proportion of clusters of each category between FCC and NFCC is significantly different. Submedium, medium, and large cluster categories are better represented in FCC, with most - if not all - clusters of the large category being part of this group. However, small NFCC are higher in number, representing more than half of NFCC cells for the entire loading path of all tests.

However, small FCC were shown to play an important role in the mechanical behavior of the specimen. As small clusters are less deformable, their presence increases the stability of force chains. Thus, as small FCC are the most represented category in the early phases, they grant the stability necessary for the hardening phase of the specimen.

Once small clusters start merging with other categories, the stability of the force chain decreases, and bending events materialize. These events promote the increase in the local void ratio, which translates into the development of increasingly larger clusters. Both these phenomena form a feedback loop that results in a macroscopic softening phase.

Finally, a shear band is formed through a coordinated, multiforce chain bending in a narrow band. As large clusters were shown to be created around bending events, it can be assumed that they can be found around shear bands.

Through visual analysis, a relation between cluster distribution and shear band location was demonstrated. It was shown that sizable clusters (clusters with an order higher than 30% of the existent maximal) tend to be located in the region of shear bands. Furthermore, an equivalent result was obtained when calculating the average cluster order per grain. Similarly to the shear band identification, this analysis is more precise for specimens submitted to a higher mean pressure during the formation of the band (D100, D200, U200).

6.1.4 Verdict

The analysis of the topological and mechanical characteristics of clusters showed that these structures respect the characteristics of 2D loops in 3D conditions. Furthermore, the definition of clusters assures that the sum of the

volume of clusters is equal to the total volume of the envelope comprising the center of particles, validating the pavement property. Thus, it can be concluded that clusters are a valid extension of loops to 3D conditions.

6.2 Perspectives

6.2.1 Changing material and shape configurations

The simplest way to improve this study is to increase the scope of the sample data. Changing the specimen dimensions, granulometry, charging speeds, material properties, and especially the initial density should enrich the knowledge of cluster characteristics.

For example, the distribution of clusters of categories is probably different for loose specimens. As the large category is defined by the largest cluster present in significant numbers in the early phases of the test, the limit between medium and large categories may be linked to the density of the specimens. In fact, clusters of medium and large categories are probably more prevalent in looser specimens. Considering the destabilizing effects that clusters of higher orders cause around force chains, it would be interesting to observe the impact of cluster distribution in diffuse failure.

Finally, the initial idea for cluster structure was based on Bagi's space cell system [59], briefly described in Section 3.2.1. This system can partition any granular material composed of convex shapes into tetrahedra. Thus, an algorithm capable of identifying space cell systems would enable the application of the defined cluster procedure to materials composed of particles of more complex shapes, thus resulting in a less idealized material. A space cell algorithm could be based on the Euclidean distance transform (EDT) followed by a local maxima search. This procedure has been used to identify pore structures [126]. However, instead of a segmentation process, a triangulation could be created by connecting grains that share a local maximum.

6.2.2 Pathology analysis

Any form of loop-like structure created in 3D through a simple criterion will present pathological cases. The proposal of Nguyen et al. [4] created a structure that comprised 70% of the specimen. In the case of this work, clusters formed by two strings of unconnected grains and small clusters inside large ones are prime examples of pathological cases.

A better understanding of the origins of these pathologies is necessary. Then a modification of the merging criterion or the creation of an exception

rule can be defined.

6.2.3 Validation of other loop properties

Several properties of loop structures remain to be validated through clusters in 3D conditions. A good example is the analysis of the lifespan and life expectancy of loops [127]: They represent, respectively, the time a structure has continually existed and the time it has until it disappears. Both of these quantities have been shown to be directly related to the size of the loop and to impact the stability of force chains [127].

Alternatively, it has been shown that the number of loops in each category remains stable around the critical state. Furthermore, critical states have been shown to be a result of the equilibrium of the transitions between categories of loops [127]. In Section 5.3, the observed results of cluster distributions show signs of stabilization for large deformations. However, further research would be necessary for a definitive conclusion to be asserted.

6.2.4 Comparing anisotropy and stress state

The ratio between deviatoric stress and mean pressure has been related to the anisotropic state of the specimen in a macroscopic analysis [55]. This result illustrates how the direction of the grains in the microscopic space has an important effect on the macroscopic behavior. It would be interesting to study whether this relation is true in a local analysis. Clusters are a good candidate for the study of this relationship.

However, contact anisotropy and strain tensors need to be correctly defined. The Love–Weber stress and contact tensors are calculated as a function of the contact between grains. Different from loops, clusters are not completely closed by contacts. Thus, a formal definition of both tensors for these clusters has to be established.

6.2.5 Utilization of the tools developed

A possible perspective of this work stems not from the theoretical propositions but instead from the tools developed during this work. As presented in Section 3.3, a Matlab application capable of analyzing rectangular triaxial DEM simulations was developed. This application can partition the specimen, thereby allowing for a local analysis of several properties.

A good prospect is the study of precursors of shear band formation inside the specimen. First, the application can be used to determine the shear band angle and position. Then, a local analysis of the material properties (void

ratio, anisotropy, number of clusters, etc.) can be performed to investigate the existence of a precursor for shear localization.

Appendix A

Shear banding images of remaining tests

A.1 Foreword

This appendix contains shear band identification for the tests not presented in Section 4.2. Each column shows a different identification method, from right to left: cumulative deviatoric strain (grain scale), negative second-order work (grain scale), and incremental deviatoric strain (cell scale).

A.2 D28

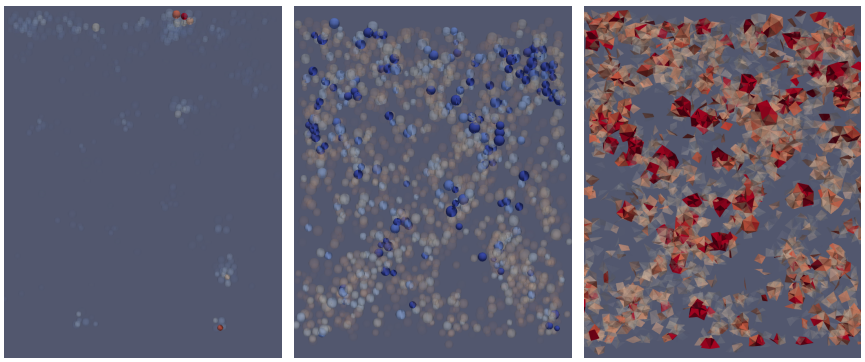

(a) Shear band identification at $\varepsilon_z = 0.051$.

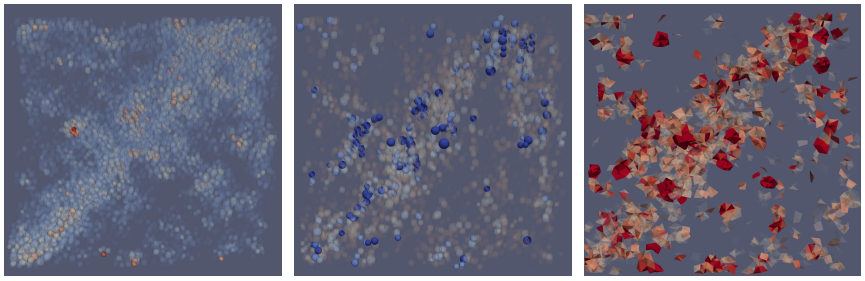

(b) Shear band identification at $\varepsilon_z = 0.177$.

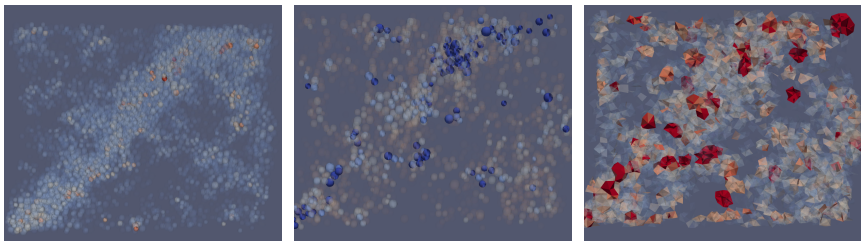

(c) Shear band identification at $\varepsilon_z = 0.291$.

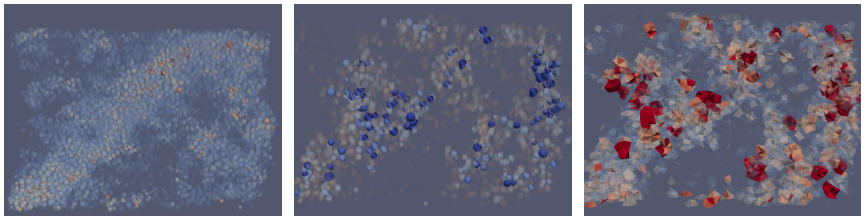

(d) Shear band identification at $\varepsilon_z = 0.373$.

Figure A.1: Shear band evolution for the test D28 at axial strains 0.051, 0.177, 0.291 and 0.373. Each column shows a different identification method, from right to left: cumulative deviatoric strain (grain scale), negative second-order work (grain scale), and incremental deviatoric strain (cell scale).

A.3 D50

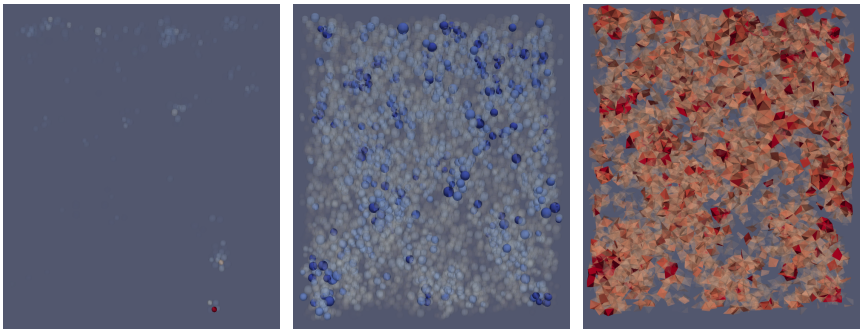

(a) Shear band identification at $\varepsilon_z = 0.066$.

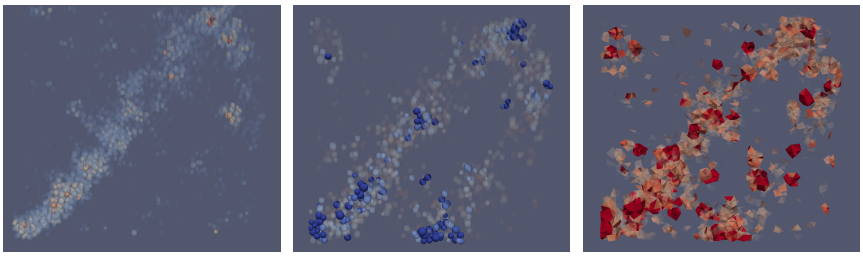

(b) Shear band identification at $\varepsilon_z = 0.173$.

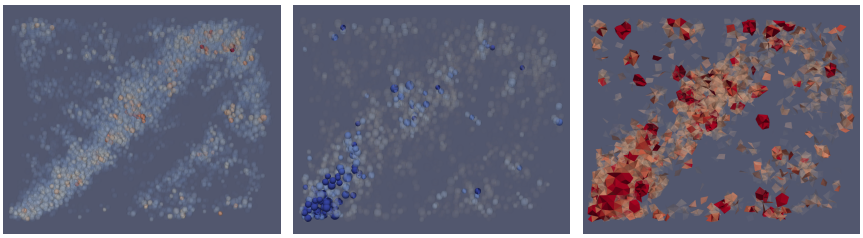

(c) Shear band identification at $\varepsilon_z = 0.292$.

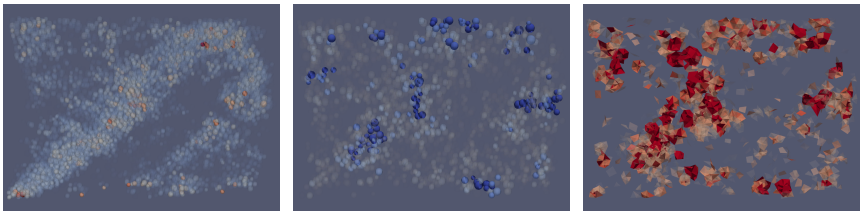

(d) Shear band identification at $\varepsilon_z = 0.378$.

Figure A.2: Shear band evolution for the test D50 at axial strains 0.066, 0.177, 0.292 and 0.378. Each column shows a different identification method, from right to left: cumulative deviatoric strain (grain scale), negative second-order work (grain scale), and incremental deviatoric strain (cell scale).

A.4 D200

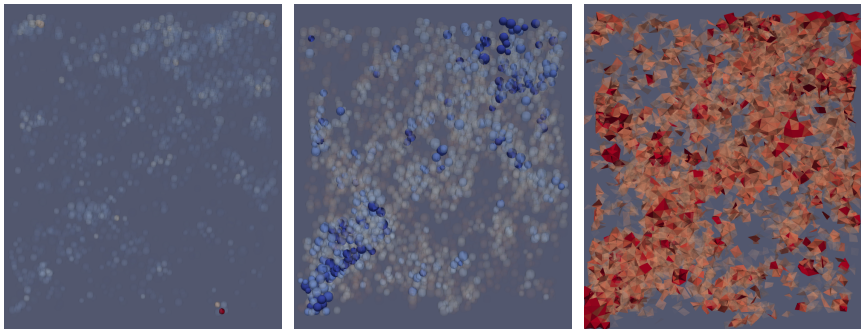

(a) Shear band identification at $\varepsilon_z = 0.121$.

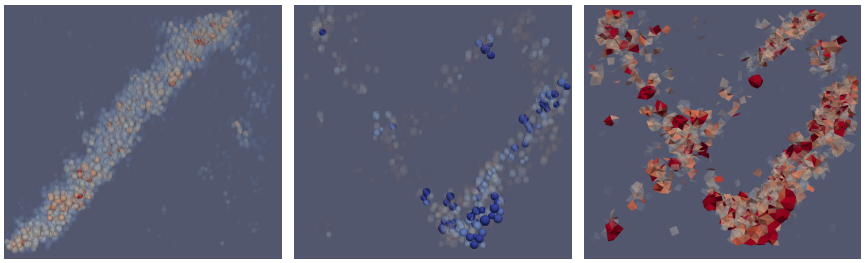

(b) Shear band identification at $\varepsilon_z = 0.224$.

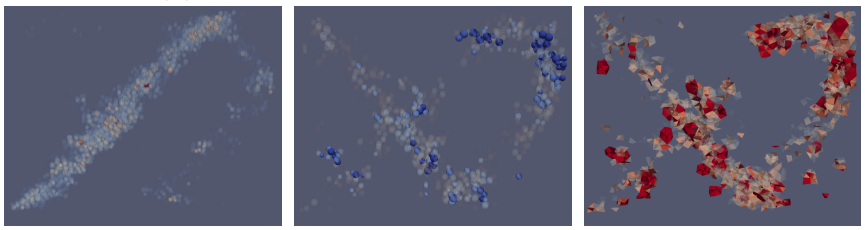

(c) Shear band identification at $\varepsilon_z = 0.298$.

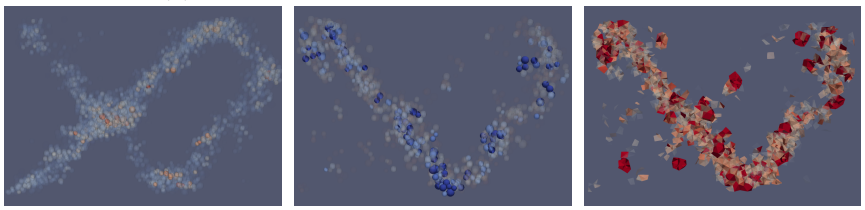

(d) Shear band identification at $\varepsilon_z = 0.386$.

Figure A.3: Shear band evolution for the test D200 at axial strains 0.121, 0.224, 0.298, 0.386. Each column shows a different identification method, from right to left: cumulative deviatoric strain (grain scale), negative second-order work (grain scale), and incremental deviatoric strain (cell scale).

A.5 Q50-100

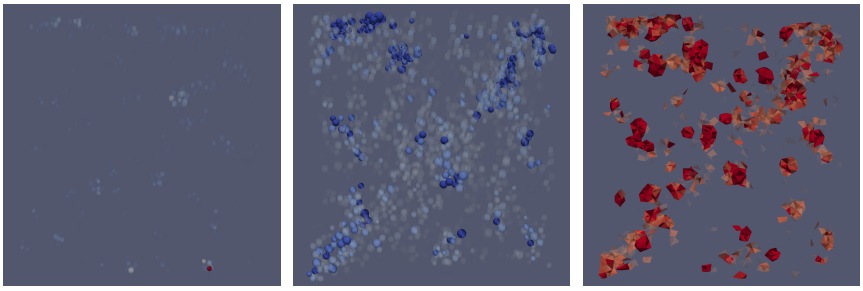

(a) Shear band identification at $p = 87.23kPa$.

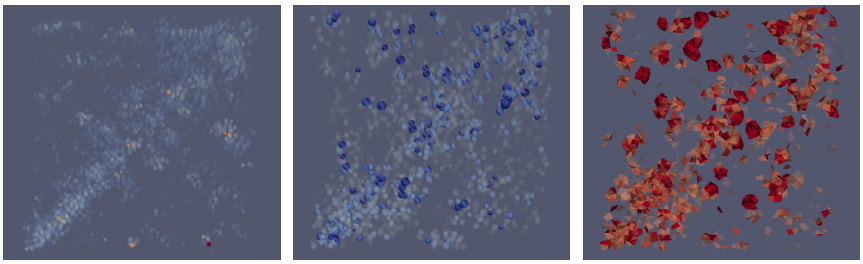

(b) Shear band identification at $p = 74.74kPa$.

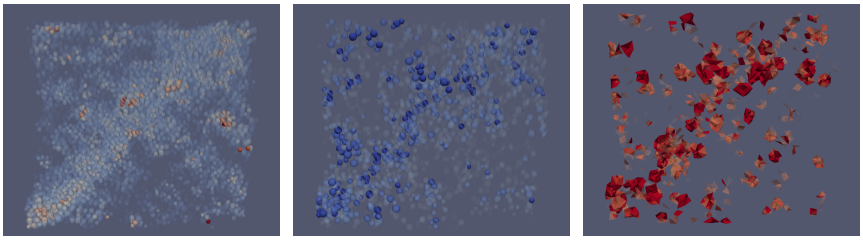

(c) Shear band identification at $p = 64.87kPa$.

Figure A.4: Shear band evolution for the test Q50-100 at mean pressure 87.23kPa, 74.74kPa and 64.87kPa. Each column shows a different identification method, from right to left: cumulative deviatoric strain (grain scale), negative second-order work (grain scale), and incremental deviatoric strain (cell scale).

A.6 Q100-150

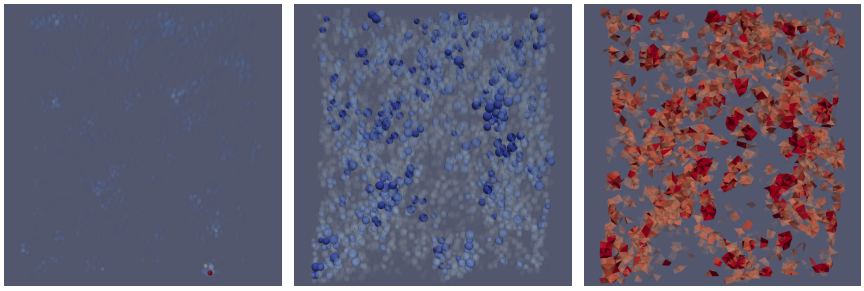

(a) Shear band identification at $p = 139.82kPa$.

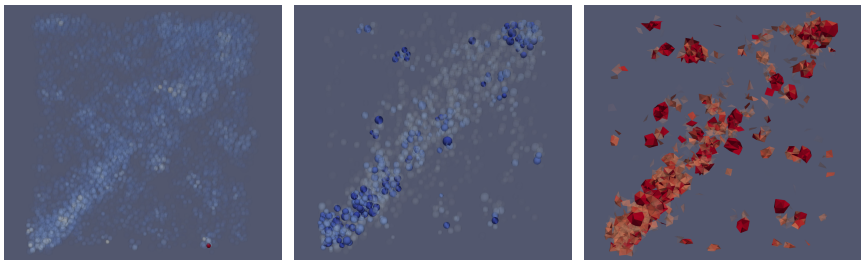

(b) Shear band identification at $p = 124.03kPa$.

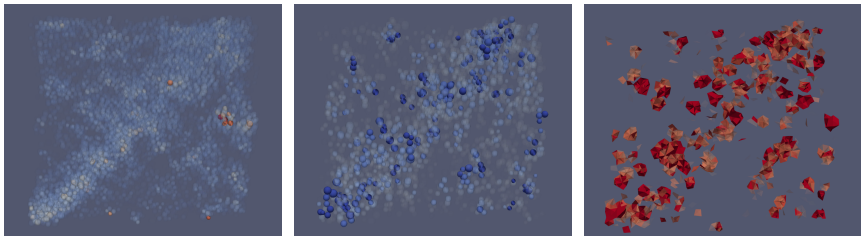

(c) Shear band identification at $p = 101.31kPa$.

Figure A.5: Shear band evolution for the test Q100-150 at mean pressure 139.82kPa, 124.03kPa and 101.31kPa. Each column shows a different identification method, from right to left: cumulative deviatoric strain (grain scale), negative second-order work (grain scale), and incremental deviatoric strain (cell scale).

A.7 Q100-200

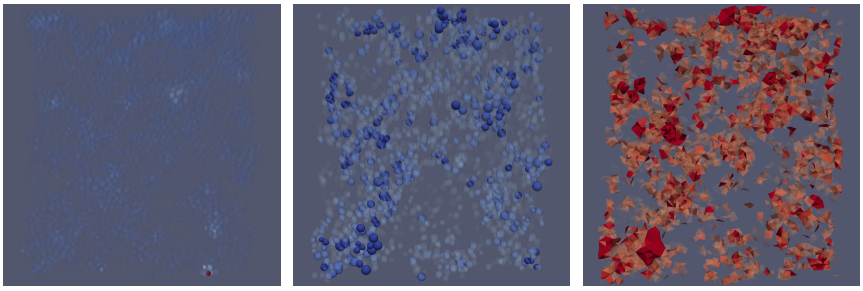

(a) Shear band identification at $p = 192.97kPa$.

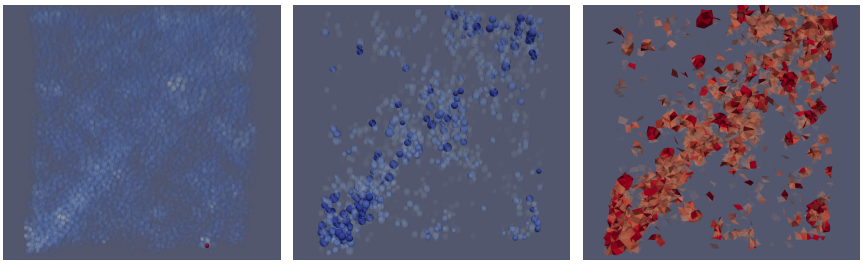

(b) Shear band identification at $p = 177.94kPa$.

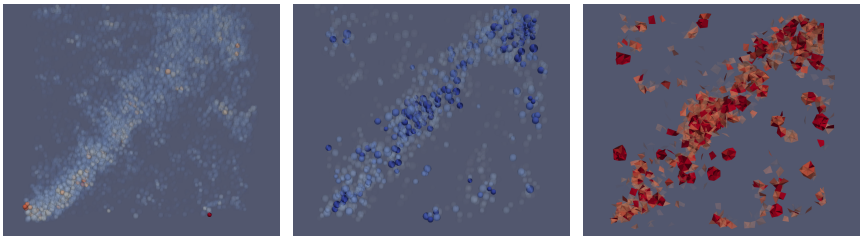

(c) Shear band identification at $p = 139.61kPa$.

Figure A.6: Shear band evolution for the test Q100-200 at mean pressure 192.97kPa, 177.94kPa and 139.61kPa. Each column shows a different identification method, from right to left: cumulative deviatoric strain (grain scale), negative second-order work (grain scale), and incremental deviatoric strain (cell scale).

A.8 Q200-100

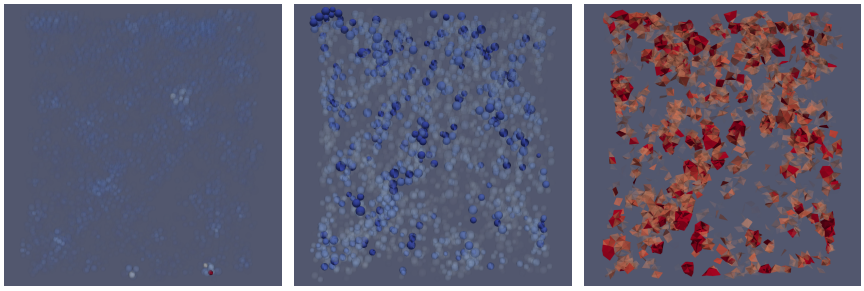

(a) Shear band identification at $p = 90.51kPa$.

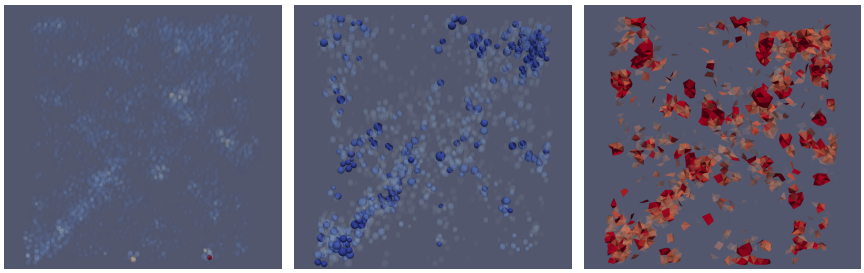

(b) Shear band identification at $p = 81.50kPa$.

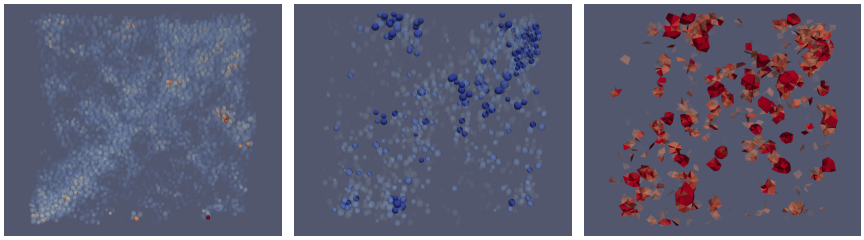

(c) Shear band identification at $p = 66.29kPa$.

Figure A.7: Shear band evolution for the test Q200-100 at mean pressure 90.51kPa, 81.50kPa and 66.29kPa. Each column shows a different identification method, from right to left: cumulative deviatoric strain (grain scale), negative second-order work (grain scale), and incremental deviatoric strain (cell scale).

A.9 U50

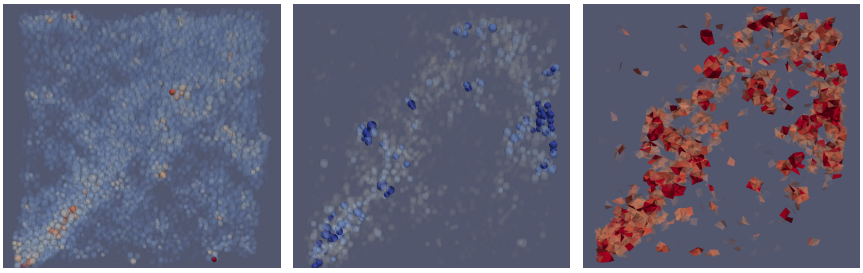

(a) Shear band identification at $\varepsilon_z = 0.146$.

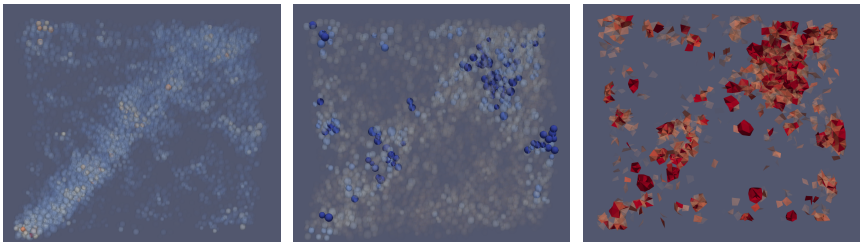

(b) Shear band identification at $\varepsilon_z = 0.255$.

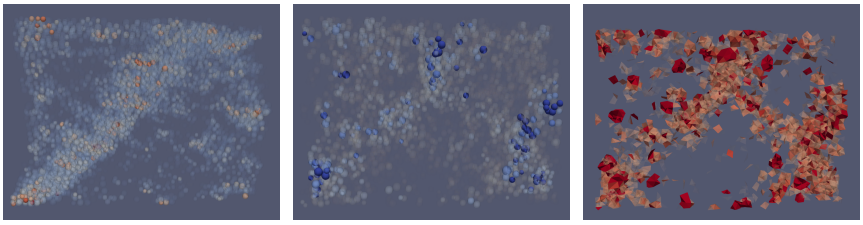

(c) Shear band identification at $\varepsilon_z = 0.378$.

Figure A.8: Shear band evolution for the test U50 at axial strain 0.146, 0.255, and 0.378. Each column shows a different identification method, from right to left: cumulative deviatoric strain (grain scale), negative second-order work (grain scale), and incremental deviatoric strain (cell scale).

A.10 U200

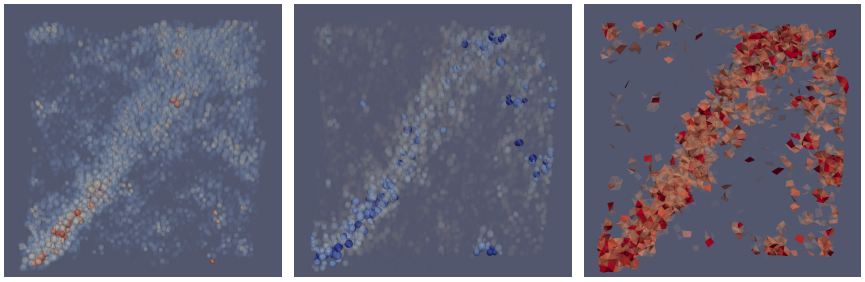

(a) Shear band identification at $\varepsilon_z = 0.154$.

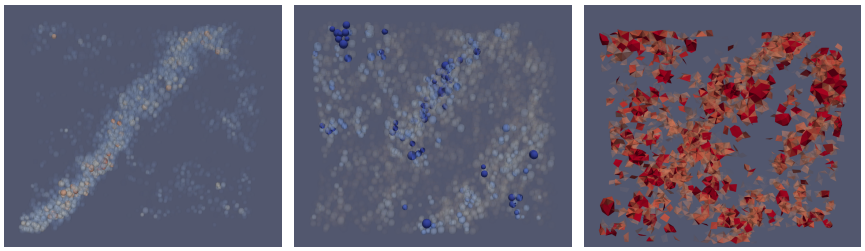

(b) Shear band identification at $\varepsilon_z = 0.260$.

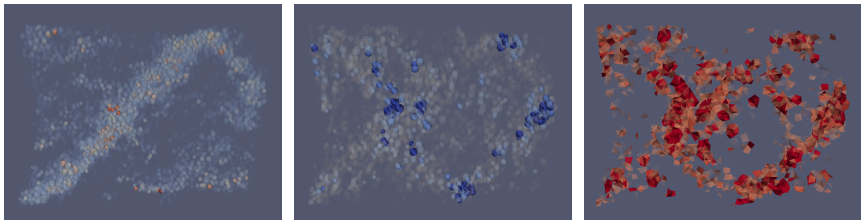

(c) Shear band identification at $\varepsilon_z = 0.386$.

Figure A.9: Shear band evolution for the test U200 at axial strain 0.154, 0.260, and 0.376. Each column shows a different identification method, from right to left: cumulative deviatoric strain (grain scale), negative second-order work (grain scale), and incremental deviatoric strain (cell scale).

Appendix B

Shear banding images of remaining tests

B.1 Forword

This appendix contains the void ratio distribution of tests not presented in section 5.2.3. The explanation of the calculation of the density map can be found in the main text.

B.2 D28

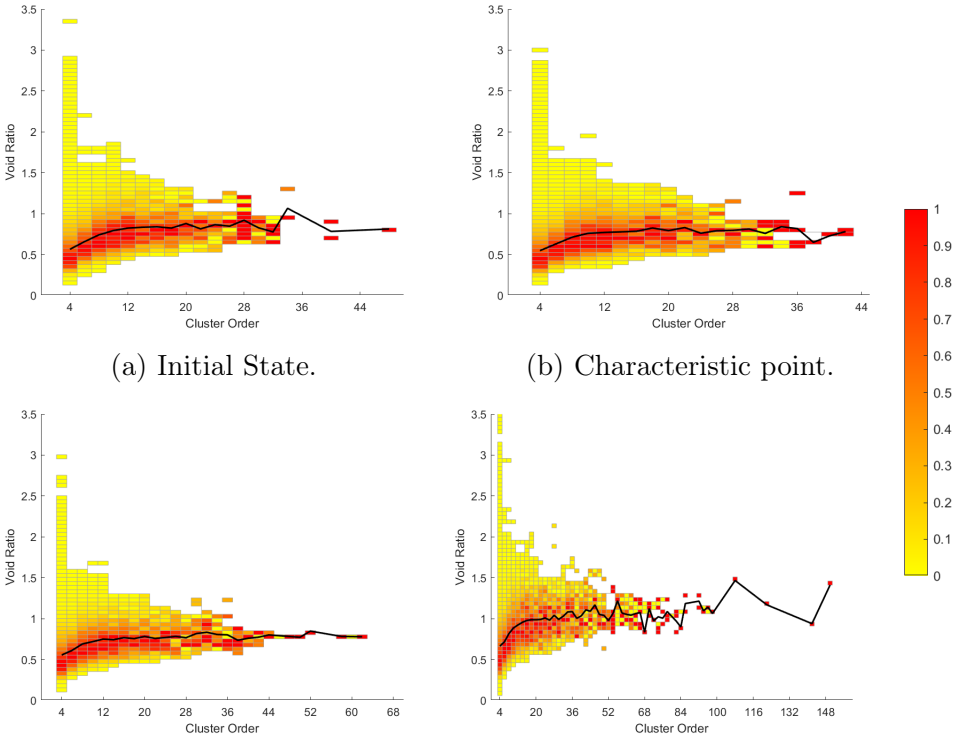

(a) Initial State.

(b) Characteristic point.

(c) Peak stress.

(d) Final state.

Figure B.1: Void ratio density map in function of cluster order for the test D28 a the initial state, characteristic point, peak stress, and final state. Point density is calculated in relation to the rectangle containing the maximum number of points for each order. The black curve represents the mean value.

B.3 D50

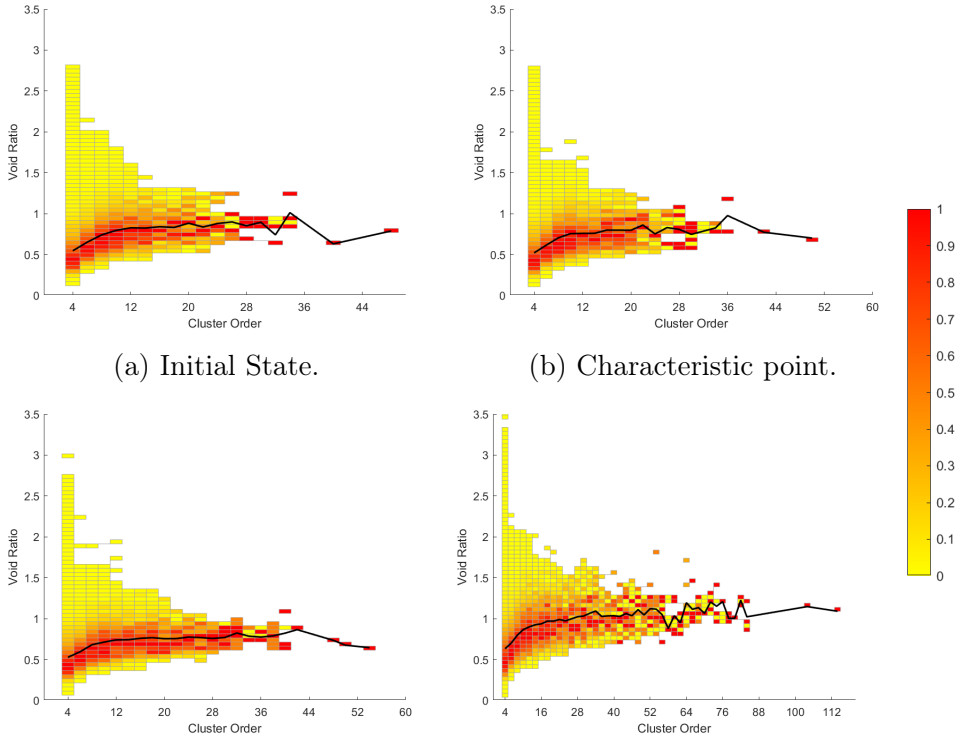

(a) Initial State. (b) Characteristic point.

(c) Peak stress. (d) Final state.

Figure B.2: Void ratio density map in function of cluster order for the test D50 a the initial state, characteristic point, peak stress, and final state. Point density is calculated in relation to the rectangle containing the maximum number of points for each order. The black curve represents the mean value.

B.4 D200

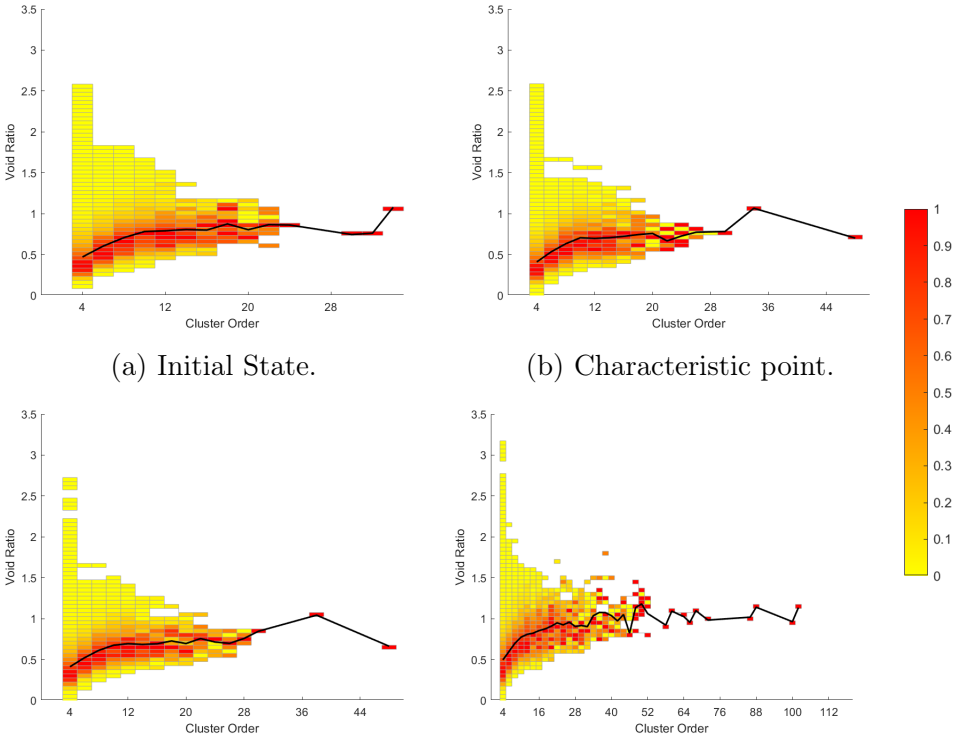

(a) Initial State. (b) Characteristic point.

(c) Peak stress. (d) Final state.

Figure B.3: Void ratio density map in function of cluster order for the test D200 a the initial state, characteristic point, peak stress, and final state. Point density is calculated in relation to the rectangle containing the maximum number of points for each order. The black curve represents the mean value.

B.5 Q50-100

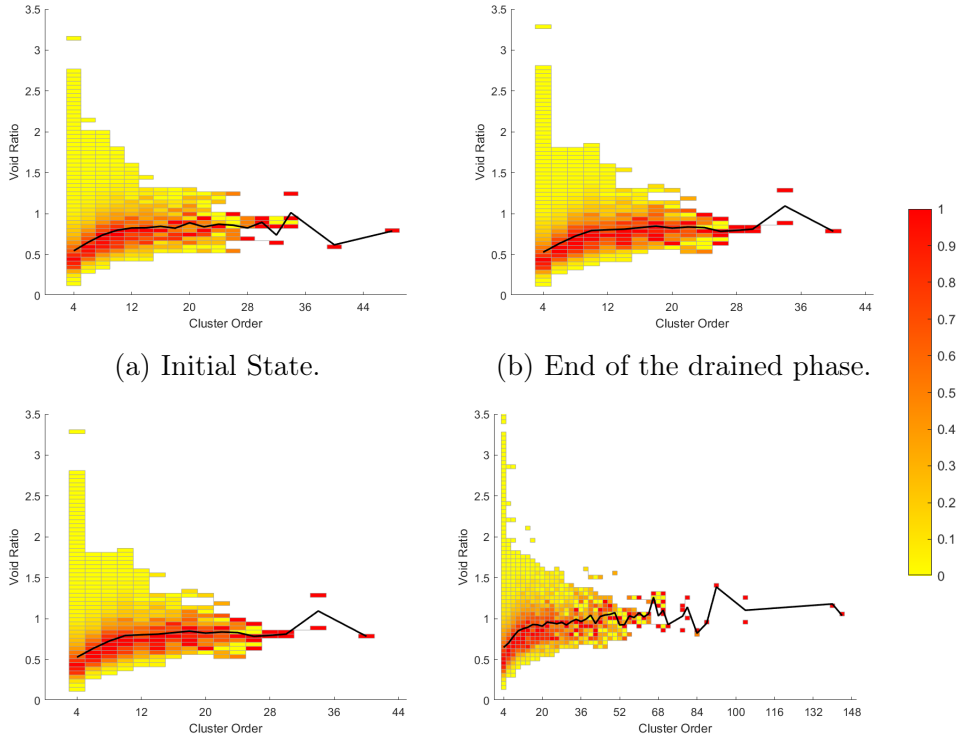

(a) Initial State.

(b) End of the drained phase.

(c) Rupture point.

(d) Final state.

Figure B.4: Void ratio density map in function of cluster order for the test Q50-100 a the initial state, end of the drained phase, rupture point, and final state. Point density is calculated in relation to the rectangle containing the maximum number of points for each order. The black curve represents the mean value.

B.6 Q100-100

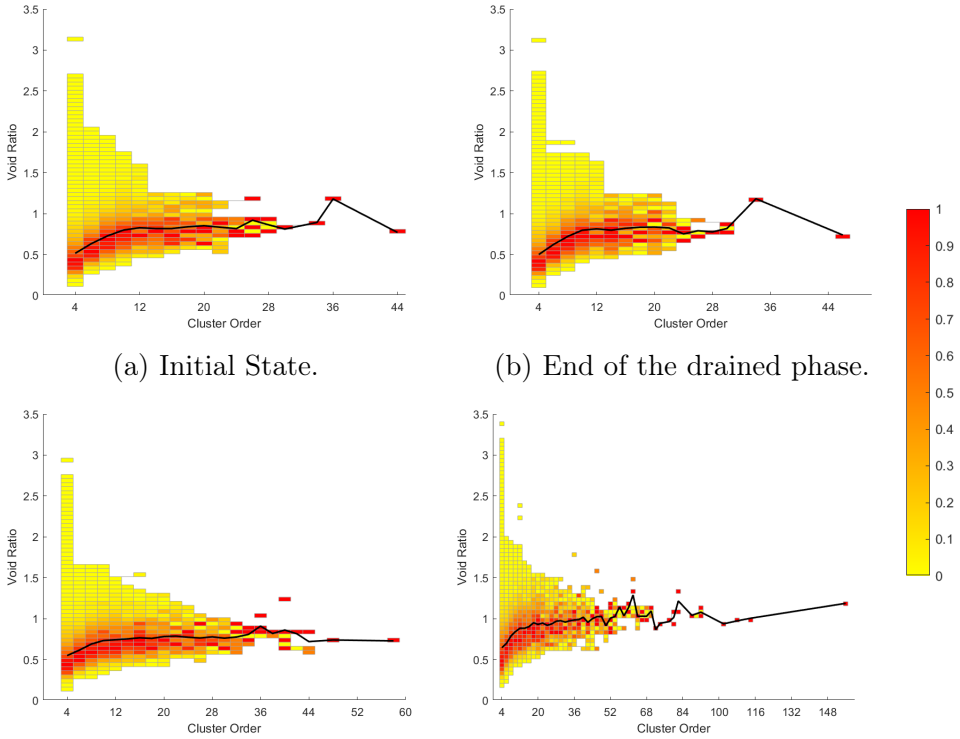

(a) Initial State.

(b) End of the drained phase.

(c) Rupture point.

(d) Final state.

Figure B.5: Void ratio density map in function of cluster order for the test Q100-100 a the initial state, end of the drained phase, rupture point, and final state. Point density is calculated in relation to the rectangle containing the maximum number of points for each order. The black curve represents the mean value.

B.7 Q100-150

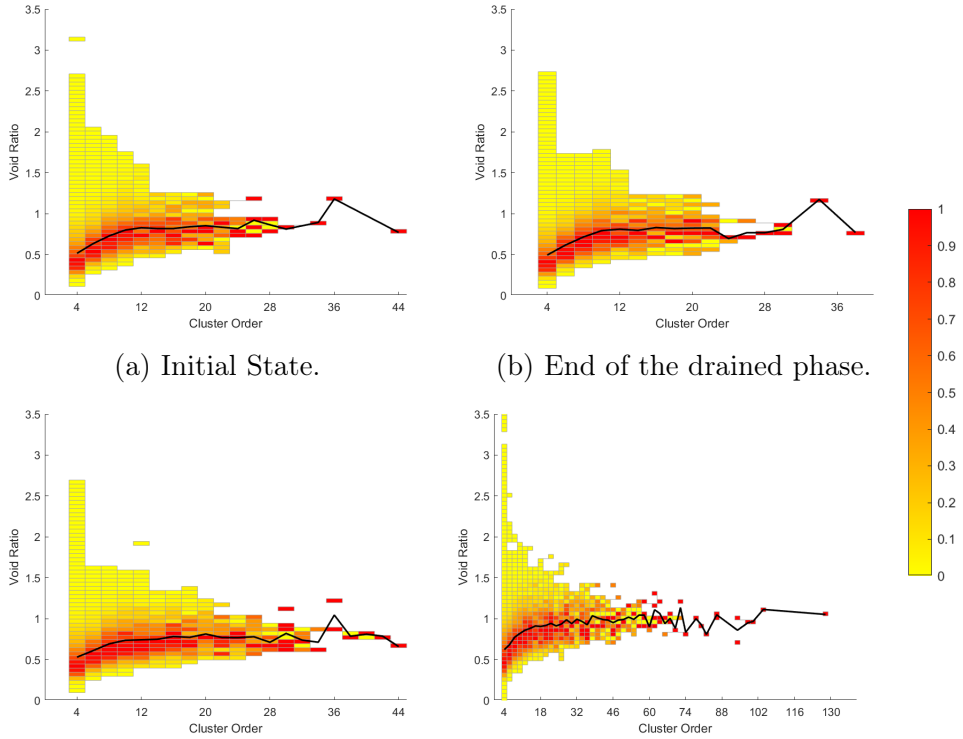

(a) Initial State.

(b) End of the drained phase.

(c) Rupture point.

(d) Final state.

Figure B.6: Void ratio density map in function of cluster order for the test Q100-150 a the initial state, end of the drained phase, Rupture point. and final state. Point density is calculated in relation to the rectangle containing the maximum number of points for each order. The black curve represents the mean value.

B.8 Q100-200

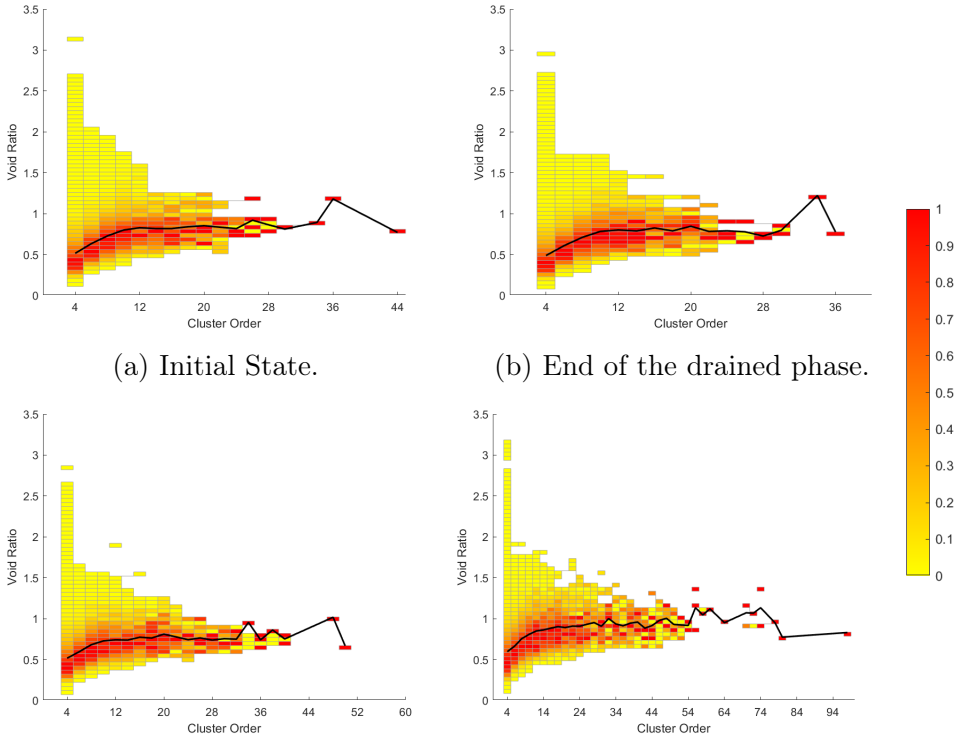

(a) Initial State.

(b) End of the drained phase.

(c) Rupture point..

(d) Final state.

Figure B.7: Void ratio density map in function of cluster order for the test Q100-200 a the initial state, end of the drained phase, rupture point, and final state. Point density is calculated in relation to the rectangle containing the maximum number of points for each order. The black curve represents the mean value.

B.9 Q200-100

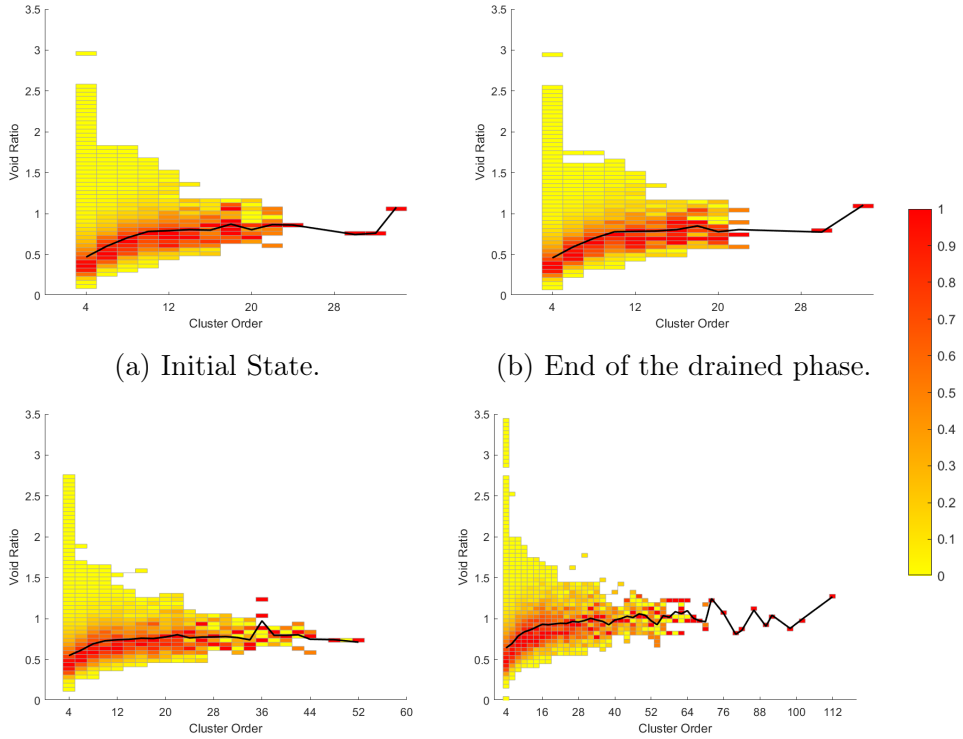

(a) Initial State.

(b) End of the drained phase.

(c) Rupture point.

(d) Final state.

Figure B.8: Void ratio density map in function of cluster order for the test Q200-100 a the initial state, end of the drained phase, peak stress, and final state. Point density is calculated in relation to the rectangle containing the maximum number of points for each order. The black curve represents the mean value.

B.10 U50

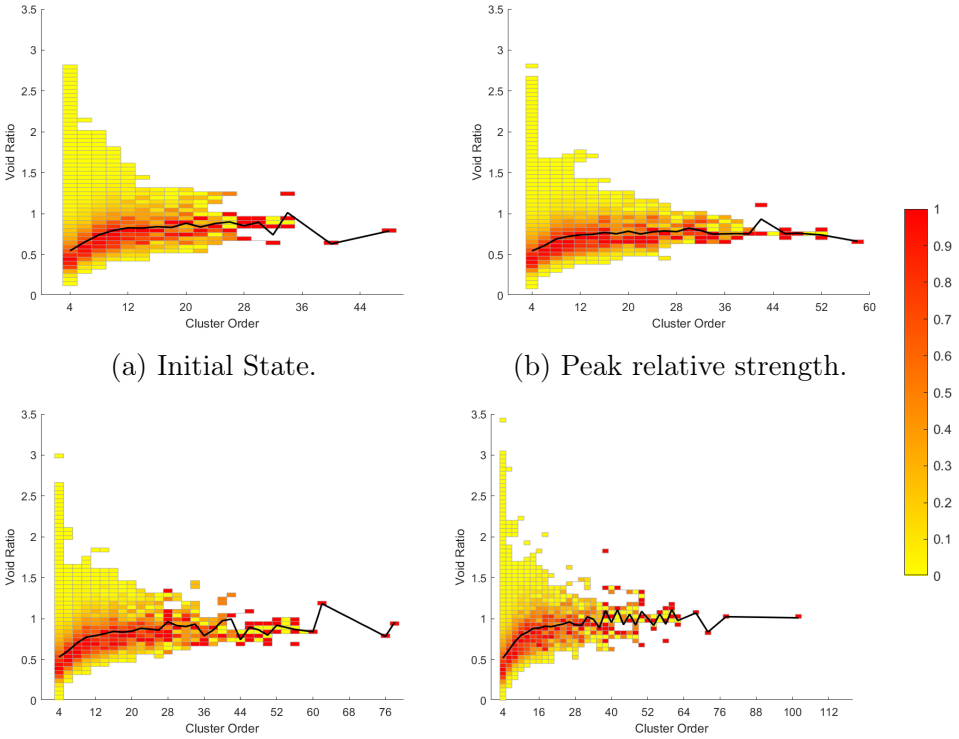

(a) Initial State.

(b) Peak relative strength.

(c) Axial strain 0.207.

(d) Final state.

Figure B.9: Void ratio density map in function of cluster order for the test U50 a the initial state, characteristic point, peak stress, and final state. Point density is calculated in relation to the rectangle containing the maximum number of points for each order. The black curve represents the mean value.

B.11 U100

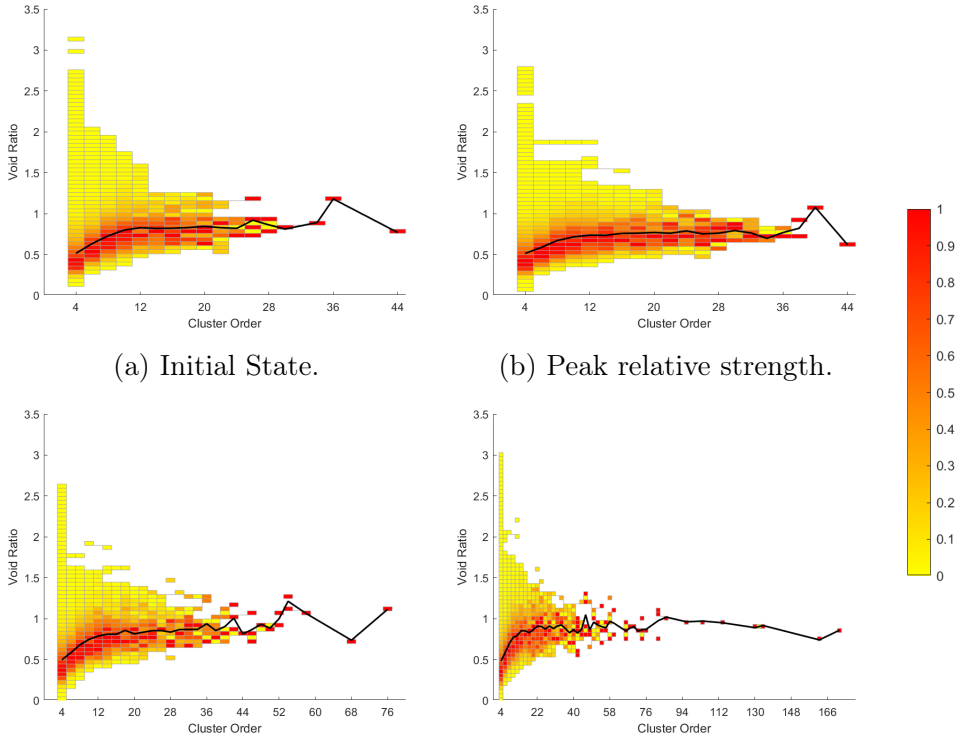

(a) Initial State.

(b) Peak relative strength.

(c) Axial strain 0.211.

(d) Final state.

Figure B.10: Void ratio density map in function of cluster order for the test U100 a the initial state, peak relative strength, and final state. Point density is calculated in relation to the rectangle containing the maximum number of points for each order. The black curve represents the mean value.

B.12 U200

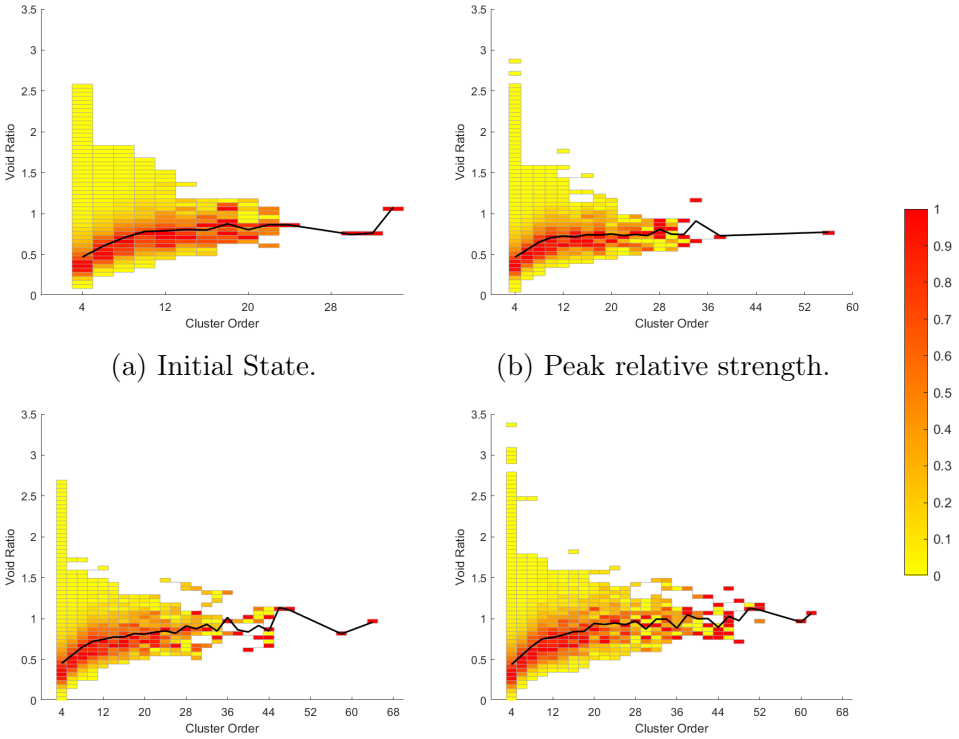

(a) Initial State.

(b) Peak relative strength.

(c) Axial strain 0.222.

(d) Final state.

Figure B.11: Void ratio density map in function of cluster order for the test U200 a the initial state, peak relative strength, and final state. Point density is calculated in relation to the rectangle containing the maximum number of points for each order. The black curve represents the mean value.

Appendix C

Cluster Orientation images of remaining tests

C.1 Forword

This appendix contains the results related to the orientation of the clusters for the remaining specimens. Only clusters formed by more than one cell are being analyzed, thus excluding clusters of the small category. Furthermore, the procedures used to obtain the following results are presented in section 3.2.1.

C.2 Cluster orientation for test D28

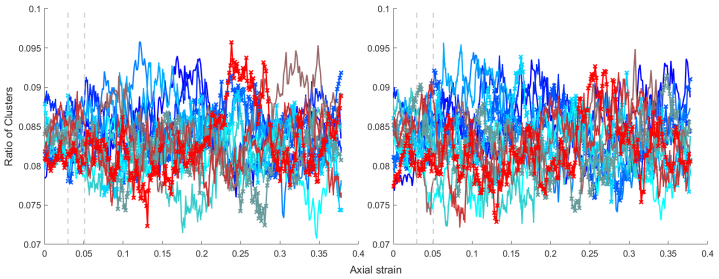

(a) Azimuth angle distribution for submedium clusters

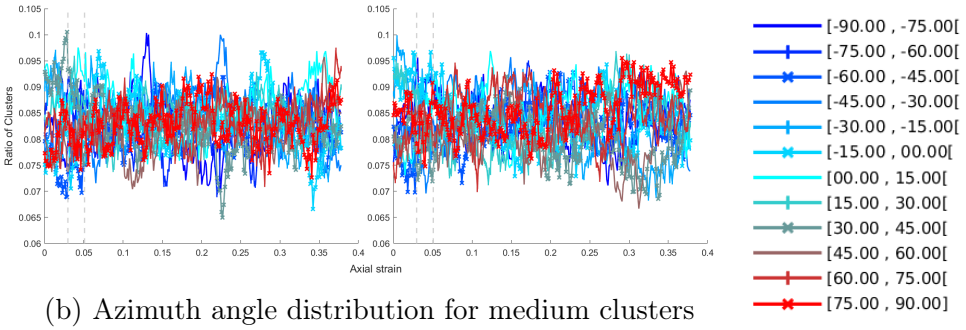

(b) Azimuth angle distribution for medium clusters

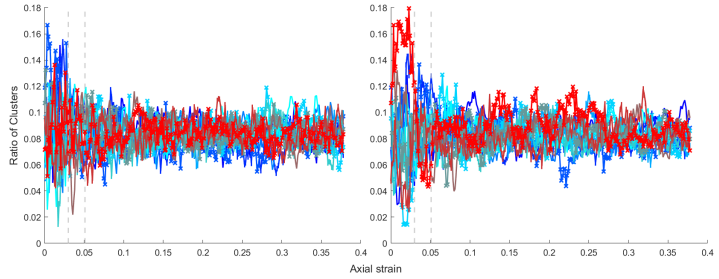

(c) Azimuth angle distribution for large clusters

Figure C.1: Evolution of cluster's azimuth angle distribution for the test D28. Surface tensor results are illustrated on the left and gravity on the right. Figures (a), (b), and (c) represent medium, submedium, and large categories, respectively. Azimuth is the rotation in the x-y plane in relation to the y-positive direction. The two dashed vertical lines represent the characteristic point and the peak deviatoric stress, respectively.

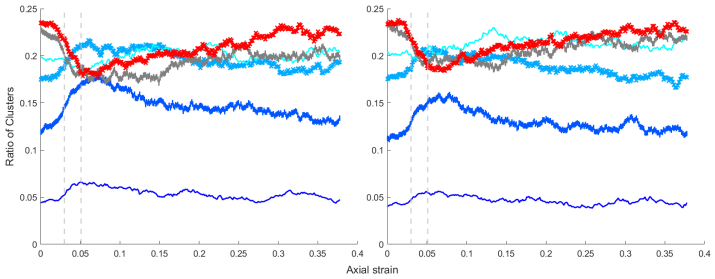

(a) Elevation angle distribution for submedium clusters

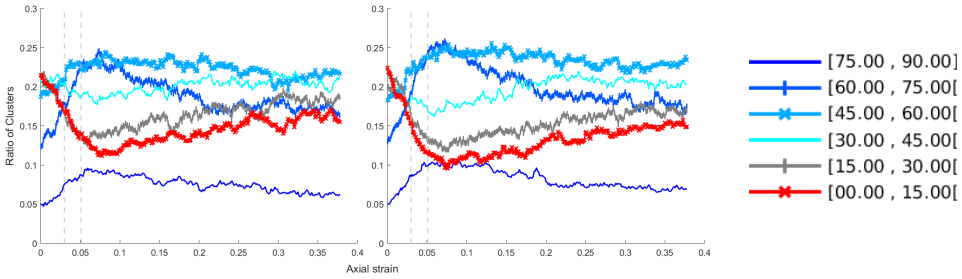

(b) Elevation angle distribution for medium clusters

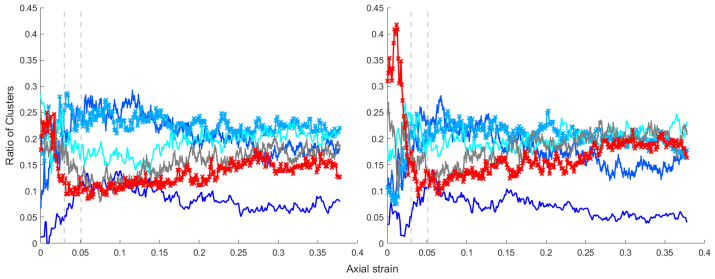

(c) Elevation angle distribution for large clusters

Figure C.2: Evolution of cluster's elevation angle distribution for the test D28. Surface tensor results are illustrated on the left and gravity on the right. Figures (a), (b), and (c) represent medium, submedium, and large categories, respectively. Elevation is the rotation in relation to the x-y plane. The two dashed vertical lines represent the characteristic point and the peak deviatoric stress, respectively.

C.3 Cluster orientation for test D50

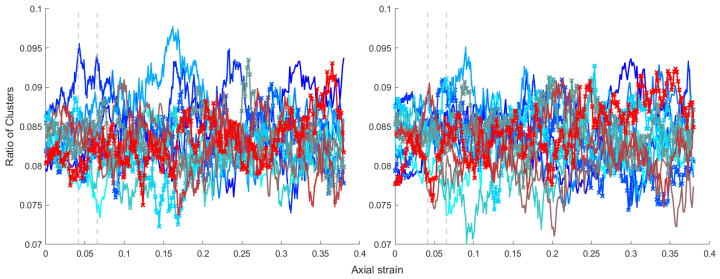

(a) Azimuth angle distribution for submedium clusters

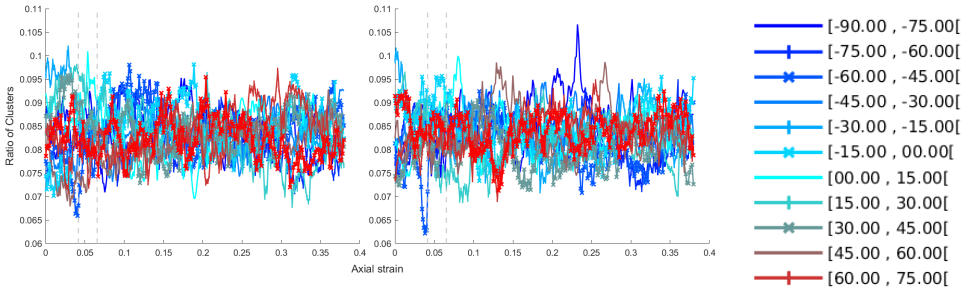

(b) Azimuth angle distribution for medium clusters

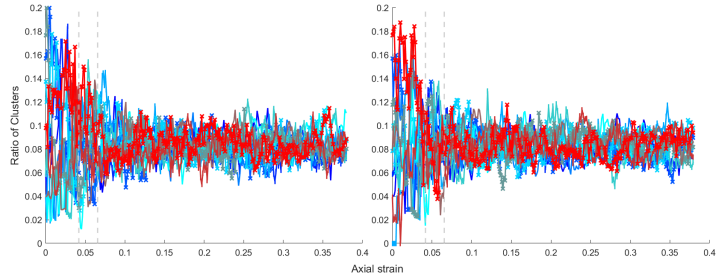

(c) Azimuth angle distribution for large clusters

Figure C.3: Evolution of cluster's azimuth angle distribution for the test D50. Surface tensor results are illustrated on the left and gravity on the right. Figures (a), (b), and (c) represent medium, submedium, and large categories, respectively. Azimuth is the rotation in the x-y plane in relation to the y-positive direction. The two dashed vertical lines represent the characteristic point and the peak deviatoric stress, respectively.

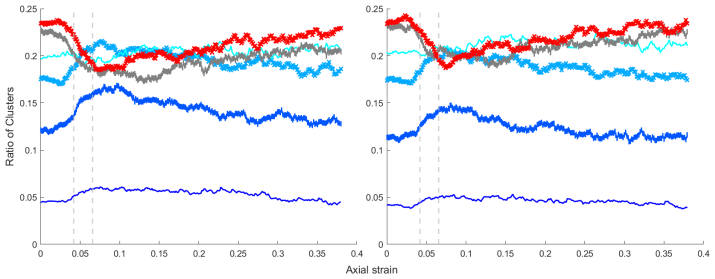

(a) Elevation angle distribution for submedium clusters

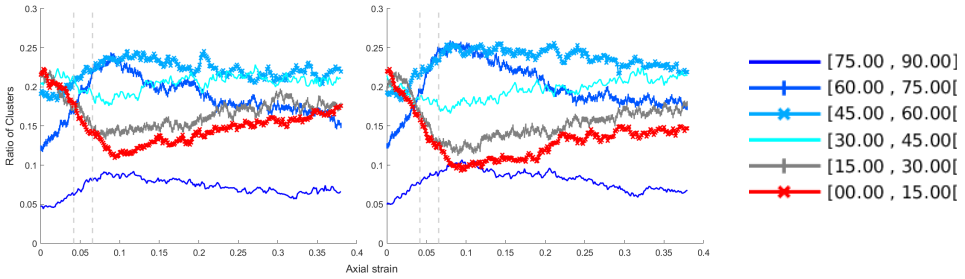

(b) Elevation angle distribution for medium clusters

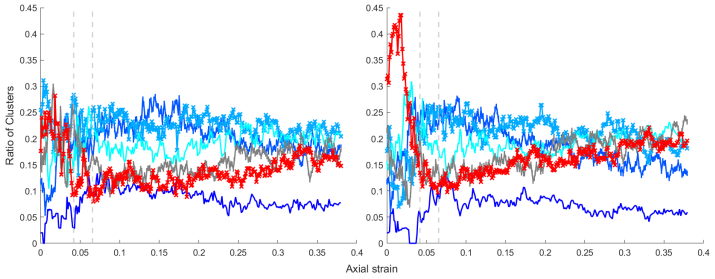

(c) Elevation angle distribution for large clusters

Figure C.4: Evolution of cluster's elevation angle distribution for the test D50. Surface tensor results are illustrated on the left and gravity on the right. Figures (a), (b), and (c) represent medium, submedium, and large categories, respectively. Elevation is the rotation in relation to the x-y plane. The two dashed vertical lines represent the characteristic point and the peak deviatoric stress, respectively.

C.4 Cluster orientation for test D200

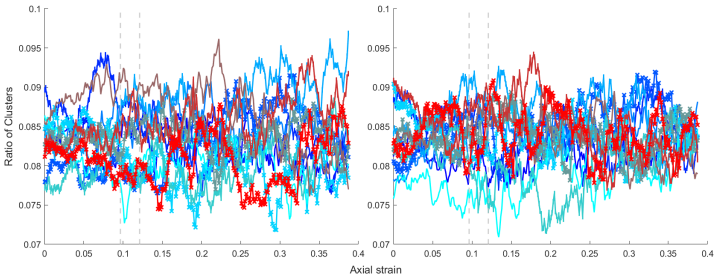

(a) Azimuth angle distribution for submedium clusters

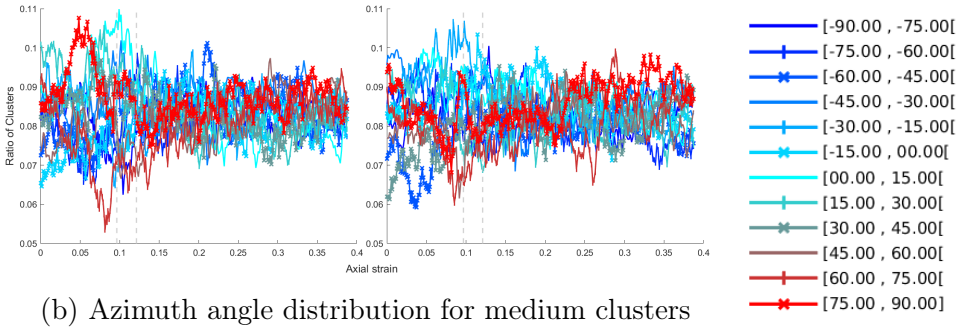

(b) Azimuth angle distribution for medium clusters

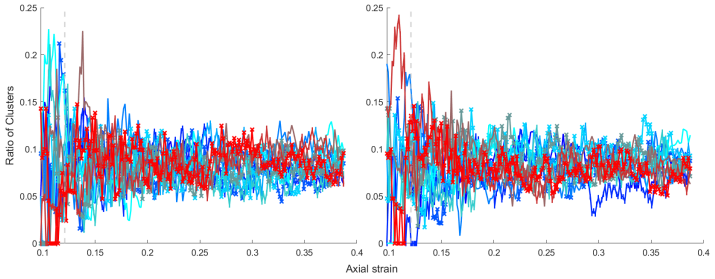

(c) Azimuth angle distribution for large clusters

Figure C.5: Evolution of cluster's azimuth angle distribution for the test D200. Surface tensor results are illustrated on the left and gravity on the right. Figures (a), (b), and (c) represent medium, submedium, and large categories, respectively. Azimuth is the rotation in the x-y plane in relation to the y-positive direction. The two dashed vertical lines represent the characteristic point and the peak deviatoric stress, respectively.

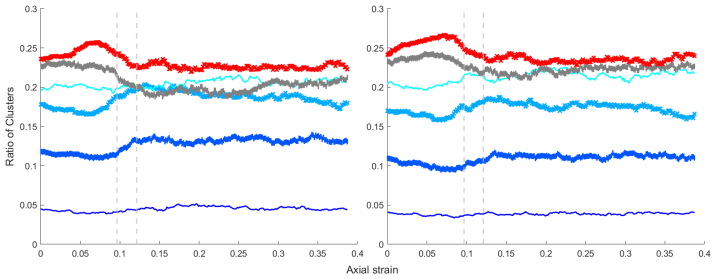

(a) Elevation angle distribution for submedium clusters

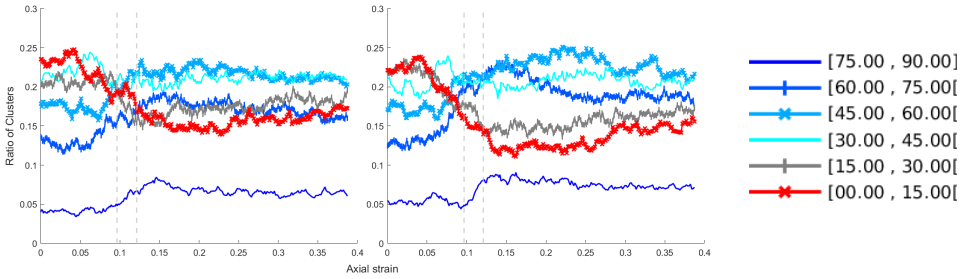

(b) Elevation angle distribution for medium clusters

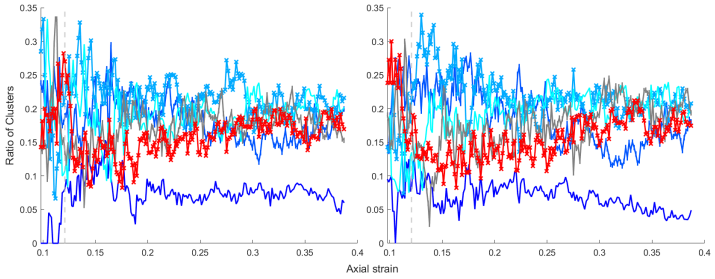

(c) Elevation angle distribution for large clusters

Figure C.6: Evolution of cluster's elevation angle distribution for the test D200. Surface tensor results are illustrated on the left and gravity on the right. Figures (a), (b), and (c) represent medium, submedium, and large categories, respectively. Elevation is the rotation in relation to the x-y plane. The two dashed vertical lines represent the characteristic point and the peak deviatoric stress, respectively.

C.5 Cluster orientation for test Q50-100

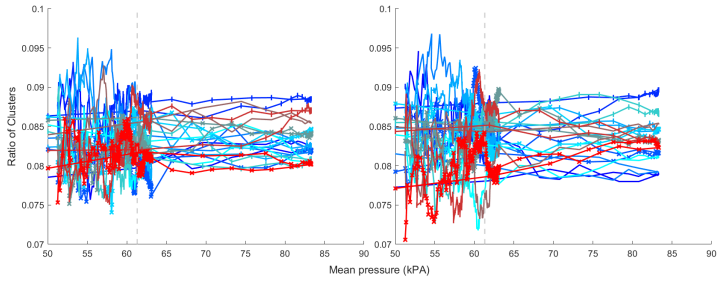

(a) Azimuth angle distribution for submedium clusters

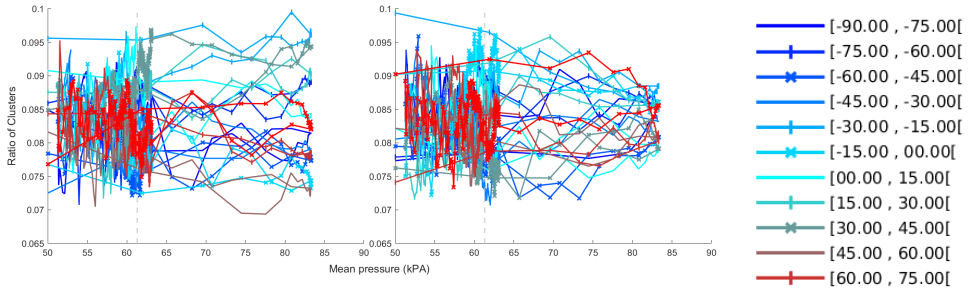

(b) Azimuth angle distribution for medium clusters

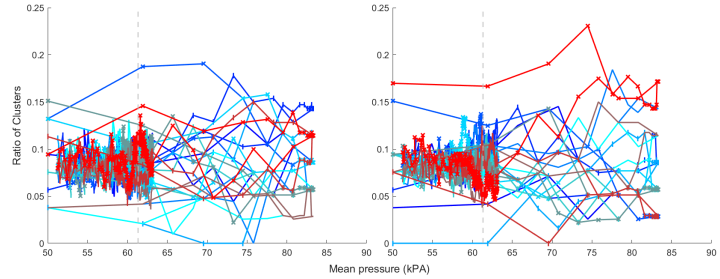

(c) Azimuth angle distribution for large clusters

Figure C.7: Evolution of cluster's azimuth angle distribution for the test Q50-100. Surface tensor results are illustrated on the left and gravity on the right. Figures (a), (b), and (c) represent medium, submedium, and large categories, respectively. Azimuth is the rotation in the x-y plane in relation to the y-positive direction. The vertical dashed line represent the rupture point.

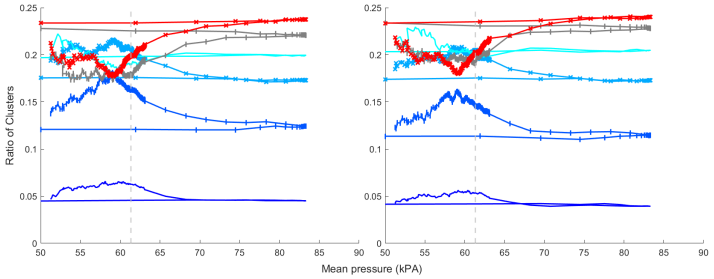

(a) Elevation angle distribution for submedium clusters

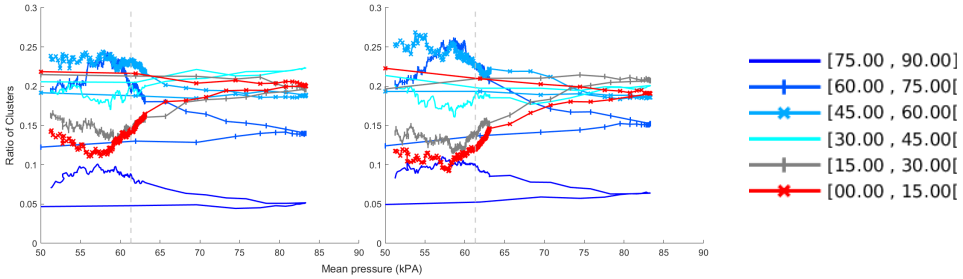

(b) Elevation angle distribution for medium clusters

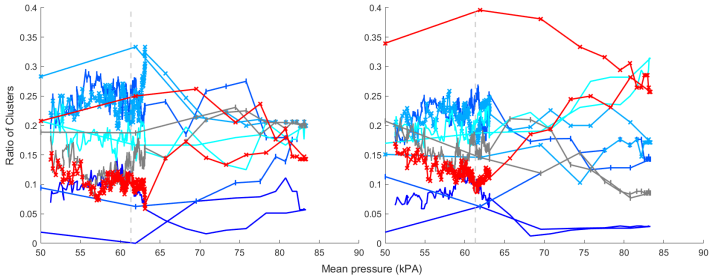

(c) Elevation angle distribution for large clusters

Figure C.8: Evolution of cluster's elevation angle distribution for the test Q50-100. Surface tensor results are illustrated on the left and gravity on the right. Figures (a), (b), and (c) represent medium, submedium, and large categories, respectively. Elevation is the rotation in relation to the x-y plane. The vertical dashed line represent the rupture point.

C.6 Cluster orientation for test Q100-100

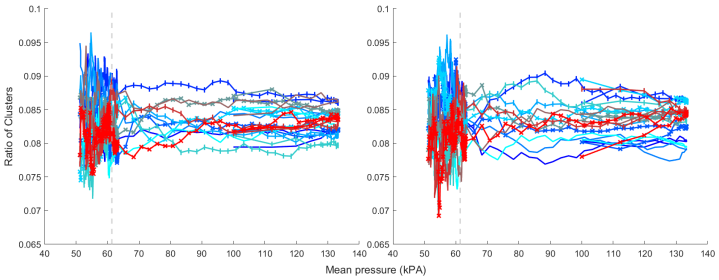

(a) Azimuth angle distribution for submedium clusters

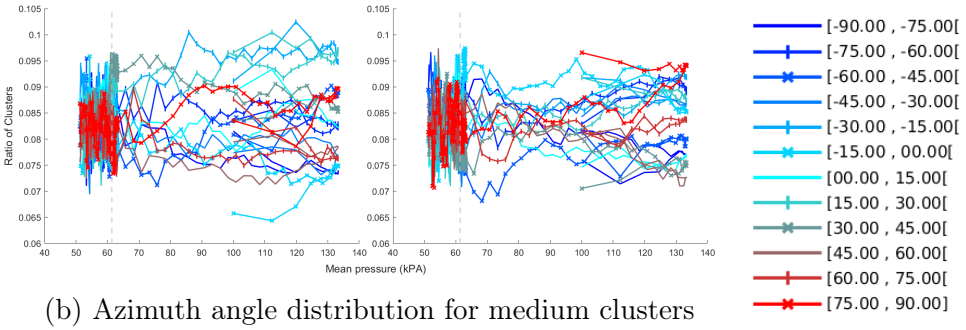

(b) Azimuth angle distribution for medium clusters

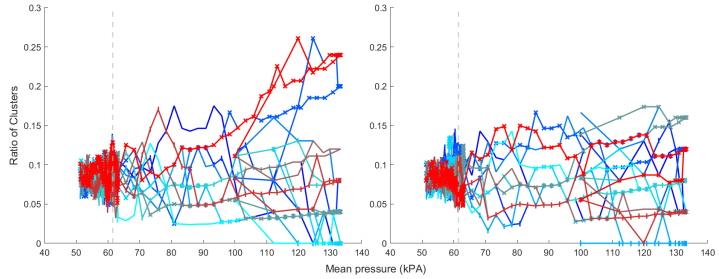

(c) Azimuth angle distribution for large clusters

Figure C.9: Evolution of cluster's azimuth angle distribution for the test Q100-100. Surface tensor results are illustrated on the left and gravity on the right. Figures (a), (b), and (c) represent medium, submedium, and large categories, respectively. Azimuth is the rotation in the x-y plane in relation to the y-positive direction. The vertical dashed line represent the rupture point.

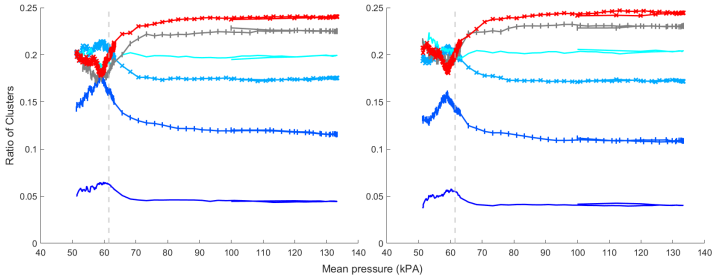

(a) Elevation angle distribution for submedium clusters

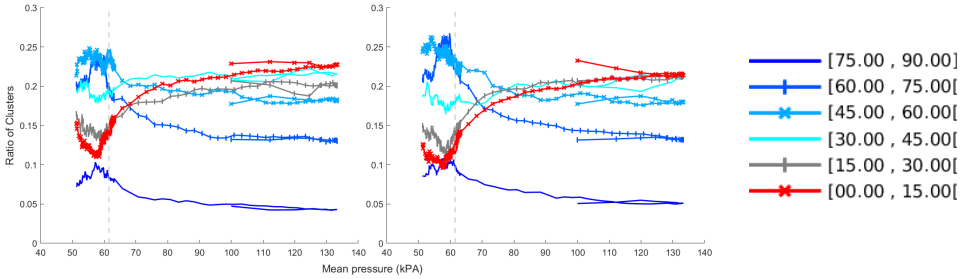

(b) Elevation angle distribution for medium clusters

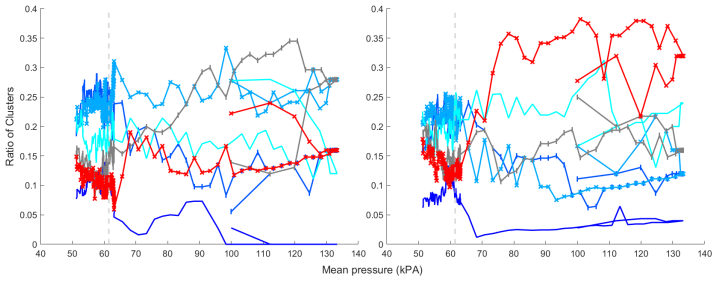

(c) Elevation angle distribution for large clusters

Figure C.10: Evolution of cluster's elevation angle distribution for the test Q100-100. Surface tensor results are illustrated on the left and gravity on the right. Figures (a), (b), and (c) represent medium, submedium, and large categories, respectively. Elevation is the rotation in relation to the x-y plane. The vertical dashed line represent the rupture point.

C.7 Cluster orientation for test Q100-150

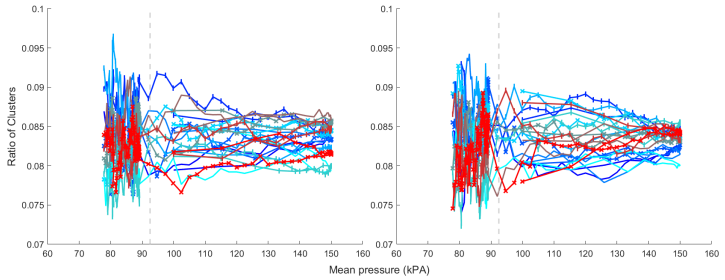

(a) Azimuth angle distribution for submedium clusters

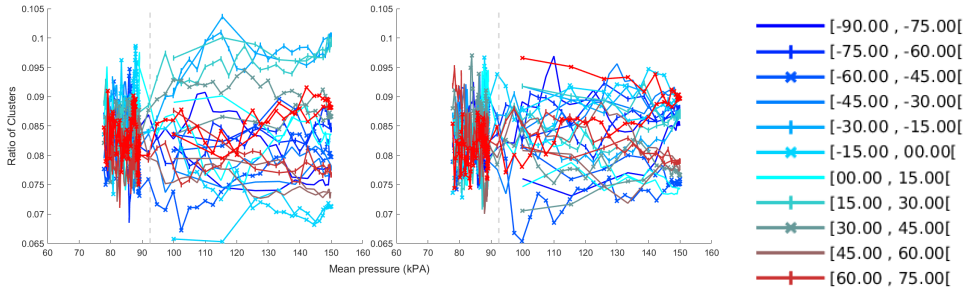

(b) Azimuth angle distribution for medium clusters

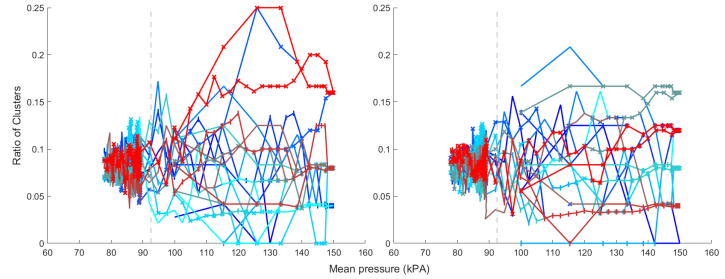

(c) Azimuth angle distribution for large clusters

Figure C.11: Evolution of cluster's azimuth angle distribution for the test Q100-150. Surface tensor results are illustrated on the left and gravity on the right. Figures (a), (b), and (c) represent medium, submedium, and large categories, respectively. Azimuth is the rotation in the x-y plane in relation to the y-positive direction. The vertical dashed line represent the rupture point.

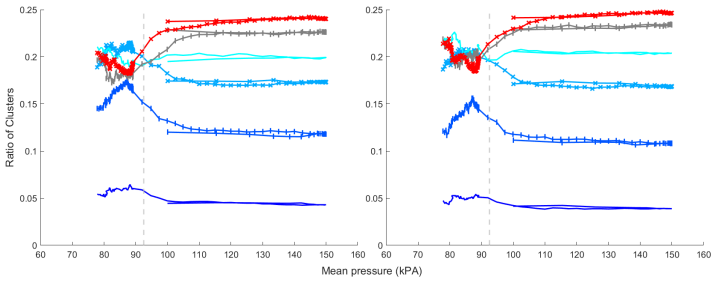

(a) Elevation angle distribution for submedium clusters

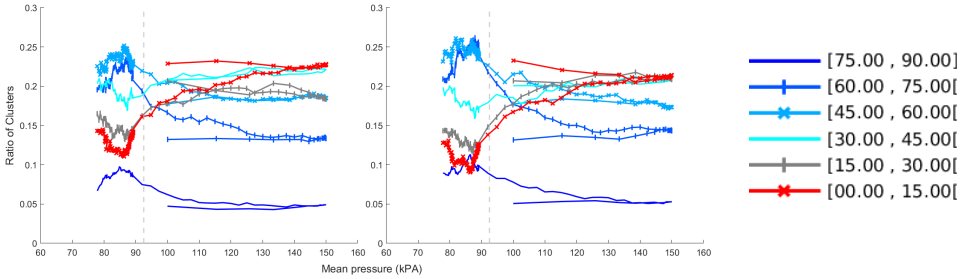

(b) Elevation angle distribution for medium clusters

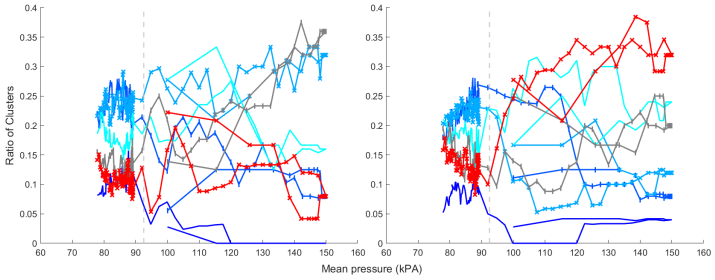

(c) Elevation angle distribution for large clusters

Figure C.12: Evolution of cluster's elevation angle distribution for the test Q100-150. Surface tensor results are illustrated on the left and gravity on the right. Figures (a), (b), and (c) represent medium, submedium, and large categories, respectively. Elevation is the rotation in relation to the x-y plane. The vertical dashed line represent the rupture point.

C.8 Cluster orientation for test Q100-200

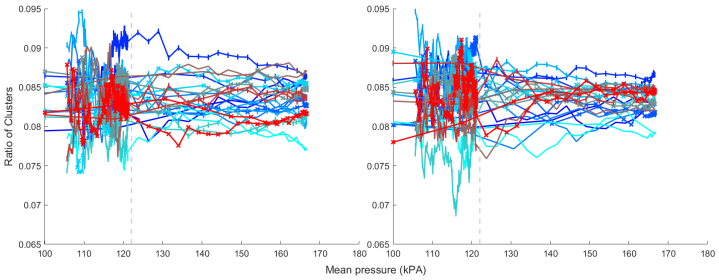

(a) Azimuth angle distribution for submedium clusters

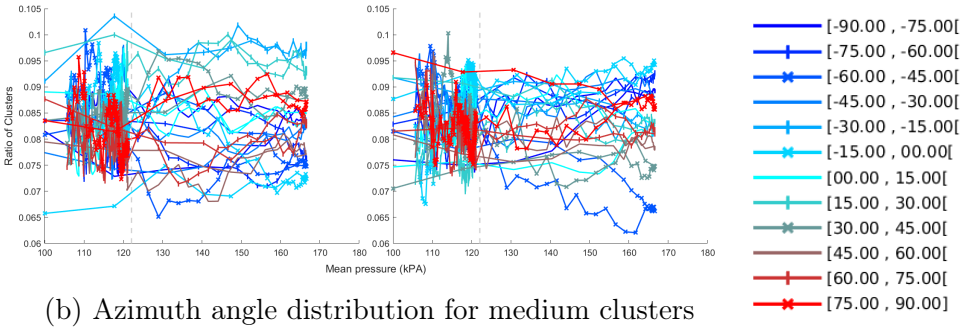

(b) Azimuth angle distribution for medium clusters

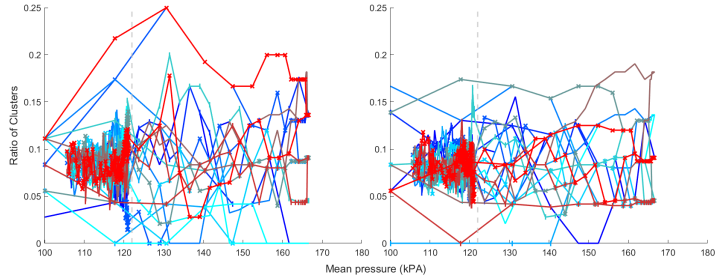

(c) Azimuth angle distribution for large clusters

Figure C.13: Evolution of cluster's azimuth angle distribution for the test Q100-200. Surface tensor results are illustrated on the left and gravity on the right. Figures (a), (b), and (c) represent medium, submedium, and large categories, respectively. Azimuth is the rotation in the x-y plane in relation to the y-positive direction. The vertical dashed line represent the rupture point.

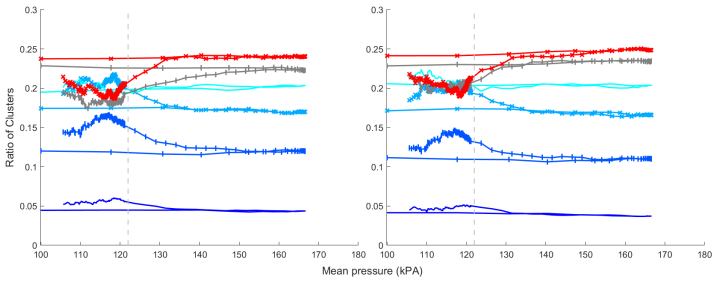

(a) Elevation angle distribution for submedium clusters

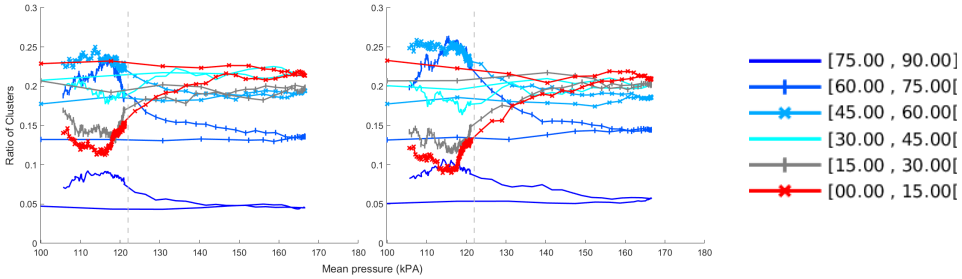

(b) Elevation angle distribution for medium clusters

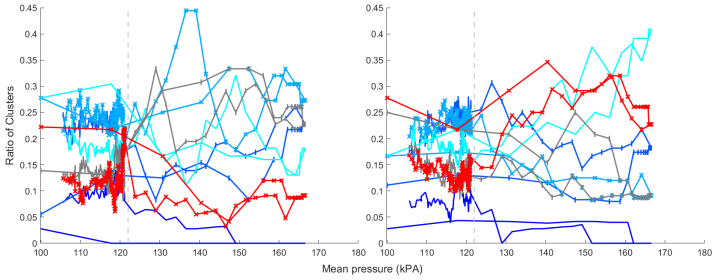

(c) Elevation angle distribution for large clusters

Figure C.14: Evolution of cluster's elevation angle distribution for the test Q100-200. Surface tensor results are illustrated on the left and gravity on the right. Figures (a), (b), and (c) represent medium, submedium, and large categories, respectively. Elevation is the rotation in relation to the x-y plane. The vertical dashed line represent the rupture point.

C.9 Cluster orientation for test Q200-100

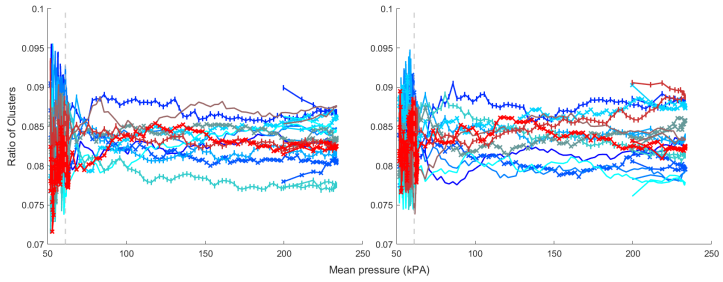

(a) Azimuth angle distribution for submedium clusters

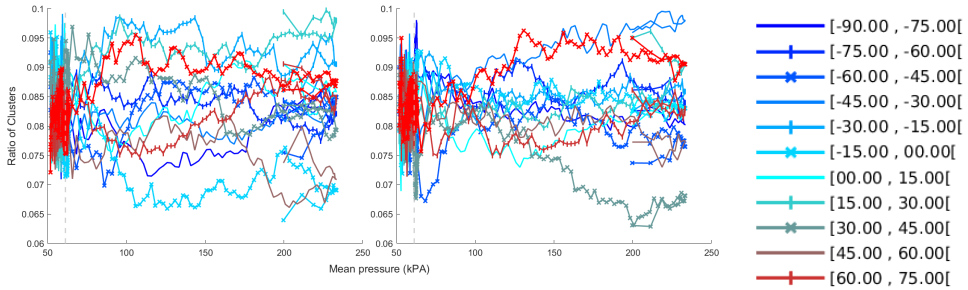

(b) Azimuth angle distribution for medium clusters

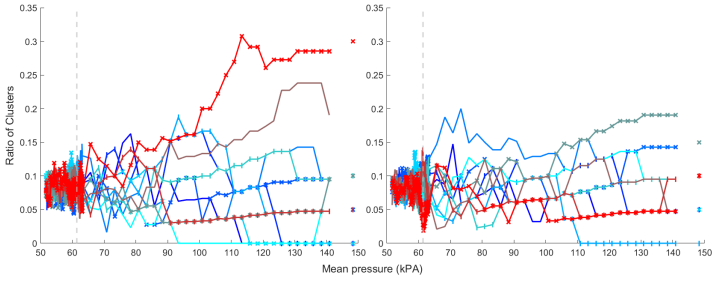

(c) Azimuth angle distribution for large clusters

Figure C.15: Evolution of cluster's azimuth angle distribution for the test Q200-100. Surface tensor results are illustrated on the left and gravity on the right. Figures (a), (b), and (c) represent medium, submedium, and large categories, respectively. Azimuth is the rotation in the x-y plane in relation to the y-positive direction. The vertical dashed line represent the rupture point.

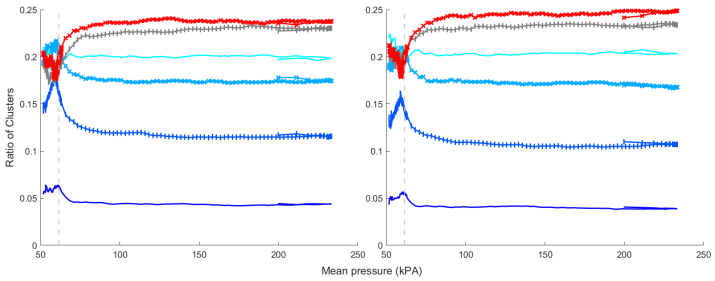

(a) Elevation angle distribution for submedium clusters

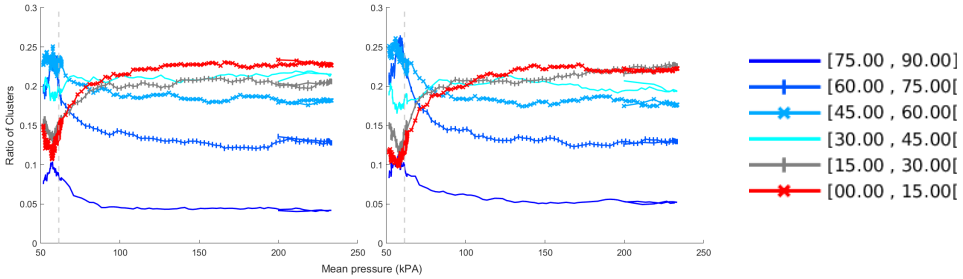

(b) Elevation angle distribution for medium clusters

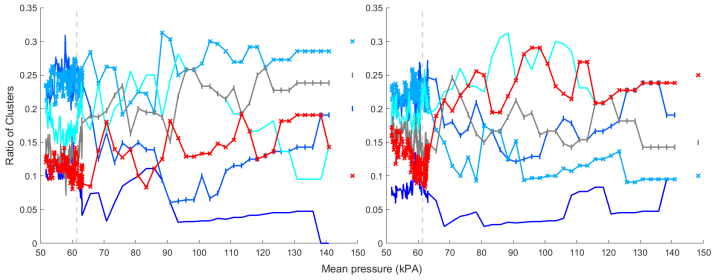

(c) Elevation angle distribution for large clusters

Figure C.16: Evolution of cluster's elevation angle distribution for the test Q200-100. Surface tensor results are illustrated on the left and gravity on the right. Figures (a), (b), and (c) represent medium, submedium, and large categories, respectively. Elevation is the rotation in relation to the x-y plane. The vertical dashed line represent the rupture point..

C.10 Cluster orientation for test U50

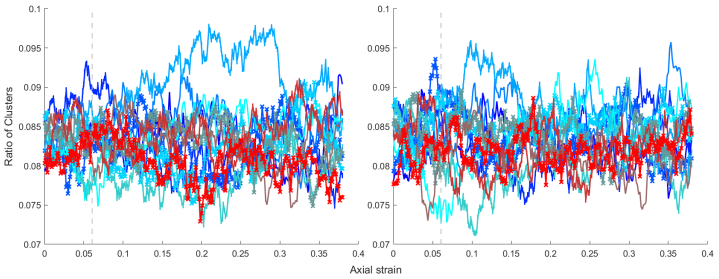

(a) Azimuth angle distribution for submedium clusters

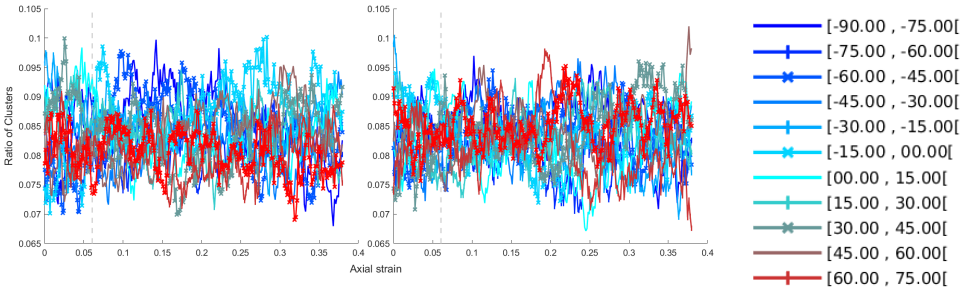

(b) Azimuth angle distribution for medium clusters

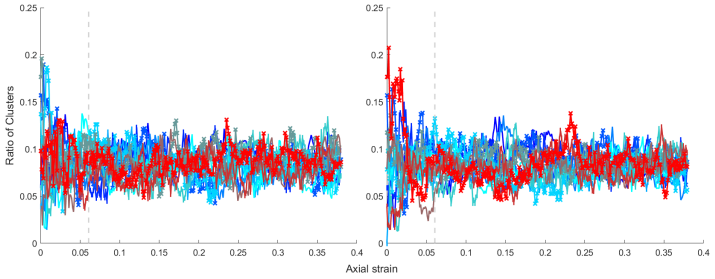

(c) Azimuth angle distribution for large clusters

Figure C.17: Evolution of cluster's azimuth angle distribution for the test U50. Surface tensor results are illustrated on the left and gravity on the right. Figures (a), (b), and (c) represent medium, submedium, and large categories, respectively. Azimuth is the rotation in the x-y plane in relation to the y-positive direction. The vertical dashed line represent the peak relative strenght.

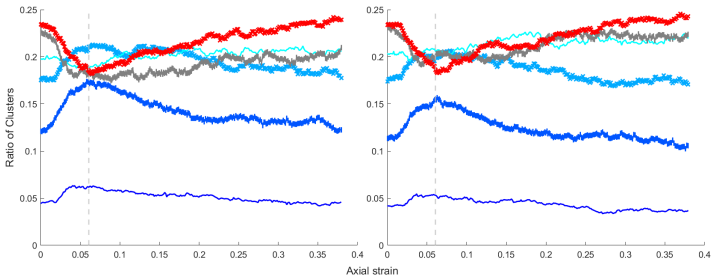

(a) Elevation angle distribution for submedium clusters

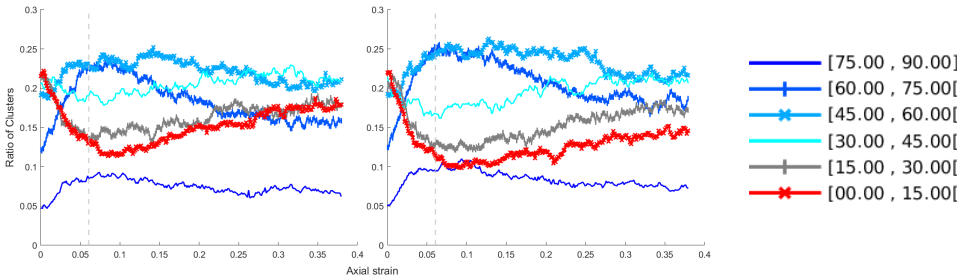

(b) Elevation angle distribution for medium clusters

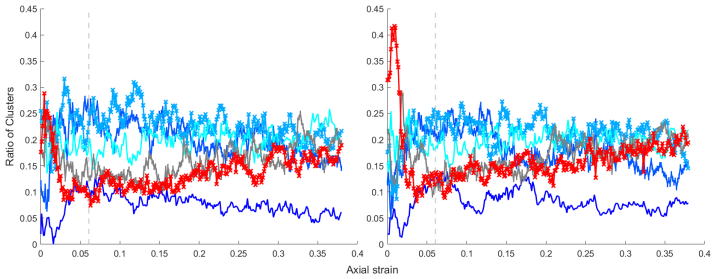

(c) Elevation angle distribution for large clusters

Figure C.18: Evolution of cluster's elevation angle distribution for the test U50. Surface tensor results are illustrated on the left and gravity on the right. Figures (a), (b), and (c) represent medium, submedium, and large categories, respectively. Elevation is the rotation in relation to the x-y plane. The vertical dashed line represent the peak relative strenght.

C.11 Cluster orientation for test U100

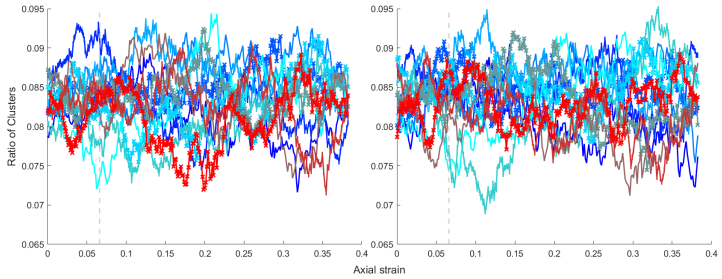

(a) Azimuth angle distribution for submedium clusters

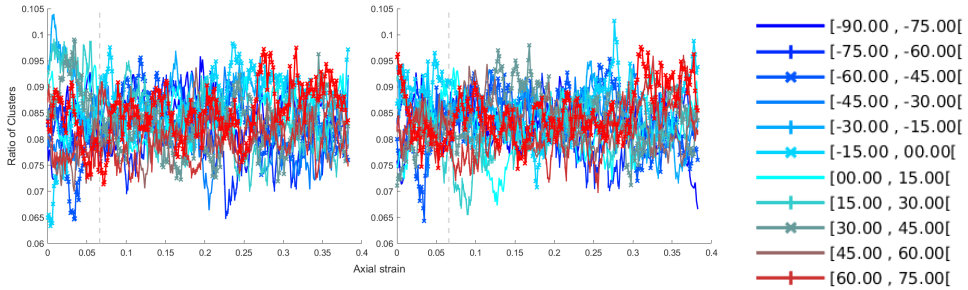

(b) Azimuth angle distribution for medium clusters

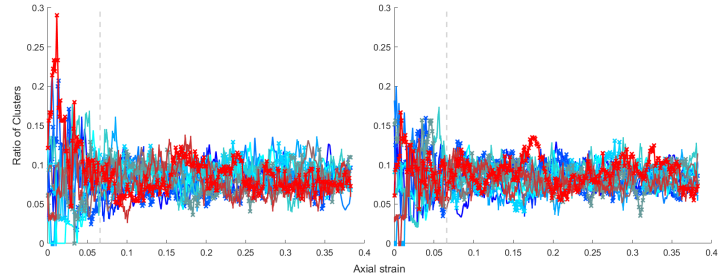

(c) Azimuth angle distribution for large clusters

Figure C.19: Evolution of cluster's azimuth angle distribution for the test U100. Surface tensor results are illustrated on the left and gravity on the right. Figures (a), (b), and (c) represent medium, submedium, and large categories, respectively. Azimuth is the rotation in the x-y plane in relation to the y-positive direction. The vertical dashed line represent the peak relative strenght.

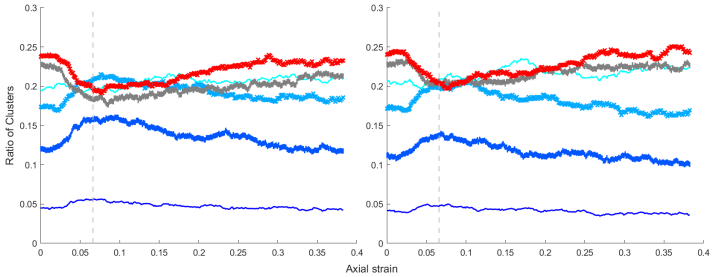

(a) Elevation angle distribution for submedium clusters

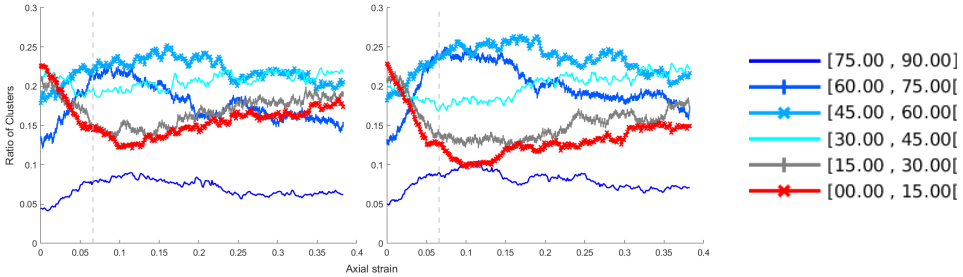

(b) Elevation angle distribution for medium clusters

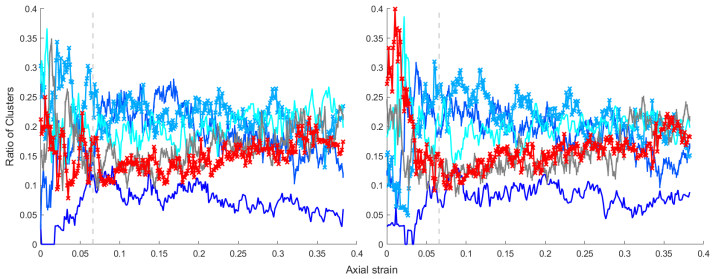

(c) Elevation angle distribution for large clusters

Figure C.20: Evolution of cluster's elevation angle distribution for the test U100. Surface tensor results are illustrated on the left and gravity on the right. Figures (a), (b), and (c) represent medium, submedium, and large categories, respectively. Elevation is the rotation in relation to the x-y plane. The vertical dashed line represent the peak relative strenght.

C.12 Cluster orientation for test U200

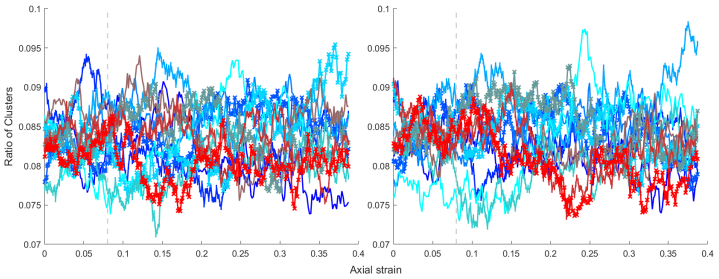

(a) Azimuth angle distribution for submedium clusters

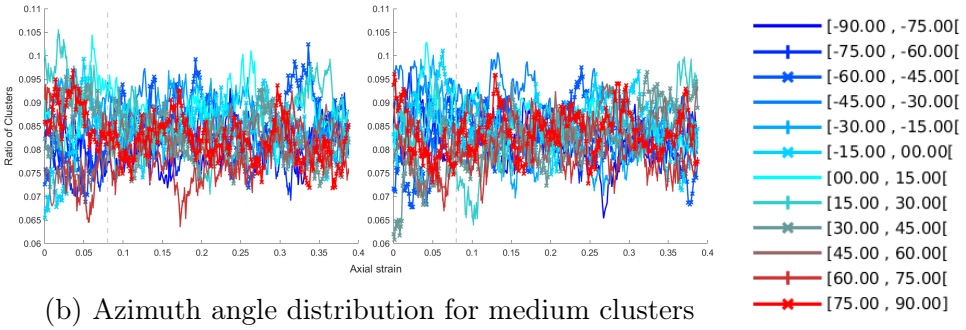

(b) Azimuth angle distribution for medium clusters

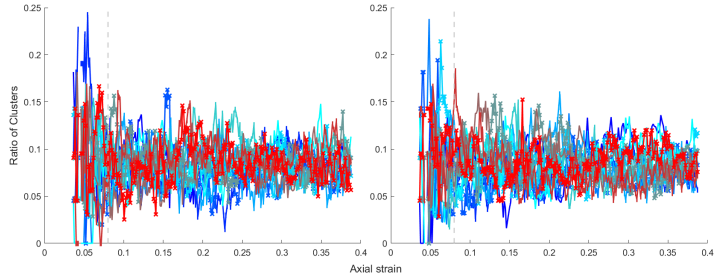

(c) Azimuth angle distribution for large clusters

Figure C.21: Evolution of cluster's azimuth angle distribution for the test U200. Surface tensor results are illustrated on the left and gravity on the right. Figures (a), (b), and (c) represent medium, submedium, and large categories, respectively. Azimuth is the rotation in the x-y plane in relation to the y-positive direction. The vertical dashed line represent the peak relative strenght.

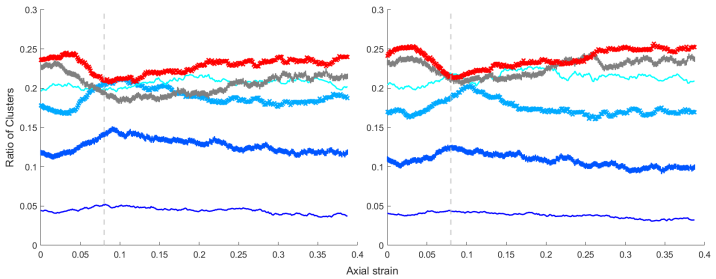

(a) Elevation angle distribution for submedium clusters

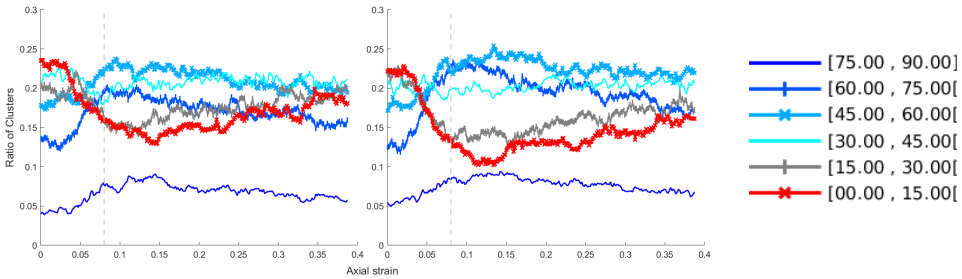

(b) Elevation angle distribution for medium clusters

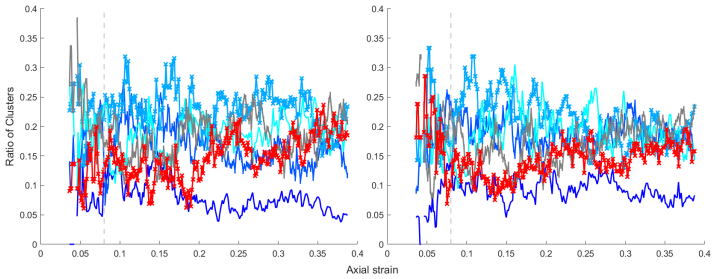

(c) Elevation angle distribution for large clusters

Figure C.22: Evolution of cluster's elevation angle distribution for the test U200. Surface tensor results are illustrated on the left and gravity on the right. Figures (a), (b), and (c) represent medium, submedium, and large categories, respectively. Elevation is the rotation in relation to the x-y plane. The vertical dashed line represent the peak relative strenght.

Appendix D

Cluster vs Force chains images of remaining tests

D.1 Forword

This appendix contains the results relating clusters and force chains for the remaining specimens. The procedures used to obtain the following results are presented in section 5.4.1.

D.2 Cluster and force chain test D28

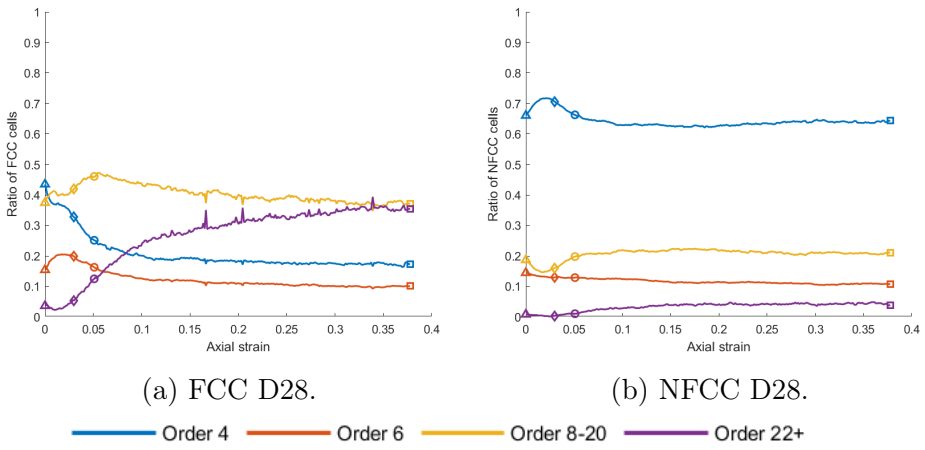

(a) FCC D28. (b) NFCC D28.

Figure D.1: Distribution of the ratio of cells between force chain clusters (FCC) and non-force chain clusters (NFCC) for test D28.

D.3 Cluster and force chain test Q50-100

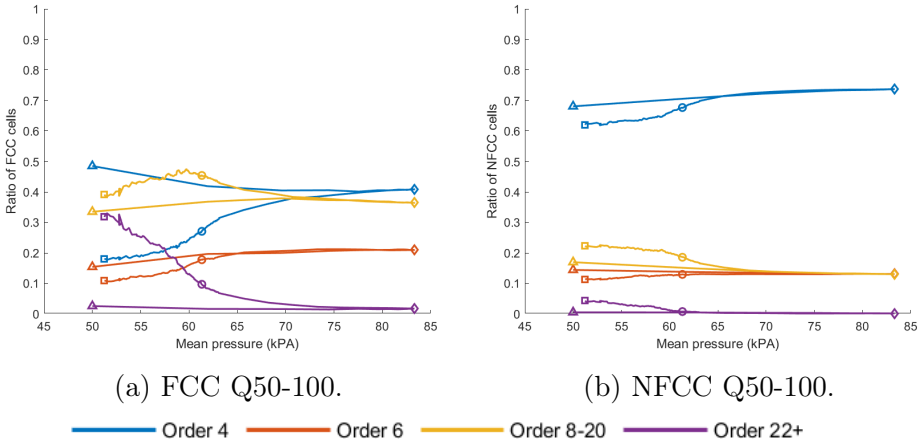

(a) FCC Q50-100. (b) NFCC Q50-100.

Figure D.2: Distribution of the ratio of cells between force chain clusters (FCC) and non-force chain clusters (NFCC) for test Q50-100.

D.4 Cluster and force chain test Q100-100

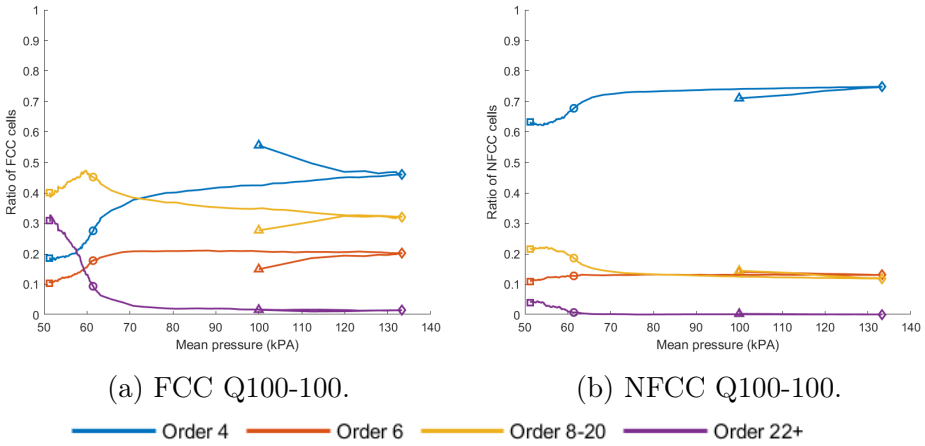

(a) FCC Q100-100. (b) NFCC Q100-100.

Figure D.3: Distribution of the ratio of cells between force chain clusters (FCC) and non-force chain clusters (NFCC) for test Q100-100.

D.5 Cluster and force chain test Q100-150

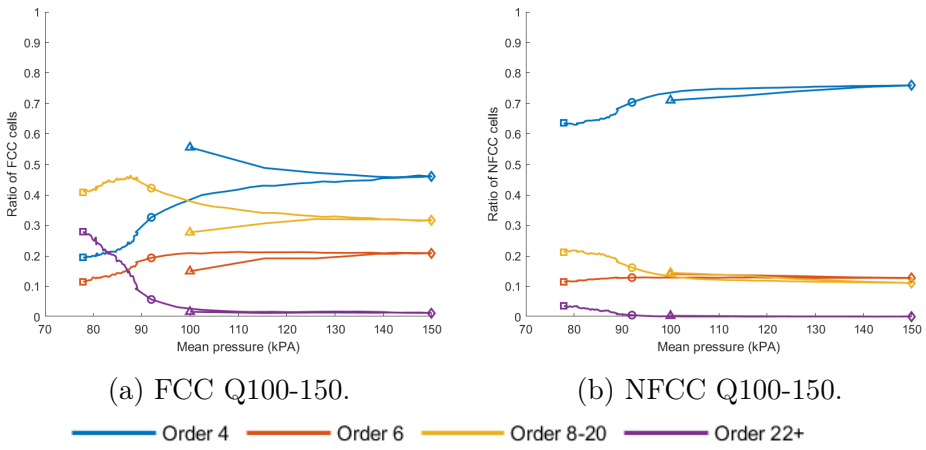

(a) FCC Q100-150. (b) NFCC Q100-150.

Figure D.4: Distribution of the ratio of cells between force chain clusters (FCC) and non-force chain clusters (NFCC) for test Q100-150.

D.6 Cluster and force chain test Q100-200

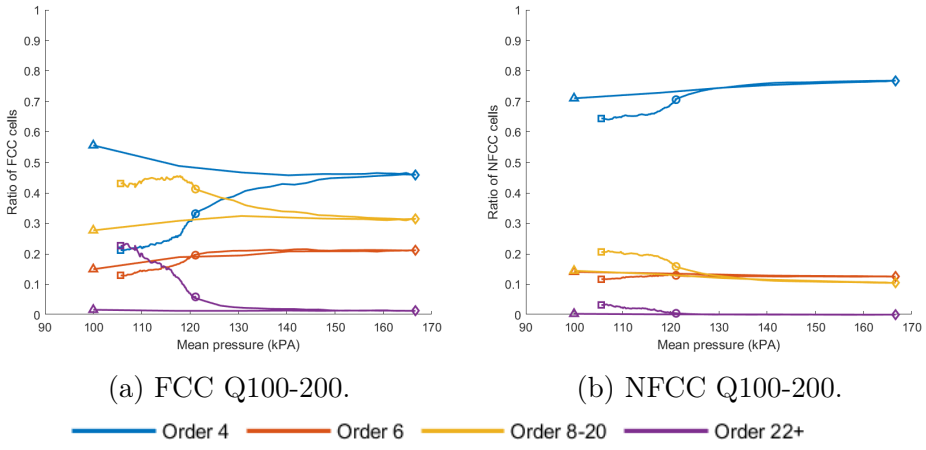

(a) FCC Q100-200. (b) NFCC Q100-200.

Figure D.5: Distribution of the ratio of cells between force chain clusters (FCC) and non-force chain clusters (NFCC) for test Q100-200.

D.7 Cluster and force chain test Q200-100

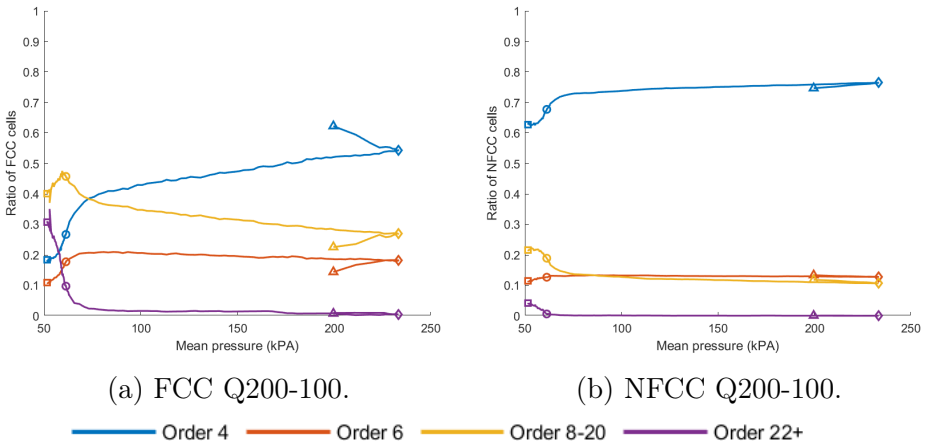

(a) FCC Q200-100. (b) NFCC Q200-100.

Figure D.6: Distribution of the ratio of cells between force chain clusters (FCC) and non-force chain clusters (NFCC) for test Q200-100.

D.8 Cluster and force chain test U50

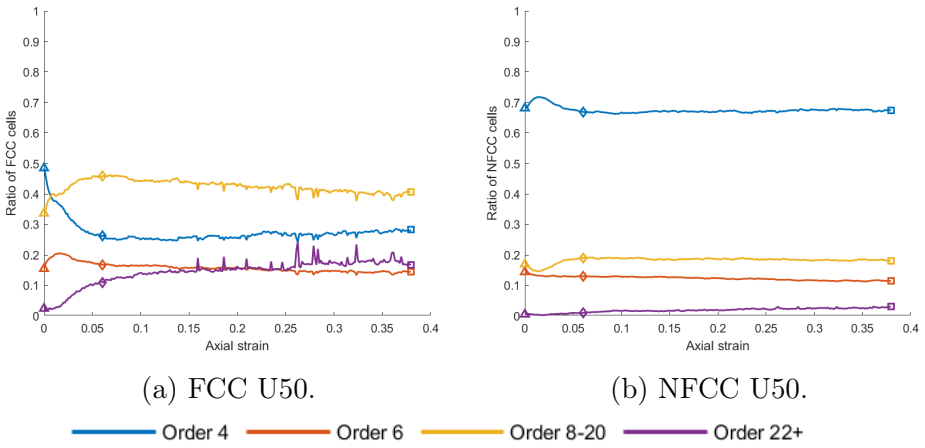

(a) FCC U50. (b) NFCC U50.

Figure D.7: Distribution of the ratio of cells between force chain clusters (FCC) and non-force chain clusters (NFCC) for test U50.

D.9 Cluster and force chain test U100

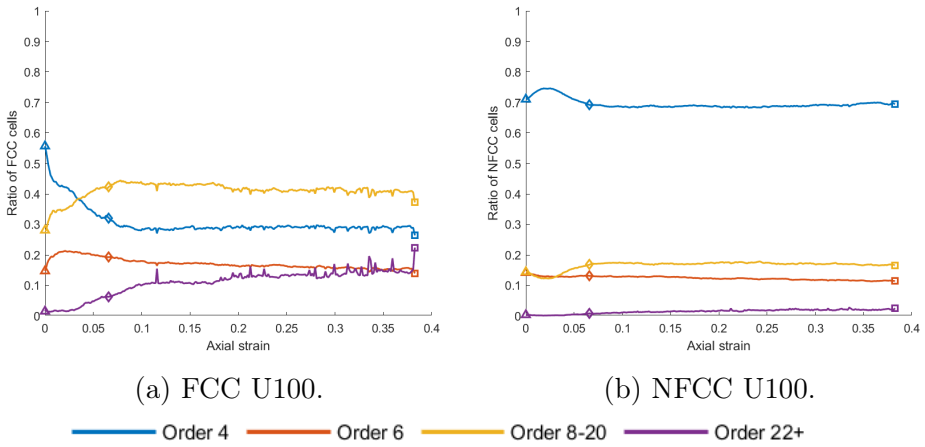

(a) FCC U100. (b) NFCC U100.

Figure D.8: Distribution of the ratio of cells between force chain clusters (FCC) and non-force chain clusters (NFCC) for test U100.

D.10 Cluster and force chain test U200

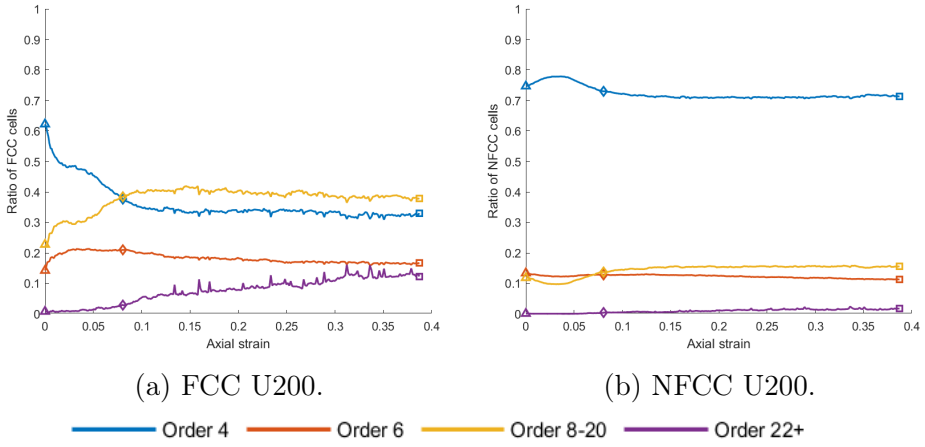

(a) FCC U200. (b) NFCC U200.

Figure D.9: Distribution of the ratio of cells between force chain clusters (FCC) and non-force chain clusters (NFCC) for test U200.

Appendix E

Cluster vs Shear bands images of remaining tests

E.1 Forword

This appendix contain the images relating Shear bands and Clusters for the tests that were not presented in section 5.4.2. The first two column shows the identification of the shear band through two methods (cumulative deviatoric strain and negative second-order work respectively), while the third represents the location of sizable clusters.

E.2 D28

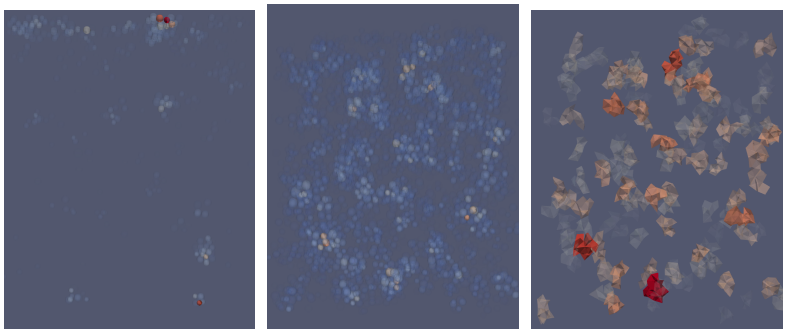

(a) Shear band identification at $\varepsilon_z = 0.051$.

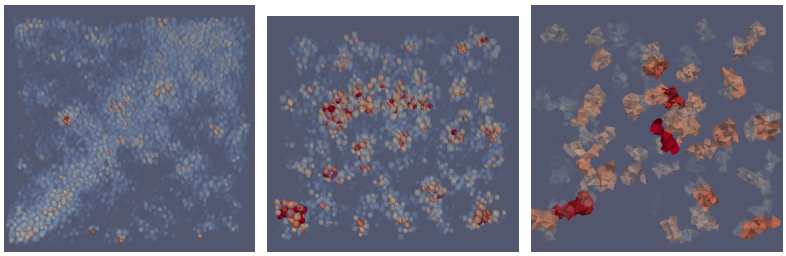

(b) Shear band identification at $\varepsilon_z = 0.177$.

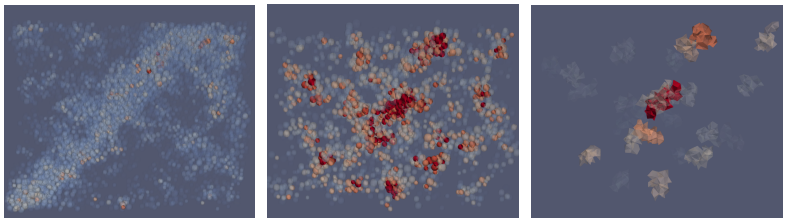

(c) Shear band identification at $\varepsilon_z = 0.291$.

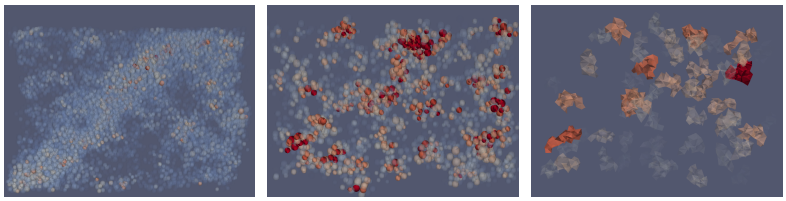

(d) Shear band identification at $\varepsilon_z = 0.373$.

Figure E.1: Comparison between Cluster and Shear band locations for the test D28. Figures (a), (b), (c) illustrates axial strains 0.177, 0.291 and 0.373, respectively. The first column illustrate the the shear band (cumulative deviatoric strain method), the second column is grain's average cluster order, while the third represents the distribution of sizable clusters.

E.3 D50

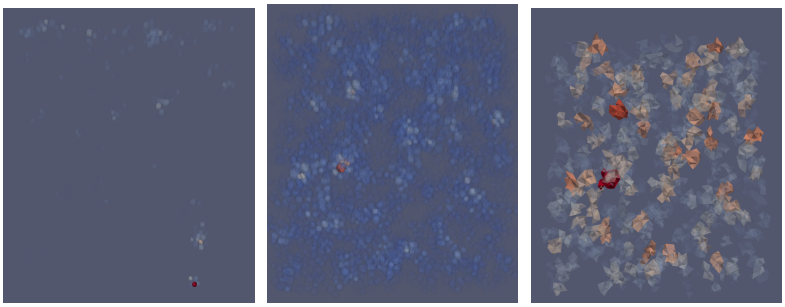

(a) Shear band identification at $\varepsilon_z = 0.066$.

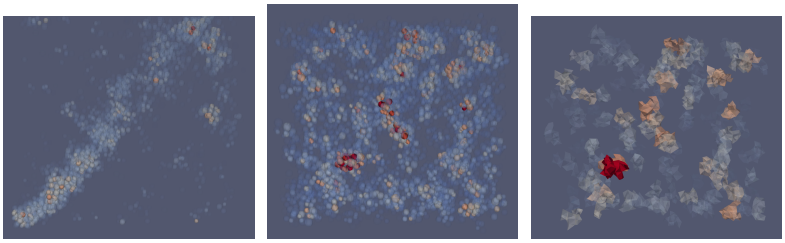

(b) Shear band identification at $\varepsilon_z = 0.173$.

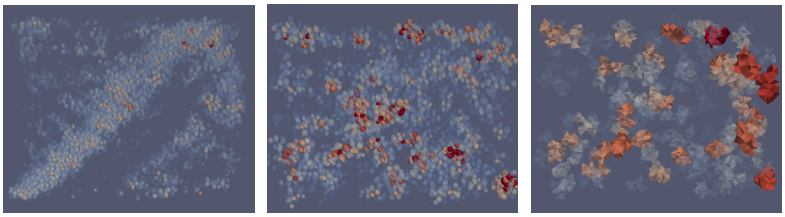

(c) Shear band identification at $\varepsilon_z = 0.292$.

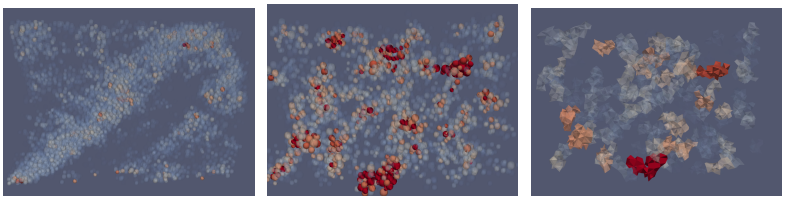

(d) Shear band identification at $\varepsilon_z = 0.378$.

Figure E.2: Comparison between Cluster and Shear band locations for the test D50. Figures (a), (b), (c), (d) illustrates axial strains 0.066, 0.173, 0.292, and 0.378, respectively. The first column illustrate the the shear band (cumulative deviatoric strain method), the second column is grain's average cluster order, while the third represents the distribution of sizable clusters.

E.4 D200

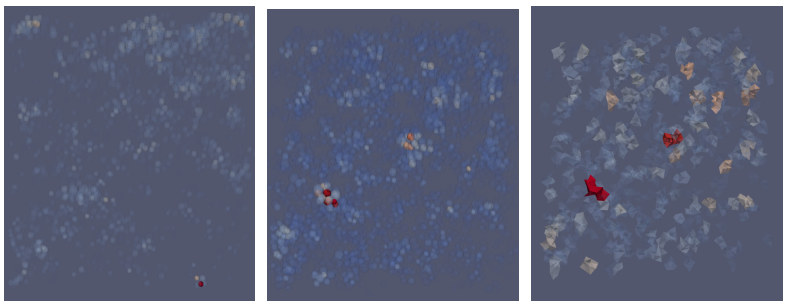

(a) Shear band identification at $\varepsilon_z = 0.121$.

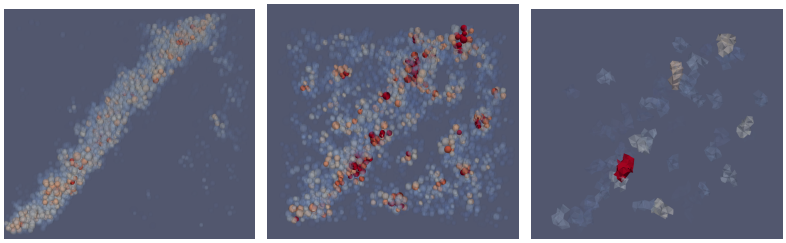

(b) Shear band identification at $\varepsilon_z = 0.224$.

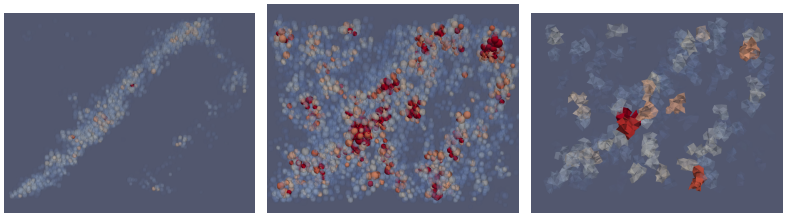

(c) Shear band identification at $\varepsilon_z = 0.298$.

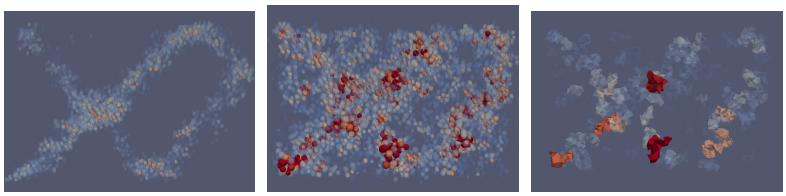

(d) Shear band identification at $\varepsilon_z = 0.386$.

Figure E.3: Comparison between Cluster and Shear band locations for the test D200. Figures (a), (b), (c), (d) illustrates axial strains 0.121, 0.224, 0.298, and 0.386, respectively. The first column illustrate the the shear band (cumulative deviatoric strain method), the second column is grain's average cluster order, while the third represents the distribution of sizable clusters.

E.5 Q50-100

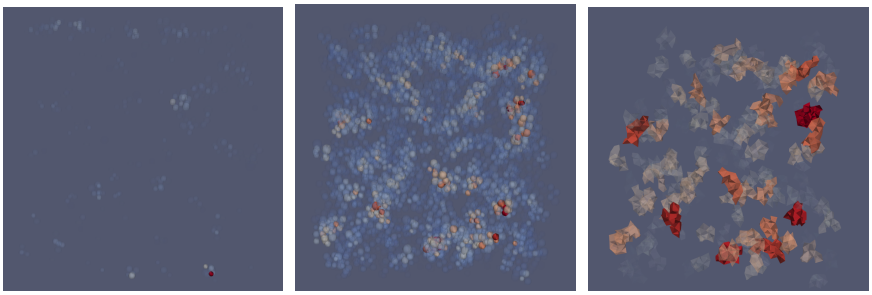

(a) Shear band identification at $p = 87.23kPa$.

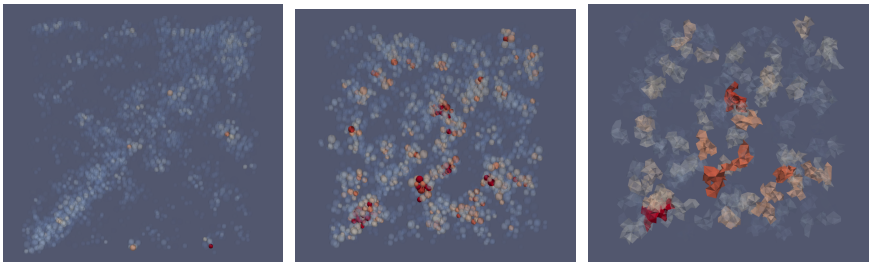

(b) Shear band identification at $p = 74.74kPa$.

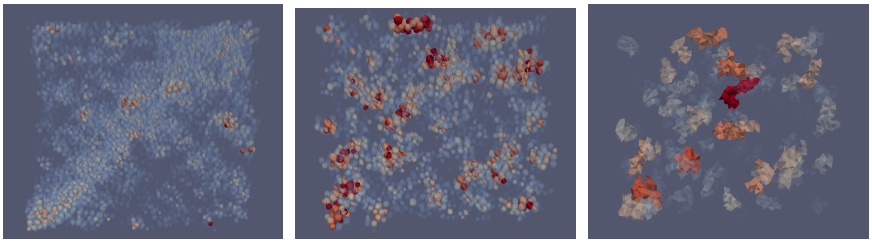

(c) Shear band identification at $p = 64.87kPa$.

Figure E.4: Comparison between Cluster and Shear band locations for the test Q50-100. Figures (a), (b), (c) illustrates mean pressure 87.23kPa, 74.74kPa, and 64.87kPa, respectively. The first column illustrate the the shear band (cumulative deviatoric strain method), the second column is grain's average cluster order, while the third represents the distribution of sizable clusters.

E.6 Q100-150

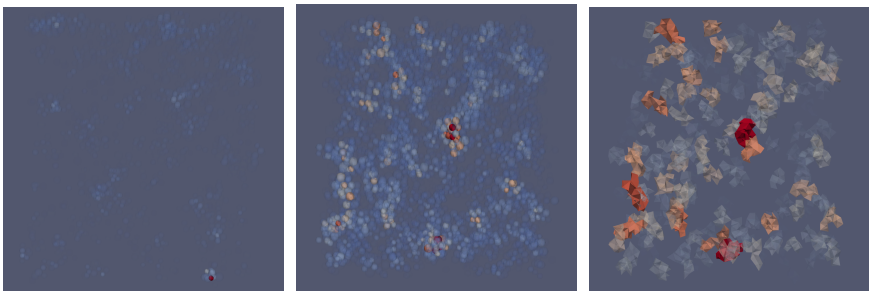

(a) Shear band identification at $p = 139.82kPa$.

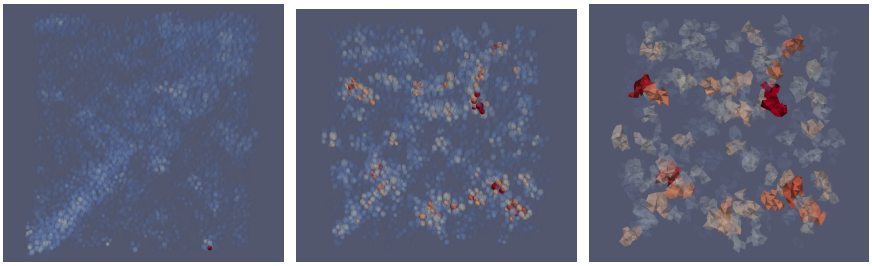

(b) Shear band identification at $p = 124.03kPa$.

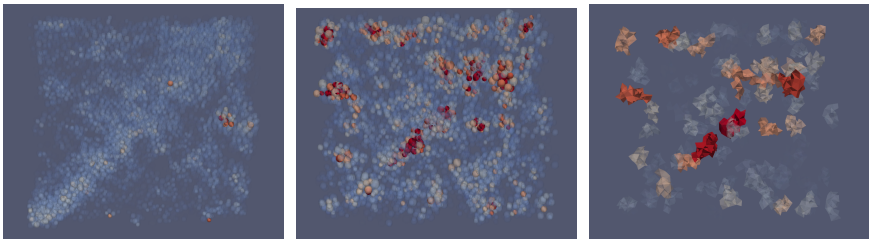

(c) Shear band identification at $p = 101.31kPa$.

Figure E.5: Comparison between Cluster and Shear band locations for the test Q100-150. Figures (a), (b), (c) illustrates mean pressure 139.82kPa, 124.03kPa, and 101.31kPa, respectively. The first column illustrate the the shear band (cumulative deviatoric strain method), the second column is grain's average cluster order, while the third represents the distribution of sizable clusters.

E.7 Q100-200

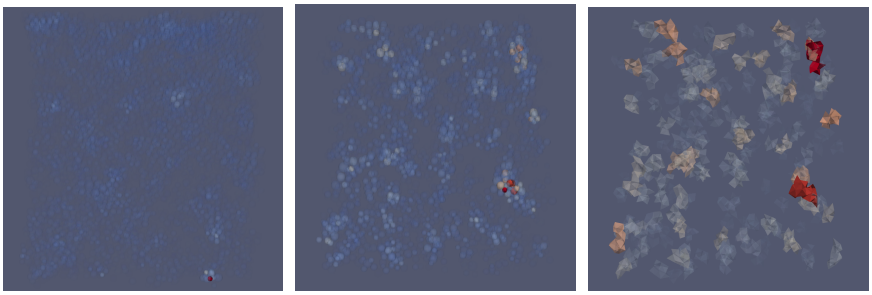

(a) Shear band identification at $p = 192.97kPa$.

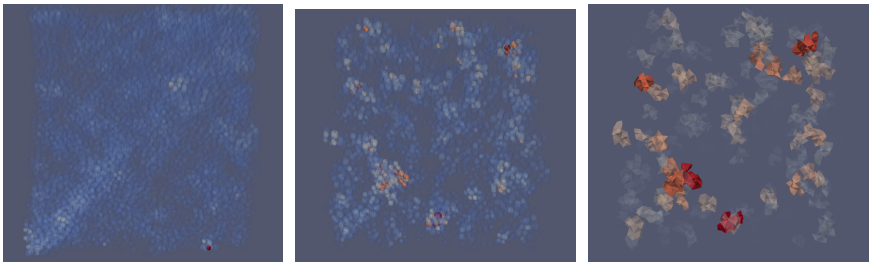

(b) Shear band identification at $p = 177.94kPa$.

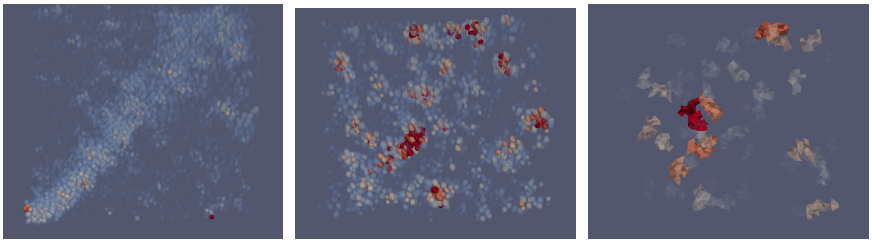

(c) Shear band identification at $p = 139.61kPa$.

Figure E.6: Comparison between Cluster and Shear band locations for the test Q100-150. Figures (a), (b), (c) illustrates mean pressure 192.97kPa, 177.94kPa, and 139.61kPa, respectively. The first column illustrate the the shear band (cumulative deviatoric strain method), the second column is grain's average cluster order, while the third represents the distribution of sizable clusters.

E.8 Q200-100

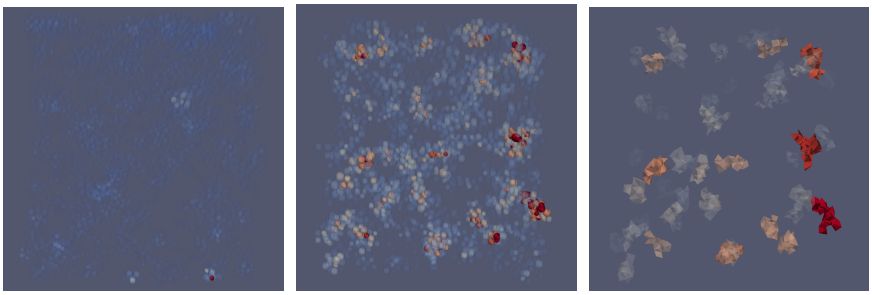

(a) Shear band identification at $p = 90.51kPa$.

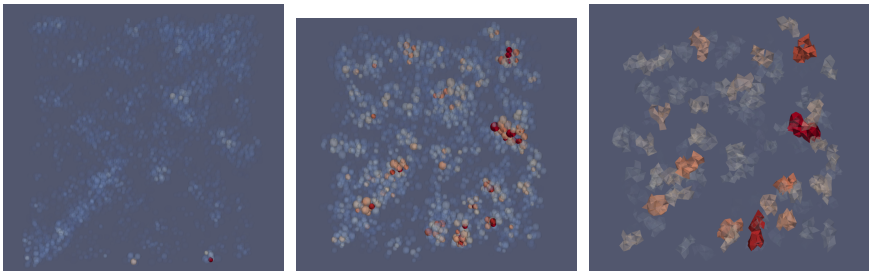

(b) Shear band identification at $p = 81.50kPa$.

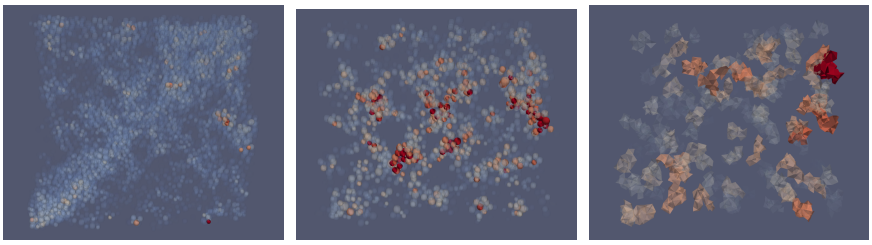

(c) Shear band identification at $p = 66.29kPa$.

Figure E.7: Comparison between Cluster and Shear band locations for the test Q200-100. Figures (a), (b), (c) illustrates mean pressure 90.51kPa, 81.50kPa, and 66.29kPa, respectively. The first column illustrate the the shear band (cumulative deviatoric strain method), the second column is grain's average cluster order, while the third represents the distribution of sizable clusters.

E.9 U50

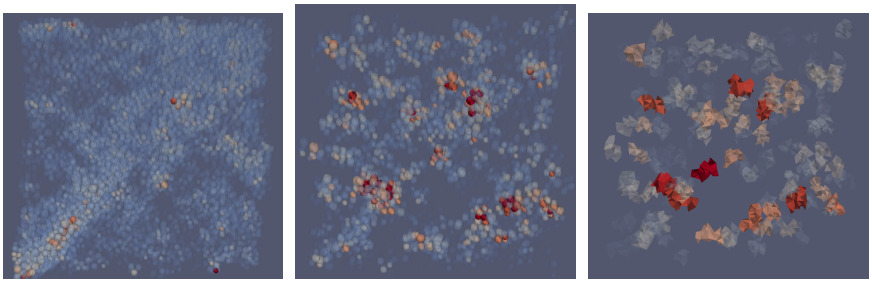

(a) Shear band identification at $\varepsilon_z = 0.146$.

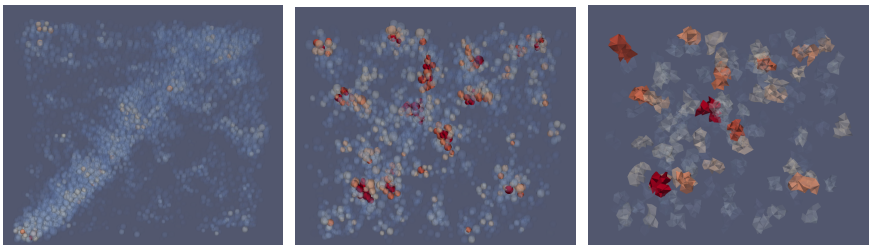

(b) Shear band identification at $\varepsilon_z = 0.255$.

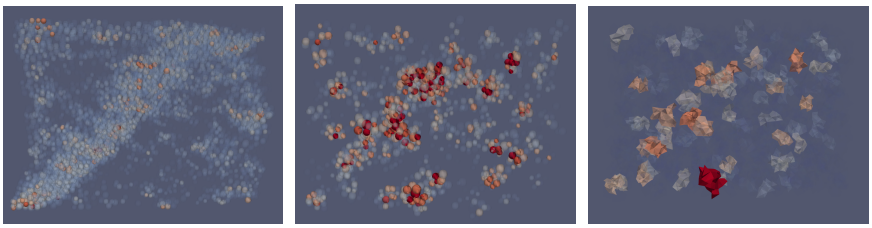

(c) Shear band identification at $\varepsilon_z = 0.378$.

Figure E.8: Comparison between Cluster and Shear band locations for the test U50. Figures (a), (b), (c) illustrates axial strain 0.146, 0.255, and 0.378, respectively. The first column illustrate the the shear band (cumulative deviatoric strain method), the second column is grain's average cluster order, while the third represents the distribution of sizable clusters.

E.10 U200

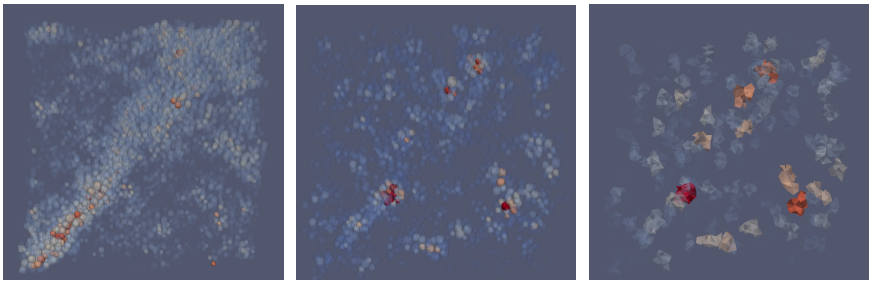

(a) Shear band identification at $\varepsilon_z = 0.154$.

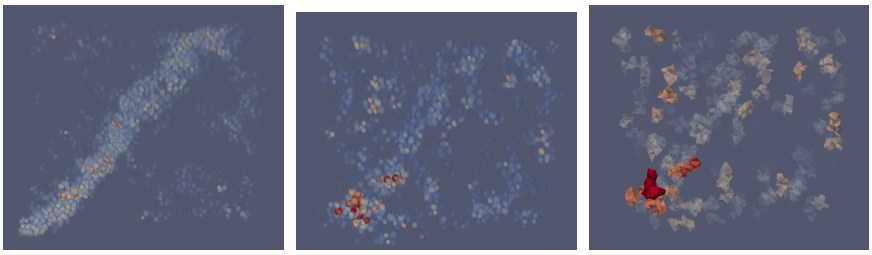

(b) Shear band identification at $\varepsilon_z = 0.260$.

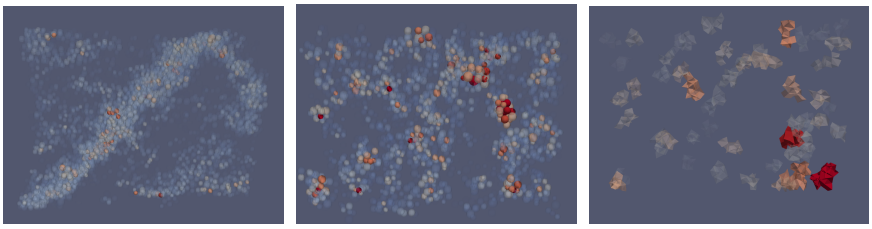

(c) Shear band identification at $\varepsilon_z = 0.388$.

Figure E.9: Comparison between Cluster and Shear band locations for the test U200. Figures (a), (b), (c) illustrates axial strain 0.154, 0.260, and 0.388, respectively. The first column illustrate the the shear band (cumulative deviatoric strain method), the second column is grain's average cluster order, while the third represents the distribution of sizable clusters.

Appendix F

Bibliography

[1] Katalin Bagi. Analysis of microstructural strain tensors for granular assemblies. *International Journal of Solids and Structures*, 43(10):3166–3184, May 2006. Cited in pages 1, 10

[2] A. Tordesillas. Force chain buckling, unjamming transitions and shear banding in dense granular assemblies. *Philosophical Magazine*, 87(32):4987–5016, November 2007. Cited in pages 1, 14, 34, 54

[3] François Nicot and Félix Darve. The H-microdirectional model: Accounting for a mesoscopic scale. *Mechanics of Materials*, 43(12):918–929, December 2011. Cited in pages 2, 16

[4] Ngoc-Son Nguyen, Hélène Magoariec, Eric Vincens, and Bernard Cambou. On the definition of a relevant meso-scale for upscaling the mechanical behavior of 3D granular materials. *Granular Matter*, February 2020. SPRINGER. Cited in pages 2, 25, 26, 117

[5] Islam Tahsina. Effect of Fine Content on Shear Strength Behavior of Sandy Soil. Technical report, Bangladesh University of Engeneering and Technolygy, 2017. Cited in pages XI, 5

[6] Matthew R. Kuhn. Structured deformation in granular materials. *Mechanics of Materials*, 31(6):407–429, June 1999. Cited in page 5

[7] Gang Ma, Richard A. Regueiro, Wei Zhou, and Jiaying Liu. Spatiotemporal analysis of strain localization in dense granular materials. *Acta Geotechnica*, 14(4):973–990, August 2019. Cited in pages 5, 6, 7

[8] Félix Darve, Francois Nicot, Antoine Wautier, and Jiaying Liu. Slip lines versus shear bands: Two competing localization modes. *Mechanics Research Communications*, page 103603, October 2020. Cited in pages 5, 6

[9] A. Daouadji, F. Darve, H. Al Gali, P. Y. Hicher, F. Laouafa, S. Lignon, F. Nicot, R. Nova, M. Pinheiro, F. Prunier, L. Sibille, and R. Wan. Diffuse failure in geomaterials: Experiments, theory and modelling: DIFFUSE FAILURE IN GEOMATERIALS. *International Journal for Numerical and Analytical Methods in Geomechanics*, 35(16):1731–1773, November 2011. Cited in page 5

[10] Waiching Sun. Final Report: Cryo-mechanics of unsaturated frozen soils during freeze-thaw cycles. Technical report, Columbia University, 2018. Publisher: 20765. Cited in pages XI, 5

[11] P. W. Rowe. The Relation Between the Shear Strength of Sands in Triaxial Compression, Plane Strain and Direct. *Géotechnique*, 19(1):75–86, 1969. Cited in page 6

[12] Hajime Matsuoka. Stress-Strain Relationships of Sands Based on the Mobilized Plane. *Soils and Foundations*, 14(2):47–61, June 1974. Cited in page 6

[13] S. Nemat-Nasser. On Behavior of Granular Materials in Simple Shear. *Soils and Foundations*, 20(3):59–73, September 1980. Cited in page 6

[14] H. B. Mühlhaus and I. Vardoulakis. The thickness of shear bands in granular materials. *Géotechnique*, 37(3):271–283, September 1987. Cited in page 6

[15] M. Oda, K. Iwashita, and H. Kazama. Micro-Structure Developed in Shear Bands of Dense Granular Soils and its Computer Simulation — Mechanism of Dilatancy and Failure—. In N. A. Fleck and A. C. F. Cocks, editors, *IUTAM Symposium on Mechanics of Granular and Porous Materials*, pages 353–364, Dordrecht, 1997. Springer Netherlands. Cited in page 6

[16] M Oda, H Kazama, and J Konishi. Effects of induced anisotropy on the development of shear bands in granular materials. *Mechanics of Materials*, 28(1-4):103–111, July 1998. Cited in pages 6, 7

[17] Masao Satake. Finite difference approach to the shear band formation. In *Thirteenth Southeast Asian Geotechnical Conference*, page 4, November 1998. Cited in page 6

[18] Matthew R. Kuhn. Are granular materials simple? An experimental study of strain gradient effects and localization. *Mechanics of Materials*, 37(5):607–627, May 2005. arXiv:1901.07339 [cond-mat]. Cited in page 6

[19] Xiaoqiang Gu, Maosong Huang, and Jiangu Qian. Discrete element modeling of shear band in granular materials. *Theoretical and Applied Fracture Mechanics*, 72:37–49, August 2014. Cited in pages 6, 7

[20] Huaxiang Zhu, François Nicot, and Félix Darve. Meso-structure organization in two-dimensional granular materials along biaxial loading path. *International Journal of Solids and Structures*, 96:25–37, October 2016. Cited in pages 6, 15, 16, 30, 100

[21] Shuo Zhou, Antoinette Tordesillas, Mehdi Pouragha, James Bailey, and Howard Bondell. On local intrinsic dimensionality of deformation in complex materials. *Scientific Reports*, 11(1):10216, December 2021. Cited in page 6

[22] Khalid A. Alshibli, Susan N. Batiste, and Stein Sture. Strain Localization in Sand: Plane Strain versus Triaxial Compression. *Journal of Geotechnical and Geoenvironmental Engineering*, 129(6):483–494, June 2003. Cited in page 6

[23] J. Chu, S.-C. R. Lo, and I. K. Lee. Strain softening and shear band formation of sand in multi-axial testing. *Géotechnique*, 46(1):63–82, 1996. _eprint: https://doi.org/10.1680/geot.1996.46.1.63. Cited in page 6

[24] Abouzar Sadrekarimi and Scott M. Olson. Shear Band Formation Observed in Ring Shear Tests on Sandy Soils. *Journal of Geotechnical and Geoenvironmental Engineering*, 136(2):366–375, 2010. Cited in page 6

[25] Antoine Le Bouil, Axelle Amon, Sean McNamara, and Jérôme Crassous. Emergence of Cooperativity in Plasticity of Soft Glassy Materials. *Phys. Rev. Lett.*, 112(24):246001, June 2014. Publisher: American Physical Society. Cited in page 6

[26] Jacques Desrues and Gioacchino Viggiani. Strain localization in sand: an overview of the experimental results obtained in Grenoble using stereophotogrammetry. *International Journal for Numerical and Analytical Methods in Geomechanics*, 28(4):279–321, 2004. Cited in page 6

[27] J. P. Bardet and J. Proubet. A numerical investigation of the structure of persistent shear bands in granular media. *Géotechnique*, 41(4):599–613, 1991. Cited in page 6

[28] Jiaying Liu, François Nicot, and Wei Zhou. Sustainability of internal structures during shear band forming in 2D granular materials. *Powder Technology*, 338:458–470, October 2018. Cited in pages 6, 15, 16, 82, 108

[29] Xilin Lü, Sheng Zeng, Liuchi Li, Jiangu Qian, and Maosong Huang. Two-dimensional discrete element simulation of the mechanical behavior and strain localization of anisotropic dense sands. *Granular Matter*, 21(2):37, May 2019. Cited in pages 6, 7, 9, 18, 49

[30] Jiaying Liu, Antoine Wautier, Stéphane Bonelli, François Nicot, and Félix Darve. Macroscopic softening in granular materials from a mesoscale perspective. *International Journal of Solids and Structures*, 193-194:222–238, 2020. Cited in pages 6, 7, 10, 12, 14, 15, 16, 34, 49, 100

[31] Rodaina Aboul Hosn, Luc Sibille, Nadia Benahmed, and Bruno Chareyre. Discrete numerical modeling of loose soil with spherical particles and interparticle rolling friction. *Granular Matter*, 19(1), February 2017. Cited in page 7

[32] Masanobu Oda and Kazuyoshi Iwashita. Study on couple stress and shear band development in granular media based on numerical simulation analyses. *International Journal of Engineering Science*, 38(15):1713–1740, October 2000. Cited in page 7

[33] Matthew R. Kuhn and Katalin Bagi. Contact rolling and deformation in granular media. *International Journal of Solids and Structures*, 41(21):5793–5820, October 2004. arXiv:1901.07342 [cond-mat]. Cited in page 7

[34] Antoinette Tordesillas, Sebastian Pucilowski, Steven Tobin, Matthew R. Kuhn, Edward Andò, Gioacchino Viggiani, Andrew Druckrey, and Khalid Alshibli. Shear bands as bottlenecks in force transmission. *EPL (Europhysics Letters)*, 110(5):58005, June 2015. Cited in page 7

[35] François Nicot, Ali Daouadji, Farid Laouafa, and Félix Darve. Second-order work, kinetic energy and diffuse failure in granular materials. *Granular Matter*, 13(1):19–28, February 2011. Cited in page 7

[36] Poul V. Lade. Static Instability and Liquefaction of Loose Fine Sandy Slopes. *Journal of Geotechnical Engineering*, 118(1):51–71, 1992. Cited in page 7

[37] Dariusz Wanatowski, Jian Chu, and Wai Loke. Drained instability of sand in plane strain. *Canadian Geotechnical Journal*, 47:400–412, March 2010. Cited in page 7

[38] R. Hill. A general theory of uniqueness and stability in elastic-plastic solids. *Journal of the Mechanics and Physics of Solids*, 6(3):236–249, 1958. Cited in page 7

[39] François Nicot, Luc Sibille, and Félix Darve. Failure in rate-independent granular materials as a bifurcation toward a dynamic regime. *International Journal of Plasticity*, 29:136–154, 2012. Cited in page 7

[40] François Nicot and Félix Darve. A micro-mechanical investigation of bifurcation in granular materials. *International Journal of Solids and Structures*, 44(20):6630–6652, 2007. Cited in pages 7, 8

[41] François Nicot, Luc Sibille, and Félix Darve. Bifurcation in granular materials: An attempt for a unified framework. *International Journal of Solids and Structures*, 46(22-23):3938–3947, November 2009. Cited in pages 7, 8

[42] Adriane Clerc. *Mesoscopic scale analysis of inertial transition in granular materials*. PhD thesis, Aix-Marseille Université, 2022. Cited in pages 7, 8, 12

[43] François Nicot and Félix Darve. Diffuse and localized failure modes: Two competing mechanisms. *International Journal for Numerical and Analytical Methods in Geomechanics*, 35(5):586–601, April 2011. Cited in page 7

[44] François Nicot, Luc Sibille, Frédéric Donze, and Félix Darve. From microscopic to macroscopic second-order work in granular assemblies. *Mechanics of Materials*, 39(7):664–684, July 2007. Cited in page 8

[45] Nejib Hadda, François Nicot, Franck Bourrier, Luc Sibille, Farhang Radjai, and Félix Darve. Micromechanical analysis of second order work in granular media. *Granular Matter*, 15(2):221–235, April 2013. Cited in page 8

[46] Nejib Hadda, François Nicot, Richard Wan, and Félix Darve. Microstructural self-organization in granular materials during failure. *Comptes Rendus Mécanique*, 343(2):143–154, February 2015. Cited in page 8

[47] Na Deng. *Micromechanics of Critical State and its emergence in multiscale modeling of soil failure*. PhD thesis, Universite Grenoble Alpes, 2022. Cited in pages XI, 8, 18

[48] M Satake. Fabric tensor in granular materials. In *Deformation and Failure of granular materials*, pages 63–68, Delft; NDL; Rotterdam, 1982. International Union of Theoretical and Applied Mechanics. Cited in page 9

[49] Richard J. Bathurst and Leo Rothenburg. Observations on stress-force-favbric relationship in idealized granular materials. *Mechanics of Materials*, 9(1):65–80, June 1989. Cited in pages 9, 10, 16

[50] L. Rothenburg and R. J. Bathurst. Analytical study of induced anisotropy in idealized granular materials. *Géotechnique*, 39(4):601–614, December 1989. Cited in page 9

[51] Xiang Song Li and Yannis F. Dafalias. Anisotropic Critical State Theory: Role of Fabric. *Journal of Engineering Mechanics*, 138(3):263–275, March 2012. Cited in page 9

[52] Augustus Edward Hough Love. *A treatise on the mathematical theory of elasticity*. Cambridge university press, Cambridge, 1927. Cited in page 10

[53] J Weber. Recherches concernant les contraintes intergranulaires dans lesmilieux pulvérulents. *Bulletin de Liaison des Ponts-et-Chaussées*, 20:1–20, 1966. Cited in page 10

[54] K Bagi. On the definition of stress and strain in granular assemblies through the relation between micro-and macro-level characteristics. *Powders & grains*, 93:117–121, 1993. Cited in page 10

[55] Farhang Radjai, Dietrich E. Wolf, Michel Jean, and Jean-Jacques Moreau. Bimodal Character of Stress Transmission in Granular Packings. *Physical Review Letters*, 80(1):61–64, January 1998. Cited in pages 10, 13, 15, 32, 118

[56] M. Satake. Tensorial form definitions of discrete-mechanical quantities for granular assemblies. *International Journal of Solids and Structures*, 41(21):5775–5791, October 2004. Cited in pages 10, 15

[57] Ngoc-Son Nguyen, Hélène Magoariec, and Bernard Cambou. Local stress analysis in granular materials at a mesoscale. *International Journal for Numerical and Analytical Methods in Geomechanics*, 36(14):1609–1635, October 2012. Cited in pages 10, 15

[58] NP Kruyt and L Rothenburg. Micromechanical definition of the strain tensor for granular materials. *J. Appl. Mech.*, 1996. ASME. Cited in pages 10, 12

[59] Katalin Bagi. Stress and strain in granular assemblies. *Mechanics of Materials*, 22(3):165–177, March 1996. Cited in pages 10, 11, 22, 23, 117

[60] Catherine O'Sullivan, Jonathan D. Bray, and Shaofan Li. A new approach for calculating strain for particulate media. *International Journal for Numerical and Analytical Methods in Geomechanics*, 27(10):859–877, August 2003. Cited in page 10

[61] O. Durán, N.P. Kruyt, and S. Luding. Analysis of three-dimensional micromechanical strain formulations for granular materials: Evaluation of accuracy. *International Journal of Solids and Structures*, 47(2):251–260, January 2010. Cited in page 10

[62] Jie Zhang, Robert P. Behringer, and Isaac Goldhirsch. Coarse-Graining of a Physical Granular System. *Progress of Theoretical Physics Supplement*, 184:16–30, 2010. Cited in page 10

[63] S. Bonelli, O. Millet, F. Nicot, J. Rahmoun, and G. De Saxcé. On the definition of an average strain tensor for two-dimensional granular material assemblies. *International Journal of Solids and Structures*, 49(7-8):947–958, April 2012. Cited in pages 10, 12

[64] P. Dantu. Etude Statistique des Forces Intergranulaires dans un Milieu Pulverulent. *Géotechnique*, 18(1):50–55, March 1968. Cited in page 13

[65] R.P Behringer, Daniel Howell, Lou Kondic, Sarath Tennakoon, and Christian Veje. Predictability and granular materials. *Physica D: Nonlinear Phenomena*, 133(1-4):1–17, September 1999. Cited in page 13

[66] Junfei Geng, G. Reydellet, E. Clément, and R.P. Behringer. Green's function measurements of force transmission in 2D granular materials. *Physica D: Nonlinear Phenomena*, 182(3-4):274–303, August 2003. Cited in page 13

[67] A. Drescher and G. De Josselin de Jong. Photoelastic verification of a mechanical model for the flow of a granular material. In Ruud J. Schotting, Hans C. J. van Duijn, and Arnold Verruijt, editors, *Soil Mechanics and Transport in Porous Media*, pages 28–43. Springer Netherlands, Dordrecht, 2006. Cited in pages 13, 14

[68] Jie Zhang, Trush Majmudar, and Robert Behringer. Force chains in a two-dimensional granular pure shear experiment. *Chaos: An Interdisciplinary Journal of Nonlinear Science*, 18(4):041107, December 2008. Cited in pages XI, 13

[69] Farhang Radjai, Stéphane Roux, and Jean Jacques Moreau. Contact forces in a granular packing. *Chaos: An Interdisciplinary Journal of Nonlinear Science*, 9(3):544–550, September 1999. Cited in page 13

[70] J. F. Peters, M. Muthuswamy, J. Wibowo, and A. Tordesillas. Characterization of force chains in granular material. *Physical Review E*, 72(4):041307, October 2005. Cited in pages XI, 13, 14, 31, 32, 33

[71] Masanobu Oda, Junichi Konishi, and Siavouche Nemat-Nasser. Experimental micromechanical evaluation of strength of granular materials: Effects of particle rolling. *Mechanics of Materials*, 1(4):269–283, December 1982. Cited in pages 14, 34, 54, 101

[72] Farhang Radjai, Michel Jean, Jean-Jacques Moreau, and Stéphane Roux. Force Distributions in Dense Two-Dimensional Granular Systems. *Physical Review Letters*, 77(2):274–277, July 1996. Cited in page 14

[73] Maya Muthuswamy and Antoinette Tordesillas. How do interparticle contact friction, packing density and degree of polydispersity affect force propagation in particulate assemblies? *Journal of Statistical Mechanics: Theory and Experiment*, 2006(09):P09003–P09003, September 2006. Cited in page 14

[74] Antoinette Tordesillas, Jie Zhang, and Robert Behringer. Buckling force chains in dense granular assemblies: physical and numerical experiments. *Geomechanics and Geoengineering*, 4(1):3–16, March 2009. Cited in page 14

[75] Antoinette Tordesillas, David M. Walker, and Qun Lin. Force cycles and force chains. *Physical Review E*, 81(1):011302, January 2010. Cited in pages 14, 15, 16, 30, 34, 100, 101

[76] Antoine Wautier, Stéphane Bonelli, and François Nicot. Flow impact on granular force chains and induced instability. *Physical Review E*, 98(4):042909, October 2018. Cited in pages 14, 16

[77] M. Oda and H. Kazama. Microstructure of shear bands and its relation to the mechanisms of dilatancy and failure of dense granular soils. *Géotechnique*, January 1998. Cited in page 14

[78] A. Rechenmacher, S. Abedi, and O. Chupin. Evolution of force chains in shear bands in sands. *Géotechnique*, 60(5):343–351, May 2010. Cited in page 14

[79] Qicheng Sun, Feng Jin, Jianguo Liu, and Guohua Zhang. Understanding force chain in dense granular materials. *International Journal of Modern Physics B*, 24(29):5743–5759, November 2010. Cited in page 14

[80] Huaxiang Zhu, Francois Nicot, and Félix Darve. Meso-structure evolution in a 2D granular material during biaxial loading. *Granular Matter*, 18(1):3, February 2016. Cited in pages 14, 29, 34, 82, 101

[81] A. Tordesillas, C. A. H. Steer, and D. M. Walker. Force chain and contact cycle evolution in a dense granular material under shallow penetration. *Nonlinear Processes in Geophysics*, 21(2):505–519, April 2014. Cited in pages 14, 34

[82] Masao Satake. New formulation of graph-theoretical approach in the mechanics of granular materials. *Mechanics of Materials*, 16:65–72, 1992. Cited in page 14

[83] Ngoc-Son Nguyen, Hélène Magoariec, Bernard Cambou, and Alexandre Danescu. Analysis of structure and strain at the meso-scale in 2D granular materials. *International Journal of Solids and Structures*, 46(17):3257–3271, August 2009. Cited in pages 16, 30

[84] N. P. Kruyt and L. Rothenburg. On micromechanical characteristics of the critical state of two-dimensional granular materials. *Acta Mechanica*, 225(8):2301–2318, August 2014. Cited in pages 16, 30, 104

[85] P. A. Cundall. A computer model for simulating progressive, large-scale movements in blocky rock systems. *Proceedings of the International Symposium on Rock Mechanics*, 1971. Cited in page 16

[86] P. A. Cundall and O. D. L. Strack. A discrete numerical model for granular assemblies. *Géotechnique*, 29(1):47–65, March 1979. Cited in pages 16, 18

[87] Masao Satake. A discrete-mechanical approach to granular materials. *International Journal of Engineering Science*, 30(10):1525–1533, October 1992. Cited in page 16

[88] Kazuyoshi Iwashita and Masanobu Oda. Rolling Resistance at Contacts in Simulation of Shear Band Development by DEM. *Journal of Engineering Mechanics*, 124(3):285–292, March 1998. Cited in pages 16, 20

[89] Catherine O'Sullivan. Particle-Based Discrete Element Modeling: Geomechanics Perspective. *International Journal of Geomechanics*, 11(6):449–464, December 2011. Cited in page 16

[90] Yanjie Li, Yong Xu, and Colin Thornton. A comparison of discrete element simulations and experiments for 'sandpiles' composed of spherical particles. *Powder Technology*, 160(3):219–228, December 2005. Cited in pages 16, 21

[91] Ning Guo and Jidong Zhao. The signature of shear-induced anisotropy in granular media. *Computers and Geotechnics*, 47:1–15, January 2013. Cited in pages 16, 104

[92] Christoph Kloss, Christoph Goniva, Alice Hager, Stefan Amberger, and Stefan Pirker. Models, algorithms and validation for opensource DEM and CFD-DEM. *Progress in Computational Fluid Dynamics, An International Journal*, 12(2/3):140, 2012. Cited in page 17

[93] Xin Huang, Catherine O'Sullivan, Kevin J. Hanley, and Chung-Yee Kwok. Partition of the contact force network obtained in discrete element simulations of element tests. *Computational Particle Mechanics*, 4(2):145–152, April 2017. Cited in page 17

[94] Ryan C. Hurley and José E. Andrade. Friction in inertial granular flows: competition between dilation and grain-scale dissipation rates. *Granular Matter*, 17(3):287–295, June 2015. Cited in page 17

[95] A. Sufian, A. R. Russell, and A. J. Whittle. Anisotropy of contact networks in granular media and its influence on mobilised internal friction. *Géotechnique*, pages 1–14, March 2017. Cited in page 17

[96] C.M. Wensrich and A. Katterfeld. Rolling friction as a technique for modelling particle shape in DEM. *Powder Technology*, 217:409–417, February 2012. Cited in pages 18, 20

[97] A A Mirghasemi, L Rothenburg, and E L Matyas. Numerical simulations of assemblies of two-dimensional polygon-shaped particles and effects of confining pressure on shear strength. *Soils and Foundations*, 37(3):43–52, 1997. Cited in page 18

[98] C. Nouguier-Lehon, B. Cambou, and E. Vincens. Influence of particle shape and angularity on the behaviour of granular materials: a numerical analysis. *International Journal for Numerical and Analytical Methods in Geomechanics*, 27(14):1207–1226, December 2003. Cited in page 18

[99] Cécile Nouguier-Lehon. Effect of the grain elongation on the behaviour of granular materials in biaxial compression. *Comptes Rendus Mécanique*, 338(10-11):587–595, October 2010. Cited in page 18

[100] Reid Kawamoto, Edward Andò, Gioacchino Viggiani, and José E. Andrade. Level set discrete element method for three-dimensional computations with triaxial case study. *Journal of the Mechanics and Physics of Solids*, 91:1–13, 2016. Cited in page 18

[101] Nicolas Estrada, Emilien Azéma, Farhang Radjai, and Alfredo Taboada. Identification of rolling resistance as a shape parameter in sheared granular media. *Physical Review E*, 84(1):011306, July 2011. Cited in page 20

[102] Changhua Xie, Huaqing Ma, and Yongzhi Zhao. Investigation of modeling non-spherical particles by using spherical discrete element model with rolling friction. *Engineering Analysis with Boundary Elements*, 105:207–220, August 2019. Cited in page 20

[103] Riccardo Rorato, Marcos Arroyo, and Antonio Gens. Microscopic calibration of rolling friction to mimic particle shape effects in DEM. In *Fundamentals and Applications*, page 7. CIMNE, 2019. Cited in page 20

[104] Jun Ai, Jian-Fei Chen, J. Michael Rotter, and Jin Y. Ooi. Assessment of rolling resistance models in discrete element simulations. *Powder Technology*, 206(3):269–282, January 2011. Cited in page 20

[105] C. Thornton and C.W. Randall. Applications of Theoretical Contact Mechanics to Solid Particle System Simulation. In *Studies in Applied Mechanics*, volume 20, pages 133–142. Elsevier, 1988. Cited in page 21

[106] C. Thornton. Numerical simulations of deviatoric shear deformation of granular media. *Géotechnique*, 50(1):43–53, February 2000. Cited in page 21

[107] Josephine M. Boac, R. P. Kingsly Ambrose, Mark E. Casada, Ronaldo G. Maghirang, and Dirk E. Maier. Applications of Discrete Element Method in Modeling of Grain Postharvest Operations. *Food Engineering Reviews*, 6(4):128–149, December 2014. Cited in page 21

[108] Michele Marigo and Edmund Hugh Stitt. Discrete Element Method (DEM) for Industrial Applications: Comments on Calibration and Validation for the Modelling of Cylindrical Pellets. *KONA Powder and Particle Journal*, 32(0):236–252, 2015. Cited in page 21

[109] Stef Lommen, Dingena Schott, and Gabriel Lodewijks. DEM speedup: Stiffness effects on behavior of bulk material. *Particuology*, 12:107–112, February 2014. Cited in page 21

[110] Z. Yan, S. K. Wilkinson, E. H. Stitt, and M. Marigo. Discrete element modelling (DEM) input parameters: understanding their impact on model predictions using statistical analysis. *Computational Particle Mechanics*, 2(3):283–299, September 2015. Cited in page 21

[111] Adnan Sufian, Adrian R. Russell, Andrew J. Whittle, and Mohammad Saadatfar. Pore shapes, volume distribution and orientations in monodisperse granular assemblies. *Granular Matter*, 17(6):727–742, December 2015. Cited in page 31

[112] T. S. Majmudar and R. P. Behringer. Contact force measurements and stress-induced anisotropy in granular materials. *Nature*, 435(7045):1079–1082, June 2005. Cited in pages 34, 54, 101

[113] Lingran Zhang, Nho Gia Hien Nguyen, Stéphane Lambert, François Nicot, Florent Prunier, and Irini Djeran-Maigre. The role of force chains in granular materials: from statics to dynamics. *European Journal of Environmental and Civil Engineering*, 21(7-8):874–895, August 2017. Cited in pages 34, 52

[114] Gaël Combe and Jean-Noël Roux. Discrete numerical simulation, quasistatic deformation and the origins of strain in granular materials, January 2009. arXiv:0901.3842 [physics]. Cited in pages 40, 41

[115] GdR Midi. On dense granular flows. *The European Physical Journal E*, 14(4):341–365, August 2004. arXiv:cond-mat/0312502. Cited in page 41

[116] Frederic da Cruz, Sacha Emam, Michael Prochnow, Jean-Noel Roux, and Francois Chevoir. Rheophysics of dense granular materials : Discrete simulation of plane shear flows. *Physical Review E*, 72(2):021309, August 2005. arXiv:cond-mat/0503682. Cited in page 41

[117] T. Shire, C. O'Sullivan, D. Barreto, and G. Gaudray. Quantifying stress-induced anisotropy using inter-void constrictions. *Géotechnique*, 63(1):85–91, January 2013. Cited in page 43

[118] C. O'Sullivan, J. Bluthé, K. Sejpar, T. Shire, and L.Y.G. Cheung. Contact based void partitioning to assess filtration properties in DEM simulations. *Computers and Geotechnics*, 64:120–131, March 2015. Cited in page 43

[119] Ngoc-Son Nguyen, Habib Taha, and Didier Marot. A new Delaunay triangulation-based approach to characterize the pore network in granular materials. *Acta Geotechnica*, February 2021. Cited in page 43

[120] Mauricio Pinheiro, Richard G Wan, and Qiang Li. Drained-undrained response and other fundamental aspects of granular materials using DEM. *GeoEdmonton*, 2008. Cited in page 49

[121] Xiaoqiang Gu, Maosong Huang, and Jiangu Qian. DEM investigation on the evolution of microstructure in granular soils under shearing. *Granular Matter*, 16(1):91–106, February 2014. Cited in page 49

[122] Na Deng, Antoine Wautier, Yannick Thiery, Zhen-Yu Yin, Pierre-Yves Hicher, and François Nicot. On the attraction power of critical state in granular materials. *Journal of the Mechanics and Physics of Solids*, 149:104300, April 2021. Cited in pages 59, 82, 100

[123] A. Van Oosterom and J. Strackee. The Solid Angle of a Plane Triangle. *IEEE Transactions on Biomedical Engineering*, BME-30(2):125–126, February 1983. Cited in page 80

[124] Huaxiang Zhu, Guillaume Veylon, François Nicot, and Félix Darve. On the mechanics of meso-scale structures in two-dimensional granular materials. *European Journal of Environmental and Civil Engineering*, 21(7-8):912–935, August 2017. Cited in page 100

[125] Dong Hun Kang, Tae Sup Yun, and T. Matthew Evans. Pore orientation of granular materials during biaxial compression. *Computers and Geotechnics*, 59:1–11, 2014. Cited in page 104

[126] M. Roozbahani, Rodrigo Borela, and J. Frost. Pore Size Distribution in Granular Material Microstructure. *Materials*, 10(11):1237, October 2017. Cited in page 117

[127] Na Deng, Antoine Wautier, Antoinette Tordesillas, Yannick Thiery, Zhen-Yu Yin, Pierre-Yves Hicher, and François Nicot. Lifespan dynamics of cluster conformations in stationary regimes in granular materials. *Physical Review E*, 105(1):014902, January 2022. Cited in page 118

FOLIO ADMINISTRATIF

THESE DE L'INSA LYON, MEMBRE DE L'UNIVERSITE DE LYON

NOM : GONCALVES DE OLIVEIRA CHUEIRE **DATE de SOUTENANCE :** 30/06/2023
Prénoms : Joao

TITRE: Generalization of 3D meso-structures for a micro-structural approach of soil behavior

NATURE : Doctorat **Numéro d'ordre :** 2023ISAL0045
École doctorale : Mécanique, Énergétique, Génie civil et Acoustique (MEGA)
Spécialité : Génie Civil

RESUME :

Dans le domaine des matériaux granulaires, le lien entre les variables microscopiques (forces de contact et déplacements) et les variables macroscopiques (contraintes et déformations) nécessite l'utilisation d'une échelle intermédiaire appelée échelle mésoscopique. À cette échelle, les boucles sont particulièrement intéressantes car elles sont riches d'informations et sont les seules à ne pas être définies dans des conditions 3D. Ces boucles forment des polygones simples capables de diviser un milieu 2D en espaces fermés plus petits se sorte à ce que la somme de la surface des boucles est égale à la surface totale de l'échantillon. Par conséquent, l'application directe de la définition des boucles à des conditions 3D conduit à la formation de formes 2D incapables de représenter un volume.

Dans cette thèse, nous proposons d'étendre la définition des boucles au cas tridimensionnel. Dans un premier temps, une méthode d'identification des boucles (2D) basée sur la fusion de cellules créées par une triangulation de Delaunay est analysée. Ensuite, une extension de cette procédure à des conditions 3D est proposée. Comme les structures identifiées ne sont plus représentatives du concept mathématique de boucle (ou cycle), elles sont appelées Clusters. Ces structures se révèlent plus complexes que leurs homologues en 2D, ce qui nécessite un plus grand nombre de métriques pour les quantifier. C'est pourquoi les concepts de taille et d'ordre se distinguent respectivement par le nombre de grains et le nombre de frontières externes. En outre, le concept de déformabilité est introduit comme moyen de quantifier l'interconnectivité d'une structure en clusters.

Une série d'essais triaxiaux 3D complexes a été réalisée grâce au logiciel LIGGGHTS qui est basé sur la méthode des éléments discrets (DEM). Par la suite, une application a été développée pour analyser les propriétés des clusters pendant le trajet de chargement et en fonction de la proximité d'autres structures granulaires internes coexistantes (chaînes de force et bandes de cisaillement).

Il est démontré que l'indice des vides moyen et la déformabilité (capacité à se déformer) des clusters augmentent avec leur taille. En outre, une augmentation du nombre de clusters plus denses est observée pendant la phase de contraction de la déformation macroscopique et des clusters plus lâches pendant la dilatation. Enfin, une relation entre les chaînes de force, les bandes de cisaillement et les clusters est établie. Toutes les caractéristiques des clusters mentionnées sont connues pour les boucles 2D. Les clusters peuvent donc être considérés comme des extensions des boucles dans des conditions 3D.

MOTS-CLÉS :
Méthode des éléments discrets (DEM), Milieux granulaires, Mésostructures, Clusters, Tessellation de Delaunay, Chaines de force, Bande de cisaillement.
Discrete element method (DEM), Granular materials, Mesostructures, Clusters, Loops, Delaunay tessellation, Force chains, Shear bands.

Laboratoire (s) de recherche : GEOMAS

Directeurs de thèse :

DAOUADJI Ali,	Professeur des Universités, INSA Lyon	Directeur thèse
NICOT François,	Professeur des Universités, Université Savoie Mont-Blanc	Co-directeur thèse
WAUTIER Antoine,	Ingénieur Docteur, INRAE	Co-encadrant thèse

Président de jury : RADJAI Farhang

Composition du jury :

O'SULLIVAN Catherine	Professeure des Universités, Imperial College London	Rapporteur
WAN Richard	Professeur des Universités, University of Calgary	Rapporteur
DARVE Félix,	Professeur des Universités, Université Grenoble Alpes	Examinateur
KUHN Matthew	Professeur des Universités, University of Portland,	Examinateur
NOUGUIER-HERON Cécile,	Maître de Conférences, Ecole Centrale de Lyon	Examinatrice
RADJAI Farhang,	Directeur de Recherche, Université de Montpelier	Examinateur
DAOUADJI Ali	Professeur des Universités, INSA Lyon	Directeur thèse
NICOT François,	Professeur des Universités, Université Savoie Mont-Blanc	Co-directeur thèse